

Spin-to-charge conversion in low-symmetry MoTe₂/graphene van der Waals heterostructures

Nerea Ontoso Martínez

Supervisors: Dr. M. Reyes Calvo Urbina and
Prof. Fèlix Casanova

A thesis presented for the degree of
Doctor of Philosophy



University of the Basque Country
March 2022

*A mis padres.
A Lea y Greta.*

Resumen

La fabricación de los circuitos integrados se basa en la tecnología CMOS (del inglés *Complementary Metal Oxide Semiconductor*). En las últimas décadas, ha tenido lugar una exitosa miniaturización de los dispositivos electrónicos, y por lo tanto de los transistores CMOS. Sin embargo, actualmente, el tamaño de los transistores CMOS está alcanzando el límite cuántico, surgiendo la necesidad de una tecnología post-CMOS. Se han planteado diferentes estrategias como alternativa a la tecnología CMOS, entre ellas destaca el torque por transferencia de espín mediante efecto Hall de espín. Algunas de las diferentes propuestas post-CMOS y de almacenaje y lectura de datos en componentes magnéticos se basaban en la tecnología de espín, también denominada *espintrónica*. Por lo que incentivaron el estudio de la generación, transporte y detección de corrientes de espín, así como la conversión de corrientes de espín a carga en materiales que poseen interacción espín-órbita. Recientemente, en 2019, la empresa Intel propuso un dispositivo magnetoeléctrico de espín-órbita, en el que el estado magnético es leído a través del efecto Hall de espín, por lo que el estudio del control y manipulación de las corrientes de espín se ha visto estimulado más si cabe.

Mientras que la electrónica tradicional hace uso de la carga del electrón, la espintrónica usa el momento angular intrínseco que poseen los electrones. En el caso de la corriente de carga, hay un flujo neto de carga pero no de momento angular, conocido como *espín*. Por contra, en la corriente pura de espín se produce un flujo de momento angular pero no de carga. La corriente polarizada de espín se caracteriza por un flujo tanto de carga como de momento angular.

Basándose en observaciones previas, como la magnetorresistencia gigante descubierta por Fert y Grünberg, y el modelo de dos corrientes desarrollado

por Campbell, se consiguió una inyección efectiva de espines en materiales no magnéticos. Dicha inyección se puede alcanzar mediante diversas técnicas. En particular, la empleada en esta Tesis es la inyección eléctrica. Al aplicar una corriente eléctrica entre un material ferromagnético, caracterizado por una presencia mayoritaria de electrones con cierta polarización de espín, y un material no magnético, se crea una acumulación de espín en la interfaz entre ambos materiales. Esta acumulación de espín difunde en el material no magnético una distancia característica – la longitud de difusión de espín. La difusión de espín puede ser detectada usando otro material ferromagnético en contacto con el canal de espín. El voltaje generado entre el material ferromagnético actuando como detector y el canal no magnético se ve modificado por la presencia de la difusión de espines en el canal. Si la inyección de carga se encuentra separada del circuito de voltaje, esta técnica se conoce como no local y es la base para las válvulas de espín empleadas en esta Tesis.

En 2004, Geim y Novoselov aislaron, por primera vez, grafeno, una capa atómica de carbono ayudados de una cinta adhesiva. Este descubrimiento revolucionó la ciencia de materiales, iniciando un nuevo campo de estudio, el de materiales bidimensionales. Años después de su descubrimiento, el grafeno se postuló como el candidato ideal para el transporte de espín, transformando el mundo de la espintrónica.

Los materiales bidimensionales presentan tanto diversidad en la composición química, como en las diferentes fases cristalinas en las que se pueden encontrar. La estructura cristalina de estos materiales gobierna la simetría de los procesos físicos permitidos, así como su propiedades electrónicas. Las capas de átomos constituyentes de ciertos materiales bidimensionales se encuentran unidas por fuerzas de van der Waals, que se caracterizan por ser unas fuerzas débiles. Por lo tanto, estos materiales son fácilmente exfoliables usando una cinta adhesiva. Este es el caso de MoTe_2 , un material con fuerzas de van der Waals entre sus capas atómicas, que puede estar presente en diferentes estructuras cristalinas. Por otra parte, debido a su composición química, MoTe_2 posee una fuerte interacción espín-órbita por lo que los procesos de conversión de espín a carga pueden darse en este material.

Esta Tesis versa sobre el estudio de los procesos de conversión de espín a carga en MoTe_2 . Para dicha investigación, este material se combina con grafeno, que actúa como canal de espín, creandose una estructura denominada válvula de espín lateral. Tanto el grafeno como la lámina de MoTe_2 empleadas en los dispositivos son exfoliados usando una cinta adhesiva. La estructura cristalina

de MoTe_2 posee una cadena de átomos de molibdeno a lo largo de un eje cristalino, que coincide con la dirección preferencial de rotura a la hora de exfoliar el material. Es por ello que las láminas de MoTe_2 tienden a ser alargadas. Para el grafeno, ayudados de un microscopio óptico, se identifican aquellas láminas con forma de aguja sobre las que se transferirá el MoTe_2 . Ayudados de un sistema de micro-manipulación, la lámina de MoTe_2 se sitúa encima del grafeno, de tal forma que el eje largo del grafeno es perpendicular al eje largo del MoTe_2 . La heteroestructura de grafeno y MoTe_2 se mantiene unida gracias a las fuerzas de van der Waals entre ambos materiales. Posteriormente, se disponen contactos eléctricos y ferromagnéticos. Aplicando una corriente eléctrica entre el contacto ferromagnético, que sita encima del grafeno, y un extremo del grafeno, se produce una acumulación de espines en la interfaz que difunde en el canal de grafeno. Cuando esta acumulación de espín alcanza el MoTe_2 , se produce la absorción de los espines. Debido a la fuerte interacción espín-órbita que posee el MoTe_2 , los espines absorbidos son convertidos a corriente de carga. Midiendo el voltaje a lo largo de la lámina de MoTe_2 , asociado a dicha corriente de carga, se puede observar la señal correspondiente a la conversión de espín a carga. Esta configuración de medida no local es la configuración estándar en el estudio de conversión de espín a carga en una válvula lateral de espín.

La generación de una corriente de carga a raíz de una corriente de espín puede suceder en el volumen del material con fuerte interacción espín-órbita, en este caso el MoTe_2 , o en la interfaz entre ambos materiales. El primero de los procesos es conocido como efecto Hall de espín, mientras que el segundo se corresponde con el efecto Edelstein. Las configuraciones que dan lugar a conversión de espín a carga están dictadas por las simetrías del material con interacción spin-órbita o de la interfaz. Es por ello que es importante caracterizar la fase cristalina y la dirección de los ejes cristalinos en las láminas de MoTe_2 .

El **Capítulo 4** presenta una caracterización de las láminas de MoTe_2 . Primeramente, se identificará la orientación de los ejes cristalinos de las láminas de este material. Mediante la espectroscopía Raman polarizada y la microscopía electrónica de transmisión y barrido, se determina que el eje largo de las láminas de MoTe_2 se corresponde con la cadena de átomos de molibdeno. Esta determinación es crucial para el posterior análisis de resultados de conversión de espín a carga. A temperatura ambiente el MoTe_2 utilizado en esta Tesis se encuentra presente en la fase cristalina $1T'$. En la literatura se reporta una transición estructural fase de la fase $1T'$ a la fase $1T_d$ en el cristal de MoTe_2 . Sin embargo,

mediante espectroscopia Raman a baja temperatura y medidas eléctricas de la resistencia de las láminas empleadas, no se observan indicios de dicha transición de fase. A fin de realizar una caracterización completa del MoTe_2 , se estudia el comportamiento de la resistencia eléctrica cuando el material es sometido a campos magnéticos a lo largo de diferentes direcciones cristalinas. Además, se estudia el transporte de espín en una lámina de MoTe_2 . Este estudio es motivado por trabajos experimentales y teóricos que pronostican una longitud de difusión de espín relativamente grande en este material. Desafortunadamente, efectos espurios en las medidas dificultan la detección de transporte de espín directamente en el MoTe_2 .

Una vez está caracterizada la estructura cristalina, así como la dirección de los ejes cristalinos en las láminas de MoTe_2 , se procede al estudio de la conversión de espín a carga en heteroestructuras combinadas con grafeno. La polarización de los espines que son absorbidos por el MoTe_2 es controlada con ayuda de un campo magnético externo. La presencia del campo magnético induce precesión de los espines mientras difunden en el grafeno, y también modifican la dirección de la magnetización del contacto ferromagnético encargado de inyectar los espines. Las distintas contribuciones de conversión de espín a carga debidas a las diferentes polarizaciones de espín inducen una variación en el voltaje no local medido a lo largo de la lámina de MoTe_2 en función del campo magnético. Por lo tanto, la dependencia del voltaje con el campo magnético permite extraer la señal correspondiente a cada polarización de espín. Este estudio se realiza a altas temperaturas en el **Capítulo 5** y a bajas temperaturas en el **Capítulo 6**.

A altas temperaturas, se observa la conversión de espín a carga de una componente permitida por la simetría cristalina tanto del MoTe_2 como de la interfaz, y de una componente prohibida en ambos casos. Para la observación de dicha componente prohibida, las simetrías cristalinas del sistema deben ser reducidas, barajándose dos hipótesis: una fuerza de tipo cizalla en el MoTe_2 desarrollada durante la fabricación de la muestra, o una interfaz entre el grafeno y el MoTe_2 sin simetrías, en las que cualquier proceso de conversión de espín a carga esté permitido. Considerando que los procesos suceden en el volumen del MoTe_2 , ambos procesos muestran una eficiencia comparable a los materiales prototípicos usados en espintrónica.

Por otra parte, a bajas temperaturas, un nuevo efecto que provoca la conversión de espín a carga es relevante, el efecto de *proximidad*. La interacción espín-órbita es muy débil en el grafeno, sin embargo, cuando entra en contacto

con un material con fuerte interacción espín-órbita, se induce un aumento de la misma en el grafeno. Por lo tanto, efectos de conversión de espín a carga pueden ocurrir en el propio grafeno. A baja temperatura se observa una nueva contribución a la conversión de espín a carga, que es adscrita al efecto de proximidad en el grafeno.

En la configuración estándar de medida empleada en los Capítulos 5 y 6, la medida de voltaje está restringida en una dirección, a lo largo de la lámina de MoTe_2 , permitiendo detectar solo aquellos procesos de conversión de espín a carga que generen una corriente de carga en dicha dirección. En materiales de baja simetría, como es el caso de MoTe_2 , la generación de la corriente de carga puede suceder en cualquiera de las tres direcciones espaciales y es por ello que se necesita una configuración de medida que aporte versatilidad a la hora de detectar nuevas componentes de conversión.

Tanto la conversión mediante el efecto Hall de espín como mediante el efecto Edelstein tienen su efecto recíproco: el efecto Hall de espín inverso y el efecto Edelstein inverso. Mediante el teorema de reciprocidad de Onsager, la eficiencia de la conversión de espín a carga es equivalente a la de carga a espín. Esto permite que, en vez de medir el voltaje a través de la lámina de MoTe_2 , se pueda aplicar la corriente de carga a través de él, y generar una corriente de espín que viaja por el canal de grafeno y resulta en un voltaje que es medido usando el contacto ferromagnético que anteriormente hacía las veces de inyector de espines. Gracias a esto, usando una configuración de corriente en 3 dimensiones (3D) a través del MoTe_2 , nos permite acceder a configuraciones de conversión de carga a espín que permanecían inaccesibles en la configuración estándar.

En la configuración de corriente-3D, la corriente de carga se aplica desde un extremo de la lamina de MoTe_2 , a través de la interfaz con el grafeno, hasta un extremo del grafeno. De esta forma, se consigue que la corriente de carga dentro de la lámina de MoTe_2 tenga componentes en las tres direcciones espaciales. Esta corriente de carga generará una polarización de espín que difundirá en el grafeno. Usando un contacto ferromagnético dispuesto encima del grafeno, se mide el voltaje no local entre dicho contacto y el grafeno. Iterando la medida mientras se aplica la corriente de carga a lo largo de diferentes combinaciones de las tres direcciones espaciales de la lámina de MoTe_2 , se puede establecer una relación entre la señal de espín medida y la dirección de corriente eléctrica que la genera. Debido a la alta calidad de la interfaz entre el grafeno y el MoTe_2 , podemos combinar la técnica estándar de medida junto con la técnica de corriente-3D, permitiendo obtener una visión global de los procesos de con-

versión de espín a carga. Junto con la señal no convencional ya reportada en los Capítulos 5 y 6, se observa una conversión de espín a carga permitida por las simetrías cristalinas del MoTe_2 y de la interfaz. Esta componente es solo accesible debido a la versatilidad de la configuración de corriente-3D en combinación con la alta calidad de la interfaz de la heteroestructura. Estos resultados son presentados en el **Capítulo 7**.

La baja simetría que presenta el MoTe_2 en la fase $1T'$ hace que la heteroestructura de grafeno/ MoTe_2 presente diferentes configuraciones que dan lugar a conversión de espín a carga. Sin embargo, deducir el origen exacto de cada proceso de conversión de espín a carga resulta complejo. Independientemente de su origen, los materiales de baja simetría con alta eficiencia en la conversión de espín a carga, como es el caso de la heteroestructura de grafeno/ MoTe_2 , se postulan como ingredientes necesarios para la siguiente generación de dispositivos espintrónicos, debido a su reducido tamaño, a su versatilidad y eficiencia en los procesos de conversión de espín a carga.

Abstract

This Thesis presents an extensive study of the spin-to-charge conversion processes that occur in graphene/MoTe₂ van der Waals heterostructures. The spin-to-charge conversion stems from the spin-orbit coupling that materials with large atomic number present. Two different intrinsic mechanisms can lead to such conversion: spin Hall effect and Edelstein effect. For both effects, the crystal symmetries dictate which spin-to-charge conversion processes are allowed. In particular, for the Edelstein effect to occur, the inversion symmetry of the system has to be broken. Therefore, it is a process that occurs in the surfaces, interfaces, and in certain bulk materials with broken inversion symmetry.

In materials that hold high crystal symmetry and spin-orbit interaction, such as Pt, the conversion is restricted to an orthogonal configuration, where the spin current, charge current, and spin polarization have to be mutually perpendicular. In contrast, in low-symmetry materials, other configurations can lead to spin-to-charge conversion. In this Thesis, we study 1T'-MoTe₂, which is a low-symmetry material with strong spin-orbit interaction. Moreover, MoTe₂ is a van der Waals material, which means is easily exfoliable and can be easily combined with another van der Waals material, such as graphene.

In order to study the spin-to-charge conversion processes in MoTe₂, a graphene-based lateral spin valve is employed. This device consists of an elongated needle-like graphene flake which acts as spin transport channel and, on top of it, a MoTe₂ flake is placed. The stamping is performed in such a way that the long direction of the MoTe₂ flake is perpendicular to the one of graphene. To electrically connect the heterostructure, metal contacts are patterned at the ends of the graphene and MoTe₂ flakes, and ferromagnetic electrodes added to the graphene channel to act as spin injector and detectors.

In the non-local lateral spin valve configuration, the charge current and the voltage paths are separated so that spurious effects are avoided. In the standard spin-to-charge configuration in a lateral spin valve, the charge current is applied from the ferromagnetic electrode, patterned on top of graphene, to one end of the graphene flake. Therefore, a spin accumulation is created at the interface between the two materials. The generated spin accumulation will diffuse in the graphene channel until it reaches the MoTe₂ flake. In the graphene/MoTe₂ region, the spin-to-charge conversion is expected to occur. On the one hand, the spins can get absorbed into the MoTe₂, where will be converted into charge current via the spin Hall effect. On the other hand, graphene gets *proximitized* in contact with a spin-orbit coupling material, enabling the spin-to-charge conversion either via the spin Hall effect or the Edelstein effect.

Regardless of the spin-to-charge conversion origin, the generated charge current induces a non-local voltage along the MoTe₂ that is probed using the electrical contacts on the flake. In order to set the spin polarization along different directions, an external magnetic field is used. The magnetic field will control the spin polarization direction by two means: (*i*) by inducing spin precession in the spins diffusing in graphene and, (*ii*) for large enough values of the magnetic field, by pulling the direction of the ferromagnet magnetization towards the direction of the field. By measuring the non-local voltage as a function of the external magnetic field along different directions, it is possible to establish an unambiguous relation between the non-local voltage measured signal and the spin polarization that is converted into charge current. By fitting these data to a 1D spin diffusion model, it is possible to extract the efficiency of the spin-to-charge conversion. Because of Onsager reciprocity, the efficiency of the spin-to-charge conversion processes is identical to the charge-to-spin conversion, regardless of its origin. In the case of the charge-to-spin conversion measurement, the voltage and current probes are swapped with respect to the spin-to-charge configuration, therefore a charge current flows through the MoTe₂ flake, resulting into a spin accumulation injected into the graphene channel, later detected by proving the non-local voltage between the ferromagnet and the graphene channel.

We first characterized the 1T'-MoTe₂ flakes in **Chapter 4**. Due to the crystal symmetry phase, MoTe₂ presents in-plane anisotropy, therefore it is crucial to determine the crystal axes orientation of our flakes to know which spin-to-charge conversion processes are allowed by the crystal symmetry. MoTe₂ presents a molybdenum atom chain along one of the in-plane crystal axes. By

using polarized Raman spectroscopy and scanning transmission electron microscopy, we found that the preferential cleaving direction of the MoTe_2 flakes corresponds to the crystal axis where the Mo-atom chain lies. As a consequence, the resulting exfoliated MoTe_2 flakes tend to be elongated along the Mo-chain direction. Moreover, $1T'$ - MoTe_2 is expected to show a first-order phase transition from the $1T'$ to the $1T_d$ phase in bulk MoTe_2 crystals. This phase transition is associated with the splitting of a certain polarized Raman peak. When performing low-temperature polarized Raman spectroscopy, such phase transition was observed in the bulk crystal while it was absent in the MoTe_2 flakes used in our devices, exfoliated from the same crystal. Furthermore, by measuring the resistance of the MoTe_2 as a function of temperature, no fingerprint of phase transition is observed, indicating that the MoTe_2 flakes stabilise in the $1T'$ phase. To further characterize the MoTe_2 flakes, their magnetoresistive behaviour is measured. The longitudinal resistance is probed upon the presence of an external magnetic field along the different crystallographic axes of the MoTe_2 flakes. We observe that magnetoresistance is largest at low temperatures and when the magnetic field is applied along the van der Waals stacking direction. Furthermore, MoTe_2 flake has been studied as spin channel where the spins were directly injected by using ferromagnetic electrodes on top. Unfortunately spurious effects coming from the anomalous magnetoresistance hinder the proper spin detection.

Once MoTe_2 is characterized, we study the spin-to-charge conversion process using a graphene-based lateral spin valve device. At moderate-high temperatures, between 300 K and 75 K, two distinct contributions arising from the spin-to-charge conversion of two different spin orientations are observed, as presented in **Chapter 5**. In addition to the conventional configuration, where the spin polarization, the charge and spin currents are mutually perpendicular, an unconventional conversion, where the spin polarization and the induced charge current are parallel, is also observed. Whereas the conventional configuration is allowed by the crystal symmetries, the unconventional configuration requires the symmetries of the system to be reduced. One possibility is that the only $1T'$ - MoTe_2 crystal mirror is broken due to shear strain developed during the fabrication of the devices. Another possibility is that the mirror planes of graphene are not aligned with the MoTe_2 mirror plane and, thus, a non-symmetric interface is created, allowing generating a charge current from any spin polarization and spin current direction. If the spin-to-charge conversion is assumed to occur in bulk MoTe_2 , the efficiencies of the conventional and the unconventional processes are, in both cases, comparable to the best spin Hall

metals and topological insulator materials.

At low temperatures, the proximity-induced spin-to-charge conversion is expected to become relevant. As reported in **Chapter 6**, along with the generation of charge current from any in-plane spin polarization, also displayed at moderate-high temperatures, an extra contribution is observed. In this case, an out-of-plane spin polarization induces spin-to-charge conversion. The origin of this signal can be ascribed to the inverse spin Hall effect in the proximitized graphene, or to a non-orthogonal spin Hall effect in the 1T'-MoTe₂, permitted by the crystal symmetries. Since the presence of this conversion is dominant at low temperatures, this effect is more likely to arise from proximitized graphene via the spin Hall effect.

The standard spin-to-charge configuration fails to capture all the allowed spin-to-charge conversion processes that can occur in the graphene/MoTe₂ heterostructure. In order to access other spin-to-charge configurations allowed by symmetries, a new 3D-current configuration is employed in **Chapter 7**. On the grounds of Onsager reciprocity, and thanks to the high-quality interface between graphene and MoTe₂, we performed thorough charge-to-spin conversion studies by combining the standard configuration, where the charge current is applied along the spin-to-charge conversion material, with a new configuration, where the charge current flows in the three directions within the heterostructure (3D-current configuration). On top of the unconventional spin-to-charge conversion already observed, this configuration reveals a new spin generation polarized in-plane perpendicular to the charge current. This configuration, inaccessible through the standard configuration, gives new insights into the charge-to-spin processes occurring in the system. The origin of the observed new signal can be attributed to the spin Hall effect in MoTe₂ or the Edelstein effect in graphene.

MoTe₂/graphene van der Waals heterostructure has been demonstrated to show a plethora of spin-to-charge conversion processes. Although determining the precise origin of each component remains challenging, the large efficiencies observed overall make this system appealing for potential applications where efficient spin-to-charge conversion is required such as spin-orbit torque for magnetic memories, or a magnetoelectric spin-orbit device recently proposed by Intel. The combination of graphene with low-symmetry materials, where charge current can be induced with different spin polarizations, opens the door to new architectures for the mentioned devices.

Contents

Resumen	iii
Abstract	ix
1 The history of spintronics	1
1.1 From fundamentals to device technology	2
1.2 Electrical spin injection	5
1.3 Spin transport and detection	8
1.3.1 Hanle spin precession.	12
1.3.2 Spin relaxation mechanisms	13
1.4 Spin-to-charge conversion	13
1.4.1 Spin Hall effect	14
1.4.1.1 Contributions to the Spin Hall Effect	16
1.4.1.2 Spin Hall effect in metals	17
1.4.1.3 Spin absorption experiment in metals	18
1.4.2 Edelstein Effect	20
1.5 2D materials: a breakthrough in spintronics	23
1.5.1 Graphene	23
1.5.2 Other 2D materials	25
1.5.2.1 Low-symmetry TMDCs	26
1.5.3 van der Waals heterostructures	27
1.6 This Thesis	28
2 Graphene-based lateral spin valves	31
2.1 Spin transport in pristine graphene	32
2.1.1 Electrical spin injection into graphene	32
2.1.2 Spin transport and detection in graphene	33
2.1.2.1 Hanle precession	34
2.1.2.2 Spin relaxation mechanisms in graphene	36
2.2 Spin-to-charge conversion in graphene-based heterostructures	37
2.2.1 Due to SHE	38
2.2.1.1 In the SOC material	38

2.2.1.2	In the proximitized graphene	40
2.2.2	Due to Edelstein effect	42
2.2.2.1	In the SOC material	42
2.2.2.2	In the proximitized graphene	43
2.2.3	Disentangling the SCC signals in graphene-based LSV	44
2.2.3.1	Applying in-plane magnetic field along the hard axis of the FM injector (B_x)	45
2.2.3.2	Applying out-of-plane magnetic field (B_z)	48
2.2.3.3	Applying in-plane magnetic field along the easy axis of the FM injector (B_y)	50
2.3	1D spin diffusion model for SHE in a low-symmetry material	51
3	Experimental techniques	57
3.1	Sample fabrication	58
3.1.1	Graphene exfoliation via Scotch-tape technique	58
3.1.2	MoTe ₂ exfoliation in inert atmosphere	60
3.1.3	Stamping process	60
3.1.4	Contact patterning and metallization	62
3.1.4.1	Standard eBL process	62
3.1.4.2	Metal deposition	64
3.1.4.3	Lift-off	66
3.1.4.4	Fast FM electrodes oxidation	66
3.2	Sample characterization	67
3.2.1	Electrical measurements	67
3.3	Material characterization	69
3.3.1	Scanning transmission electron microscopy	69
3.3.2	Transmission electron microscopy	69
3.3.3	Atomic force microscopy	70
3.3.4	Polarized Raman spectroscopy	70
4	Molybdenum ditelluride characterization	73
4.1	Introduction	73
4.2	Crystal axes determination	74
4.3	Low-temperature polarized Raman spectroscopy	76
4.4	Magnetoresistance measurements	77
4.5	Spin transport in 1T'-MoTe ₂	79
5	Large multidirectional spin-to-charge conversion in MoTe₂ at room temperature	85
5.1	Introduction	85
5.2	Experimental details	86

5.3	Spin-to-charge conversion by applying in-plane magnetic fields	88
5.4	Spin-to-charge conversion by applying out-of-plane magnetic field	91
5.5	Quantification of the results	94
5.6	Conclusion	98
5.7	Appendices	98
5.7.1	Spin absorption	98
5.7.2	Temperature dependence of the spin-to-charge conversion measurements	100
5.7.3	Spin transport in the reference graphene channel and easy axis determination	104
5.7.4	Interface resistance between graphene and MoTe ₂	106
5.7.5	Quantification of the efficiency	107
5.7.6	Reproducibility	109
5.7.7	Spin injection from both sides of the MoTe ₂ flake	110
5.7.8	Onsager reciprocity	111
6	Low-temperature spin-to-charge conversion in graphene/MoTe₂	113
6.1	Introduction	113
6.2	Spin-to-charge conversion by applying in-plane magnetic fields	114
6.3	Unveiling the origin of each spin-to-charge conversion contribution	117
6.4	Conclusion	120
6.5	Appendices	121
6.5.1	Spin-to-charge conversion by applying out-of-plane magnetic field	121
6.5.2	Spin transport in the reference graphene channel	122
6.5.3	Temperature dependence of the interface resistance, MoTe ₂ resistivity, and graphene sheet resistance	122
6.5.4	Reproducibility	122
7	Spin-to-charge conversion in a high-quality interface graphene/MoTe₂ van der Waals heterostructure	125
7.1	Introduction	125
7.2	Device fabrication and characterization	127
7.3	Spin-to-charge conversion measurements	128
7.3.1	SCC in the standard configuration	129
7.3.2	SCC in the 3D-current configuration	131
7.4	Discussion of the results	133
7.5	Conclusion	136
8	Conclusions and future perspectives	139
	Publications	143

Acknowledgements	145
Bibliography	146

Chapter 1

The history of spintronics

A successful downscaling of electronic devices has occurred over the past decades. Nowadays, the size of the CMOS-FETs (Complementary Metal Oxide Semiconductor - Field Effect Transistor) is reaching its quantum limit, triggering the research for beyond-CMOS technology. The reduced size of the CMOS devices gives rise to an increment in the tunneling and leakage current, having direct impact on their performance. In terms of materials challenges, the continued scaling of devices hinders the reliable insulation of the dielectric material. Moreover, the large number of CMOS devices per unit-area increases the power consumption and demands efficient thermal dissipation [1–3]. Benchmarking devices points the way on how beyond-CMOS technology has to evolve. A recent work of benchmarking devices includes new switching mechanism for the different computational variables, such as spin-orbit or spin-transfer torque via spin Hall effect, ferroelectric and piezoelectric switchings [2]. In this work, spin-based devices were postulated as post-CMOS candidates. Reducing the power consumption is of vital importance and, to do so, Intel proposed in 2019, a magnetoelectric spin-orbit (MESO) device combining ferroelectric/magnetoelectric switching and spin Hall effect readout of magnetic elements, which enables voltage scalability, non-volatile logic-in-memory, and compatibility with traditional architecture [4]. In the forthcoming sections, an overview about the development of spintronics from metal to bidimensional material-based devices is given.

1.1 From fundamentals to device technology

Apart from charge, electrons possess intrinsic angular momentum, known as *spin*, which can be used to carry information in the same way charge has been used in *electronics*. The field that aims at transporting and manipulating spin currents is called *spintronics*. The birth of spintronics dates back to the discovery of giant and tunneling magnetoresistance phenomena. Magnetoresistance is defined as a change in the electrical resistance upon the presence of an external magnetic field.

In 1936, Mott observed how, at sufficient low temperatures, electrons with opposite spin do not mix during scattering events and, hence, conductivity can be expressed as a sum of two independent terms [5]. Later, the two-current model was extended by Campbell and co-workers in 1967 and Fert and Campbell in 1968 [6, 7]. This model paved the way for the discovery of giant magnetoresistance (GMR) in 1988. The groups led by Peter Grünberg [8] and Albert Fert [9] discovered, simultaneously and independently that the resistance of a magnetic multilayer changed dramatically, upon the presence of an external magnetic field, showing a *giant* magnetoresistance effect. Not only the discovery but its explanation earned Grünberg and Fert the Nobel prize in Physics, in 2007.

The magnetic multilayer system showing GMR consisted of two ferromagnetic (FM) metallic layers separated by a non-magnetic (NM) metallic slab with nanometric thickness. This structure is also known as *vertical spin valve*. A FM material, due to the exchange interaction, possesses a majority of electrons with spin in a certain direction giving rise to the overall magnetization. The direction of the magnetization of the two FM layers can be either parallel to each other [parallel configuration in Fig. 1.1(a)] or antiparallel [Fig. 1.1(c)]. According to the two-current model, the resistance for an electron flowing through the trilayer device will depend on the relative orientation of the electron spin and the magnetization of the FM. When a charge current (I_c), defined as the same amount of spin-up and spin-down electrons moving in the same direction, is applied to the system, if the electron spin is parallel to the direction of the magnetization of the FM, the resistance for that electron to travel will be, say, high. However, if the electron spin is antiparallel to the magnetization, the resistance will be low. The two-channel model resistor scheme for parallel and antiparallel configurations is represented in Fig. 1.1(b) and Fig. 1.1(d), respectively.

In the case of parallel alignment between the magnetization of the FMs, the electron spin can be either parallel or antiparallel to the magnetization of both FM. If it is parallel, it will go through a high resistance path as sketched in the red branch in the equivalent circuit in Fig. 1.1(b). In contrast, if it is antiparallel, the electron will go through a low resistance state corresponding to the blue branch in Fig. 1.1(b). On the other side, for the antiparallel alignment between the magnetization of the FMs, the electrons will go through a high and a low resistance states, as represented in the resistor scheme in Fig. 1.1(d). The total resistance in the parallel configuration (R_P) is lower than the total resistance in the antiparallel configuration (R_{AP}).

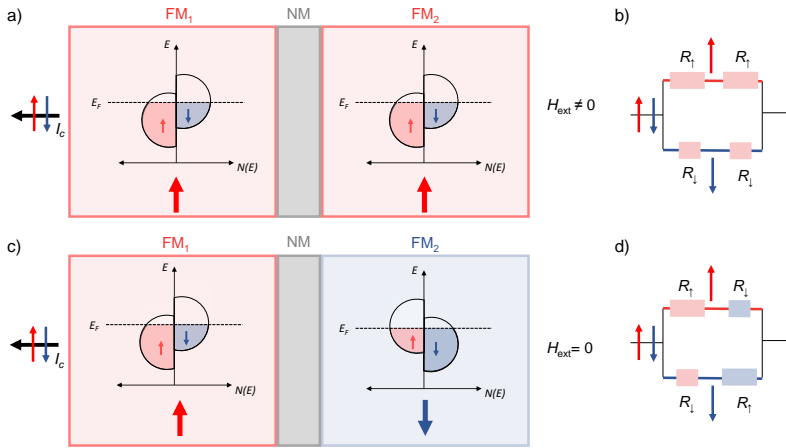


Figure 1.1: Schematics of a vertical spin valve showing GMR in the parallel and antiparallel configurations and the corresponding resistor scheme. The FM layers (light red and light blue) on both sides are separated by a NM layer (gray). (a) Charge current applied to the magnetic-multilayer device in the parallel configuration due to the presence of an external magnetic field (H_{ext}). The magnetization of FM₁ and FM₂ are represented by the bottom red thick arrows. The d -band structure is represented according to the simplified Stoner model. The shift in the down-spin sub-band, due to the exchange interaction, makes the density of states at the Fermi energy $[N(E_F)]$ different for both spin-up and spin-down $[N_{\downarrow}(E_F) > N_{\uparrow}(E_F)]$. (b) Equivalent circuit using the two-current model for the parallel case. (c) Charge current applied to the magnetic-multilayer device in the antiparallel configuration. The magnetization of FM₁ and FM₂ are represented by the red and blue thick arrows, respectively. For each FM, the d -band structure is shown in the simplified Stoner model. The exchange interaction shifts in opposite directions spin sub-bands in FM₁ and FM₂ and, hence, the total magnetization is opposite. Accordingly, the density of states at the Fermi energy changes for the spin-up spin-down electrons, being different in the two FMs. (d) Equivalent circuit using the two-current model for the antiparallel case. Figure adapted from Ref. [10].

The GMR parameter depends on the difference between R_P and R_{AP} as follows:

$$GMR(\%) = \frac{R_{AP} - R_P}{R_P} \times 100. \quad (1.1)$$

The realization of large GMR devices at room temperature [11,12] established the transition from fundamental physics to applications since these devices can detect sub-nT magnetic fields and are suitable as precise magnetic field sensors [13–15].

In order to improve the GMR parameter, a thin insulating layer was introduced between the two FM slabs. This stack is known as magnetic tunnel junction (MTJ), whose performance is quantified by the tunnelling magnetoresistance (TMR). MTJ consists of two FM layers where the magnetization of the first FM layer is pinned and the magnetization of the second FM easily follows the direction of the external magnetic field. In this configuration, the electrons tunnel through the insulating layer keeping their spin and, hence, the charge current gets spin polarized when it is applied through a FM. In 1975, M. Jullière measured for the first time tunneling conduction in a Fe/Ge/Co stack and observed how electrons keep their spin when tunneling with a TMR of 14% [16]. Years later, Al_2O_3 was used as a insulating layer, improving the TMR at room temperature up to 11.8% [17]. Much higher effect was later obtained using single-crystalline Fe/MgO/Fe stacks, exhibiting TMR values of up to 220% at room temperature [18,19].

The first industrial application of GMR and TMR was in the field of information technology in 1997, with the realization of GMR-based hard-disk read heads [20,21]. GMR sensor was used to detect the magnetic state of the bits in the magnetic race and, due to the good scalability and high sensitivity, GMR sensor revolutionized the hard-disk industry [22]. Moreover, Slonczewski [23] and Berger [24] independently predicted, in 1996, an important consequence of the underlying physics of GMR: spin-transfer torque (STT). When a charge current flows through a FM material (fixed layer), it becomes spin polarized and maintains its polarization when travelling through the thin NM spacer. Once the spin-polarized current reaches the second FM material (free layer), it will exert a torque on its magnetization, transferring angular momentum to it. This STT can induce precession and even switch the magnetization. STT is now widely used in the MRAM (Magnetic Random Access Memory) technology [25]. However, the large current density needed to write the magnetic state (typically in the order of 10^7Acm^{-2}) compromises further evolution of

STT-MRAMs [26]. Alternative to STT, a new way to *write* a magnetic state on the FM layer has emerged, the spin-orbit torque (SOT) [27,28]. The origin of the torque relies on the generation of a spin current in a NM material due to the presence of strong spin-orbit coupling (SOC). SOT bridges two different research areas in spintronics: the manipulation of electron spin in NM materials and the one based on magnetic multi-layer devices.

Along with the revolution caused first by GMR and later by STT, different spin-based logic proposals were made. While Datta and Das, back in 1990, proposed the spin field-effect transistor based on the transport and manipulation of spin currents by means of electric field [29], Dery and co-workers proposed spin accumulation in semiconductor/FM multiterminal structure to conform a logic gate [30]. In 2010, Behin-Aein and co-workers proposed pure spin currents to directly switch the magnet, constituting a cascade process [31]. These proposals triggered the study of the generation, transport and detection of spin currents, which we will discuss in Section 1.2 and 1.3. The possibility of using the SOC in NM materials to also generate spin currents for SOT, or to detect spin currents for the MESO device, is a driving force in the study of spin-to-charge conversion (SCC) which will be discussed in Section 1.4.

1.2 Electrical spin injection

Spin injection into NM materials can be achieved using FM materials via electrical injection [32], spin pumping [33], or spin-dependent Seebeck effect [34]; or using NM materials via Spin Hall Effect [35,36] or Edelstein effect [37,38]. In this section, the electrical spin injection using FM materials is explained.

FM materials present a net magnetization even in the absence of an external magnetic field. In FM materials such as Fe, Co and Ni, the overall magnetization is due to the exchange interaction that shifts one of the $3d$ spin sub-band with respect to the other [39]. These spin sub-bands are not completely filled and, hence, one of them will present more occupied states than the other, giving rise to the overall magnetization of the material. On the case of an over-idealized Stoner model, the $3d$ band scheme for FM materials is represented in each FM layer in Fig. 1.1. For the red FM₁, the sub-band of blue spins, say down-spins (\downarrow), is shifted with respect to the red spins, say, up-spins (\uparrow). The Fermi energy, E_F , lies inside both bands, therefore, they are not completely filled. The filling of the up-spin sub-band (represented by the red background) is larger than in the

down-spin sub-band (blue background) leading to an overall up magnetization represented by the thick red up-arrow. On the contrary, for the blue FM [FM₂ in Fig. 1.1(c)], the up-spin sub-band is less filled than the down-spin sub-band, yielding an overall down magnetization, represented by the blue thick down-arrow. Typically, the spins which determine the overall magnetization of the FM are named *majority spins*, while the others are *minority spins*. The two-current model states that the electrical conduction in FM materials can be understood as two currents of spin-up and spin-down electrons in parallel, with different transport properties. Based on the two-current model and using the Einstein relation, the electrical conductivity in a FM material becomes a spin-dependent parameter given by:

$$\sigma_{\uparrow,\downarrow} = e^2 N_{\uparrow,\downarrow}(E_F) D_{\uparrow,\downarrow}, \quad (1.2)$$

where $N_{\uparrow,\downarrow}(E_F)$ is the spin-dependent density of states at the Fermi energy, e is the elementary charge, and $D_{\uparrow,\downarrow}$ is the spin-dependent diffusion coefficient, given by:

$$D_{\uparrow,\downarrow} = \frac{1}{3} v_{F\uparrow,\downarrow} \lambda_{e\uparrow,\downarrow}, \quad (1.3)$$

where $v_{F\uparrow,\downarrow}$ is the spin-dependent Fermi velocity of the electrons and $\lambda_{e\uparrow,\downarrow}$ is the spin-dependent electron mean free path.

Before delving further into the spin injection process, few basic concepts have to be defined. A *charge current density* (\mathbf{j}_c) is defined as electrons with opposite spins moving in the same direction [Fig. 1.2(a)]. When the amount of spin-up moving in one direction is the same as the spin-down moving in the opposite direction, the flow of charge is zero but there is a net flow of spin angular momentum known as *pure spin current density* (\mathbf{j}_s) [Fig. 1.2(b)]. Likewise, if there is an unbalance in the spin-up and the spin-down electron moving in one direction, charge current coexists together with spin current, the so-called *spin-polarized current density* [Fig. 1.2(c)].

When applying a charge current through a FM material, due to the difference in the conductivity for spin-up and spin-down electrons, the charge current gets spin polarized. The current spin polarization of a FM material (α_{FM}) is defined as:

$$\alpha_{FM} = \frac{\sigma_{\uparrow} - \sigma_{\downarrow}}{\sigma_{\uparrow} + \sigma_{\downarrow}}. \quad (1.4)$$

For NM materials, the conduction of both spins is the same ($\sigma_{\uparrow} = \sigma_{\downarrow} = \sigma$)

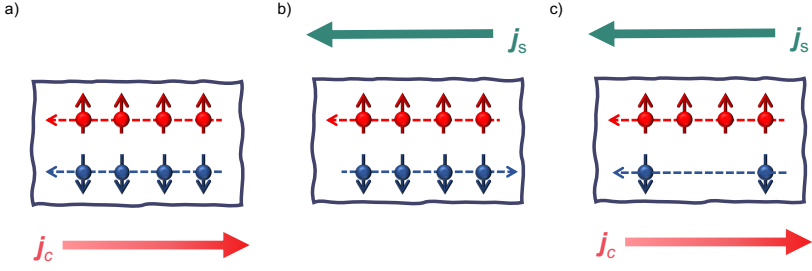


Figure 1.2: **Definition of currents.** (a) Charge current. The same amount of electrons with spin-up (in red), and electrons with spin-down (in blue) are moving in the same direction. The direction of the movement is represented by the dashed arrow. The resulting charge current is represented by the bottom red thick arrow. The total flow of spin angular momentum is zero. (b) Pure spin current. Electrons with opposite spins move in opposite directions. The spin current is defined in the direction in which spin-up electrons are moving, represented by the top green thick arrow. The total flow of charge is zero. (c) Spin-polarized current. There is an imbalance between spin-up and spin-down electrons moving in one direction. There are a net flow of charge, represented by the bottom red arrow, and spin angular momentum, represented by the top green arrow.

and, thus, the charge current does not get spin polarized when flowing through them.

The difference in the conductivity between different spin orientation has a large impact when a FM material is placed in contact with a NM material and a charge current is applied between them [40–43]. The difference in the conductivity creates a splitting in the electrochemical potential for spins up (μ_{\uparrow}) and down (μ_{\downarrow}) at the FM/NM interface. This leads to a spin accumulation, which is defined as $\mu_s = \mu_{\uparrow} - \mu_{\downarrow}$. A gradient in the spin electrochemical potential ($\nabla\mu_{\uparrow,\downarrow}$) is the driving force of the up(down)-spin current in the same way a gradient in the charge electrochemical potential ($\nabla\mu_c$) is the driving force of the charge current:

$$\mathbf{j}_c = \frac{\sigma}{e} \nabla\mu_c \quad (1.5)$$

$$\mathbf{j}_{\uparrow,\downarrow} = \frac{\sigma_{\uparrow,\downarrow}}{e} \nabla\mu_{\uparrow,\downarrow}, \quad (1.6)$$

where the sum of the spin-up (\mathbf{j}_{\uparrow}) spin-down (\mathbf{j}_{\downarrow}) current densities results into the charge current density ($\mathbf{j}_c = \mathbf{j}_{\uparrow} + \mathbf{j}_{\downarrow}$) and the difference into the spin current density ($\mathbf{j}_s = \mathbf{j}_{\uparrow} - \mathbf{j}_{\downarrow}$).

Under the assumption that the spin-flip scattering time (τ_s) is much larger than the momentum scattering time (τ_p), μ_{\uparrow} and μ_{\downarrow} can be defined at any

point of the junction. The dynamics of the spins diffusing in any material are governed by the diffusive Bloch equation [44]:

$$D_s \nabla^2 \boldsymbol{\mu}_s - \frac{\boldsymbol{\mu}_s}{\tau_s} = 0, \quad (1.7)$$

where the first term corresponds to the diffusion of the spin accumulation and the second term corresponds to the spin relaxation term. Considering the spin accumulation in a NM material along the x -direction, the 1D-solution to the equation is given by:

$$\mu_s = A \exp(-x/\lambda_s^{NM}) + B \exp(x/\lambda_s^{NM}), \quad (1.8)$$

where A and B are defined by the boundary conditions due to the continuity of charge and spin currents, λ_s^{NM} is the spin diffusion length in the NM, and is related to the spin lifetime as $\lambda_s = \sqrt{\tau_s D_s}$, being D_s the spin diffusion coefficient which is the weighted average of the spin-dependent diffusion coefficient:

$$D_s = \frac{\sigma_\downarrow D_\uparrow + \sigma_\uparrow D_\downarrow}{\sigma_\uparrow + \sigma_\downarrow}. \quad (1.9)$$

1.3 Spin transport and detection

Back in 1985, Johnson and Silsbee [45] were able to inject spins from a FM material (FeNi) to a NM one (Al) with an efficiency ranging from 6% to 8%. Years later, spin injection and detection in semiconductors were achieved using circularly polarized light and semiconducting FM materials [46–49]. However, it was lacking an efficient spin injection from FM metals [50, 51]. Several studies showed efficient spin injection into semiconductors using a *local lateral spin valve* (local LSV) geometry, where a charge current is applied from one FM to the other through a NM channel and the voltage is measured between the same two FM electrodes [52, 53] [see Fig. 1.3(a)]. Using this geometry, different artifacts mimicking the spin signal can arise, such as anisotropic magnetoresistance or anomalous Hall effect [54]. In order to remove spurious contributions and based on the *potentiometric technique* used to measure spin accumulation in gold films [55] [Fig. 1.3(b)], Filip and co-workers developed the *non-local lateral spin valve* (non-local LSV) [56] [see Fig. 1.3(c)].

Figure 1.3(c) shows the non-local LSV configuration where the charge current path and the voltage path are separated to avoid any spurious effect. The charge current is applied from FM₁ to the left side of the NM channel. The

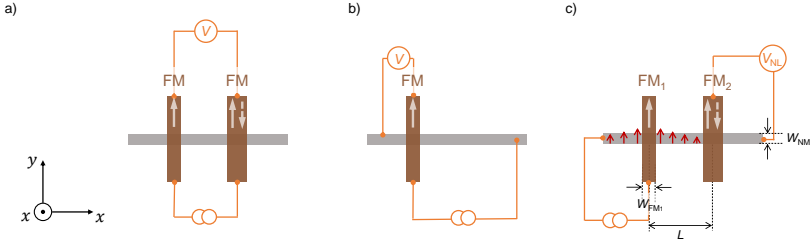


Figure 1.3: Different measurement configurations to detect the spins injected from a FM into a NM channel. The magnetization of each FM is represented by the arrow on top. The magnetization of the first FM is fixed while the magnetization of the second one changes from $+y$ to $-y$. (a) Local LSV configuration. The charge current is applied between the two FM electrodes and the voltage is measured between them. (b) Potentiometric configuration. The current is applied between the FM and one side of the NM channel and the voltage is probed between FM and the other side of the channel. (c) Non-local LSV configuration. The current is applied between FM₁, acting as spin injector, and one side of the the NM channel. The spin accumulation generated at the interface diffuses to both sides of the spin injector (represented by the red arrows). The voltage is measured between FM₂ and the NM channel. The relative orientation between the spins and the magnetization of FM₂ will give rise to different values of V_{NL} . The two FM electrodes are separated by a distance L , with a width w_{FM_i} . The width of the NM channel is represented by w_{NM} .

current spin polarization in the FM material will create a spin accumulation at the FM/NM interface.

Assuming band structures as the one shown in Fig. 1.4, and an ideal spin injection without spin flip at the interface, when the electrons flow from NM to FM, the minority spins accumulate at the interface [57]. At the interface, the spin accumulation (μ_s) is due to the difference between μ_{\uparrow} and μ_{\downarrow} . If the direction of the current is reversed, the majority spins accumulate at the interface accordingly. The spin accumulation created at the interface diffuses in the channel with a characteristic length – the spin diffusion length (λ_s). FM₂ can only detect the spins which are aligned with its magnetization axis, by probing the voltage build up at the junction between NM and FM₂. The non-local voltage is defined as the difference in the voltage between the detector and the NM channel and it is given by $V_{NL} = (\mu_{\uparrow, \downarrow} - \mu_c)/(-e)$. By using this technique, any magnetoresistance which does not depend on spins is suppressed since the charge current path and the voltage path are completely separated. Often a non-local resistance (R_{NL}) is given, which is the non-local voltage normalized by the applied charge current (I_c), $R_{NL} = V_{NL}/I_c$.

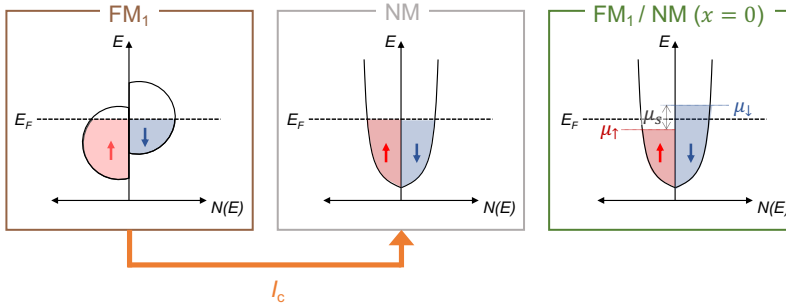


Figure 1.4: **Band scheme in the spin injection process from FM to NM.** Using the simplified Stoner model, the d -bands of FM_1 are represented for the spin-up and the spin-down sub-bands. The total magnetization of the FM_1 is up. The s -bands in NM present the same amount of spin-up and spin-down electrons. When a charge current (I_c), represented by the orange arrow, is applied from FM_1 to NM, more up-spin electrons flow from NM to FM_1 because $\sigma_{\uparrow}|_{FM_1} > \sigma_{\downarrow}|_{FM_1}$. This leads to a down-spin accumulation (μ_s) at the FM_1/NM , which sites at $x = 0$, due to the difference between the spin-up and spin-down electrochemical potentials.

This spin detection technique relies on the spin accumulation created at the FM/NM interface. However, the spin accumulation created at the interface is reduced if the spins enter into the FM. This phenomenon is known as *spin absorption* [42, 44, 58–61], and happens when the spin finds a less resistive path when flowing to the FM instead of accumulating at the interface. This phenomenon is enhanced by the conductivity mismatch problem in this kind of devices, where usually the resistivity of the FM is much lower than the one of the NM, promoting the spin absorption to the FM. Likewise, this effect also happens at the injector electrode, where the efficiency of the spin injection can be diminished due to the back-flow of spins. The conductivity mismatch issue was firstly theoretically reported by Schmidt and co-workers [41] and the solution to it, by adding a tunnel barrier (TB), was proposed by Rashba [58].

From the experimental side, the conductivity mismatch problem was observed by Jedema and co-workers [62] when using a NiFe/Cu/NiFe LSV, the obtained current spin polarization was around 2% while it was greatly improved when using TB and substituting Cu by Al (Co/TB/Al/TB/Co) [63]. TBs play a crucial role providing high spin-dependent resistance, enhancing the spin polarization of the injected spin current, and avoiding the back-flow of the spins once they are injected into the NM channel. By sweeping the magnetic field in the in-plane easy axis, and due to the different shape anisotropy between the injector and detector, it is possible to access a parallel or antiparallel configura-

ration of the LSV. By measuring V_{NL} , while the magnetic field is swept, the signal will dramatically change from the parallel to the antiparallel configuration. This abrupt change in the signal allows us to define the spin signal as the semi-difference between parallel (R_{NL}^P) and antiparallel state (R_{NL}^{AP}):

$$\Delta R_{NL} = \frac{R_{NL}^P - R_{NL}^{AP}}{2}. \quad (1.10)$$

The spin signal can be calculated taking into account the continuity of the spin currents and the charge current at the interfaces in Eq. 1.8, leading to [42]:

$$\Delta R_{NL} = 2R_s^{NM} \exp\left(\frac{L}{\lambda_s^{NL}}\right) \frac{\prod_{i=1}^2 \left(\frac{P_i R_i}{1 - P_i^2} + \frac{\alpha_{FM} R_s^{FM}}{1 - \alpha_{FM}^2} \right)}{\prod_{i=1}^2 \left(1 + \frac{2 R_i}{1 - P_i^2} + \frac{2 R_s^{FM}}{1 - \alpha_{FM}^2} \right) - \exp\left(\frac{2L}{\lambda_s^{NM}}\right)}, \quad (1.11)$$

where the i -index corresponds to the two different interfaces FM₁/NM and FM₂/NM, $P_{i=1}$ corresponds to the polarization of the FM₁/NM interface, which in the following will be referred as P_{inj} , and $P_{i=2}$ the polarization of the FM₂/NM interface, in the following P_{det} . R_i corresponds to the resistance of each FM _{i} /NM interface, and $R_s^{FM(NM)}$ is the spin resistance of the FM or NM, given by:

$$R_s^{FM(NM)} = \frac{\rho_{FM(NM)} \lambda_s^{FM(NM)}}{A_{FM(NM)}}, \quad (1.12)$$

where $\rho_{FM(NM)}$ is the resistivity of the FM or NM, $A_{FM} = w_{FM} w_{NM}$ is the area of the interface, and $A_{NM} = w_{NM} t_{NM}$ is the cross-section of the NM channel, being t_{NM} the thickness of the NM.

The spin signal will depend on whether each FM/NM junction is transparent, TB or a mix between both. If the interface resistance of both FM _{i} /NM are lower than the spin resistance of each FM ($R_1, R_2 \ll R_s^{FM}$), the contact between FM/NM is transparent, and the signal will initially decrease very abruptly and then as an exponential decay. If the interface resistances are larger than the spin resistance of the NM ($R_1, R_2 \gg R_s^{NM}$), the spin signal will decay as an exponential and will be larger than in the transparent contact case [42].

By measuring the spin signal for different values of L , it is possible to fit the results to Eq. 1.11 and extract the spin injection (α_{FM} , P_i) and the spin transport (λ_s^{NM}) parameters of the LSV.

1.3.1 Hanle spin precession.

Throughout the spin transport, the electron spins can undergo a coherent precession, known as Hanle precession, under the presence of an external magnetic field perpendicular to the spin polarization direction (B_\perp). During the time the spins are diffusing in the channel (t) their direction will be modified by an angle $\psi = \omega t$, where ω is the Larmor frequency $\omega = g\mu_B B_\perp / \hbar$, g is the g -factor of the electron, μ_B is the Bohr magneton, and \hbar is the reduced Plank constant.

For low enough magnetic fields, the magnetization of the detector will lie along its easy axis and will only detect the projection of the spin onto its magnetization, thus the detected voltage will be proportional to $\pm \cos(\psi)$. The normal distribution of electrons that, once injected, will arrive at the detector within a diffusion time t is given by:

$$\mathcal{P}(t) = \frac{1}{\sqrt{4\pi D_c t}} \exp\left(-\frac{L^2}{4D_c t}\right), \quad (1.13)$$

where D_c is the charge diffusion coefficient. If a diffusive transport is assumed for both spin and charge, then $D_c = D_s$. Considering the spin precession around a perpendicular magnetic field and its relaxation over time, the spin accumulation with spin polarization parallel to the magnetization of the detector (easy axis, y -direction) will be given by:

$$\mu_{s_y} \propto \mathcal{P}(t) \cos(\psi) \exp(-t/\tau_s), \quad (1.14)$$

where the exponential term $[\exp(-t/\tau_s)]$ corresponds to the spin-flip scattering. The non-local resistance probed at the detector will be given by the addition of all the spins arriving to the detector over the diffusion time t , with the following form:

$$R_{NL}(B_\perp) \propto \int_0^\infty \mathcal{P}(t) \cos(\psi) \exp(-t/\tau_s) dt. \quad (1.15)$$

For larger magnetic fields, the magnetization of the detector will be pulled towards the direction of the magnetic field until it is aligned. Taking into account the angle pulled out of the easy axis (Θ), the R_{NL} will be given by [63]:

$$R_{NL}(B_\perp, \Theta) = R_{NL}(B_\perp) \cos^2(\Theta) + |R_{NL}(B_\perp = 0)| \sin^2(\Theta). \quad (1.16)$$

When the magnetization is parallel to the magnetic field ($\Theta = \pi/2$), no precession occurs. By fitting the experimental data to the previous equation, the spin lifetime (τ_s) and the spin polarization ($\sqrt{P_{inj}P_{det}}$) can be quantified.

1.3.2 Spin relaxation mechanisms

The spin accumulation is a non-equilibrium situation because spin is not a conservative quantity and can flip between up and down states. There are different mechanisms that cause spin accumulation to relax to an unpolarized state of equilibrium. The different spin relaxation mechanism an electron can undergo while travelling in a NM are [61, 64]: (i) Elliott-Yafet [65, 66], (ii) D'Yakonov-Perel [67, 68], (iii) Bir-Aronov-Pikus mechanism in *p*-doped semiconductors (spin-flip due to the exchange interaction in electron-hole scattering event) [69, 70], and (iv) hyperfine interaction [71, 72], which is the magnetic interaction between the magnetic moment of the electron and the nucleus. However, the most common ones are Elliott-Yafet and D'Yakonov-Perel mechanisms.

On the one hand, Elliott-Yafet mechanism emerges from the probability an electron has to flip its spin while scattering with a defect (impurity, phonon...) mediated by the SOC of the material. Under Elliott-Yafet scattering, τ_s is proportional to the momentum scattering time ($\tau_s \propto \tau_p$). On the other hand, D'Yakonov-Perel occurs in systems with broken inversion symmetry. The absence of this symmetry together with the SOC creates a different effective magnetic field at any *k*-point in the band structure. This induces spin precession, leading to a dephase in the spin orientation in between scattering events. Therefore, τ_s is inversely proportional to the momentum scattering time ($\tau_s \propto 1/\tau_p$).

1.4 Spin-to-charge conversion

As mentioned before, different techniques can be used to generate spin currents in NM materials. In Section 1.3, electrical spin injection using FM materials has been discussed. However, spin currents can also be generated using NM materials via spin Hall effect or Edelstein effect. Both effects occur in systems with strong SOC, while the latter also needs the inversion symmetry to be broken. In this section, a physical explanation of each process is given.

SOC stems from the interaction between the spin and the orbital angular

momentum, and the strength of the SOC interaction scales with Z^4 , being Z the atomic number. Those materials with large Z will present high SOC while the ones with low Z will present negligible SOC [73, 74].

1.4.1 Spin Hall effect

Early theoretical studies [67,75] considered that electrons deflect in different directions depending on their spins when scattering with impurities, due to SOC. This scattering process will generate a spin imbalance with an associated spin current [Fig. 1.5(a)]. Without being aware of the work from D'yakonov and Perel, in 1999, Hirsch gave the name of *spin Hall effect* (SHE) to this phenomenon, and was predicted to happen in paramagnetic materials [76]. Reciprocally, a spin current should induce a charge current, which is known as inverse spin Hall effect (ISHE) [Fig. 1.5(b)].

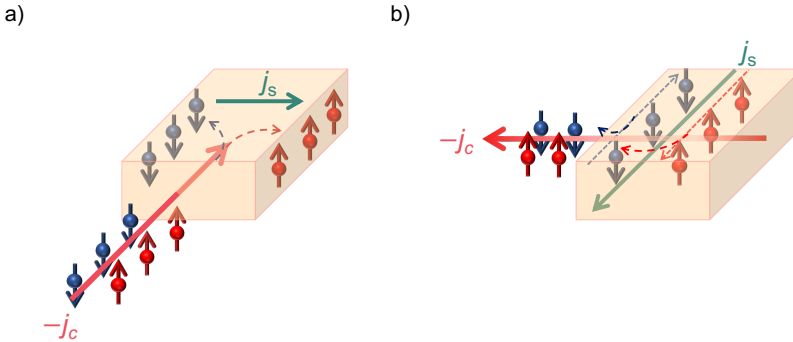


Figure 1.5: **SHE and ISHE process in a high symmetry SOC material.** (a)

By applying a charge current into a SOC material, electrons with opposite spins will deflect to opposite sides inducing a transverse spin current. (b) When a spin current is injected into a SOC material, spins will deflect in the same direction generating a transverse charge current.

Upon applying an electric field in a strong SOC material, a spin current is generated following:

$$j_i^\alpha = \sigma_{ij}^\alpha E_j, \quad (1.17)$$

where j_i^α is the spin current along the i -direction with spin polarization along α -direction generated when an external electric field (E_j) along the j -direction is applied and σ_{ij}^α denotes the spin Hall conductivity tensor. It is important to note that the crystal symmetry of the SOC material determines the tensor elements that are allowed. When the SOC material has high symmetry [see

Fig. 1.5(a)], that is at least two mirror planes in the crystal structure, only the tensor elements where the spin polarization, charge current, and spin current are mutually perpendicular ($i \neq j \neq \alpha$), are allowed. In this case, Eq. 1.17 has the following form:

$$\mathbf{j}_s = \left[\frac{\hbar}{e} \right] \theta_{SH} \mathbf{j}_c \times \mathbf{s}, \quad (1.18)$$

where \mathbf{j}_s is the generated spin current, θ_{SH} is the spin Hall angle, parameter which gives the efficiency of the interconversion between charge current and spin current, and \mathbf{j}_c is the applied charge current ($\mathbf{j}_c = \sigma \mathbf{E}$). For low-symmetry materials, non-orthogonal configurations are allowed [77,78] bringing flexibility in spintronic devices.

For disordered systems in the diffusive regime, the relation between the spin Hall conductivity tensor and the spin Hall angle is:

$$\theta_{ij}^\alpha = \frac{\sigma_{ij}^\alpha}{\sigma}. \quad (1.19)$$

In the reciprocal effect, ISHE, from an existing spin current a charge current is generated [see Fig. 1.5(b) for the high symmetry material case]. The respective equations for the ISHE in a general case is:

$$j_i = \sigma_{ij}'^\alpha E_j^\alpha \quad (1.20)$$

and, in particular, in a high symmetry material is:

$$\mathbf{j}_c = \left[\frac{e}{\hbar} \right] \theta_{ISH} \mathbf{j}_s \times \mathbf{s}, \quad (1.21)$$

where $\sigma_{ij}'^\alpha$ is the inverse spin Hall conductivity tensor and E_j^α is the gradient of the spin potential in the j -direction generated by the spins polarized along α . In Eq. 1.21, θ_{ISH} is the inverse spin Hall angle, which gives the efficiency of the conversion of a spin current into a charge current. Due to Onsager reciprocity, the efficiencies of the charge-to-spin and spin-to-charge conversions have to be the same, $\sigma_{ij}^\alpha = \sigma_{ji}'^\alpha$ and $\theta_{SH} = \theta_{ISH}$ [35].

In this Thesis, the values of σ_{ij}^α are given in units of $\left[\frac{\hbar}{e} \right]$. Discrepancies in the literature when comparing σ_{ij}^α can come from the difference in units, $\left[\frac{\hbar}{2e} \right]$ instead of $\left[\frac{\hbar}{e} \right]$, or from the definition of θ_{ij}^α , being $\theta_{ij}^\alpha = 2 \frac{\sigma_{ij}^\alpha}{\sigma}$ instead the relation we use here (see Eq. 1.19). A thorough discussion can be found in the Supplementary Information of Ref. [79].

1.4.1.1 Contributions to the Spin Hall Effect

When E. H. Hall tried to measure the ordinary Hall effect in ferromagnetic materials, he observed an extra contribution at zero magnetic field, which came to be known as the anomalous Hall effect (AHE) [80]. In 1954, Karplus and Luttinger [81] claimed the SOC to be the origin of the AHE. The SOC acts as an effective magnetic field that deflects the spin-up and spin-down in opposite directions. This is known as the intrinsic contribution to the AHE. In addition, scattering with impurities can also give rise to AHE. Two different scattering mechanisms can be distinguished: skew scattering and side jump. The skew-scattering mechanism was proposed by Smit in 1958 and it arises from the spin-dependent scattering process caused by the SOC of impurities in the lattice [82]. In 1970, Berger suggested that the side-jump scattering is due to the opposite electric field the electrons with opposite spin orientation feel when approaching an impurity [83]. SHE is essentially the same effect as AHE but in NM materials and, hence, the mechanisms giving rise to AHE are also contributions for the SHE [84–91].

The intrinsic contribution involves concepts of topology and geometry that have been formulated recently. An electron in an n -band level with k -state has a non-vanishing mean velocity [92]. Lately, this description has been completed by adding a term corresponding to the transverse velocity that an electron can acquire in the presence of an electric field [93]:

$$\mathbf{v}_n(k) = \frac{1}{\hbar} \nabla_k \varepsilon_n(k) - \frac{e}{\hbar} \mathbf{E} \times \mathbf{\Omega}_n(k), \quad (1.22)$$

where k is the wave vector and can be always confined to the first Brillouin zone, $\varepsilon_n(k)$ is the energy level of an electron in a periodic potential and the second term corresponds to the *anomalous velocity*, which is transverse to the electric field (\mathbf{E}) and to the Berry curvature $\mathbf{\Omega}_n(k)$. The anomalous velocity term gives rise to the Hall current. $\mathbf{\Omega}_n(k)$ is gauge-invariant and calculated over the n -band in the momentum space.

The anomalous velocity term has not been always included and still the formula has succeeded in describing electronic properties in the past [92]. The symmetry plays an important role in determining when $\mathbf{\Omega}_n(k)$ can be neglected. On the case of materials which hold time-reversal and spatial inversion symmetries, the Berry curvature vanishes. Time-reversal symmetry is represented by the time transformation $T:t \rightarrow -t$. In a system that holds time-reversal symmetry, when the time transformation is applied, the momentum and the spin of a given particle should reverse as well ($k \rightarrow -k$, $s \rightarrow -s$). Spatial inversion

symmetry is held in a system which has a symmetry center and, hence, an atom in the (x, y, z) position in the crystal is indistinguishable from one located at $(-x, -y, -z)$.

In certain materials, at least one of the aforementioned symmetries, is not present and, therefore, the Berry curvature is non-zero giving rise to a transverse contribution to the electron velocity. This is the case of FM materials, in which time-reversal symmetry is broken due to the magnetization of the system, and the electrons acquire a transverse velocity causing the AHE [87].

While, in the AHE case, time-reversal symmetry is broken due to the magnetization of the FM, in the SHE case both time-reversal and inversion symmetries hold in materials such as Pt, Ta, W... In these materials, the total Berry curvature will be zero and, one can expect to have zero anomalous velocity. Although the total Berry curvature is zero, the spin Berry curvature is opposite for both spins and, therefore, the spin Berry curvature is the one creating the anomalous velocity in the SHE. The spin Berry curvature ($\Omega_{ij,n}^\alpha$) will be different for each direction of the spin polarization α and the spin Hall conductivity (σ_{ij}^α) can be calculated using the Kubo formula [36, 94]:

$$\sigma_{ij}^\alpha = -\left(\frac{e}{\hbar}\right) \int \frac{d^3\mathbf{k}}{(2\pi)^3} \sum_n f[\varepsilon_n(k)] \Omega_{ij,n}^\alpha(\mathbf{k}), \quad (1.23)$$

where $f[\varepsilon_n(k)]$ is the Fermi-Dirac distribution function.

1.4.1.2 Spin Hall effect in metals

Different measurement configurations were proposed in order to detect spins via SHE in metal devices [76, 95–97]. In 2006, Valenzuela and Tinkham measured for the first time SHE in a metal-based LSV [98]. A CoFe electrode was used as spin injector into Al through an Al_2O_3 tunnel barrier to improve the spin injection. In the used configuration, by applying a charge current (I_c) from the FM to the Al stripe, a spin accumulation is created at the interface and diffuses to both sides of the injector. On one side, a pure spin current flows along the Al channel, and due to the ISHE, a transverse current is generated creating a transverse voltage (V_{SH}) in the Hall arms of the Al channel, see Fig. 1.6(a). The associated spin Hall resistance ($R_{SH} = V_{SH}/I_c$) is measured as the magnetic field is swept in the out-of-plane direction, see Fig. 1.6(b). In high symmetry materials such as Al, the generated charge current via ISHE has to be perpendicular to both spin current and spin polarization. Due to fabrication constraints, the only measurable voltage is limited to the y -direction and the

spin current has to propagate in the Al channel along the x -direction. The only possible spin polarization that fulfills the ISHE requirement is the out-of-plane spin polarization. The signal changes linearly with the magnetic field for low enough magnetic fields. In this regime, the magnetization of the FM is pulled in the direction of the field. For large enough values of the field, the magnetization saturates and the R_{SH} value flattens out. Figure 1.6(b) shows the measured spin Hall resistance (grey open circles) and the sine of the angle between the magnetization and the magnetic easy-axis direction (black line). R_{SH} follows the pulling of the direction of the FM until it saturates at $\sim \pm 2$ T. By fitting the curve, the Al spin Hall angle of Al was extracted, $\theta_{SH}^{Al} \approx (1-3)10^{-4}$.

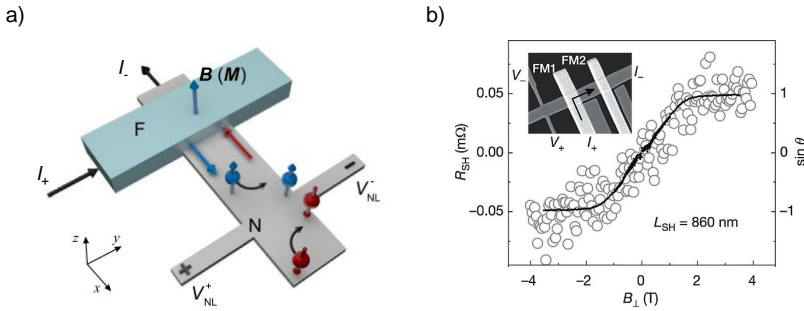


Figure 1.6: **Spin Hall effect in a metallic device.** (a) Measurement configuration and sketch of the ISHE. A charge current is applied from an out-of-plane magnetized FM electrode to a NM channel, while a voltage drop is measured between the Hall arms in a non-local configuration. (b) Measured spin Hall resistance as a function of the out-of-plane magnetic field (grey open circles). The black line corresponds to the sine of the angle between the magnetization and the magnetic easy axis of the FM electrode. The inset is a scanning electron microscopy image of the device. Figure adapted from Refs. [36, 98].

1.4.1.3 Spin absorption experiment in metals

The configuration used in the previous experiment requires long λ_s of the SOC material and a large enough θ_{SH} . The former is needed so that the spin current diffuses long enough in the material to reach the voltage probes, and the latter is needed to detect a measurable signal. In NM materials, these two parameters tend to compensate so that if λ_s is large, θ_{SH} is small and the other way around, since both parameters are governed by the strength of the SOC. In materials with high SOC, the SCC efficiency is large, but the spin current cannot diffuse for long distances. In contrast, in materials with low SOC, the SCC efficiency is small, and the spin current can travel long distances. This is the case of Pt and Al, respectively. Pt, one of the foremost examples of SOC material [99],

at room temperature, $\lambda_s^{Pt} \sim 1$ nm and $\theta_{SH}^{Pt} \sim 8\%$ [100] while for Al, λ_s^{Al} ranges between 500–700 nm and the θ_{SH}^{Al} ranges between 0.01–0.03% at low temperatures [98]. In order to overcome this issue, and trying to access the SHE in different SOC materials, the spin absorption technique was proposed by Vila and co-workers [99]. The device consisted of two FM electrodes (Py), a NM spin channel (Cu) and a stripe made of a SOC material (Pt), see Fig. 1.7(a). By applying a charge current from Py to Cu, a spin accumulation is created at the interface that diffuses to both sides of the Py. When the diffusive spin current reaches the Pt stripe, it is absorbed because R_s^{Pt} is lower than R_s^{Cu} [101, 102]. Due to the short λ_s^{Pt} , when the spin current is absorbed into Pt it can be assumed to flow along the vertical direction (z -direction). Pt is a high symmetry material, hence, the resulting charge current via ISHE is along the y -direction [see Fig. 1.7(c) and Eq. 1.21]. Reciprocally, if a charge current is applied along the Pt stripe, a spin current along the z -direction is generated due to the SHE with spins polarized along x -direction [see Fig. 1.7(d)]. The signals corresponding to the SHE and ISHE configuration are represented in Fig. 1.7(b) at 10 K when the magnetic field is swept in the in-plane hard axis of the Py wires.

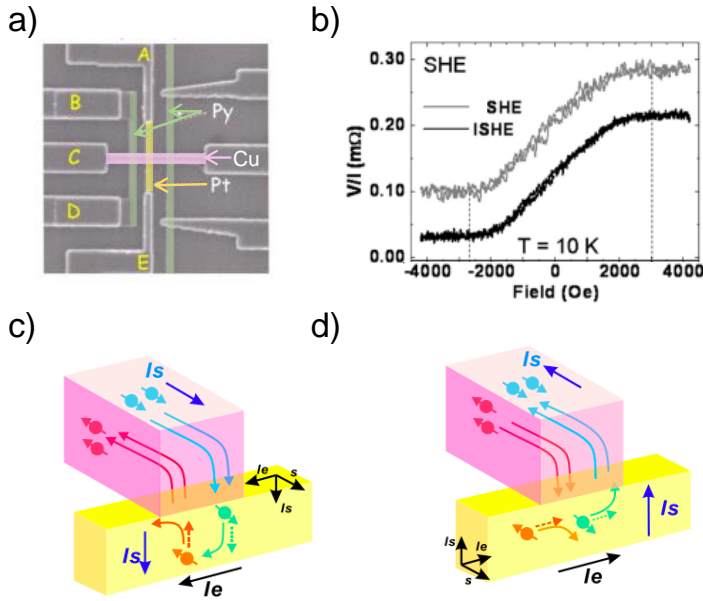


Figure 1.7: **Spin absorption technique.** (a) Scanning electron microscope image of the device. The Py electrodes are colored in green, the Pt stripe in yellow, and the Cu channel in pink. (b) SHE and ISHE measurement recorded at 10 K using a Pt thickness of 20 nm. In the SHE (ISHE) the voltage is probed between contacts B-C (E-A), while the current is applied between E-A (B-C). (c) Sketch of the SHE in Pt. The diffusive spins in Cu when reaching the Pt wire are absorbed, creating a spin current denoted by I_s . Via SHE, this spin current generates a transverse charge current along the Pt stripe, I_e . (d) Sketch of the ISHE in Pt. When a charge current (denoted by I_e) is applied along the Pt stripe, a transverse spin current (I_s) is generated via ISHE. The resulting spins accumulate at the interface and diffuse into Cu, being later detected using the FM electrode. Figure adapted from Refs. [35, 99].

1.4.2 Edelstein Effect

Besides the SHE, there is another effect in which spin accumulations are converted into a charge current but with a different physical origin, the Edelstein effect (EE). This process is also known as spin galvanic effect [103] or current-induced spin polarization [104–106]. In a non-magnetic system with broken inversion symmetry, upon the presence of an external electric field and due to the SOC, an homogeneous spin accumulation with spin polarization perpendicular to the electric field is generated. This effect has been observed in metallic Rashba interfaces [107–110], semiconductors [103, 111, 112], surface states of topological insulators [113–117] and oxide Rashba interfaces featuring

a two-dimensional electron gas [118,119]. The vast majority of systems showing Rashba effect are 2D systems [120], where the Edelstein effect is also known as Rashba-Edelstein effect (REE).

Due to the broken inversion symmetry, together with the SOC, the band structure of a Rashba system is modified, presenting a splitting as shown in Fig. 1.8(a). Such spin splitting has been measured in different systems such as surfaces or interfaces containing Bi, Pb, W, Au... [121–124] and gives rise to spin-momentum locking, that is, for a given value of the momentum (k) the spin is fixed. By cutting the band at the Fermi energy, the band appears as two concentric circles with opposite spin helicity in the momentum space [see Fig. 1.8(b)]. When a charge current is applied to the system, the contours of each spin-split band are shifted in the direction of the electrons movement (x -direction), creating a spin accumulation with polarization along the $-y$ -direction, due to the imbalance in the red and blue filled areas in Fig. 1.8(c). This spin accumulation can diffuse resulting in a 3D pure spin current. Reciprocally, when a spin accumulation with polarization along the y -direction is injected into the system, the two Fermi contours are shifted in opposite directions, yielding a charge current along the x -direction, which is called inverse Rashba-Edelstein effect (IREE).

The SCC efficiency via Inverse Edelstein effect (IEE), in a fully 2D system, is given by $\alpha_{IEE} = j_c^{2D} / j_s^{2D}$. If the spin accumulation is injected from a 3D into the 2D system, contrary to θ_{SH} and α_{IEE} , the efficiency is given by $\lambda_{IEE} = j_c^{2D} / j_s^{3D}$, which has dimensions of length. A careful discussion about the comparison between the SHE and EE efficiencies can be found in Ref. [125].

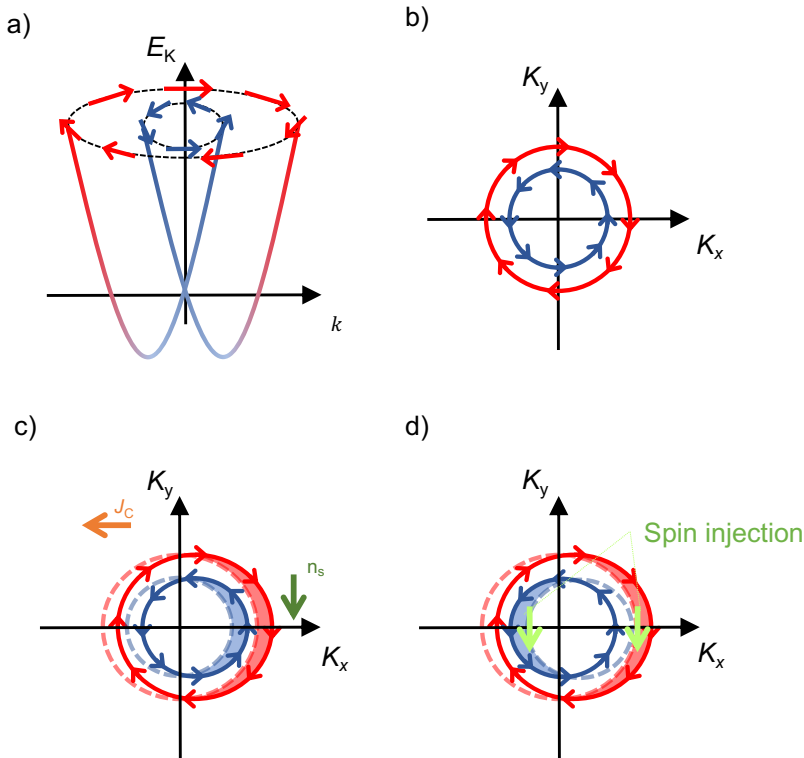


Figure 1.8: **Band structure of a Rashba system showing Edelstein effect.**

(a) Two spin-split bands in a Rashba system. (b) Fermi contours of the bands at a certain energy. The bands are concentric with opposite spin helicity. (c) When a charge current is applied to the system, the Fermi contours shift in the direction of electron's movement generating a net spin accumulation transverse to the applied charge current. This effect is known as Edelstein effect. (d) When a spin current is injected into a Rashba system (represented by the light green arrows), the Fermi contours are shifted in opposite directions, generating a charge current. This is known as inverse Edelstein Effect. Figure adapted from Ref. [126].

In topological insulators, the spin generation is very similar to the one of Rashba systems. However, only one band (with linear dispersion, associated to the topologically protected surface states) is present at the Fermi energy. In this scenario, the induced spin accumulation is larger since there is no compensation from the inner Fermi contour with opposite spin helicity [116,127].

1.5 2D materials: a breakthrough in spintronics

Back in 2004, Andre Geim and Kostya Novoselov isolated single layer graphene flakes using the Scotch-tape technique, and measured electrical transport on them [128, 129]. This discovery was a milestone in material science and opened the door to the discovery of other two-dimensional (2D) materials showing exotic properties. In 2010, Geim and Novoselov were awarded with the Nobel Prize in Physics.

1.5.1 Graphene

Graphene consists of a single 2D layer of carbon atoms in a honeycomb arrangement. This arrangement is a particular case of an hexagonal crystal lattice with two-atoms basis [A sub-lattice atoms in green, and B sub-lattice atoms in red represented in Fig. 1.9(a)]. Back in 1947, P. R. Wallace predicted graphene electronic structure [130]. The electronic properties of this material are described by Dirac fermions, massless relativistic particles whose energy dependence with the momentum is linear. At low energies, the band dispersion in the momentum space can be seen as two cones touching at the so-called Dirac point [see Fig. 1.9(b)]. The conduction band (CB) and valence band (VB) touch at the Dirac point and, hence, graphene is a zero-gap material. The linear dispersion occurs in six vertices of the hexagonal Brillouin zone (momentum space). Three of the vertices are equivalent and labeled as K , and the other three equivalent vertices, as K' points. The two inequivalent sublattices break the in-plane inversion symmetry in graphene resulting in additional degree of freedom, where the carriers in inequivalent valleys carry different information. This phenomenon opens the door to the desired electric generation and detection of the valley polarization, being the grounds for *valleytronics* [131]. This feature led to the observation of new exotic transport phenomena in graphene such as half-integer Quantum Hall Effect [132], minimum conductivity [133], or supercurrents [134].

By moving the Fermi energy up or down, the carrier density in graphene can be tuned changing from hole-doped to electron-doped as shown in Fig. 1.9(b). This tuning can be done by electrostatic gating.

Graphene is a weak SOC material, in the order of μeV , because of the low atomic number of carbon ($Z=6$). Moreover, it is characterized by a low

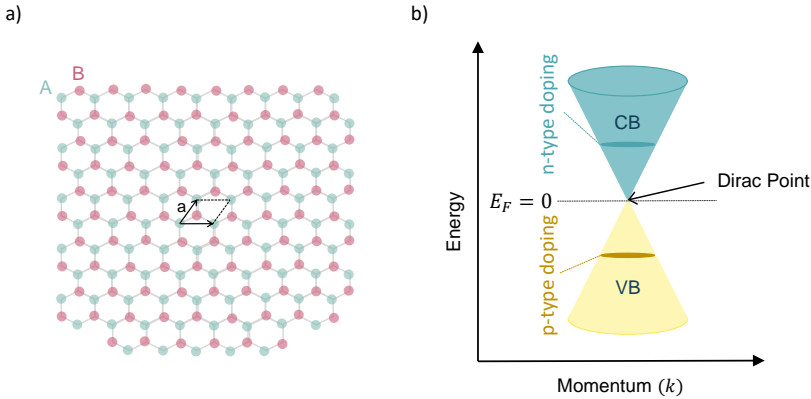


Figure 1.9: **Graphene.** (a) Graphene crystal lattice where the two sub-lattices, A in green and B in red, are represented. The distance between atoms of the same sublattice is given by a and it is represented by the arrows. (b) Linear energy dispersion as a function of momentum for graphene. The upper cone, conduction band, touches the valence band at the Dirac point, where the Fermi energy is zero. By increasing the Fermi energy, graphene starts to be n -doped, in contrast, by decreasing the Fermi energy, graphene starts to be p -doped. The tuning of the energy level can be done by electrostatic gating.

hyperfine interaction.. These two properties give rise to long spin diffusion length, making graphene an ideal candidate for spin transport [135–142]. In the context of spintronics, the first demonstration of spin transport in graphene at room temperature was done by Tombros and co-workers in 2007, using the non-local LSV configuration [143]. This configuration became the standard one to characterize spin transport properties in graphene as, for example, when the spin transport was modulated by electrostatic gating [144, 145]. Moreover, electric fields can also induce spin drift and modulate the spin injection [146–148]. The spin transport properties of graphene were improved by stacking it with hexagonal boron nitride, which can act as a substrate in graphene LSVs [149], as encapsulating layer [150–153], and as a tunnel barrier [154–156]. In Chapter 2, a detailed explanation of the development and improvement of graphene-based spin devices is given.

1.5.2 Other 2D materials

The discovery of graphene triggered the study of other 2D materials providing a new playground for spintronics [128, 157, 158]. Layered materials bonded by weak out-of-plane van der Waals forces are the inception for 2D materials, where the layers can be peeled off until the ultimate monolayer limit. In the 2D form, materials can behave different from the 3D counterpart, for instance, transition metal dichalcogenides (TMDCs) have an indirect band gap in the bulk, but show a direct band gap in the monolayer, making them suitable for optoelectronic applications [159–161].

TMDCs are materials where the transition metal atom (usually Mo or W) is sandwiched between two chalcogen atoms (S, Se or Te). Similar to graphene, single layer TMDCs in the hexagonal crystal lattice show energetically degenerate but inequivalent valleys at the K and K' points in the momentum space. These valleys add an extra degree of freedom that can be used to carry information in valley-based devices. Due to the large valley separation in momentum space, the valley degree of freedom is expected to be robust against scattering events. As in graphene, in the monolayer, in-plane inversion symmetry is explicitly broken. However, SOC is much stronger in TMDCs than in graphene. The broken inversion symmetry together with the strong SOC induces a large spin-splitting in the VB while the CB remains degenerate at the valleys. The spin-splitting in the VB is about 0.15 eV in MoS₂, 0.43 eV in WS₂, 0.18 eV in MoSe₂ and 0.46 eV in WSe₂ [162]. Due to time-reversal symmetry, the spin-splitting at the K and K' valleys must be opposite, shifting the up-spin sub-band in the K valley to higher energy than the down-spin sub-band and the opposite in the K' valley. This couples the spin and valley degrees of freedom (spin-valley locking), opening the door to a new way to encode information [163–166].

Besides TMDCs, hexagonal boron nitride (hBN) and black phosphorus have also recently attracted attention. hBN is a high- κ dielectric with similar crystal structure and lattice parameters as graphene and it has been integrated in spintronic devices [149–156]. When graphene is combined with hBN, because it reduces the trapped charge concentration and is atomically flat, hBN boosts the electrical properties of graphene [167]. Moreover, hBN is studied in the context of optics for the phonon-polariton transport [168, 169]. On the other hand, black phosphorus is characterized by an in-plane anisotropy inducing an anisotropic band structure where the effective charge-carrier mass is different

in the two in-plane directions [170–172]. Black phosphorus exhibits relatively long spin relaxation length ($\sim 6 \mu\text{m}$) [173], but the need of full encapsulation to avoid degradation of the material makes the device fabrication difficult [174].

1.5.2.1 Low-symmetry TMDCs

Beyond the diversity in the chemical composition of TMDCs, the crystal structure can also vary. In the present Thesis, special emphasis should be placed for the low-symmetry TMDC materials. Crystal symmetry governs the physical properties of crystalline solids [175]. When lowering the crystal symmetry, novel transport phenomena are allowed, such as non-linear Hall effect [176], valley magnetoelectricity in non-centrosymmetric crystals [177], or magnetochiral anisotropy in chiral crystals [178, 179].

As representative crystal phases of TMDCs, we can consider: the high-symmetry 2H phase, with hexagonal Bravais lattice and space group 194 [Fig. 1.10(a)], and two low-symmetry phases: the $1T_d$ phase, with orthorhombic Bravais lattice and space group 31 [Fig. 1.10(b)], and the $1T'$ phase, with monoclinic Bravais lattice, and space group 11 [Fig. 1.10(c)]. Materials in different crystal phases show a plethora of exotic effects, like superconductivity [180], charge density waves [181], quantum spin Hall semimetal behaviour [182–185], or ferroelectricity [186]. Low-symmetry phases not only show exotic effects, but they also exhibit different electrical behaviour. While most of the TMDCs in the 2H phase are semiconducting [187], $1T'$ and $1T_d$ phases can show metallic or semimetallic behaviour.

This is the particular case for MoTe_2 , which appears in three different crystal coordinations: trigonal prismatic coordination, i.e., 2H- MoTe_2 , or distorted octahedral coordination, i.e., $1T'$ - MoTe_2 and $1T_d$ - MoTe_2 . While the 2H- MoTe_2 is a n -type semiconductor [188, 189], $1T'$ - MoTe_2 behaves as a semimetal [190]. Moreover, $1T'$ - MoTe_2 is expected to show a phase transition to the $1T_d$ phase when the temperature is below 240 K [191–202]. $1T_d$ - MoTe_2 is expected to present large spin Hall conductivity [203] and has been widely studied in the context of Weyl physics [195, 198]. Considering all the above, $1T'$ - MoTe_2 is a fascinating material to be studied in the framework of spintronics (see Chapter 4 for a detailed characterization of this material).

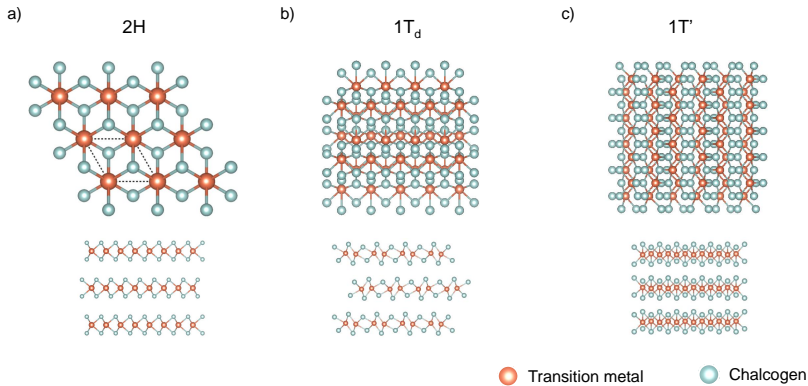


Figure 1.10: **TMDCs crystal structure.** Different crystal structures in which TMDCs can grow. Upper panel corresponds to the top view, and bottom panel to the side view. The transition metal atom is in orange while the chalcogen atom is in blue. (a) High symmetry 2H crystal phase. (b) Low-symmetry $1T_d$ crystal phase. (c) Low-symmetry $1T'$ crystal phase. Figure adapted from Ref. [204].

1.5.3 van der Waals heterostructures

Looking beyond pure 2D materials, van der Waals heterostructures enrich even more the 2D world forging a *Legoland*, based on the combination of different 2D materials [205]. Individual 2D materials are continuously obtained using the Scotch-tape technique [128, 129]. Each 2D material constitutes one *Lego* brick, which can be combined with other 2D materials by van der Waals stacking. Despite the complex technique for stacking different types of 2D materials, sophisticated multilayers have been fabricated up to date. One of the first heterostructures was hBN/graphene, where hBN acts as a high-quality substrate [149]. Later, MoS_2 or WS_2 acting as a tunnel barrier were combined with graphene working as an electrode [206, 207]. The tunneling heterostructures demonstrate a new kind of electronic devices: field-effect tunnelling transistors.

One of the of the most challenging van der Waals stackings is *magic-angle twisted bilayer graphene*. By combining two graphene layers, twisted by a particular “magic” angle (1.1°), graphene changes from behaving as a correlated insulator (Mott insulator) to a superconductor, by applying a small electric field to the system [209, 210]. The presence of an insulating state close to a superconducting one is a characteristic feature of high- T_c superconductors. Magic-angle twisted bilayer graphene is therefore a surprisingly simple system to study high- T_c superconductivity without the need of subjecting the system

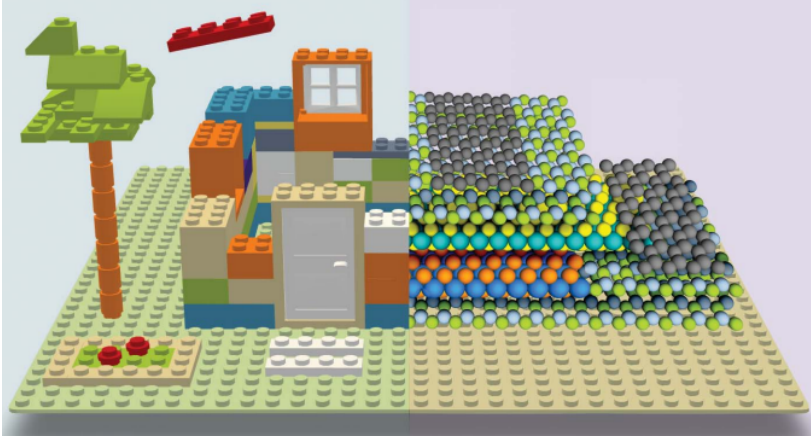


Figure 1.11: **Legoland**. Artistic representation of how stacking different 2D materials, a new world of physical properties is created. Each 2D material is represented by a Lego block and they can be placed one on top of the other. Figure extracted from Ref. [208].

to extremely large magnetic fields or changing composition to tune the carrier density (as in cuprates, the best known family of high- T_c superconductors), which can be simply done by electrical gating.

Van der Waals heterostructures have also revolutionised the research field of spintronics. As mentioned before, graphene is the ideal candidate to propagate spin currents due to its weak SOC and hyperfine interaction. The combination of graphene, as a spin channel, with strong SOC materials opens the door to a plethora of spin-based experiments. In the forthcoming Chapter, a detailed explanation of the graphene-based van der Waals heterostructures in spintronic devices is given.

1.6 This Thesis

This Thesis is based on the study of the SCC phenomena in graphene-based LSVs. This process relies on the presence of strong SOC, which is provided by in the low-symmetry TMDC, $1T'$ -MoTe₂. At the hands of the low crystal symmetry, non-orthogonal SCC processes are allowed. Low-symmetry SOC materials bring flexibility to the SCC configuration. Additionally, when graphene is placed in contact with a SOC material, its SOC is enhanced and SCC processes can take place in graphene. The different SCC processes that occur in the low-

symmetry MoTe₂/graphene van der Waals heterostructures are studied along this Thesis. The manuscript is divided in 8 Chapters in total.

Chapter 1 provides a general introduction to the history of spintronics. The most relevant discoveries in metal spintronics are included such as the achievement of efficient spin injection, essential for the pioneer experiments of SCC via SHE. Special emphasis is placed on the breakthrough of 2D materials in spintronics. Since its discovery, graphene was postulated as an ideal material to transport spin information over long distances due its weak SOC and hyperfine interaction. The discovery of graphene prompted the discovery of other bidimensional materials such as TMDCs and, in particular, of low-symmetry TMDCs, as 1T'-MoTe₂.

Chapter 2 gives a detailed explanation of graphene-based LSVs. Firstly electrical spin injection in graphene is discussed, followed by spin transport and detection. The different SCC processes that can be observed in graphene-based LSV combined with a SOC material are thoroughly studied, as well as SCC signals caused by the different spin polarization directions. Lastly, a detailed spin transport model to quantify the efficiency of the SCC via SHE in MoTe₂ is explained.

Chapter 3 introduces the experimental techniques used in the fabrication of graphene-based LSVs. The step-by-step process to create the graphene/MoTe₂ van der Waals heterostructure is disclosed. Finally, the different techniques for electrical and material characterization of the final heterostructure are described.

Chapter 4 presents the characterization of MoTe₂. Firstly, the crystal structure and crystal axes of the exfoliated MoTe₂ flakes are determined via polarized Raman spectroscopy and scanning transmission electron microscopy. Once the crystal axes of the MoTe₂ are determined, the magnetoresistive behaviour of MoTe₂ flakes was measured when the magnetic field is applied along different crystallographic directions. Lastly, spin transport experiments are carried out in MoTe₂ flakes.

Chapter 5 and **Chapter 6** investigate the SCC process in graphene / MoTe₂ LSV in the standard LSV configuration. While Chapter 5 focuses on the study at moderately high temperatures, Chapter 6 focuses on the SCC at low temperatures where new effects such as proximity-induced SCC is dominant. In the case of moderately high temperatures, any in-plane spin polarization induces SCC. In order to observe such an effect, the crystal symmetries

of the system have to be reduced, and different scenarios are considered. At lower temperatures, along with the previous observation, an out-of-plane spin polarization also induces SCC, and a detailed discussion of the possible origin is presented.

Chapter 7 explores the SCC phenomena combining the previously studied standard configuration with a new configuration, in which the charge current is applied along different directions within the MoTe_2 flake. This study provides new insights into the SCC processes that can take place in the graphene / MoTe_2 heterostructure.

Chapter 8 collects the main results and future perspectives.

Chapter 2

Graphene-based lateral spin valves

Despite the great advances and improvements achieved in metal-based spintronic devices, efficient spin transport at room temperature over long distances was still lacking. Since the discovery of graphene, this material has been postulated as a great candidate to be integrated in spin-based devices. Its weak SOC and negligible hyperfine interaction makes graphene suitable to transport spin information. Indeed, graphene exhibits the longest λ_s ever measured at room temperature enabling the spin transport in complex devices [151, 155, 211–214]. Van der Waals heterostructures based on graphene are claimed to be crucial in the next generation of spin-based devices where TMR [215–217], spin logic gates [218, 219], spin-transfer torque [220, 221], spin manipulation [222–224], or SCC [225–235] phenomena have been measured.

In this Thesis, graphene-based LSVs are used in order to study the SCC process in combination with a low-symmetry high-SOC van der Waals material, MoTe_2 . A graphene-based LSV consists of two FM electrodes placed on top of a graphene channel. In between the two FM electrodes, a SOC material can be added in order to achieve SCC, either directly in the material or by imprinting the SOC in graphene itself, as will be discussed in Section 2.2. Graphene can be obtained via exfoliation, using the Scotch-tape technique, or via Chemical Vapor Deposition (CVD) and shaping it via an etching process. In this Chapter, a detailed explanation of graphene-based LSVs is given.

2.1 Spin transport in pristine graphene

In this section, we will first introduce the concept of electrical spin injection into graphene and, subsequently, we will explain the dynamics of spin transport and detection in graphene.

2.1.1 Electrical spin injection into graphene

As introduced in Section 1.2, in order to overcome the conductivity mismatch problem, TBs can be introduced between the FM injector and the NM channel to have an efficient spin polarization. The pioneering work from Tombros and co-workers demonstrated an efficient spin polarization (10%) into graphene using Co electrodes with a TB of AlO_x [143]. Subsequent works using MgO as a TB also showed a spin polarization of about 5% [236,237]. Since sputter deposition damages the surface quality of graphene, inducing defects [238], other techniques have been used, such as atomic layer deposition of Al_2O_3 [239], thermal evaporation of metals followed by air exposure, such as yttrium (whose spin polarization was not larger than 15%) [240], titanium [222] or Al [143]; or e-beam evaporation of oxides as Al_2O_3 [147], SrO [241], or MgO [211].

The inefficient spin injection directly from the FM to graphene is due to the lower spin resistance of the FM in comparison with the one of the graphene channel. Spins tend to relax towards the path with lower spin resistance, flowing back to the FM, which acts as a spin sink, instead of flowing into graphene. The role of the insulating layer between the FM and the graphene is to avoid this back-flow due its high resistance. Yet, if the resistance of the insulating layer is comparable to the graphene spin resistance (R_s^{gr}) spin relaxation mechanisms occur at the interface. Significant effort has been put to improve the quality of the barriers. By placing a Ti seed layer between MgO and graphene, Han and co-workers improved the spin polarization of the electrode up to 30% [242].

2D materials are expected to act as ideal TB as they do not present pinholes. hBN was demonstrated to be a good TB since the resistance of the barrier depends exponentially on the thickness and it is pinhole free [206]. However, if the resistance of the hBN layer is comparable to the one of graphene, the conductivity mismatch issue is not fully overcome [152, 154, 155, 243]. Chemically functionalized graphene can also be used as a TB, achieving spin polarization up to 45% for fluorinated graphene and 17% for hydrogenated graphene at low

temperatures [244,245]. Unfortunately, the spin signal in chemically functionalized graphene at room temperature vanishes [246]. Recent studies observed very efficient spin injection into graphene using bilayer or trilayer hBN [247–249]. However, the sample-dependent variability of the resistance of the TB using hBN [155] together with the demanding fabrication process make hBN a challenging material to be used as a TB combined with graphene.

2.1.2 Spin transport and detection in graphene

After electrical spin injection, i.e when I_c is applied between FM_1 and one side of graphene, a spin accumulation is created at the interface and diffuses to both sides of the graphene channel [Fig. 2.1(a)]. The spin current eventually reaches FM_2 and, by measuring the voltage generated between FM_2 and graphene (V_{NL}), the transport along the graphene channel will be inferred. By sweeping the magnetic field along the easy axis of the FMs, the relative orientation of the FMs changes from parallel to antiparallel due to the different shape anisotropies, inducing a sign change in the non-local resistance R_{NL} ($R_{NL} = V_{NL}/I_c$), see Fig. 2.1(b). The semi-difference between the parallel and the antiparallel value is represented by ΔR_{NL} (see Eq. 1.10).

By fitting the dependence of ΔR_{NL} with the distance between FM electrodes (L) to Eq. 1.11, the spin diffusion length of graphene (λ_s^g) can be determined. However, it is difficult to obtain the same polarization between FMs and NM (P_{inj} and P_{det}) and contact resistances (R_i) in different LSVs. To properly extract the spin transport parameters of graphene, precession measurements are usually performed.

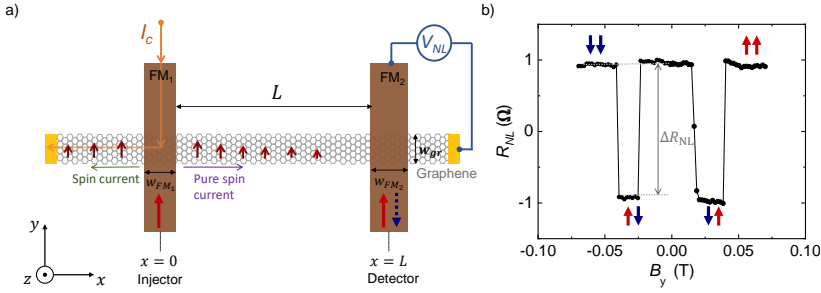


Figure 2.1: **Graphene-based lateral spin valve.** (a) Schematic of the device. FM electrodes are placed on top of graphene separated by a distance L , while non-magnetic electrodes are placed at both graphene ends (yellow contacts). The green arrow represents the spin polarized current direction, while the purple arrow represents the pure spin current direction. The spin accumulation induced by I_c is represented by the red arrows on top of graphene. The length of the arrows represents the spin accumulation value exhibiting exponential decay. V_{NL} is probed using FM_2 and the non-magnetic contact on graphene. The width of the graphene flake is represented by w_{gr} . (b) Measurement of the non-local resistance as a function of the magnetic field along the in-plane easy axis (y -direction). The amplitude of the signal (ΔR_{NL}) is represented by the grey vertical arrow and the magnetization states of the FM are displayed by the red and blue arrows. This signal has been measured at room temperature using a few-layer exfoliated graphene flake with TiO_x as a TB and Co as a FM.

2.1.2.1 Hanle precession

As explained in Section 1.3.1, spin precession measurements can be used to characterize the spin transport parameters. In this case, by applying an out-of-plane magnetic field (B_z), the parameters λ_s^{gr} , τ_s^{gr} , and D_s^{gr} can be extracted. If B_z is not large enough to pull the magnetization towards the direction of the field, the spins will precess when diffusing in the graphene channel [Fig. 2.2(a)]. This precession occurs in the $y-x$ -plane and the measured signal will oscillate accordingly. The initial state of the relative magnetization of the FMs can be parallel [blue solid circles in Fig. 2.2(b), R_{NL}^P] or antiparallel [red open circles in Fig. 2.2(b), R_{NL}^{AP}] and the corresponding curve should be equivalent but for the sign. This allows to remove any background by applying again Eq. 1.10. An example of a typical ΔR_{NL} curve is shown in the inset of Fig. 2.2(b).

At zero magnetic field, the amplitude of the signal is maximum and corresponds to ΔR_{NL} when sweeping the magnetic field along the y -direction. As the precession starts when the magnetic field increases, the signal starts to decrease until it vanishes when the parallel and antiparallel state signals take the same value. This condition corresponds to an average spin precession of 90° ,

that is, the arriving spins will be polarized along the x -direction while the magnetization of the detector is along y -direction. Since FM₂ is only sensible to the projection of the spin polarization onto the direction of its magnetization, the measured signal vanishes. For large enough magnetic fields, the magnetization of the electrodes starts to be pulled and the signal saturates, taking the same value for both parallel and antiparallel initial states.

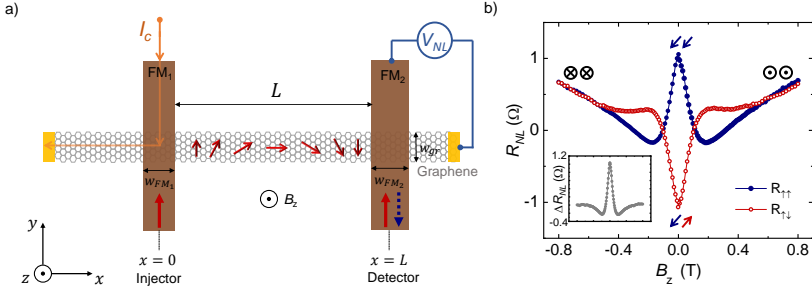


Figure 2.2: **Hanle precession in a graphene-based lateral spin valve.** (a) Schematic of the device and measurement layout. FM electrodes are placed on top of graphene separated by a distance L , while the non-magnetic electrodes are placed at both graphene ends (yellow contacts). The spin accumulation at the FM₁/graphene interface, created by applying an I_c between FM₁ and the left side of graphene, while diffusing through the graphene channel will precess in the x - y -plane due to the external magnetic field along the z -direction. The spin precession is represented by the red arrows in the graphene channel. (b) Non-local resistance as a function of the external out-of-plane magnetic field. The blue curve corresponds to R_{NL} measured after setting the FM electrodes in a parallel magnetization configuration, while the red curve corresponds to an antiparallel configuration. The magnetization of the FMs are represented by the pair of arrows. Inset ΔR_{NL} vs B_z obtained from the data in the main panel. This Hanle precession signal was measured in the same graphene-based LSV as the one in Fig. 2.1(b) at room temperature.

If $L \gg \lambda_s$, spins stay longer in the channel than in the vicinity of the contacts and, consequently, the influence in the spin transport from the contact is almost negligible. Considering 1D spin transport, with $L \gg \lambda_s$, the dynamics of the spin accumulation determined by the Bloch equation takes the following form:

$$D_s \frac{\partial \mu_s}{\partial x^2} - \frac{\partial \mu_s}{\tau_s} + \boldsymbol{\omega} \times \boldsymbol{\mu}_s = 0, \quad (2.1)$$

where an extra term corresponding to the spin precession is added in comparison with Eq. 1.7. $\boldsymbol{\omega}$ corresponds to the Larmor frequency and depends on the external magnetic field \boldsymbol{B} .

Considering the simplest case, where the magnetic field is out of plane, spin lifetime is isotropic, and the TB is ideal, together with the boundary conditions,

Eq. 2.1 can be solved, yielding [44, 250]:

$$\Delta R_{NL} = \frac{P^2 \cos^2 \Theta R_{sq}^{gr} \lambda_s^{gr}}{w_{gr}} \Re \left[\frac{\exp \left(-\frac{L}{\lambda_s^{gr}} \sqrt{1 - i\omega\tau_s^{gr}} \right)}{\sqrt{1 - i\omega\tau_s^{gr}}} \right], \quad (2.2)$$

where R_{sq}^{gr} is the sheet resistance of graphene. This equation is numerically equivalent to Eq. 1.15, and the polarization of the injector and detector are assumed to be the same ($P = P_{inj} = P_{det}$).

2.1.2.2 Spin relaxation mechanisms in graphene

During the propagation of the spin carriers, the polarization of the spin current decays due to spin relaxation mechanisms. In metals and semiconductors, the four main spin relaxation mechanisms are usually discussed [61]: Elliott-Yafet [65, 66], D'yakonov-Perel [67, 68], Bir-Aronov-Pikus [69] and hyperfine interaction [71, 72].

In graphene, the hyperfine interaction is negligible due to the low presence of isotopes with nuclear magnetic moment. Due to the diffusive transport of electrons, the nuclear fields on the spins average out, so that the hyperfine mechanisms can be neglected for graphene [251].

Bir-Aronov-Pikus mechanism accounts for the electron-hole exchange interaction and the spin-flip process that can occur. This effect is important in heavily p -doped semiconductors, but can be disregarded in graphene.

Elliott-Yafet mechanism accounts for the change in the spin polarization of a Bloch electron due to the scattering with phonons or impurities. In doped graphene, this mechanism depends on the carrier concentration and the strength of the SOC [252–254].

D'yakonov-Perel mechanism takes into account the spin dephasing between scattering events. Due to the double degenerated bands in graphene, SOC can be understood as an effective field that makes the spin precess in a direction determined by the direction of the motion of the electron and, hence, the scattering randomizes precession [44, 255].

Both Elliott-Yafet and D'yakonov-Perel mechanisms overestimate τ_s^{gr} in graphene. For the case of Elliott-Yafet, considering typical values of carrier concentration of 10^{12} cm^{-2} and the strength of SOC of $10 \text{ } \mu\text{eV}$, τ_s is calculated to be around $10 \text{ } \mu\text{s}$, which is 4 orders of magnitude larger than the ones ex-

tracted in Hanle measurements in pristine graphene [143, 211]. For the case of D'yakonov-Perel, τ_s is predicted to be around 1 μs which, again, is longer than the values reported experimentally. Understanding the additional relaxation mechanism is still a puzzling aspect of graphene-based devices. Considering other intrinsic relaxation sources, Van Tuan and co-workers claimed that the entanglement of the spin with the valley degree of freedom leads to fast spin relaxation at energies close to the Dirac point [256]. This mechanism explains the dependence of τ_s^{gr} with the carrier concentration that cannot be explained using Elliott-Yafet mechanism. Magnetic impurities, as extrinsic sources of spin relaxation, should also be considered [257]. Impurities with local magnetic moments can behave as spin hot spots inducing high spin relaxation rates. Due to exchange interaction, the electron spin can flip when interacting with the magnetic moment of the impurity. These impurities may come from the fabrication process [257–259]. The encapsulation of graphene with hBN has proven to dramatically increase the spin lifetime of graphene [150, 151, 155, 156, 260, 261], since hBN seals the graphene, acting as a protection layer and avoiding contamination during the fabrication process of the device.

2.2 Spin-to-charge conversion in graphene-based heterostructures

In the field of spintronics, even though graphene is an ideal candidate to transport spin currents over long distances due to its low SOC (see previous Section), this means a limitation on the manipulation of such spin currents. However, SOC can be enhanced in graphene by proximity to another 2D material in van der Waals heterostructures [262–269], inducing weak antilocalization [270–274], or spin lifetime anisotropy [275–277], and allowing the electrical control of spin currents [222, 223] and, more recently, of the SOC-induced spin precession [224]. Spin-orbit proximity in graphene also induces SHE [226–228] and REE [225, 228, 229, 232, 235], giving rise to electrically controllable SCC.

Most of the SCC experiments based on spin-orbit proximity place a semiconducting high-SOC van der Waals material on top of graphene, which then has to be structured so that it can be used as an electrode for the proximitized region [225–228, 232]. However, if graphene is combined with a conducting (metallic or semimetallic) van der Waals material, SCC can be measured by directly probing the voltage across both materials. In this case, disentangling the origin of each SCC process remains challenging as it can either occur via

SHE in the high-SOC material itself, or in the proximitized graphene; or via EE at the surface of the high-SOC material, or at the proximitized graphene. Hereunder, each contribution is deeply discussed.

2.2.1 Due to SHE

2.2.1.1 In the SOC material

Along this Chapter, it has been mentioned how crucial are the crystal symmetries in regard of the permitted SCC processes. Crystalline systems are grouped in 230 space groups, where the 32 crystal classes and the 14 different Bravais lattices are considered. The lower the number of the space group is, the fewer symmetry operations are granted, and more independent elements in the spin Hall conductivity tensor, σ_{ij}^α , are allowed. The higher the number of the space group is, the more σ_{ij}^α elements are correlated via symmetry operation and the number of independent elements in the tensor reduces.

Representative crystal phases in which TMDCs typically grow are the 2H phase, which corresponds to space group 194, 1T' phase, corresponding to space group 11, and 1T_d phase, corresponding to space group 31. The elements for each spin polarization of the spin Hall conductivity tensor for the 2H phase are given by:

$$\sigma_{ij}^x = \begin{pmatrix} 0 & 0 & 0 \\ 0 & 0 & \sigma_{yz}^x \\ 0 & \sigma_{zy}^x & 0 \end{pmatrix} \quad \sigma_{ij}^y = \begin{pmatrix} 0 & 0 & \sigma_{xz}^y \\ 0 & 0 & 0 \\ \sigma_{zx}^y & 0 & 0 \end{pmatrix} \quad \sigma_{ij}^z = \begin{pmatrix} 0 & \sigma_{xy}^z & 0 \\ \sigma_{yx}^z & 0 & 0 \\ 0 & 0 & 0 \end{pmatrix} \quad (2.3)$$

where 6 elements are allowed and only 3 are independent. The relation among them are: $\sigma_{zx}^y = -\sigma_{zy}^x$, $\sigma_{xz}^y = -\sigma_{yz}^x$ and $\sigma_{xy}^z = -\sigma_{yx}^z$.

For the 1T' phase, the spin Hall conductivity tensor is given by:

$$\sigma_{ij}^x = \begin{pmatrix} 0 & \sigma_{xy}^x & 0 \\ \sigma_{yx}^x & 0 & \sigma_{yz}^x \\ 0 & \sigma_{zy}^x & 0 \end{pmatrix} \quad \sigma_{ij}^y = \begin{pmatrix} \sigma_{xx}^y & 0 & \sigma_{xz}^y \\ 0 & \sigma_{yy}^y & 0 \\ \sigma_{zx}^y & 0 & \sigma_{zz}^y \end{pmatrix} \quad \sigma_{ij}^z = \begin{pmatrix} 0 & \sigma_{xy}^z & 0 \\ \sigma_{yx}^z & 0 & \sigma_{yz}^z \\ 0 & \sigma_{zy}^z & 0 \end{pmatrix} \quad (2.4)$$

where the 13 granted elements are independent.

For the $1T_d$ phase, the spin Hall conductivity tensor is given by:

$$\sigma_{ij}^x = \begin{pmatrix} 0 & 0 & 0 \\ 0 & 0 & \sigma_{yz}^x \\ 0 & \sigma_{zy}^x & 0 \end{pmatrix} \quad \sigma_{ij}^y = \begin{pmatrix} 0 & 0 & \sigma_{xz}^y \\ 0 & 0 & 0 \\ \sigma_{zx}^y & 0 & 0 \end{pmatrix} \quad \sigma_{ij}^z = \begin{pmatrix} 0 & \sigma_{xy}^z & 0 \\ \sigma_{yx}^z & 0 & 0 \\ 0 & 0 & 0 \end{pmatrix} \quad (2.5)$$

where the 6 non-zero elements are independent.

In order to obtain the spin Hall conductivity tensor for different space groups, one can check appendix in Ref. [78] or [278]. While only six orthogonal elements are granted in both the 2H and $1T_d$ phases, 13 orthogonal and non-orthogonal elements are allowed in the $1T'$ phase. Moreover, the symmetries of the system determine not only how many tensor elements are permitted, but also the relation between them. Both in the 2H and $1T_d$ phases, 6 elements are assured. However, for the 2H phase, only 3 of them are independent, while all 6 are independent in the $1T_d$ phase.

In high-symmetry materials, i.e., where at least two mirrors are present, the SHE only allows to generate spin current perpendicular to the direction of the spin polarization and charge current. When a spin current along the z -direction, with spin polarization along the x -direction, enters into a SOC material, the generated charge current is along the y -direction [see Fig. 2.3(a)]. If the crystal symmetry is lower, i.e., with one mirror present, two different spin polarization orientations can generate charge current along the direction perpendicular to the mirror plane (y -direction) with the spin current along the z -direction, that is spin polarization orientation along z - and x -directions [see Fig. 2.3(b)]. This particular case is of interest in order to switch out-of-plane FM since it is possible to generate, via SHE, out-of-plane spin polarization parallel to the spin current direction. This has been studied in spin-orbit torque experiments where the spins induce a switching in the direction of the FM magnetization [202, 279, 280]. If the crystal symmetry is further reduced, no mirror is present and any spin polarization direction can induce a charge current along the y -direction with the spin current along the z -direction. In order to reduce the symmetry constrains of the SCC processes, low-symmetry 2D materials can be used to study SHE conversion, or high-symmetry materials where the symmetries are broken by applying strain to the system [202, 231, 233, 235, 279, 281, 282].

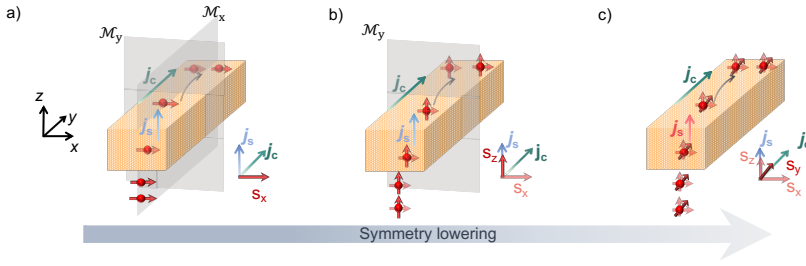


Figure 2.3: ISHE process in low-symmetry materials. (a) High-symmetry SOC material presenting two perpendicular mirror planes. Only a spin polarization along x -direction, with spin current along z -direction can generate a charge current along y -direction. Note that the charge current, spin current and spin polarization are mutually perpendicular. (b) If the crystal symmetry is lowered, only one mirror plane is present and, together with the previous configuration, an out-of-plane spin polarization induces as well charge current in the y -direction, perpendicular to the mirror plane, with spin current parallel to the spin polarization. (c) If the crystal symmetry is further lowered, any spin polarization can induce a charge current along the y -direction with spin current in z -direction.

2.2.1.2 In the proximitized graphene

Graphene is very sensitive to the environment, allowing to boost its SOC via chemical functionalization, adatom decoration or substrate engineering [259, 283–289]. The disadvantage of these approaches is that they reduce the electronic quality of graphene. However, a van der Waals heterostructure of graphene with a TMDC material will preserve graphene electronic quality while SOC can be imprinted on it via spin-orbit proximity [290].

The initial experiments combining graphene/TMDCs showed gate tunability of the spin absorption into MoS_2 [222, 223]. Afterwards, strong spin-valley coupling in graphene/ WS_2 and graphene/ MoS_2 was demonstrated, inducing spin lifetime anisotropy [275, 277]. These results boosted the study of SCC in graphene/TMDCs heterostructures.

In this regard, Avsar and co-workers observed in a graphene/ WS_2 heterostructure an enhancement of the graphene SOC up to 17.6 meV, allowing the observation of (I)SHE in graphene [291], although unleashed scientific controversy with the double Hall bar design used to measure the effect [292]. A theoretical work by Gmitra and co-workers reported a graphene-SOC enhancement in the order of 0.2 meV in a graphene/ MoS_2 heterostructure [263]. The large difference in the strength of the induced SOC in graphene by MoS_2 or WS_2 was also theoretically reported [264, 266, 268]. According to the theoretic-

cal works, the proximity-induced SOC in graphene/TMDCs present mainly two contributions: Rashba SOC and a new type of SOC, denoted as valley-Zeeman SOC, which dominates over the other [271]. Valley-Zeeman SOC couples the spin and valley degrees of freedom. Due to such coupling, the relation between intra and intervalley scattering plays a crucial role. If the intervalley scattering is dominant, the electron is scattered from one valley to the other, changing its mass accordingly. This process reduces the averaged mass of the electron and so the strength of the induced SOC, which is directly linked with the spin Hall conductivity. Moreover, as Fig. 2.4(a) shows, the spin Hall conductivity σ_{xy}^z of the proximitized graphene changes with the carrier concentration of graphene. The largest value of σ_{xy}^z is reported for graphene/WS₂. In addition, σ_{xy}^z changes sign when changing the carrier type in graphene, which can be tuned via electrostatic gating. Although the expected value of σ_{xy}^z in graphene/MoS₂ heterostructure is not the largest reported, the induced SHE in graphene was unequivocally observed for the first time by Safer and co-workers in such system [226].

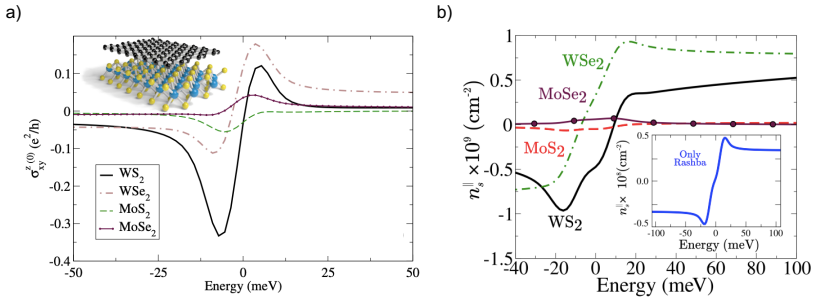


Figure 2.4: **Spin-to-charge conversion for different graphene/TMDC van der Waals heterostructures.** (a) Dependence of the spin Hall conductivity as a function of the band energy for different graphene/TMDCs heterostructures. Figure adapted from Ref. [266]. (b) Non-equilibrium spin density for different graphene/TMDCs heterostructures. In the inset, the non-equilibrium spin density is calculated for a pure Rashba system for graphene/WS₂. Figure adapted from Ref. [268].

Different experimental works report the gate tunability of σ_{xy}^z via electrostatic gating in graphene/WS₂ [228] and graphene/WSe₂ [227]. In these cases, the experimental values are larger than the theoretical calculations, indicating the possibility that extrinsic contributions, such as localized defects, may also contribute to the SHE induced in graphene [228].

2.2.2 Due to Edelstein effect

EE occurs in systems with broken inversion symmetry and SOC (see Section 1.4.2). In a SOC material, EE can occur at the surface or at the bulk. In addition, in a graphene/SOC material heterostructure EE can also occur in the graphene by proximity.

2.2.2.1 In the SOC material

On the one hand, if the inversion symmetry is broken in the bulk of a material, bulk EE can be observed. By applying an external electric field, a macroscopic spin polarization is expected to be induced in the bulk of such materials [293]. This is the particular case of Weyl semimetals, which host spin-polarized surface, known as Fermi arcs [294]. Other than Weyl semimetals, chiral materials lack inversion and mirror symmetries, and gate-tunable EE has been recently observed in Te [179]. Additionally, the bulk EE has also been observed in other systems with strong SOC and broken inversion symmetry such as bulk Rashba materials [295–297]. In particular, the $1T_d$ phase presents broken inversion symmetry, therefore, any material with high-SOC in this crystal phase is expected to show bulk EE. Contrary to this, the $1T'$ phase preserves the inversion symmetry so does not allow the bulk EE.

On the other hand, at the surface of a SOC material, inversion symmetry is broken by definition. The surface EE leads to a spin accumulation when a charge current is applied along the surface. In order to know the allowed components at the surface EE in a SOC material, its crystal symmetries are crucial. In the case of the $1T'$ phase, only one mirror plane is present, say \mathcal{M}_y mirror symmetry, which corresponds to a mirror plane along the x -direction and, in consequence $y \rightarrow -y$. While the electric field, associated to the charge current, is a vector, the spin polarization is a pseudovector, consequently, when applying the mirror symmetry to them the effect is different [175].

For the case of vectors, and in particular the electric field \mathbf{E} , the resulting electric field when the \mathcal{M}_y mirror symmetry is applied, is given by:

$$\mathcal{M}_y \mathbf{E}(x, y, z) = \begin{pmatrix} E_x \\ -E_y \\ E_z \end{pmatrix}. \quad (2.6)$$

For the case of pseudo-vectors, in particular the spin polarization (\mathbf{s}), the re-

sulting spin polarization after the symmetry operation is given by:

$$\mathcal{M}_y s(x, y, z) = \begin{pmatrix} -s_x \\ s_y \\ -s_z \end{pmatrix}. \quad (2.7)$$

If the electric field reverses sign, the spin polarization should also reverse the sign. Therefore, if the SOC material contains a single \mathcal{M}_y mirror, an electric field along the x - and z -directions can induce spin polarization along y , via surface EE, while an electric field along the y -direction can induce spin polarization along x - and z -directions.

2.2.2.2 In the proximitized graphene

When a SOC material is combined with graphene, a hybrid system is formed at the interface between both materials, which we have referred to as “proximitized graphene” (see Section 2.2.1.2). This new interfacial system accounts for the surface of the SOC material facing the graphene flake, the interface between both materials, and the graphene modified by the presence of the SOC material. In this case, the EE in the surface of the SOC material and the one induced in graphene are indistinguishable. For the sake of simplicity, we will refer to this effect as EE in proximitized graphene from now on.

In the case of graphene/TMDCs heterostructures, the Rashba SOC in graphene stems from the breaking of the inversion symmetry due to the proximity with the TMDC [262, 265]. In such graphene/TMDC Rashba system, when a charge current is applied, a spin accumulation via EE is created, with spin polarization perpendicular to the applied charge current. This spin accumulation will diffuse away from the proximitized region. REE has been observed in different graphene/TMDCs heterostructures such as monolayer WS_2 [225, 228], TaS_2 [229], MoTe_2 [230], and also in graphene/ $(\text{Bi}_{0.5}\text{Sb}_{0.85})_2\text{Te}_3$, which is a topological insulator [232]. Moreover, REE in proximitized graphene is gate-tunable. By tuning the carrier type in graphene, the induced spin-density can change sign as shown in Fig. 2.4(b) [228, 268].

The allowed SCC configurations via EE at the interface between the two materials are determined by the mirror alignment between them. If on top of graphene, which contains two mirror planes, a SOC material is placed, which none of its mirrors are aligned with the ones of graphene, the interface has no symmetry and any spin polarization can be induced via EE when a charge

current is applied to the interface. In contrast, if certain mirrors of the SOC material are aligned with those of graphene, the symmetry of the interface is determined by the number of aligned mirrors.

2.2.3 Disentangling the SCC signals in graphene-based LSV

Graphene-based LSVs combine graphene with a SOC material in order to study the SCC conversion process. In particular, in this Thesis, the SOC material is 1T'-MoTe₂, a low-symmetry material. As Fig. 2.5 represents, the graphene channel sites along the x -direction, and the long axis of MoTe₂ along the y -direction. In order to measure SCC, we will use by default what we call “standard SCC configuration”, also sketched in Fig. 2.5. The charge current (I_c) is applied between the FM and graphene, in order to inject spins into the graphene channel, and the non-local voltage (V_{NL}) is measured along the long axis of MoTe₂, from which the non-local resistance $R_{NL} = V_{NL}/I_c$ is obtained.

As discussed above, SCC can have different origins. Moreover, if a low-symmetry material such as MoTe₂ is studied, non-orthogonal elements in the spin Hall conductivity tensor are allowed. In order to identify how these components will influence the R_{NL} signal, the contributions from each spin polarization when sweeping the magnetic field along the three different directions are analyzed.

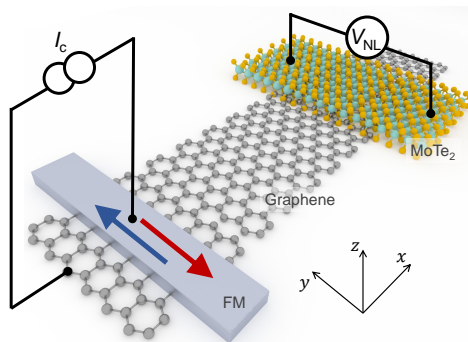


Figure 2.5: **Standard SCC configuration in graphene-based LSV in combination with MoTe₂.** Sketch of a graphene-based LSV with MoTe₂ being the SOC material. In the standard SCC, the charge current is applied between the FM and graphene and the voltage is probed along the MoTe₂ flake. Due to the shape anisotropy, the magnetization of the FM lies along the $\pm y$ -direction, corresponding to the blue/red arrows.

By applying a magnetic field along the different directions (x , y , and z), the direction of the spin polarization $\mathbf{s} = (s_x, s_y, s_z)$ is controlled. Moreover, the magnetization of the FM electrode tends to lie along its easy axis, which, due to the shape anisotropy, corresponds to the y -direction. Thus, the FM magnetization can be along the $+y$ -direction (blue arrow on the FM in Fig. 2.5) or $-y$ -direction (red arrow on the FM in Fig. 2.5). The non-local resistance measured when the initial state of the FM is along the $+y$ -direction is referred to as R_{NL}^\uparrow , whereas when the initial state of the FM is along the $-y$ -direction is referred to as R_{NL}^\downarrow .

In the following, we will discuss the expected shape of the R_{NL} curve as a function of the magnetic field in the different directions by considering the most general case in which spin polarization in any of the three directions induces SCC, regardless of its origin.

2.2.3.1 Applying in-plane magnetic field along the hard axis of the FM injector (B_x)

By applying B_x , the orientation of the injected spins is affected in two different ways: by precession and via pulling of the FM. Initially, at zero magnetic field, the Co magnetization lies along the easy axis, so that $\mathbf{s}=(0, \pm s_y, 0)$. Figure 2.6(a) represents the direction of the magnetization along the $+y$ -direction, hence, the spin polarization is $\mathbf{s}=(0, +s_y, 0)$. The associated signal to the SCC of $+s_y$ spins is maximum at zero field, represented by the blue solid line (R_{NL}^\uparrow) in Fig. 2.6(b). Likewise, if the initial state of magnetization is along the $-y$ -direction, the polarization of the injected spins is $\mathbf{s}=(0, -s_y, 0)$ and the corresponding signal is represented by the red dashed line (R_{NL}^\downarrow) in Fig. 2.6(b).

For relatively low values of B_x , since the direction of the injected spins is perpendicular to the direction of the field, the spins in the graphene channel will precess in the $y-z$ -plane [see Fig. 2.6(c)]. As precession starts, the s_y component of the spins arriving to the MoTe₂ is reduced and, thus, R_{NL} associated to the SCC of s_y spins decreases. The resulting symmetric Hanle curve is equivalent to the standard Hanle precession using a FM detector (Fig. 2.2), since it also comes from spin precession and is symmetric with B_x . If the initial state of the magnetization is along the $+y$ -direction, at certain positive value of B_x , the spins reaching the MoTe₂ will be polarized along the $+z$ -direction (R_{NL}^\uparrow). In contrast, spins will be polarized along the $-z$ -direction at certain negative value of B_x . R_{NL} associated to the SCC of s_z spins will also depend on the precession, resulting in an antisymmetric Hanle curve in this cases. Figure 2.6(d)

represents the corresponding signal when the initial state of the magnetization is along the $+y$ -direction (blue solid line, R_{NL}^\uparrow) or along the $-y$ -direction (red dashed line, R_{NL}^\downarrow). The two curves are antisymmetric with the magnetic field and have opposite sign for the same value of B_x .

For large enough values of B_x , the magnetization of the FM is pulled towards the direction of the field, until it aligns. Figure 2.6(e) shows the case where the magnetization of FM is along the $+x$ -direction and, hence, s_x spins are injected. R_{NL} associated to the SCC of s_x spins is independent of the two initial states of the magnetization, since it comes from the pulling of the magnetization, which is the reason why the blue (R_{NL}^\uparrow) and red curves (R_{NL}^\downarrow) are one on top of each other in Fig. 2.6(f). These S-shaped curves are antisymmetric with the field and both have the same sign.

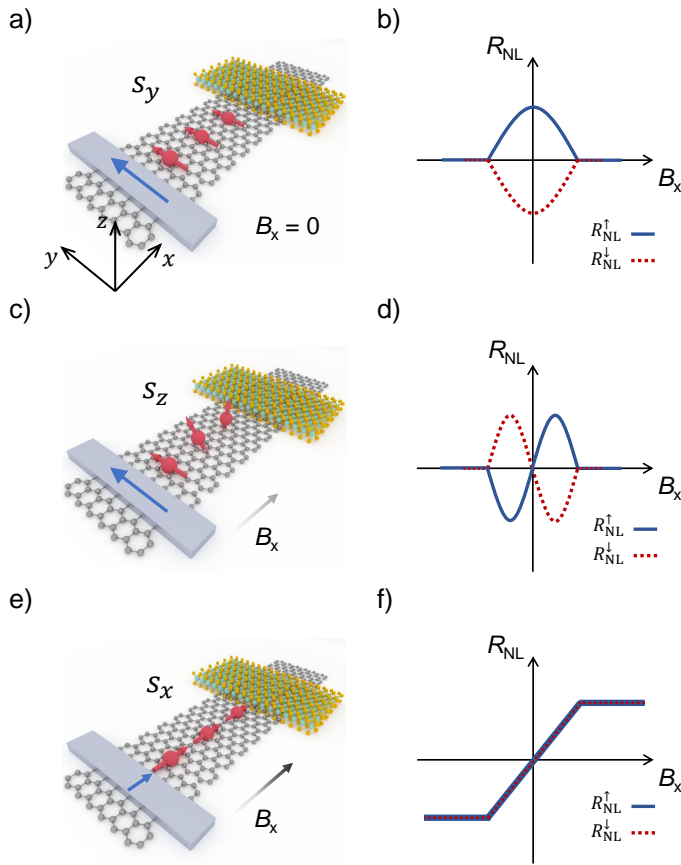


Figure 2.6: **Standard SCC measurement contributions by applying an in-plane magnetic field along the hard axis of the FM injector.** (a) At zero magnetic field, the magnetization of the FM lies along the easy axis ($+y$ -direction) and the injected spins are polarized along the same direction. (b) R_{NL} as a function of B_x generated by the SCC of s_y . The solid blue and dashed red curves correspond to the two different initial states of the magnetization, $+y$ and $-y$ directions respectively. These are symmetric Hanle curves. (c) For intermediate values of B_x , the injected spins precess in the y - z -plane. (d) R_{NL} as a function of B_x generated by the SCC of s_z , which depends on the initial state of the magnetization ($+y$ -direction corresponds to solid blue curve and $-y$ -direction corresponds to dashed red curve). These are antisymmetric Hanle curves. (e) For large values of B_x , the magnetization of the FM is aligned in the direction of the field. Consequently, the injected spins are parallel to B_x . (f) R_{NL} as a function of B_x generated by the SCC of s_x , which arises from the magnetization rotation and, hence, does not depend on the initial state of the magnetization. The curve shows an S-shape, which is antisymmetric with the magnetic field.

2.2.3.2 Applying out-of-plane magnetic field (B_z)

By applying B_z , the orientation of the injected spins is also affected in two different ways, by precession and via pulling of the FM. Figure 2.7(a) represents the direction of the magnetization along the $+y$ -direction, therefore, the spin polarization is $\mathbf{s}=(0, +s_y, 0)$. The associated signal to the SCC of $+s_y$ spins is maximum at zero field, represented by the blue solid line (R_{NL}^\uparrow) in Fig. 2.7(b). Likewise, if the initial state of magnetization is along the $-y$ -direction, the polarization of the injected spins is $\mathbf{s}=(0, -s_y, 0)$ and the corresponding signal is represented by the red dashed line (R_{NL}^\downarrow) in Fig. 2.7(b).

For relatively low values of B_z , since the direction of the injected spins is perpendicular to the direction of the field, the spins in the graphene channel will precess in the $y-x$ -plane [see Fig. 2.7(c)]. As precession starts, the s_y component of the spins reaching the MoTe₂ is reduced, so the spin signal associated to the SCC of s_y spins decreases, showing a symmetric Hanle curve. If the initial state of the magnetization is along the $+y$ -direction, at certain positive value of B_z , the spins reaching the MoTe₂ will be polarized along the $+x$ -direction. In contrast, spins are polarized along the $-x$ -direction at certain negative value of B_z . This Hanle precession for the s_z is antisymmetric with the magnetic field along the z -direction. Figure 2.7(d) represents the corresponding signal when the initial state of the magnetization is along the $+y$ -direction (blue solid line) or along the $-y$ -direction (red dashed line). It is important to note that this effect occurs over a wider range of B_z in comparison to the spin precession under B_x , since the magnetic field needed to pull the magnetization out of plane is higher.

For large enough values of B_z , the magnetization of the FM is pulled towards the direction of the field, until it aligns. Figure 2.7(e) shows the situation where the magnetization of FM is along the $+z$ -direction and, hence, s_z spins are injected spins. These S-shaped curves are antisymmetric with the field and both signals have the same sign.

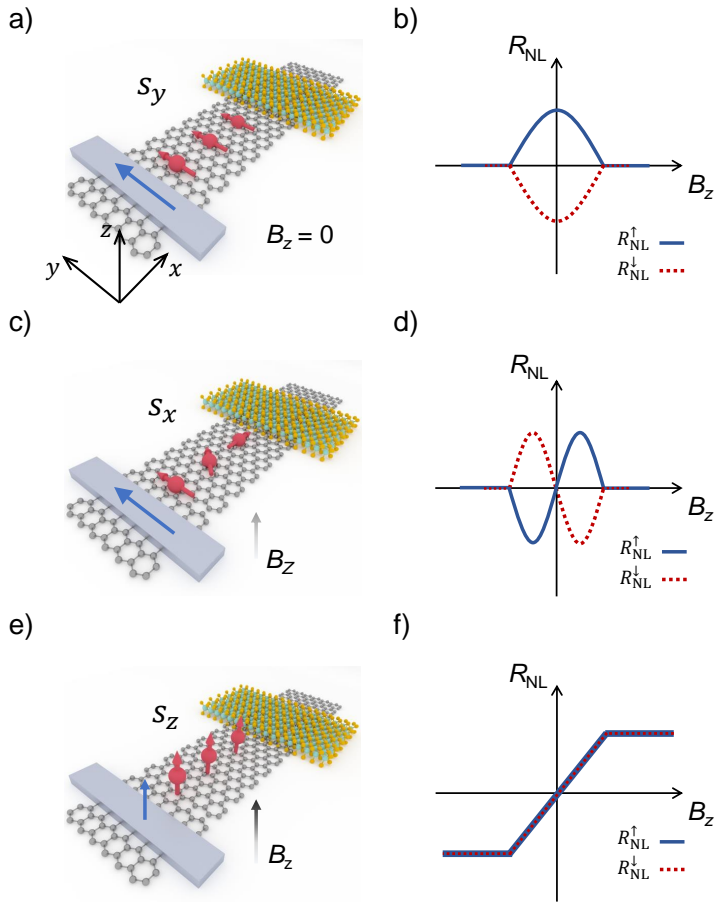


Figure 2.7: Standard SCC measurement contributions by applying an out-of-plane magnetic field. (a) At zero magnetic field, the magnetization of the FM lies along the easy axis ($+y$ -direction) and the injected spins are polarized along the same direction. (b) R_{NL} as a function of B_z generated by the SCC of s_y . The solid blue and the dashed red curves correspond to the two different initial states of the magnetization, $+y$ and $-y$ directions respectively. These are symmetric Hanle curves. (c) For intermediate values of B_z , the injected spins precess in the $y-x$ -plane. (d) R_{NL} as a function of B_z generated by the SCC of s_x , which depends on the initial states of the magnetization ($+y$ -direction corresponds to solid blue curve and $-y$ -direction corresponds to dashed red curve). These are antisymmetric Hanle curves. (e) For large values of B_z , the magnetization of the FM is aligned in the direction of the field. Consequently, the injected spins are parallel to B_z . (f) R_{NL} as a function of s_z generated by the SCC of s_z arises from the magnetization rotation and, thus, spins does not depend on the initial state of the magnetization. The curve shows an S-shape which is antisymmetric with the magnetic field

2.2.3.3 Applying in-plane magnetic field along the easy axis of the FM injector (B_y)

Due to the shape anisotropy, the easy axis of the Co electrode and, consequently, its magnetization at zero field, lies along the y -axis. By applying enough magnetic field along the $\pm y$ -direction (B_y), the magnetization of the electrode and, thus, the spin polarization of the injected current can be switched (the coercive field of Co electrodes is typically < 0.05 T). However, B_y does not induce spin precession during the spin transport along the graphene channel because \mathbf{s} and B_y are parallel to each other and, as a result, the spin polarization is restricted to be $\pm s_y$ [Fig. 2.8(a)]. The corresponding contribution to the SCC signal when sweeping B_y only comes from s_y spins and it is shaped as a squared hysteretic loop [Fig. 2.8(b)].

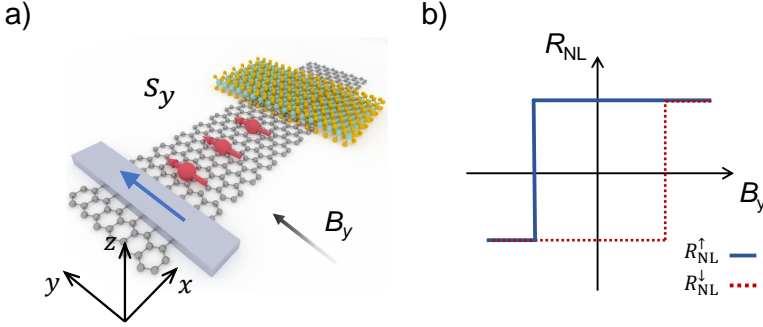


Figure 2.8: **Standard SCC measurement contributions by applying an in-plane magnetic field along the easy axis of the FM injector.** (a) At zero magnetic field, the magnetization of the FM lies along the easy axis ($+y$ -direction) and the injected spins are polarized along the same direction. (b) R_{NL} as a function of B_y generated by the SCC of s_y . The solid blue and dashed red curves correspond to the two different initial states of the magnetization, $+y$ and $-y$ directions respectively.

Table 2.1 summarizes the shape of the different SCC components to the R_{NL} curves, coming from the different spin polarizations, as a function of B_x , B_y , and B_z .

Table 2.1: **Shape of the R_{NL} curve generated by the SCC of each spin polarization for different directions of the magnetic field.**

	R_{NL} from s_x	R_{NL} from s_y	R_{NL} from s_z
B_x	S-shape	Symmetric Hanle	Antisymmetric Hanle
B_y	–	Hysteresis loop	–
B_z	Antisymmetric Hanle	Symmetric Hanle	S-shape

2.3 1D spin diffusion model for SHE in a low-symmetry material

When a SOC material is placed on top of graphene, if the spin resistance of the material is lower than the one of graphene, the spin current will be absorbed and then converted into a measurable charge current in the SOC material (see Section 1.4.1.3). To quantify the efficiency of the SCC, we solved the 1D spin diffusion model considering the geometry of the device. When the SCC process is studied using a low-symmetry material, different spin polarizations can generate a charge current. Our model accounts for the different spin polarizations generating charge current.

When an external out-of-plane magnetic field (B_z) is applied to a graphene-based LSV with a SOC material (see Fig. 2.5), the spin accumulation is given by the 1D-Bloch equation (Eq. 2.1). In this situation, the spin precession will occur in the $x-y$ -plane and, hence, the spin accumulation will only have contributions from the spins polarized along x (μ_{s_x}) and y (μ_{s_y}) [see Fig. 2.7(a,c)]. The spin accumulation for each component can be written as:

$$\begin{aligned} \mu_{s_x} = & -iA \exp\left(\frac{x}{\lambda_s^{gr}} \sqrt{1 + i\omega\tau_s^{gr}}\right) + iB \exp\left(\frac{x}{\lambda_s^{gr}} \sqrt{1 - i\omega\tau_s^{gr}}\right) \\ & - iC \exp\left(-\frac{x}{\lambda_s^{gr}} \sqrt{1 + i\omega\tau_s^{gr}}\right) + iD \exp\left(-\frac{x}{\lambda_s^{gr}} \sqrt{1 - i\omega\tau_s^{gr}}\right), \end{aligned} \quad (2.8)$$

$$\begin{aligned} \mu_{s_y} = & A \exp\left(\frac{x}{\lambda_s^{gr}} \sqrt{1 + i\omega\tau_s^{gr}}\right) + B \exp\left(\frac{x}{\lambda_s^{gr}} \sqrt{1 - i\omega\tau_s^{gr}}\right) \\ & + C \exp\left(-\frac{x}{\lambda_s^{gr}} \sqrt{1 + i\omega\tau_s^{gr}}\right) + D \exp\left(-\frac{x}{\lambda_s^{gr}} \sqrt{1 - i\omega\tau_s^{gr}}\right), \end{aligned} \quad (2.9)$$

where A , B , C , and D are coefficients determined by the boundary conditions and depend on the device geometry.

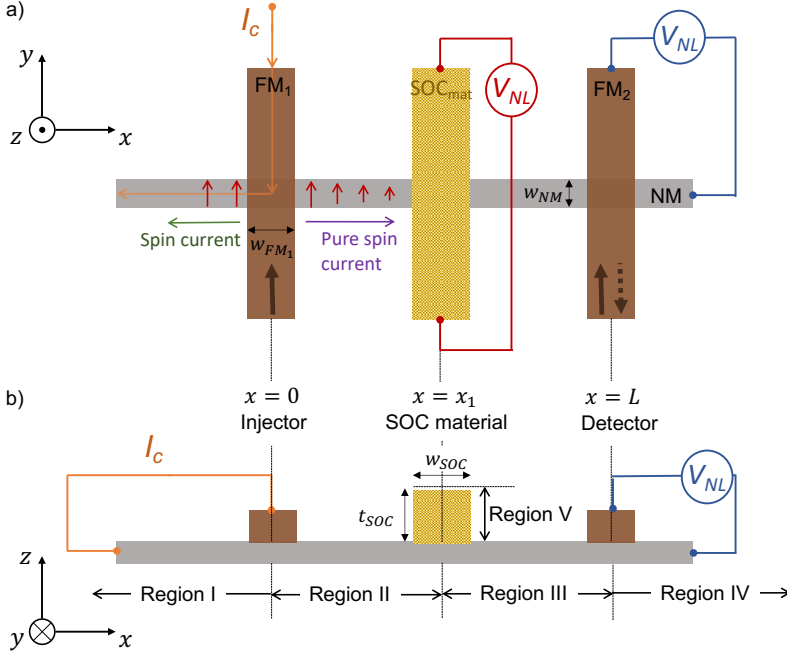


Figure 2.9: **Sketch of a graphene-based LSV with a SOC material between the FM contacts.** (a) Top view of a LSV with a SOC material (yellow) on top of a graphene channel (grey) and two FM contacts (brown) at both sides of the SOC material. I_c is injected from FM₁ to the graphene channel (orange arrows). This current generates a spin current (green arrow) and a pure spin current (purple arrow) in each side of the FM, respectively. The amplitude of the spin accumulation is given by the length of the red arrows in the graphene channel. Two different measurement configurations can be performed depending on the place where the voltage is measured: (i) to characterize the spin absorption, the voltage is probed in the FM₂ with respect to the graphene (blue configuration); (ii) to study the SCC process, the voltage is probed along the SOC material (red configuration). The dark brown arrows in the FM contacts represent the magnetization orientation that can be flipped by applying a magnetic field. (b) Side view of panel a. The injector is placed at $x=0$, the SOC material at $x=x_1$ and the detector at $x=L$. All the regions used in the calculations are depicted as well as the geometrical parameters of the FMs and SOC material.

When the spin current flowing in the graphene channel finds a material with strong SOC (see Fig. 2.9), it can be absorbed and converted into charge current via ISHE. This process of spin absorption depends on the interface resistance between the graphene channel and the SOC material. In the case

the spin current is partially absorbed, there will be a spin accumulation inside the material along the vertical direction (z -direction):

$$\mu_{s_x} = E \exp\left(\frac{z}{\lambda_s^{SOC}}\right) + F \exp\left(-\frac{z}{\lambda_s^{SOC}}\right), \quad (2.10)$$

$$\mu_{s_y} = G \exp\left(\frac{z}{\lambda_s^{SOC}}\right) + H \exp\left(-\frac{z}{\lambda_s^{SOC}}\right), \quad (2.11)$$

where λ_s^{SOC} corresponds to the spin diffusion length of the SOC material, and E , F , G and H are determined by the precession in the graphene channel and the confinement induced by the thickness of the SOC material, t_{SOC} .

In the layout of the device, five different regions can be distinguished (see Fig. 2.9):

- **Region I:** It is a semi-infinite region going from $x \rightarrow -\infty$ up to FM_1 , which is placed at $x = 0$ with a contact resistance R_{c_1} . This FM contact acts as spin injector.
- **Region II:** This region goes from $x = 0$ to $x = x_1$, where the SOC material is placed. In this region, it is assumed that $\lambda_s^{gr} \gg w_{SOC}$, being w_{SOC} the width of the SOC material. The interface resistance between the SOC material and the graphene channel is R_{int} .
- **Region III:** This region extends from the SOC material to FM_2 acting as a spin detector, positioned at $x = L$. The spin transport properties of this region are the same as in region II.
- **Region IV:** Semi-infinite region from the spin detector to $x \rightarrow \infty$. FM_2 contact resistance is denoted by R_{c_2} . The spin transport properties of this region (τ_s^{gr} , D_s^{gr} and R_s^{gr}) are the same as in Region I.
- **Region V:** This region is along the z -direction. It extends from the graphene channel to the thickness of the SOC material, t_{SOC} . The spin transport in this region is perpendicular to the graphene plane and is considered to have an irrelevant spin precession since, in general, SOC materials have short spin diffusion length and spin lifetime. It is characterized by the resistivity of the SOC material, ρ_{SOC} , and its thickness t_{SOC} .

The boundary conditions in the system used to determine the spin accumulation are the following:

- The spin accumulation vanishes in the infinity. $\mu_s \rightarrow 0$ when $x \rightarrow \pm\infty$.
- The spin accumulation is continuous everywhere in the graphene channel but at the interface graphene/SOC material, where the discontinuity is given by $\Delta\mu_s = eR_{int}I_s^{int}$. I_s^{int} is the spin current crossing the interface between graphene and the SOC material.
- The spin relaxation at the interface between graphene and SOC material is not considered. The spin current at the interface is the same as the spin current at the bulk of the SOC material at $z = 0$, $I_s^{int} = I_s^{SOC}$.
- The spin currents in graphene and in the SOC material are, respectively, defined by:

$$I_{s_{x(y)}}^{gr} = -\frac{w_{gr}}{eR_s^{gr}} \frac{\partial\mu_{s_{x(y)}}}{\partial x}, \quad (2.12)$$

and

$$I_{s_{x(y)}}^{SOC} = -\frac{w_{gr}w_{SOC}}{e\rho_{SOC}} \frac{\partial\mu_{s_{x(y)}}}{\partial z}. \quad (2.13)$$

- The discontinuities of I_s^{gr} are given by the following equations for $x = 0$ under the injector, for $x = x_1$ under the SOC material, and for $x = L$ under the detector:

$$x = 0 \quad \Delta I_{s_x}^{gr} = -\frac{\mu_{s_x}(x=0)}{eR_{c_1}}, \quad (2.14)$$

$$x = 0 \quad \Delta I_{s_y}^{gr} = P_{inj}I_c - \frac{\mu_{s_y}(x=0)}{eR_{c_1}}, \quad (2.15)$$

$$x = x_1 \quad \Delta I_{s_{x(y)}}^{gr} = -\frac{\mu_{s_{x(y)}}^{gr}(x=x_1) - \mu_{s_{x(y)}}^{SOC}(z=0)}{eR_{int}}, \quad (2.16)$$

and

$$x = L \quad \Delta I_{s_{x(y)}}^{gr} = -\frac{\mu_{s_{x(y)}}(x=L)}{eR_{c_2}}. \quad (2.17)$$

Two different experiments can be performed using this kind of devices: (i) the spin absorption experiment, where the voltage is probed between FM₂ and the graphene channel (blue configuration in Fig. 2.9), and (ii) the SCC study, where the voltage is probed along the SOC material (red configuration in Fig. 2.9).

First, the spin precession signal should be measured in a pristine graphene part of the device, where the SOC material is not playing any role. From the fitting of the spin precession, the spin transport parameters of pristine graphene are extracted. Then, the spin signal is measured in the absorption configuration. Part of the injected spins from FM₁ will be absorbed into the SOC material, and part will arrive to FM₂, thus, the spin signal will be reduced when comparing it with the pristine graphene signal. The spin signal at the detector ($x = L$) is determined using:

$$R_s(x = L) = \frac{P_{det}\mu_{s_y}(x = L)}{eI}, \quad (2.18)$$

where \pm stands for the parallel and antiparallel states between the magnetization of the injector and detector.

When the magnetic field is strong enough, the magnetization of the FM electrodes starts to be pulled towards the direction of the magnetic field. This pulling of the FM has to be taken into account in the non-local resistance measured at the detector (blue measurement configuration in Fig. 2.9) so that Eq. 1.16 can be rewritten as:

$$R_{NL}^{P(AP)} = +(-)R_s(x = L) \cos^2 \Theta + R_{||} \sin^2 \Theta, \quad (2.19)$$

where the $+(-)$ stands for the parallel (antiparallel) relative magnetization state of the injector and detector, Θ is the angle between the orientation of the magnetization and its easy axis (y -axis), and $R_{||}$ is the spin signal induced by the non-precessing spins. Considering Eq. 1.10 and Eq. 2.19, ΔR_{NL} takes the following form:

$$\Delta R_{NL} = \frac{R_{NL}^P - R_{NL}^{AP}}{2} = R_s(x = L) \cos^2 \Theta. \quad (2.20)$$

Now, if this signal is measured across the SOC material with the spin absorption configuration (red measurement configuration in Fig. 2.9), then it is possible to extract λ_s^{SOC} provided that the spin resistance of the SOC material is larger than the resistance of the interface between SOC material and graphene ($R_s^{SOC} > R_{int}$).

Once the spin-dependent transport parameters are characterized in the graphene channel, it is possible to quantify the efficiency of the SCC process. If the spin current is absorbed from the graphene to the SOC material, it will be converted into charge current, due to the ISHE, creating a non-local resistance measured along the SOC material flake. This non-local resistance will be given by the following formula for each of the possible spin polarizations (μ_{s_x} and μ_{s_y}):

$$R_{SH}^{x(y)} = \theta_{zy}^{x(y)} \rho_{SOC} \chi_{shunt} \bar{I}_{s_{x(y)}} / w_{SOC}. \quad (2.21)$$

Due to geometrical constrains in the device, the measured charge current can only be along the y -direction and the spin current has to flow along the z -direction, since it is absorbed from graphene to the SOC material. χ_{shunt} is the shunting factor due to the fact that graphene acts as a parallel channel for the converted charge current and $\bar{I}_{s_{x,y}}$ is the average spin current in the SOC material, $\bar{I}_{s_{x(y)}} = \frac{1}{t_{SOC}} \int_0^{t_{SOC}} I_{s_{x(y)}}(z) dz$.

As shown in Section 2.2.3.2, the contribution of each spin polarization to the SCC have a different dependence with the magnetic field and, moreover, some of them also depend on the initial state of the FM. In the case of an out-of-plane magnetic field, the contributions to the signal of s_x and s_y depend both on the initial state of the magnetization, $R_{NL}^{\uparrow,\downarrow}$ as:

$$R_{NL}^{\uparrow,\downarrow} = +(-) R_{SH}^{x(y)} \cos \Theta + R_{SH}^{\parallel} \sin \Theta, \quad (2.22)$$

where \pm corresponds to the magnetization initial state of the FM injector, $+(-)y$ -direction, respectively. R_{SH}^{\parallel} is the SCC of the spins pointing along B_z . In order to remove any signal that does not depend on the initial state of the magnetization, the SCC signal is defined as:

$$R_{SCC} = \frac{R_{NL}^{\uparrow} - R_{NL}^{\downarrow}}{2} = R_{SH}^{x(y)} \cos \Theta. \quad (2.23)$$

In particular, the contribution of s_y to the signal is a symmetric Hanle curve [see Fig. 2.7(b)], while the contribution of s_x is an antisymmetric Hanle [see Fig. 2.7(d)]. In order to separate each component, R_{SCC} has to be symmetrized and anti symmetrized and the resulting data is fit to:

$$R_{SCC}^{anti} = R_{SH}^x \cos \Theta, \quad (2.24)$$

and

$$R_{SCC}^{symm} = R_{SH}^y \cos \Theta. \quad (2.25)$$

Chapter 3

Experimental techniques

Van der Waals materials are characterized by the weak van der Waals forces that bond the individual atomic planes. Thanks to the fragile nature of the forces, these materials can be easily exfoliated, and combined with other van der Waals materials, such as graphene, where the van der Waals forces keep the materials bound.

The mechanical exfoliation of van der Waals materials by means of an adhesive tape, is known as Scotch-tape technique [128, 129], and it has been widely used to fabricate spintronic devices [143, 148, 151, 211, 222–226, 230, 234, 275, 277, 296, 298–301]. The assembling of van der Waals heterostructures is assisted by dry viscoelastic stamping [302]. Once a heterostructure is formed, it can be later patterned via electron-beam lithography, followed by metal deposition and lift-off processes, in order to electrically contact it.

In this Chapter, it is explained the step-by-step fabrication process and the final characterization of the van der Waals graphene-based LSVs, used to study SCC. Although the fabrication procedure is the same, each heterostructure requires a tailored design for the patterning of the contacts.

3.1 Sample fabrication

Highly-doped Si with 300 nm of thermally grown SiO₂ is used as a substrate for the graphene-based LSV. The size of the substrate is 5 mm × 5 mm, and it is previously patterned with an array of numbered crosses 500 μm apart. These structures act as reference coordinates, essential for the later location of the exfoliated flake of interest on the substrate. The SiO₂ layer is crucial to: (i) enhance the optical contrast of graphene flakes [303], and (ii) to apply electrostatic gating to the graphene flake using the Si as bottom contact.

The first step, prior to exfoliation, is the cleaning of the substrates. Initially, the substrates are immersed in acetone in an ultrasound bath for 5 minutes and, subsequently, by another 5 minutes in isopropanol (IPA) in the ultrasound bath. Later, they are dried by blowing N₂.

3.1.1 Graphene exfoliation via Scotch-tape technique

Once the substrates are cleaned, the graphene flake is exfoliated first. Prior to the transfer, the substrates are heated at 120 °C in a hot plate for 5 minutes, to remove any water from the surface. Graphene is hydrophobic [304,305] and, hence, removing any water from the surface of the substrates is crucial to transfer a large amount of material. A piece of graphite (supplied by *NGS Naturgraphit GmbH*) acts as a matrix on where the blue tape is placed. The blue tape (*Nitto SPV 224P* [306]) is peeled-off from the graphitic crystal until the amount of material on the tape is enough to be transferred onto the Si/SiO₂ substrates. After the heating of the substrate, the blue tape can be placed on the substrate. On the one hand, if the substrate is still too hot, the glue from the blue tape is melted and consequently transferred to it, emerging residues on the substrate. On the other hand, a lot of graphene flakes are transferred. For the samples fabricated in this Thesis, the substrate was one minute out from the hot plate before placing the blue tape on top, so that the amount of transferred graphene was still large but the glue residues are reduced. Once the blue tape is on the substrate, gentle pressure is applied for a few seconds. Afterwards, the blue tape is slowly peeled off from the substrate.

Although this process is known as the Scotch-tape technique [128, 129], the tape we utilize is blue Nitto tape instead. While Scotch tape is useful to exfoliate 2D materials with stronger inter-layer forces, in the case of van der

Waals materials, we prefer to use blue Nitto tape since it leaves fewer residues, although its adhesion force is lower.

Figure 3.1 exemplifies the graphene flakes transferred on a substrate using the Scotch-tape technique. A marker used as a reference to later locate the flakes is also visible. As highlighted by the dashed white rectangle, certain areas of the substrate present a large density of graphene flakes, presenting differences in the contrast among them. The more visible the graphene flake is, the thicker it is. In the case of the graphene-based LSVs, we look for graphene flakes with a needle-like shape, like the one highlighted by the dashed white rectangle in Fig. 3.1(b). The low contrast of this particular flake hints it is single-layer graphene. In order to align the MoTe_2 flake on top of graphene, it is important to have proper contrast, therefore, the use of single-layer graphene flakes difficulties further fabrication steps. For the sake of simplicity, in the following, the few-layer graphene flakes are going to be referred to as graphene, although it might not correspond to a single-layer graphene flake.

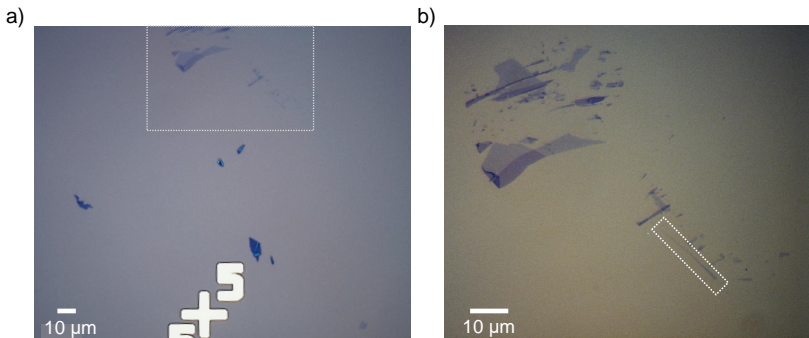


Figure 3.1: Graphene flakes on Si/SiO_2 substrates transferred using the Scotch-tape technique. (a) Optical image of graphene exfoliation on Si/SiO_2 substrate. The numbered marker used as a reference to later locate the flakes is also visible. The dashed white rectangle indicates an area with a larger density of graphene flakes. (b) Zoom of the area highlighted by the dashed white rectangle in panel a. A typical needle-shape graphene flake employed for the fabrication of the LSVs is highlighted by the dashed white rectangle.

In contrast to CVD-graphene or the chemical exfoliation process of graphene, a crucial advantage of the Scotch-tape micro-mechanical cleaving technique is that the top surface of the graphene flake has not been exposed to any chemical or material. This is crucial for the high-quality interface van der Waals heterostructures. Indeed, we observed that, if the graphene flake was chemically cleaned before the stamping of the next 2D material, the interface resistance between both materials was larger than if the stamping was performed without

the chemical cleaning, meaning that some organic residues from the cleaning process remained on top of graphene.

3.1.2 MoTe₂ exfoliation in inert atmosphere

MoTe₂ has been reported to be sensitive to ambient conditions as effects of the oxidation when exposed to air [307–309]. This oxidation comes from the Te atoms, which are more prone to oxidation [310]. In order to prevent surface oxidation, and to keep a non-oxidized interface between graphene and MoTe₂, the exfoliation of the latter is performed in a glovebox with Ar atmosphere.

Once the graphene flake is identified on a substrate [Fig. 3.2(a)], the MoTe₂ flake is exfoliated. Initially, a small piece of a transparent polymer (polydimethylsiloxane, PDMS) is placed at the edge of a microscope crystal slide. The PDMS acts as a substrate for the MoTe₂ exfoliation and, since it is transparent, allows us to lay the MoTe₂ on top of the pertinent graphene flake.

Following the same Scotch-tape technique, initially the blue tape is placed on a MoTe₂ crystal piece. Once there is enough material on the blue tape, it is settled on top of the PDMS and, by applying gentle pressure, the MoTe₂ is transferred. Using an optical microscope, an elongated needle-like MoTe₂ flake is searched. Figure 3.2(b) shows an exfoliation of MoTe₂ on PDMS, and the desired flake is marked by the dashed rectangle.

Once both flakes are identified, the next step is the stamping of MoTe₂ on graphene.

3.1.3 Stamping process

The stamping process is achieved with the help of an optical microscope inside the glovebox. The Si/SiO₂ substrate is placed on a stage, which can be moved in the plane (x and y directions and rotation), and it is controlled from outside of the glovebox. The microscope crystal slide, with the PDMS containing the desired MoTe₂ flake, is held by a mechanical arm, which can be moved in all three directions (x , y , and z) remotely, and it is placed between the microscope objective and the stage, where the substrate is as shown in Fig. 3.3. Initially, by changing the focus of the microscope from one flake to the other, while keeping a safe distance between the MoTe₂ and graphene flakes, the substrate is rotated in such a way the MoTe₂ flake is perfectly perpendicu-

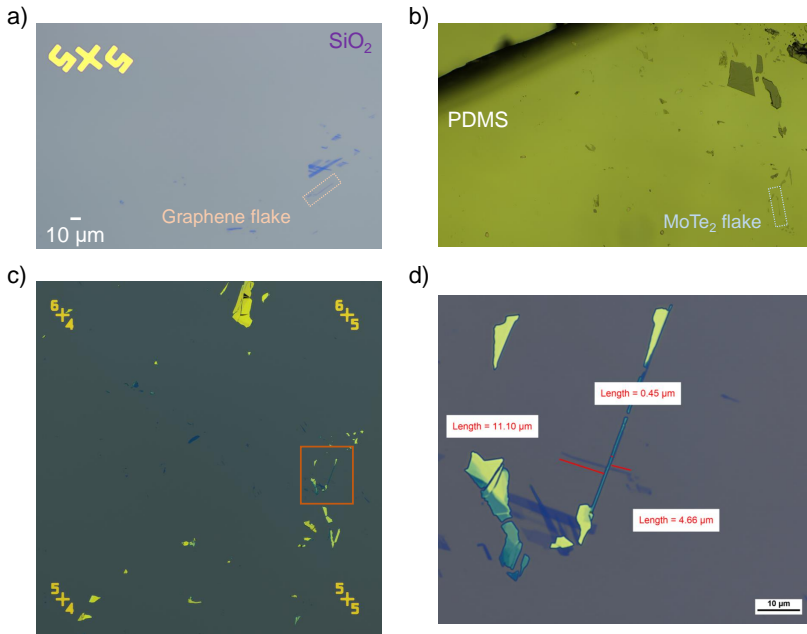


Figure 3.2: Fabrication steps of a graphene/MoTe₂ van der Waals heterostructure. (a) The graphene flake is identified in a Si/SiO₂ substrate. The position on the flak is known with respect to the markers that are previously patterned on it. (b) MoTe₂ is mechanically cleaved on PDMS, a transparent and flexible polymer. A needle-shaped MoTe₂ flake is sought and highlighted by the grey dashed rectangle. (c) Final van der Waals heterostructure highlighted with the orange rectangle, with respect to the four markers on the Si/SiO₂ substrate. The distance between markers is 500 μm. (d) Zoom of the orange square in previous panel. The MoTe₂ needle-shaped flake is placed on top of the chosen graphene flake. The left side of the graphene is 11.1 μm long, while the right side is 4.7 μm. The width of the MoTe₂ flake is ~ 450 nm.

larly aligned at the middle of the graphene flake. This process is consecutively performed while the distance between flakes is reduced, by moving downwards the mechanical arm, until the PDMS gets in contact with the substrate. Once it is in contact, the MoTe₂ flake should be stamped as slow as possible, while any possible misalignment between the flakes is corrected. After the MoTe₂ flake is stamped on top of graphene, the PDMS is peeled-off fast by bringing up the mechanical arm, making sure the MoTe₂ remains on the graphene. At the end of this process, the van der Waals heterostructure is successfully formed, as shown in Fig. 3.2(c,d), and ready to be patterned.

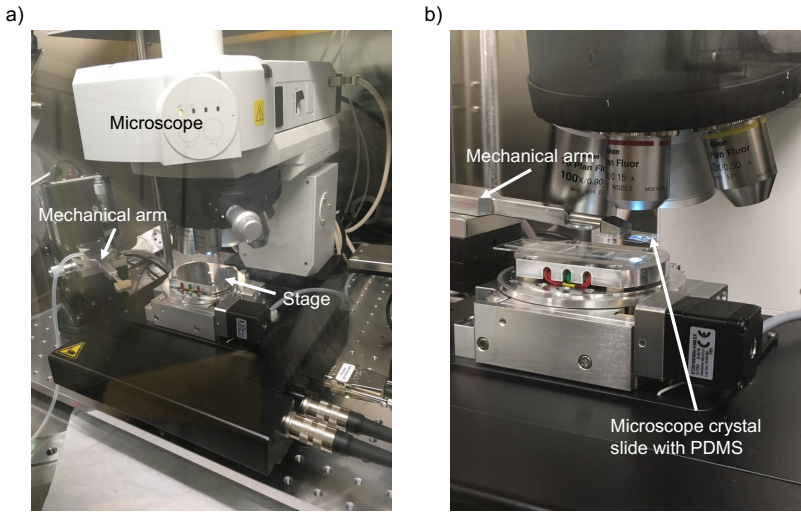


Figure 3.3: **Stamping system inside the glovebox.** (a) Optical microscope inside the glovebox. The different important parts are tagged. (b) The mechanical arm holding the microscope crystal slide with the PDMS is placed between the microscope objective and the stage in order to perform the stamping.

3.1.4 Contact patterning and metallization

For contact patterning, the electron-beam lithography (eBL) technique, with a tailored design for each heterostructure, is adopted. The patterning and the subsequent metallization, have been carried out in a clean environment in the *CIC nanoGUNE BRTA* cleanroom facility. The amount and size of the particles within the cleanroom are strictly controlled in the different cleanroom bays, where the lithography bay presents the lowest amount of particles with size $\geq 0.1 \mu\text{m}$ per cubic feet, 3500. To start with, the standard eBL process followed during the fabrication of the samples is described. The successive metallization via e-beam or thermal evaporation, and the lift-off processes are also detailed in the following sections.

3.1.4.1 Standard eBL process

Before the lithography process, the sample is covered with a polymer sensitive to the exposure of the electron beam, known as e-beam resist. This e-beam resist is diluted in a solvent, which eases the spin coating and the subsequent developing.

In this Thesis, we use polymethyl methacrylate with anisole solvent (PMMA) resist, which is a conventional e-beam resist. In particular, we use double-layer PMMA with two different molecular weights and anisole concentrations, which vary the sensitivity to the e-beam exposure. The first PMMA layer is 495K PMMA A4, and the second layer is 950K PMMA A2, where the first number (495K or 950K) corresponds to the molecular weight and the second one (A4 or A2) to the concentration of polymer in anisole, in %. The first resist layer is thicker and creates an undercut to ease the lift-off process.

Each resist layer is spin-coated at 4000 rpm with an acceleration of 1000 rpm during 60 seconds, followed by hard baking at 180 °C during 90 seconds. Afterwards, the sample is ready to be loaded into the eBL system. In this Thesis, two equivalent eBL systems have been used: *Raith150 TWO* and *Raith e-Line* [311]. Both systems reach the same resolution, and have a load-lock where the sample is loaded on a metallic stage, fixed by a clamp. Subsequently, the sample is transferred into the main chamber, where the base pressure is $\sim 10^{-5}$ Torr. The fundamental parameters in the eBL system are: the e-beam voltage; the aperture, which together with the voltage determines the current of the e-beam; the size of the writing field, which is the area of the sample that can be written without moving the position of the beam, just by deflection; the working distance; and the dose. For all the lithography steps involved in the Thesis, the voltage is set to 10 kV and the working distance to 10 mm. The aperture and the corresponding working field size are varied. Figure 3.4(a) shows a representative design of the contacts in a graphene/MoTe₂ heterostructure. While the left panel displays the design in the whole substrate, the right panel is a zoom in the region close to the heterostructure. For small features, where the accuracy is crucial, the aperture is set to 10 μm and the corresponding write field size is 100 μm . An area of 100 $\mu\text{m} \times 100 \mu\text{m}$, centered in the heterostructure, is patterned with the aforementioned characteristics of the e-beam [see Fig. 3.4(a)]. For contacts away from this area, the aperture is increased to 120 μm and the write field size is set to 1000 μm . The 120 μm aperture loses accuracy but the exposure time is considerably reduced. That is the reason why the aperture is enlarged for the patterning of the electrodes far from the heterostructure, and the different working fields have to be stitched, taking into account that some misalignment can happen when the beam moves to write the whole contact structure.

In the case of the graphene/MoTe₂ heterostructure, four small crosses close to the heterostructure separated 80 μm apart, are firstly pattern using the

10 μm aperture, as shown in Fig. 3.4(b). These crosses are used as alignment marks, in order to be as accurate as possible when patterning the electrodes on the flakes.

After the exposure of the resist to the e-beam, the bonds of the e-beam resist are modified in such a way that, when the sample is immersed in the corresponding chemical developer, the resist is removed. If the e-beam resist is positive (negative) the part of the resist which is removed is the part which has (not) been exposed to the beam. Both the 495K PMMA A4 and 950K PMMA A2 resists are positive, therefore, when the sample is immersed in methyl isobutyl ketone diluted in IPA (MIBK/IPA 1:3) for 60 seconds, and later into IPA to stop the developing process for other 60 seconds, the resist is removed in those parts which have been exposed to the beam, corresponding to the contacts, as can be seen in Fig. 3.4(c).

3.1.4.2 Metal deposition

After the developing of the patterned design, different materials can be deposited on the sample. For the LSVs, firstly the non-magnetic electrodes are patterned, followed by the corresponding metallization with Ti/Au. The evaporation of both materials is performed *in situ* in a high vacuum evaporation system, with 10^{-7} mbar base pressure (*Kurt J. Lesker*). Whereas the evaporation of the Ti layer is using the e-beam technique, the Au evaporation is thermal. In the following, the basis of each technique is explained.

e-beam evaporation

In the e-beam evaporation, a current is applied to a W filament. This filament thermionically emits electrons which are later focused by magnetic fields into a crucible with the material we want to evaporate, in this case Ti. The temperature of the material starts to increase until the atoms evaporate. The evaporated atoms reach the sample forming a continuous layer. For the non-magnetic electrodes, 5 nm of Ti are evaporated at a rate of 1 $\text{\AA}/\text{s}$.

Thermal evaporation

This evaporation relies on the Joule heating. When a charge current is applied on a thermal boat, it heats up and so the temperature of the material inside the boat increases. When the temperature of the material is high enough, it starts to evaporate. Small wires of Au are placed on the boat which is then heated. A layer of 100 nm of Au is evaporated at a rate of 0.8 $\text{\AA}/\text{s}$.

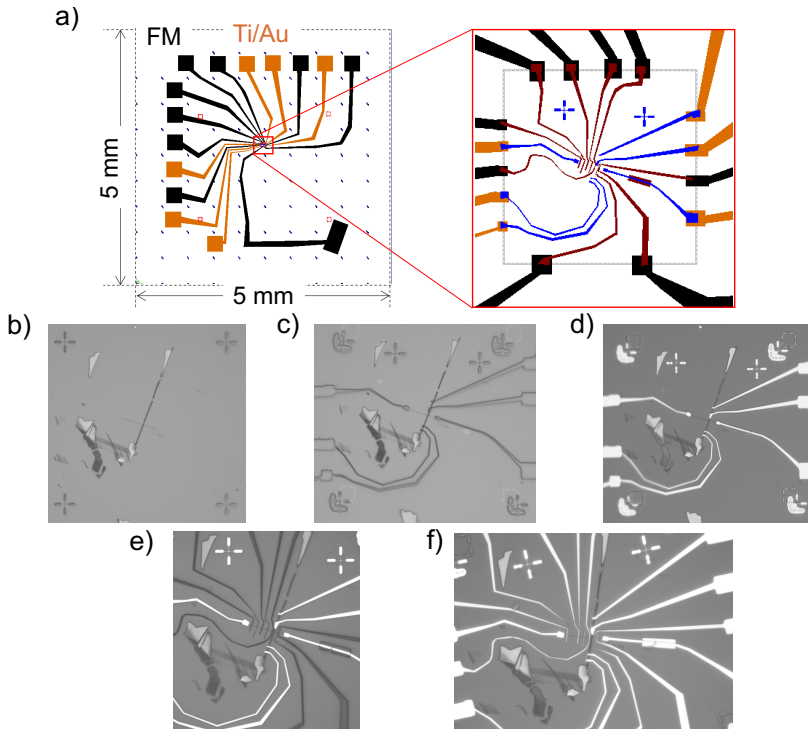


Figure 3.4: eBL design and black and white optical microscope pictures of the fabrication steps in a graphene/MoTe₂ heterostructure. (a) Contacts design in a 5 mm × 5 mm, where the Ti/Au electrodes are in orange and the FM electrodes in black. The electrodes end in a big square, used to electrically connect the sample with the electrical equipment. The highlighted red square corresponds to the area close to the heterostructure. In the right panel, the grey square corresponds to the area of 100 μm × 100 μm patterned with the 10 μm aperture. The outer electrodes are patterned with the 120 μm aperture. The blue contacts corresponds to the Au electrodes, while the brown ones to FM. (b) Picture of the heterostructure after the developing of the alignment marks patterned close to the heterostructure. (c) Picture after the development of the non-magnetic electrodes. (d) Heterostructure after the lift-off of the non-magnetic electrodes, where only the Ti/Au electrodes are present. (e) Development of the second eBL step to pattern the FM electrodes. (f) Picture of the final device after the three eBL steps and two metallizations.

To avoid Ti oxidation, the subsequent Au evaporation of the electrodes should be performed *in situ*. Interestingly, other materials can be used as a seed layer of Au, as Cr or Pd. The work function of these materials should be as close as possible to the work function of the contacted material. In our case, the Ti is the one that shows lower electrical noise when contacting MoTe₂.

3.1.4.3 Lift-off

When the metallic layers are evaporated in the whole sample, the next step is the lift-off process. The substrate is immersed in a solvent to remove any resist. By removing the resist, the material evaporated on top is also removed and, therefore, the metallic layer only remains in those parts where there was no resist. For PMMA, the remover used is acetone and the sample is left in acetone for few hours. Once the PMMA resist is dissolved, the sample is rinsed in IPA to remove the organic residues left by the acetone. After the lift-off process, the sample looks like the example in Fig. 3.4(d).

In the samples we use to study the SCC process, we also need FM contacts. In order to pattern the FM electrodes, a subsequent spin-coating and eBL step followed by the metal evaporation are needed. The eBL process requires the same conditions as the one of the non-magnetic electrodes, where the crosses patterned close to the heterostructure are crucial to align the FM electrodes to the previous metallic contacts. Fig. 3.4(e) displays a picture after the developing of the FM patterned contacts after the developing. However, the evaporation of the FM electrodes is carried out in a particular fashion.

As we have explained in Chapter 1 and 2, a TB is crucial to have proper spin injection from the FM to the NM channel. In our case, we use TiO_x as the TB. Firstly, 0.3 nm of Ti are deposited via e-beam evaporation at a rate of 0.2 Å/s. This Ti layer is exposed to air for 10 minutes to induce the oxidation of the Ti, creating a TiO_x layer. This non-continuous layer presents enough resistance to properly inject spins. Next, 35 nm of Co are e-beam evaporated at a rate of 1 Å/s. To prevent the Co oxidation, 5 nm of Au are deposited to cap the FM electrodes. After the lift-off process, an example of the final heterostructure is shown in Fig. 3.4(f).

3.1.4.4 Fast FM electrodes oxidation

Although, the FM electrodes are capped, the Au only covers the top part of the electrodes, while the lateral side of the FM contacts is exposed to air after the lift-off process. On certain occasions, we observed a fast degradation of the Co electrodes right after taking the sample out from the cleanroom. Figure 3.5(b) shows an optical microscope image of the bubbles created at the FM electrodes as a consequence of the fast degradation.

After analyzing different variables such as base pressure of the evaporation chamber, rate of the evaporation, thickness of the capping Au layer, pre-evaporation of Co, etc., the crucial factor was the humidity in the laboratories. If the humidity of the laboratory is above 80%, the Co undergoes a fast oxidation process. While electrically measuring the Co electrodes also a degradation is observed [see for instance in Fig. 5.15(b)], it is boosted by the humidity in the environment.

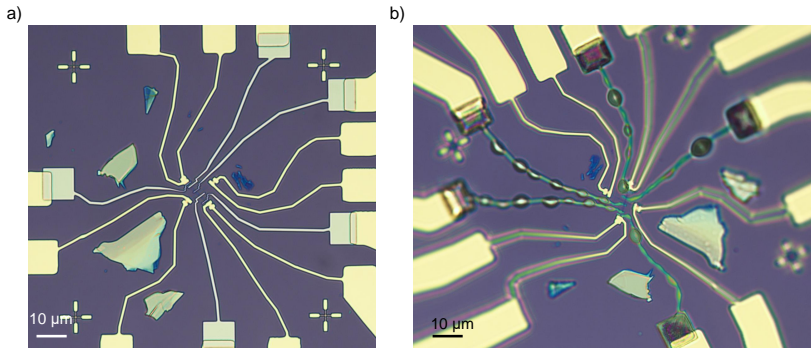


Figure 3.5: Fast degradation of FM electrodes. (a) Optical microscope image of the heterostructure right after the lift-off process of the FM electrodes. (b) Optical image after 30 minutes in a laboratory with high humidity. Only the Co electrodes show degradation.

Chiefly, for the samples fabricated for the study of spin transport in $1T'$ - MoTe_2 (see Section 4.5), the patterning and metallization of non-magnetic electrodes is omitted, and the FM electrodes are directly patterned.

3.2 Sample characterization

Once the sample is fabricated, electrical and material characterization can be performed.

3.2.1 Electrical measurements

The set-up system is a Physical Property Measurement System (PPMS) from *Quantum Design*. In this system, the temperature can vary from 1.8 K to 400 K, and the magnetic field can reach ± 9 T. As the applied currents and the induced voltages in the heterostructures, are very low (in the order of micro or nano Volts or Amperes), an electrical set-up designed for the measurement of

such low values is used.

3

Firstly, the substrate is glued to a chip carrier with 8 electrical contacts. Among all the contacts we patterned on the heterostructure, only 8 can be connected to the chip carrier at the same time. The sample and the pins of the chip carrier are connected using an Al wire-bonder. The chip carrier is then fixed in the rotatory stick, which enters into the cryostat. The design of the chip-carrier together with the rotatory stick allows to change the direction of the magnetic field with respect to the sample surface.

Using a switchboard, the current and voltage probes are selected and connected to the electrical setup. A *6221 Keithley* is used as a current source while a *2182A Keithley* acts as a nanovoltmeter. In order to remove thermoelectric effects that are constant or linear with time, and to reduce noise, a Delta mode is used. This mode, also known as “DC reversal technique”, applies alternated positive and negative pulses of current and the voltage is probed in each pulse (V_M) (see Fig. 3.6). Each cycle of Delta measurement contains three pulses of charge current, on which the voltage is measured. The voltage read by a Delta configuration in the n^{th} cycle is given by [312]:

$$V_{n^{\text{th}} \text{Delta}} = \left(\frac{V_{M_n} - 2V_{M_{n+1}} + V_{M_{n+2}}}{4} \right) \cdot (-1)^{n-1}, \quad (3.1)$$

the $(-1)^{n-1}$ term is used due to the polarity reversal of every other calculated Delta reading. This makes all the calculated Delta readings in the same polarity and can be averaged out later. In our case, the Delta reading is repeated several times, in most of our experiments 128 or 256 times, to further reduce the noise. Additionally, the delay time, that is the time that passes since the charge current pulse starts and the voltage measurement, is usually set to 20 ms.

In general, we calculate the resistance (R) of our signal, which is the ratio between the averaged voltage (V) and the applied charge current (I_c), $R = V/I_c$. Usually this resistance is measured as a function of the temperature [$R(T)$] or the magnetic field [$R(H)$].

Once the sample is electrically characterized, we proceed with the material characterization.

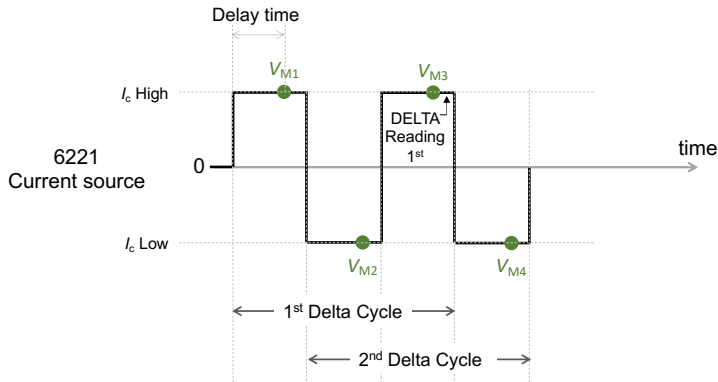


Figure 3.6: **Delta measurement process scheme.** Figure adapted from Ref. [312].

3.3 Material characterization

3.3.1 Scanning transmission electron microscopy

Scanning transmission electron microscopy (STEM) is a microscopy technique that, focuses an electron beam on the sample surface. The incident electrons interact with the atoms in the sample. The secondary electrons, which are emitted from excited atoms due to the incident electron beam, are detected and the information about the topography can be extracted. By analyzing the secondary electrons point by point, the whole image of the sample is formed. In this Thesis, the SEM was performed in the same eBL *Raith* equipment uses for the lithography of the electrodes.

3.3.2 Transmission electron microscopy

Transmission electron microscopy (TEM) is a microscopy technique that forms an image by detecting the electrons that are transmitted through a ultrathin sample, called lamella. TEM microscopy was used to determine the crystallographic direction of the MoTe_2 flakes. The system used was a *Titan 60-300 TEM/STEM* instrument from *FEI*, Netherlands, in STEM mode with an acceleration voltage of 300 kV. The MoTe_2 lamella used to determine the the crystal direction was cut by focused ion beam (FIB). This microscopy technique was carried out by Andrey Chuvilin and Evgenii Modin in *CIC nanoGUNE*.

3.3.3 Atomic force microscopy

Atomic force microscopy (AFM) was used to determine the thickness of the MoTe₂ and graphene flakes. A sharp tip is attached to a cantilever which is bend due to the atomic interaction with the surface of the sample. An incident laser on the cantilever changes the deflection accordingly, and it is detected through a photodetector. The AFM instrument to characterize the thickness of the flakes is from *Agilent Technologies* [313].

3.3.4 Polarized Raman spectroscopy

Raman spectroscopy is used to measure lattice vibration excitation modes in a material. When a monochromatic light, usually a laser, is shined on the surface of a material, it interacts with the molecular vibrations of the material. This interactions shifts the backscattered light and contains information about the vibrational modes. This shift is known as Raman shift, and it is often expressed in the units of cm^{-1} . Polarized Raman spectroscopy relies on the excitation and detection of polarized light. By analyzing the polarized backscattered light, information about the molecular orientation and symmetry of the crystal structure can be extracted.

Two different equipment has been used to characterize the MoTe₂ crystal structure: the *WITec Confocal Raman* to perform polarized Raman spectroscopy at room temperature [314] and *Renishaw inVia Raman Microscope* where a *Linckam* chamber is coupled, and temperature can be controlled down to 80 K [315, 316].

Raman spectroscopy is an established technique to characterize the thickness of the graphene flakes. From fitting the 2D peak ($\sim 2700 \text{ cm}^{-1}$) to a single Lorentzian, if it is monolayer, or to multiple Lorentzian curves, the thickness of the graphene layer is known [317–319]. Unfortunately, the flakes used for the graphene-based LSVs are relatively narrow ($\sim 500 \text{ nm}$) so the Raman signal from the graphene was not large enough to see the graphene Raman peaks and perform the fitting. The fitting of the Raman peaks was achieved in graphene flakes from other works in our laboratory [224, 226, 227] and, therefore, a relation between the optical contrast and the thickness could be established. This, together with the AFM technique, helped us to characterize the thickness of the used graphene flakes.

The TEM and polarized Raman spectroscopy were used to determine the crystallographic directions of the MoTe₂ needle-shaped flakes. Once that was known, these techniques were not repeated in all our devices.

Chapter 4

Molybdenum ditelluride characterization

4.1 Introduction

Layered TMDC materials have attracted a lot of attention in the past years. The discovery of graphene triggered the research of other 2D materials showing exotic physical properties. By reducing the crystal symmetry of 2D materials, new effects become allowed, making low-symmetry 2D materials an appealing materials system to study. A handy example is molybdenum ditelluride (MoTe_2).

In this Thesis, we study $1\text{T}'\text{-MoTe}_2$ grown by *HQ Graphene* company. $1\text{T}'\text{-MoTe}_2$ is characterized by a molybdenum atomic chain along the a -crystal axis, sandwiched by tellurium atoms. Each layer of MoTe_2 is separated by a van der Waals gap [see Fig. 4.1(a)] in the c -axis. The angle between a and b crystal axes is 90° while between a and c is 93.83° . Figure 4.1 sketches the different side views of the $1\text{T}'\text{-MoTe}_2$ crystal structure. The a - c plane view is represented in Fig. 4.1(a), where the Mo chain is along the a -axis and the c -direction corresponds to the vertical stacking direction. Figure 4.1(b) shows the b - c plane, where the distance between layers is the van der Waals gap. This plane coincides with the mirror plane (\mathcal{M}_a), perpendicular to the Mo chain. Figure 4.1(c) represents the top-view of the crystal, corresponding to the b - a crystal plane. The Mo chain is highlighted by the green zigzag line

and the mirror plane is represented by the purple line.

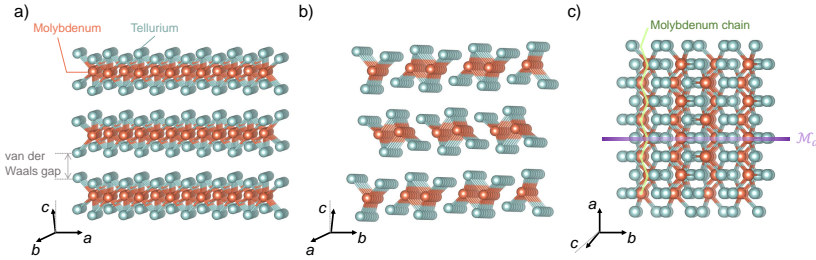


Figure 4.1: $1T'$ -MoTe₂ crystal lattice along the three different crystal planes. The molybdenum atoms (orange) sandwiched between tellurium atoms (blue). The gap between layers of MoTe₂ corresponds to the van der Waals gap. (a) View of the a - c crystal plane. The Mo chain lies along the a -axis while the c -axis corresponds to the stacking direction. (b) View of the b - c crystal plane. The Mo chain is perpendicular to the plane. This plane corresponds to the mirror plane (\mathcal{M}_a). (c) b - a crystal plane. The Mo chain is represented by the green zigzag line and is perpendicular to the mirror plane \mathcal{M}_a [320].

4.2 Crystal axes determination

The crystal anisotropy of MoTe₂ and the presence of only one mirror plane in the crystal structure are directly linked to the the properties of the spin Hall conductivity tensor (see Eq. 2.4). In order to establish a relation between the allowed components in the SHE tensor and the corresponding crystal axis, it is crucial to determine the crystallographic directions of the MoTe₂ flakes.

$1T'$ -MoTe₂ crystal tends to grow forming needles, suggesting a preferential growth direction. Moreover, from exfoliation using the Scotch-tape technique [128, 129], we observe a tendency in the MoTe₂ flakes to be elongated. In order to determine the crystal structure in $1T'$ -MoTe₂ flakes, two different techniques have been used: polarized Raman spectroscopy and Scanning Transmission Electron Microscopy (STEM).

Polarized Raman spectroscopy measurements were performed in two elongated needle-like flakes, similar to the ones used in the SCC studies (Chapter 5, 6 and 7). By combining a confocal microscope with a linearly polarized green laser ($\lambda = 532$ nm), the Raman signal polarized parallel to the direction of the laser is detected through a spectrometer. The incident laser can be polarized parallel to the long axis of the flake or perpendicular to it, while the detected Raman signal is the one polarized parallel to the incident polarization. The

presence or absence of the peak at $\sim 260\text{ cm}^{-1}$ determines the crystal direction [202,321]. Figure 4.2(a,b) shows the intensity of the Raman peaks for two different 1T'-MoTe₂ flakes in two different measurement configurations each. On the one hand, the green line corresponds to the configuration where the incident laser is perpendicular to the long direction of the flake. From the presence of the Raman peak at $\sim 260\text{ cm}^{-1}$, it can be determined that the long direction of the MoTe₂ flake corresponds to the crystal *b*-axis. On the other hand, the blue line corresponds to a polarization parallel to the long direction of the MoTe₂ flake, where the absence of the peak reveals that the direction corresponds to the *a*-axis of the crystal, where the Mo chain lies.

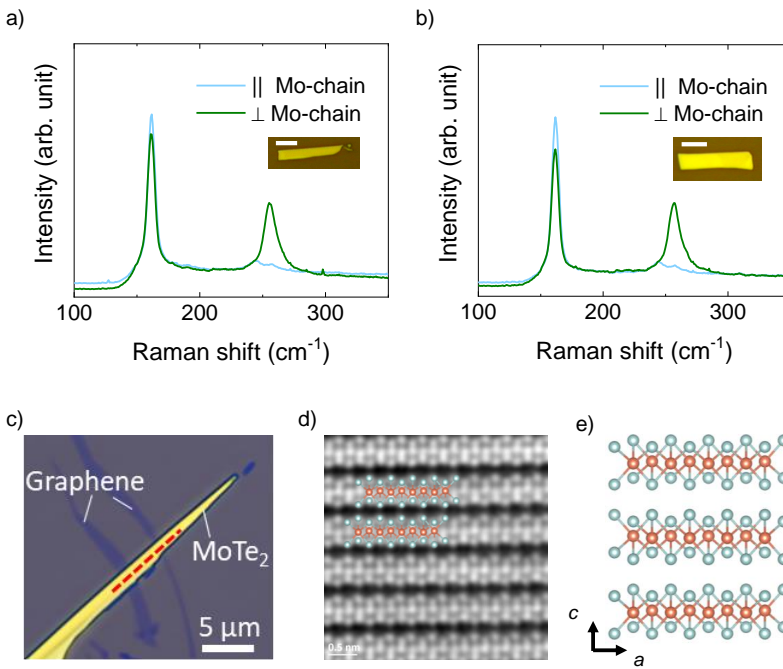


Figure 4.2: **Determination of the crystallographic orientation of MoTe₂ elongated flakes.** (a-b) Polarized Raman spectroscopy of two different elongated flakes. The intensity of the Raman peaks is represented as a function of the Raman shift for two different directions of the polarized incident light. The respective flake in which the measurements were done are shown as an inset. The scale bar corresponds to 5 μm. (c) Optical image of the needle-shaped MoTe₂ flake on top of two graphene flakes. (d) STEM image of the flake along the red dashed line shown in panel c. It shows the cleaving direction of the flake along the crystallographic axis, where the zigzag Mo chain lies (*a*-axis). The crystallographic structure of the 1T'-MoTe₂ is superimposed. (e) Detail of the superimposed crystal structure in panel d.

Unfortunately, the spot size of the laser used to perform Raman spectroscopy is $\sim 2\text{--}4\ \mu\text{m}$, larger than the width of the prototypical MoTe_2 flakes used in the graphene-based LSVs ($\sim 400\text{--}500\ \text{nm}$) and, hence, the crystallographic axes could not be determined in the same flakes where the SCC was studied. In order to characterize the crystal axes in narrower flakes, STEM was used. Figure 4.2(c) shows an optical image of the MoTe_2 flake where STEM was performed. Interestingly, this flake was stamped on graphene flakes, following the same procedure as the one for a real device. In case the crystal axes of MoTe_2 were somehow altered during fabrication, it should be observed by STEM. A longitudinal cut was taken on the MoTe_2 along the red dashed line in Fig. 4.2(c). STEM was performed along the line and the observed crystal structure is shown in Fig. 4.2(d). This image presents the cleaving direction of the flake along the crystallographic axis where the Mo chain lies (a -axis). The crystallographic structure superimposed to the STEM image is shown in detail in Fig. 4.2(e). The Mo chain is along the a -axis and the vertical direction corresponds to the stacking direction.

The crystal orientation of the elongated MoTe_2 flakes determined via polarized Raman spectroscopy is in agreement with the one obtained via STEM, i.e., the long direction of the needle-shaped MoTe_2 flakes corresponds to the direction of the a -axis.

4.3 Low-temperature polarized Raman spectroscopy

Previous crystal axes determination, in Section 4.2, was performed at room temperature, where the MoTe_2 flake is expected to be in the $1\text{T}'\text{-MoTe}_2$ phase. However, bulk MoTe_2 crystals undergo a first-order phase transition from the $1\text{T}'$ phase to the 1T_d phase at around 240 K when cooling [191]. Structural transitions are known to be altered by pressure [194, 322] and impurity doping [323–325]. The phase transition in MoTe_2 has been reported mostly in studies on bulk crystals of $1\text{T}'\text{-MoTe}_2$ [191–193, 195–198], with only few on MoTe_2 thin flakes [199–201, 321]. Some works suggest the possibility of a layer-dependent phase transition [200, 201].

In order to distinguish the phase transition, polarized Raman spectroscopy can be performed, where a splitting in the $\sim 133\ \text{cm}^{-1}$ mode should appear if such transition occurs [192, 193]. Figure 4.3(a) shows polarized Raman spectroscopy measurements performed with a green laser for temperatures ranging

from 300 K to 80 K in a piece of bulk MoTe_2 crystal. A splitting of the peak at $\sim 133 \text{ cm}^{-1}$ is observed for temperatures below 240 K down to 80 K, which is the lowest temperature the system can achieve. In contrast, Fig. 4.3(b) shows the Raman measurements performed on a flake exfoliated from the bulk piece, shown in the right panel. The data are an average of the measurements taken at the three red dots on the flake. These data do not show any splitting of the peak down to 80 K, meaning that our flakes stabilised in the $1\text{T}'$ phase. This fact was also probed by measuring the resistance of the flakes, where no hysteretic behaviour was observed [see Fig. 4.4(b), Fig. 4.6(b) and Fig. 5.13(b)].

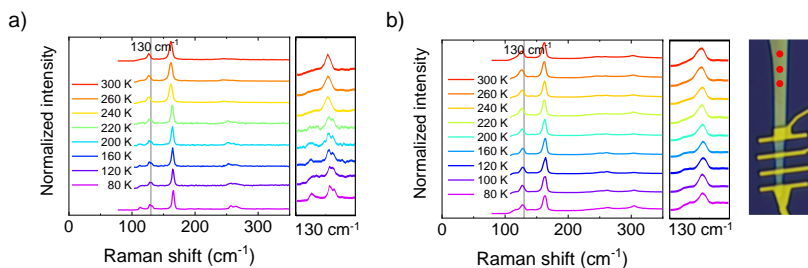


Figure 4.3: **Low-temperature polarized Raman on MoTe_2 .** (a) Polarized Raman spectroscopy on a bulk MoTe_2 crystal as a function of temperature. A splitting of the peak at 130 cm^{-1} appears for temperatures below the expected phase transition around 240 K [193]. (b) Polarized Raman spectroscopy on a MoTe_2 flake exfoliated from the bulk crystal in panel a, as a function of temperature. The data for each temperature correspond to the average of the measurements taken at the red circles on the MoTe_2 flake. The splitting of the peak at 130 cm^{-1} is absent at all measured temperatures.

The polarized Raman spectroscopy, together with the temperature-dependent resistance measurements of the $1\text{T}'$ - MoTe_2 flakes, suggest the flakes stabilise in the $1\text{T}'$ phase. These measurements are in agreement with other reports where no phase transition is observed in $1\text{T}'$ - MoTe_2 flakes down to 5 K [202]. In the forthcoming, for the sake of brevity, $1\text{T}'$ - MoTe_2 will be referred as to MoTe_2 .

4.4 Magnetoresistance measurements

Magnetoresistance is a change in the electrical resistance upon the presence of an external magnetic field. Magnetoresistance in normal metals is characterized by a low variation with the magnetic fields, and it theoretically saturates for high values of the field [326,327]. With the discovery of 2D materials, non-saturating magnetoresistance, together with an increase of several orders

of magnitude in the resistance as a function of the magnetic field, has been observed in materials such as Cd_3As_2 , NbSb_2 , and WTe_2 [328–331]. The non-saturating magnetoresistance in WTe_2 arises from its crystal phase, the $1T_d$ phase. Although we have proven to have MoTe_2 in the $1T'$ phase, it is of interest to characterize the resistance of the material as a function of the magnetic field in different directions.

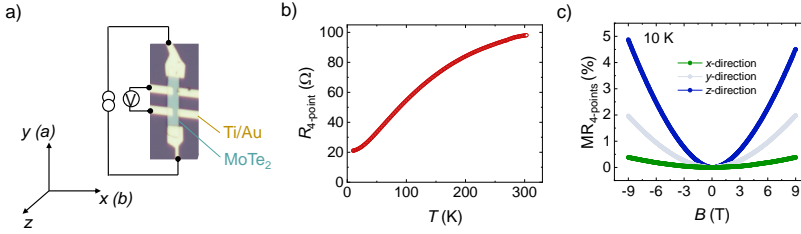


Figure 4.4: **Magnetoresistance measurements on a MoTe_2 Hall bar.** (a) Optical image of the MoTe_2 exfoliated flake contacted by non-magnetic Ti/Au electrodes. A sketch of the 4-point resistance configuration ($R_{4\text{-point}}$) is included. (b) Longitudinal 4-point resistance as a function of temperature. (c) Magnetoresistance as a function of the magnetic field measured at 10 K in a 4-point configuration. The magnetic field is applied along the x -direction (green curve), y -direction (light blue curve), and z -direction (dark blue curve).

Figure 4.4(a) shows an optical image of a MoTe_2 flake contacted with Ti/Au electrodes. In the absence of an external magnetic field, the 4-point resistance is measured as a function of temperature [Fig. 4.4(b)]. This resistance is measured using the configuration sketched in Fig. 4.4(a) and shows metallic-like behaviour. At 10 K, an external magnetic field is applied along the different crystal axes: along the a -axis which corresponds to the y -direction, along the b -axis which corresponds to the x -direction, and the z -direction. The magnetoresistance is given by:

$$\text{MR}(\%) = \frac{R(B) - R(B = 0)}{R(B = 0)} \times 100, \quad (4.1)$$

where $R(B)$ is the electrical resistance measured as a function of the magnetic field. Figure 4.4(c) shows a MR at 9 T of about 5% when the magnetic field is applied out of plane (dark blue curve), about 2% when the magnetic field is applied along the Mo chain direction (light blue curve) and about 0.5% when it is applied along the x -direction (green curve).

Similar measurements were performed in a flake in which the SCC process was studied (see Section 5.7.6). The MoTe_2 flake was contacted by Ti/Au and, by performing 2-point resistance measurements, the magnetoresistance

of MoTe₂ was extracted [see Fig. 4.5(a)]. Initially, the magnetic field was applied out of plane (B_z) and the magnetoresistance was measured for different temperatures from 200 K down to 10 K. For high temperatures, the MR is negligible. However, as the temperature decreases, it increases up to almost 5% at 10 K [Fig. 4.5(b)]. Figure 4.5(c) shows the angular dependence of MR at 10 K. The direction of the magnetic field is swept from 0°, which corresponds to the out-of-plane direction, to 90°, which corresponds to the y -direction along the Mo chain. The value of MR decreases as the magnetic field rotates from the out-of-plane direction to the in-plane one. These results are qualitatively similar to the ones reported for the MoTe₂ Hall bar (see Fig. 4.4).

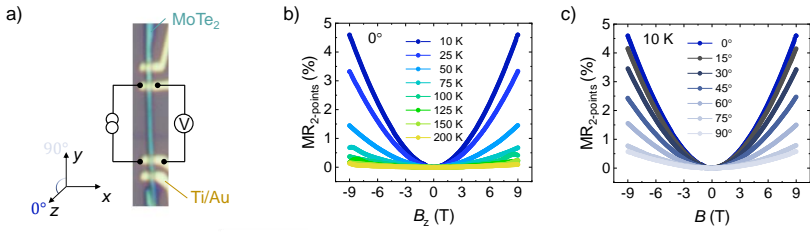


Figure 4.5: **Magnetoresistance measurements from a MoTe₂ flake used to study spin-to-charge conversion.** (a) Optical image of the MoTe₂ flake, contacted with Ti/Au electrodes, used to study spin-to-charge conversion (see Section 5.7.6). (b) Magnetoresistance in 2-point configuration and applied out-of-plan magnetic field as a function of temperature. (c) Magnetoresistance measured in 2-point configuration and magnetic field applied at different angles between the y -direction (90°) and z -direction (0°) at 10 K.

The fact that the magnetoresistance is larger for low temperatures and when the magnetic field is along the out-of-plane direction, has direct impact in the low-temperature SCC measurements performed in MoTe₂ as discussed in Chapter 6.

4.5 Spin transport in 1T'-MoTe₂

In high-SOC materials, there is a trade-off between the spin Hall angle and the spin diffusion length. If the former is large, the later is small, since both are determined by the SOC and one tends to compensate the other. Naively speaking, if the efficiency of the SCC is high, i.e., large θ_{ij}^α , the spins cannot travel long distances while keeping the spin information, i.e., short λ_s^{SOC} . In case of metals, a constant value of the product of $\theta_{ij}^\alpha \lambda_s^{SOC}$ is usually observed yielding ~ 0.1 nm for most of the studied metals, such as Pt, W or Ta, where

the value of θ_{ij}^α is large (in the order of 10%), but λ_s is in the order of $\sim 1\text{--}10$ nm [35,99,332–335]. Opposite to this, Al, as discussed in Section 1.4.1.3, shows large values of λ_s^{Al} , which ranges between 500–700 nm, and the θ_{SH}^{Al} ranges between 0.01–0.03% at low temperatures [98]. In contrast, $1T_d\text{-MoTe}_2$ was reported to present $\theta_{ij}^\alpha \sim 0.32$ and $\lambda_s^{\text{MoTe}_2} \sim 2.2 \mu\text{m}$ [282], being both values extraordinarily large. Also large, but seemingly more realistic results were theoretically calculated in monolayer MoTe_2 , where the $\theta_{ij}^\alpha \lambda_s^{\text{MoTe}_2}$ product was predicted to be between 1 and 50 nm [336]. These works motivated us to study spin transport in $1T'$ - MoTe_2 flakes.

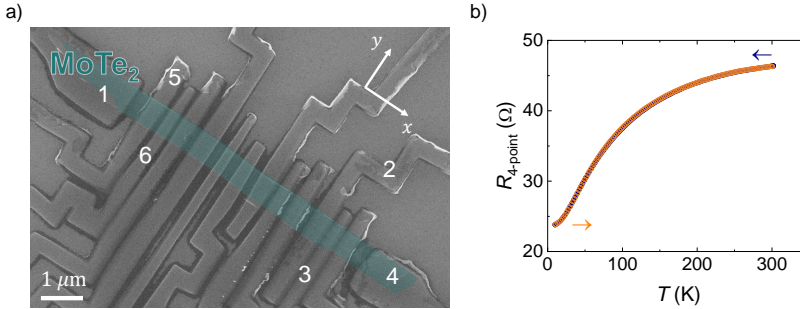


Figure 4.6: False-colored SEM image of a MoTe_2 flake contacted with Co electrodes and longitudinal resistance measurement. (a) The widths of the Co electrodes are different so that the coercive fields changes. The numbers are on the contacts used in the measurements. (b) Resistance of the MoTe_2 flake, measured in 4-point configuration ($V_{56}I_{14}$), when cooling down (blue solid circles), and when warming-up (open orange circles). The two measurements are one on top of each other, therefore, no fingerprint of phase transition is observed.

Figure 4.6(a) shows a SEM image of the device containing a MoTe_2 flake with several FM electrodes on top. The distance between electrodes is ~ 250 nm and, due to the different widths of the electrodes, each FM electrode has different coercive field, allowing us to access to the parallel and antiparallel states. The contacts involved in the experiments are labeled with numbers. Initially, the four-point resistance of the MoTe_2 is measured as a function of temperature. By applying the charge current between contacts 1 and 4 and measuring the voltage between contacts 5 and 6 ($V_{56}I_{14}$), the temperature dependence of the MoTe_2 resistance was measured when cooling down (blue solid circles) and warming-up (orange open circles). The MoTe_2 flake shows metallic-like behaviour and no fingerprint of phase transition is observed [see Fig. 4.6(b)].

In order to measure spin transport in MoTe₂, the magnetic field is applied along the easy axis of the FM electrodes (y -direction), while the resistance is measured in the non-local LSV configuration ($V_{34}I_{21}$). Due to the shape anisotropy, the magnetization of the FM aligns along the y -direction. On the one hand, by applying the magnetic field along the y -direction, at certain value of B_y , the magnetization will reverse the direction. Based on the LSV experiment, we expect to observe a signal similar to the one in Fig. 2.1. In contrast, we observed the signal plotted in Fig. 4.7(a,b). The two curves corresponds to the two sweeping directions of the field, i.e., from +0.1 T to -0.1 T, in grey, and from -0.1 T to +0.1 T in green. The shape of the measured signal at 10 K resembles an hysteresis loop, mimicking the spin signal measured in local SCC devices [337].

On the other hand, if the magnetic field is swept along the in-plane hard axis of the FM electrode (x -direction), the measurement contains four different measurement branches. Initially, (i) the magnetization is set along the $+y$ -direction (R_{NL}^\uparrow , blue curve) and then, (ii) the magnetic field is swept from 0 to +0.8 T and from 0 to -0.8 T. Prior to each sweep of the magnetic field the magnetization is set along the easy axis. Later, (iii) the magnetization is initially set along the $-y$ -direction (R_{NL}^\downarrow , red curve), and then, (iv) the magnetic field is swept. A Hanle-induced spin precession is expected, as shown in Fig. 2.2. Figure 4.7(c,d) show the non-local resistance measurement as a function of the in-plane hard axis magnetic field. In contrast, to the expected Hanle precession, these signals at 10 K and 100 K are attributed to anomalous magnetoresistance (AMR). AMR arises from the difference in the resistance of a FM stripe when the charge current direction and magnetization are parallel or perpendicular [338]. When the magnetization is set along the $\pm y$ -direction, the applied charge current and the direction of the magnetization lie in the same direction, this situation corresponds to a dip in the resistance. As the magnetic field starts to increase along the in-plane hard axis, the direction of the magnetization and the the direction of the current become perpendicular, and the non-local resistance saturates [339].

To further test the non-local MoTe₂ LSV, another configuration was used to check the spin transport. This time, the electrical configuration was $V_{64}I_{51}$ and the measurement was done at 10 K. Figure 4.8 shows the non-local resistance as a function of the in-plane easy axis magnetic field. The sweep starting at positive B_y (grey line), presents a decay in the resistance which has its lower value at negative B_y . Interestingly, the negative sweeping (green line), does

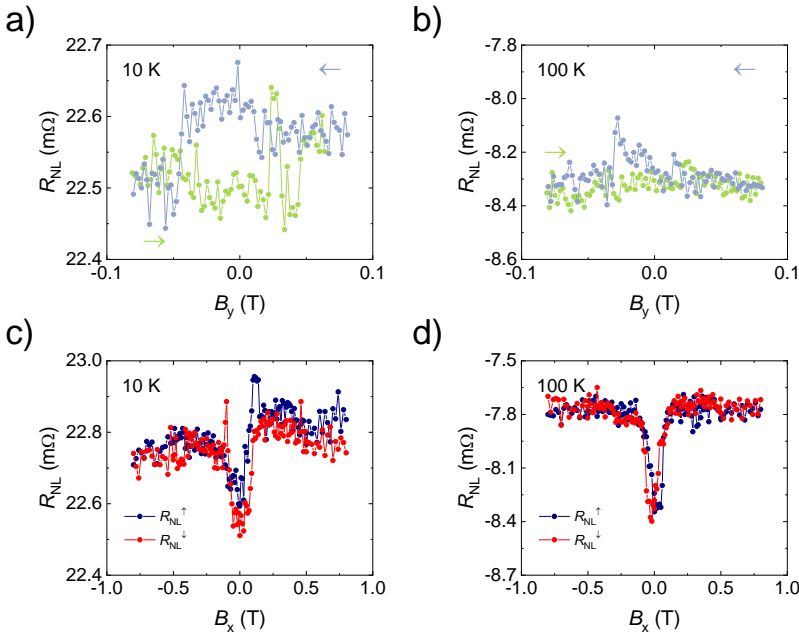


Figure 4.7: **Non-local resistance measurements as a function of the in-plane fields performed in the non-local lateral spin valve configuration.** (a,b) Non-local resistance measured as a function of the in-plane magnetic field along the easy axis of the FMs (B_y), for two different sweeps, from positive to negative field (grey) and from negative to positive (green) at 10 K and 100 K respectively. (c,d) Non-local resistance as a function of the in-plane magnetic field along the hard axis of the FMs (B_x), for the two different initial states of the Co magnetization (red and blue curves) at 10 K, and 100 K.

not present such decay in the signal. In order to discern the spin-related origin of the signal, a minor loop was done. The green open circles correspond to a sweep in the field starting at positive B_y values. Once the low R_{NL} value is achieved, the magnetic field is stopped, and starts to sweep back. During the retrace of the field, the non-local resistance takes the same values as in the trace. This confirms the AMR origin of the signal [340]. For a LSV, when you sweep the magnetic field from positive to negative values of B_y , at certain negative value of B_y , the resistance drops due a change in the relative orientation in the magnetizations of the FMs. If at the drop of the resistance, which corresponds to the antiparallel state, B_y is swept back to positive values, the system stays in the antiparallel state until a certain positive value of the magnetic field, when the magnetization of the FM switches back to the parallel state. In this case, such hysteresis loop is not observed.

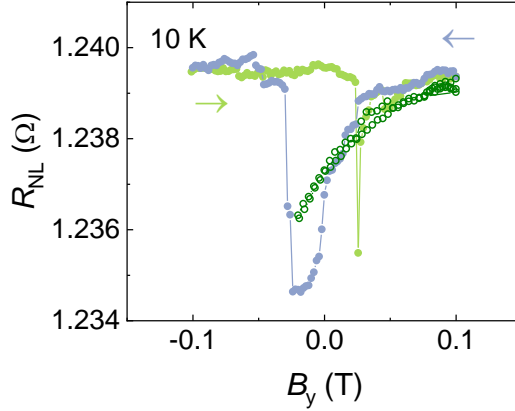


Figure 4.8: Non-local resistance measurements as a function of the in-plane fields performed in the non-local lateral spin valve configuration at 10 K.

Using the non-local LSV configuration, charge current and voltage paths are completely separated. This translates into a low baseline in the measurements. In contrast, if the charge current and voltage current share the path, the baseline increases. That is the case of Fig. 4.9, which shows the local resistance measured in the $V_{23}I_{14}$ configuration. In this configuration, when the magnetic field is swept along the in-plane easy axis, the signals at 10 K and 100 K show random switching which cannot be attributed to any particular spin-transport feature. In contrast, when the magnetic field is applied along the in-plane hard axis direction, the AMR signal becomes more evident. This AMR signal at low fields is the addition of the AMR in the y -direction, shown in Fig. 4.8, and the contribution along the x -direction, shown in Fig. 4.7(c,d). Depending on the configuration and the electrodes involved in the measurements, the AMR signal intensities vary.

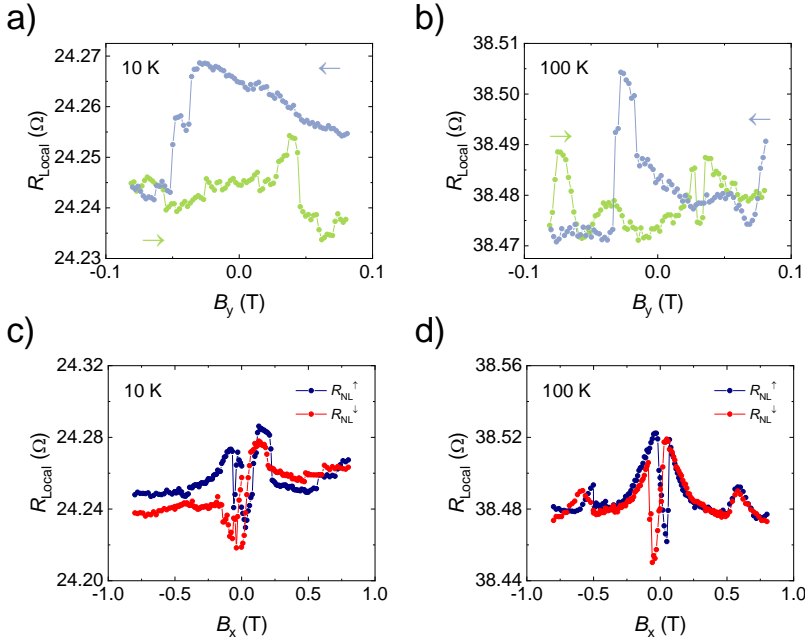


Figure 4.9: Local resistance measurements as a function of the in-plane fields performed in the local lateral spin valve configuration. (a,b) Local resistance measured as a function of the in-plane easy axis field for two different sweeps, from positive to negative field (grey) and from negative to positive (green) at 10 K, and 100 K respectively. (c,d) Local resistance as a function of the in-plane hard axis magnetic field for the two different initial states of the Co magnetization [blue (red) initial $+(-)y$ magnetization] at 10 K, and 100 K.

On the basis of these experiments, we can conclude that no spin transport is observed in MoTe_2 . Moreover, the fact that the FM has to be very close one to each other to detect the spin transport affects the measured signals. The AMR effect is dominant and can hinder the observation of spin-dependent signals. For this reason, $\lambda_s^{\text{MoTe}_2}$ could not be determined using the spin transport in MoTe_2 flakes.

Chapter 5

Large multidirectional spin-to-charge conversion in MoTe_2 at room temperature

5.1 Introduction

The spin absorption technique using LSV is a non-local method to study and quantify both the spin diffusion length and the SCC in strong SOC materials (see Section 1.4.1.3 and 2.2). The advantage of using a non-local measurement is that spurious effects related to local currents, such as Oersted fields in spin-orbit torque techniques [341] or fringe field-induced voltages in three-terminal potentiometric techniques [342, 343], are avoided. Graphene-based LSVs have been employed to study prototypical spin Hall metals as Pt [298, 344] due to the excellent spin transport of graphene [143, 148, 151, 211, 238], and they are expected to be ideal for studying TMDCs as the van der Waals interaction with graphene [222, 223, 226, 231, 275, 277] allows the formation of a good contact between them. Using this technique, both spin-to-charge and charge-to-spin conversions can be studied by exchanging the spin injection and detection terminals. In this Chapter, we report the SCC of spin currents injected in MoTe_2

by spin absorption from graphene, with full magnetic-field-induced control of the spin polarization direction. Along with a highly efficient conventional SCC, we report the simultaneous observation of another unconventional SCC, unexpected as it remains forbidden by the mirror symmetry of the 1T' phase. The simultaneous detection of SCC originating from two different spin polarization (\mathbf{s}) directions for a fixed $\mathbf{j}_c \perp \mathbf{j}_s$ configuration, which can only be explained if the symmetries of the system are reduced, opens new possibilities in the design of novel spintronic devices that could benefit from flexible configurations to generate, detect, and control spin currents.

5.2 Experimental details

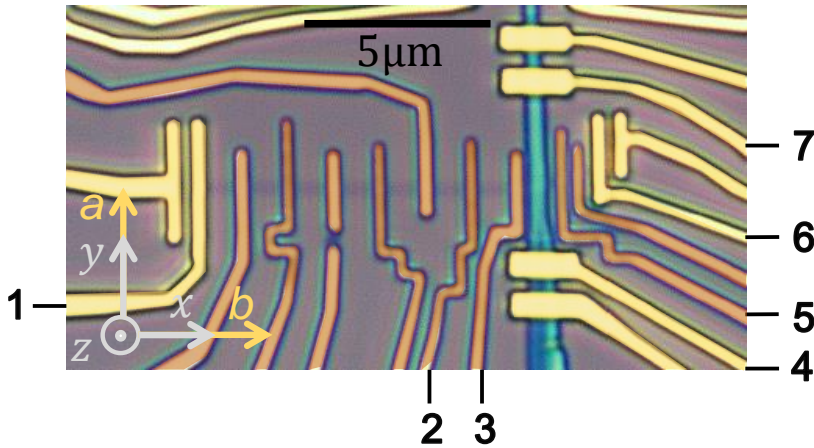


Figure 5.1: **Optical microscope image of the graphene-based LSV device where the spin absorption technique is performed.** It contains a graphene channel (grey) with a MoTe₂ flake (blue) placed on top. The ends of the graphene channel and MoTe₂ are connected to Ti/Au contacts (yellow). Several TiO_x/Co electrodes are placed on top of graphene channel (orange). The x - and y -directions corresponds to the b - and a -axes of the MoTe₂, respectively. The contacts used in the experiments are labeled with numbers.

An optical microscope image of one of our devices is shown in Fig. 5.1. An exfoliated few-layer graphene flake (590-nm wide) works as the spin transport channel. A needle-like MoTe₂ flake (890-nm wide and 11-nm thick) that acts as the SOC material is placed on top of the graphene flake, forming a van der Waals heterostructure. Several Co electrodes that work as spin injec-

tor/detectors are also placed on top of graphene. The direction of the needle-shaped flake corresponds to the a -axis of the MoTe₂ crystal, that is, the Mo zigzag chain is aligned along y , parallel to the easy axis of the Co electrode (see Chapter 4 for MoTe₂ crystal axes determination). The graphene channel and MoTe₂ are contacted with Ti/Au electrodes. The difference between the spin signal in pristine graphene and the spin signal across MoTe₂ [see Section 5.7.1 for details], is attributed to spin absorption into the MoTe₂. Since \mathbf{j}_s is absorbed into the MoTe₂, SCC is expected to occur.

To perform such measurement, we apply a constant current $I_c = 10 \mu\text{A}$ between the Co injector (Co contact 3) and graphene (Ti/Au contact 1). When electrical current is applied from a Co electrode into the graphene channel, it creates a spin accumulation at the interface, which diffuses away (\mathbf{j}_s) in the graphene channel. \mathbf{j}_s is then absorbed into the SOC material along z and converted into \mathbf{j}_c , which is detected as V_{NL} across the MoTe₂ flake along y (Ti/Au contacts 4 and 7). In all our measurements, the directions of \mathbf{j}_s (along z) and the measured V_{NL} (along y) are fixed, whereas the orientation of \mathbf{s} is controlled with the magnetic field applied along the three directions (x , y , and z).

The presence of an external magnetic field applied along the three different directions (x , y , z) controls the polarization direction of the spins reaching the MoTe₂ by two means: (*i*) inducing spin precession when the injected spins are polarized perpendicular to the direction of the field, or (*ii*) by pulling the magnetization of the Co injector towards the direction of the field. When the magnetic field is applied along the in-plane hard axis of the Co electrode direction (B_x), or along the out-of-plane direction (B_z), spin precession and pulling of the magnetization occur as detailed in Section 2.2.3.1 and 2.2.3.2, for the respective directions of the field. In contrast, if the magnetic field is applied along the easy axis of the Co injector (B_y) no precession is induced, as described in Section 2.2.3.3.

5.3 Spin-to-charge conversion by applying in-plane magnetic fields

First, we study the SCC using the conventional experimental geometry [298,344], that is, by sweeping B_x , and the resulting curves for R_{NL} vs. B_x for two different temperatures are shown in Fig. 5.2(a,b) (300 K and 100 K, respectively). The curves at other temperatures are shown in Section 5.7.2. The measurement was performed in four steps: for the first two steps, R_{NL} was measured while sweeping B_x from 0 to 1 T and 0 to -1 T, with the magnetization of Co initially saturated in the $+y$ -direction prior to each sweep (R_{NL}^\uparrow , blue curve). Then, similar measurements were repeated for the magnetization of the Co initially set along the $-y$ -direction (R_{NL}^\downarrow , red curve).

According to the conventional geometry of SCC (\mathbf{j}_s , \mathbf{j}_c and \mathbf{s} must be mutually orthogonal), the voltage V_{NL} measured along y with \mathbf{j}_s fixed along z is expected to detect the x -component of \mathbf{s} (s_x) in our experiment. As depicted in Fig. 2.6, B_x causes the Co magnetization to rotate toward x and saturates when $|B_x| > 0.3$ T (see Section 5.7.3). The corresponding variation of s_x is proportional to $\sin \Theta$ and expected to result in an R_{NL} vs. B_x curve that varies linearly below the saturation field, crosses zero for $B_x = 0$, and saturates above the saturation field [S-shaped curve, see Fig. 2.6(f)] [298,344]. Figure 5.2(a,b) shows indeed the saturation of R_{NL} when $|B_x| > 0.3$ T. However, below that saturation value, even at $B_x = 0$, we observe a non-zero value of R_{NL} that evolves differently with increasing B_x and depends on the initial Co magnetization aligned along $+y$ and $-y$ [red and blue curves, respectively, in Fig. 5.2(a,b)], suggesting the existence of nonzero SCC signal arising from the y -component of \mathbf{s} (s_y) as well. To verify this possibility, we extract the antisymmetric [Fig. 5.2(c,d)] and the symmetric [Fig. 5.2(e,f)] components of the R_{NL} vs. B_x curves. The former contribution, R_{SCC}^{anti} , shows the expected behaviour proportional to s_x , and it is independent of the initial magnetization direction, indicating SCC in MoTe₂ with the conventional symmetry. However, the latter contribution, R_{SCC}^{symm} , shows a behaviour which depends on the initial magnetization direction: R_{NL}^\uparrow is maximum at $B_x = 0$ and decreases to zero at saturation, whereas R_{NL}^\downarrow shows the same shape with opposite sign. They are thus proportional to the variation of s_y , indicating a new and unconventional SCC in our system with a $\mathbf{j}_c \parallel \mathbf{s}$ geometry [similar behaviour to the one represented in Fig. 2.6(b)].

To further confirm the SCC in this unconventional configuration, we measure R_{NL} while sweeping B_y [see sketch in Fig. 2.8(a)]. Very interestingly, we observe a square hysteresis loop for R_{NL} vs. B_y , shown in Fig. 5.2(g,h) (300 K and 100 K, respectively), with the signal switching sign at the coercive field of the Co electrode (~ 0.034 T). This behaviour corresponds to the one represented in Fig. 2.8(b). We also note an opposite sign between the measured V_{NL} corresponding to the SCC from s_x [Fig. 5.2(e,f)] and s_y [Fig. 5.2(g,h)], indicating that the sign of the conventional and unconventional SCCs are opposite.

The same measurements were performed in another device (see Section 5.7.6) and injecting from two different Co electrodes with different coercivity and detect at the same MoTe₂ flake. We observe that the switching fields for these two R_{NL} vs. B_y loops follow the coercivity of each Co injector (see Section 5.7.7). This set of control experiments shows the robustness of this unconventional SCC signal in our system.

By changing the current and voltage terminals, we measured both the direct (charge-to-spin) and the inverse (spin-to-charge) conversion for both the conventional and unconventional SCC components, which fulfills the expected Onsager reciprocity (see Section 5.7.8).

In the R_{NL} measurements presented above, \mathbf{s} is set by the variation of magnetization of the Co injector. In the R_{NL} vs. B_x curves, the variation of R_{NL} associated with SCC from s_x [R_{SCC}^{anti} , Fig. 5.2(e,f)] is proportional to the variation of the magnetization of the Co injector along the x -direction [see Fig. 2.6(e,f)]. However, the decrease of R_{SCC}^{symm} from the maximum to zero with B_x [Fig. 5.2(g,h)] can be indistinguishably associated with the decrease of s_y via the decrease of the Co magnetization along the y -direction or the spin precession in the y - z -plane [see Fig. 2.6(g,h)]. It is then important to verify that the measured R_{NL} signal corresponds to SCC and it is not originated from an artifact related to the Co magnetization, such as the AHE or the AMR. A measurement sensitive only to the spin precession is required to confirm that the true origin of the two observed contributions is SCC. It is thus convenient to perform a measurement by applying B_z , as explained in the following Section.

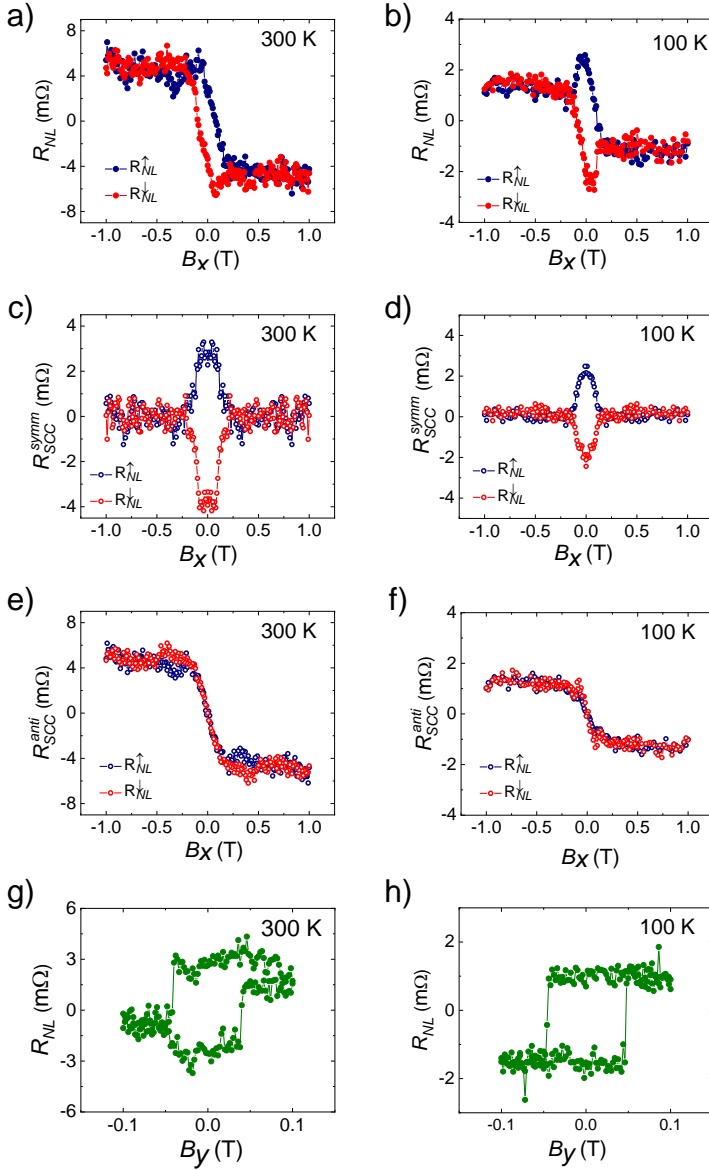


Figure 5.2: Spin-to-charge conversion in MoTe₂ using graphene-based LSV with in-plane magnetic fields. (a,b) R_{NL} vs. B_x at 300 K and 100 K, respectively, for the two different initial states of the Co magnetization (red and blue curves). (c,d) R_{SCC}^{anti} vs. B_x at 300 K and 100 K respectively for the two different initial states of the Co magnetization (red and blue curves). (e,f) R_{SCC}^{symm} vs. B_x at 300 K and 100 K respectively for the two different initial states of the Co magnetization (red and blue curves). (g,h) R_{NL} vs. B_y at 300 K and 100 K respectively.

5.4 Spin-to-charge conversion by applying out-of-plane magnetic field

To confirm the spin-related signal is convenient to perform a measurement by applying B_z . The resulting curves R_{NL} vs. B_z at two different temperatures are shown in Fig. 5.3(a,b) (300 K and 100 K, respectively). The curves at other temperatures are displayed in Section 5.7.2. The measurement was again performed in four steps: for the first two steps, R_{NL} was measured while sweeping B_z from 0 to 2 T and 0 to -2 T, initially saturating the Co magnetization along $+y$ -direction prior to each sweep (R_{NL}^\uparrow , blue curve). Then the protocol was repeated for the Co magnetization initially set along $-y$ -direction (R_{NL}^\downarrow , red curve). At low B_z regime, the direction of \mathbf{s} is dictated by the spin precession along the $x-y$ -plane, whereas the variation of the magnetization of Co along the z -direction can be neglected because the saturation occurs at much larger values (> 1.5 T) [see Fig. 2.7(c)].

To understand the overall R_{NL} signal [Fig. 5.3(a,b)], we need to consider that the two SCC components (arising from s_x and s_y) contribute to R_{NL} , but each contribution has a different dependence on increasing B_z . In particular, the contribution from s_y to SCC should give rise to a symmetric Hanle precession curve [as sketched in Fig. 2.7(a,b)], whereas the contribution from s_x should give rise to an antisymmetric Hanle precession curve [as depicted in Fig. 2.7(c,d)] [226, 344]. Both curves should also change sign when the initial magnetization direction is switched because the polarization of the injected spins are opposite. This allows us to remove the background by subtracting the two curves and obtain the pure SCC signal, R_{SCC} (see Eq. 2.23) [Fig. 5.3(c,d)]. Then, symmetrization and antisymmetrization of the R_{SCC} curve allows us to distinguish the SCC contributions due to s_x [Fig. 5.3(e,f)] and s_y [Fig. 5.3(g,h)], which have the expected corresponding behaviour as a function of B_z . From this result, we confirm that the measured V_{NL} signal indeed corresponds to the sum of a conventional $[(\mathbf{j}_s||z)\perp(\mathbf{j}_c||y)\perp(\mathbf{s}||x)]$ and an unconventional $[(\mathbf{j}_s||z)\perp(\mathbf{j}_c||\mathbf{s}||y)]$ SCC component, ruling out any artifact not coming from spin currents. As observed before, we confirm that R_{SCC}^{symm} and R_{SCC}^{anti} have opposite signs.

A misorientation between the main crystallographic axis of the MoTe₂ needle-like flake with respect to the magnetic easy axis of Co injector, in combination with the anisotropy between the conventional (orthogonal) spin Hall

conductivity tensor elements in $1T'$ -MoTe₂ could in principle lead to the observed unconventional SCC. However, the alignment accuracy of $< 1^\circ$ with the fabrication of the Co electrodes (determined from the optical microscopy image) rules out this possibility. The possibility of a tilt in the magnetic easy axis of the Co injector toward the hard axis (x -axis) to explain the observed result is also discarded (see Section 5.7.3).

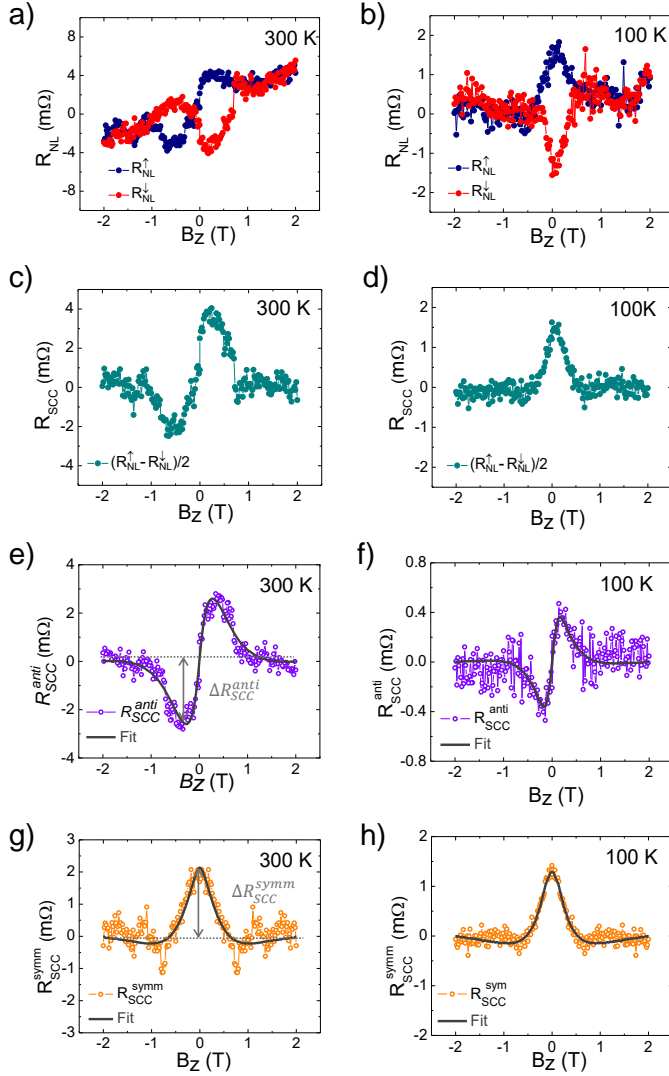


Figure 5.3: Spin-to-charge conversion in MoTe₂ using graphene-based LSV with out-of-plane magnetic field. (a,b) R_{NL} vs. B_x at 300 K and 100 K, respectively, for the two different initial states of the Co magnetization (red and blue curves). (c,d) The SCC signal $R_{SCC} = (R_{NL}^{\uparrow} - R_{NL}^{\downarrow})/2$ obtained from panel a and b, respectively. (e,f) Antisymmetric component of the R_{SCC} shown in panel c and d for 300 K and 100 K, respectively, which is fitted to the solution of the Bloch equation (Eq. 2.24) (black solid curve). It corresponds to the contribution of s_x to SCC. The amplitude of the signal (ΔR_{SCC}^{anti}), defined from the background to the peak at negative B_z because this sets the spin polarization along $+x$ -direction, is negative. (g,h) Symmetric component of the R_{SCC} shown in panel c and d for 300 K and 100 K, respectively, which is fitted to the solution of the Bloch equation (Eq. 2.25) (black solid curve). It corresponds to the contribution of s_y to SCC. The amplitude of the signal (ΔR_{SCC}^{symm}), defined from the background to the peak at zero field, is positive.

5.5 Quantification of the results

In our experimental geometry, due to the spin absorption by the MoTe₂ flake (Section 5.7.1), both the conventional and unconventional SCCs can originate from two different mechanisms, the SHE at the bulk of the MoTe₂ flake (see Section 2.2.1.1) and the EE at the proximitized graphene (see Section 2.2.2.2).

An unconventional charge-to-spin conversion effect has been reported in the low-symmetry 1T_d phase of WTe₂ [279,280] and 1T' phase of MoTe₂ [202] using spin-orbit torque measurements, where out-of-plane damping-like torque, in which the spin current parallel to the out-of-plane spin polarization ($\mathbf{j}_s \parallel \mathbf{s} \parallel z$), is observed. Such torque is allowed in crystals with a single mirror plane. This component is also allowed in our measurement geometry, since \mathbf{j}_c is measured along the a -axis, that is, across the only mirror plane of the MoTe₂ (see Chapter 4). It is interesting to note that this contribution of s_z to SCC, which should appear as an antisymmetric Hanle precession in the R_{NL} vs. B_x curve as shown in Fig. 2.6(c), is not observed in our experiments down to 75 K (see Chapter 6 for lower temperatures). Taking into account that this SCC is reported to be ~ 8 times smaller than the conventional one [202], the corresponding signal is likely below the resolution of our measurements.

In contrast, in the observed unconventional SCC, the charge current is parallel to the in-plane spin polarization ($\mathbf{j}_c \parallel \mathbf{s} \parallel y$), a case which is forbidden by symmetry both in the bulk (see Eq. 2.4) and the surface states of 1T'-MoTe₂ (see Section 2.2.2.1). A recent work reports an unexpected SCC component similar to our case ($\mathbf{j}_c \parallel \mathbf{s}$) in the 1T_d-WTe₂ below 100 K when applying \mathbf{j}_c parallel to the mirror plane and attributes it to the special spin texture of the topological Fermi arcs in the low-temperature Weyl semimetal phase [345]. However, this does not apply to our case. Although a transition into a Weyl semimetal phase associated with a structural transition from 1T' to 1T_d below 240 K has been reported in MoTe₂ [195,198], our measurements are performed in the 1T' phase (no phase transition to 1T_d is observed in our flake, see Chapter 4), where no topological surface Fermi arcs are expected. Lately, another work reports unconventional SCC in WTe₂/graphene-based LSV, where the SCC remains forbidden by the crystal symmetries [233].

If we consider the bulk SHE in MoTe₂, only the breaking of the mirror symmetry \mathcal{M}_y in the flake could account for σ_{zy}^y that is observed in our experiment. Besides, if the the crystal mirror planes from graphene and MoTe₂ are

not aligned, the interface between them is a non-symmetric interface, where a spin polarization can induced a charge current parallel to it via unconventional IEE in the proximitized graphene system, thoroughly discussed in Section 2.2.2.2 [346,347]. Importantly, unlike the case of graphene/semiconducting TMDCS, the graphene/MoTe₂ heterostructures are not annealed at high temperatures, minimizing the probability of crystallographic alignment between them [348,349]. Anyhow, only a reduction of the symmetries of the system, either at the proximitized graphene or at the bulk of the MoTe₂, can lead to the observed unconventional SCC.

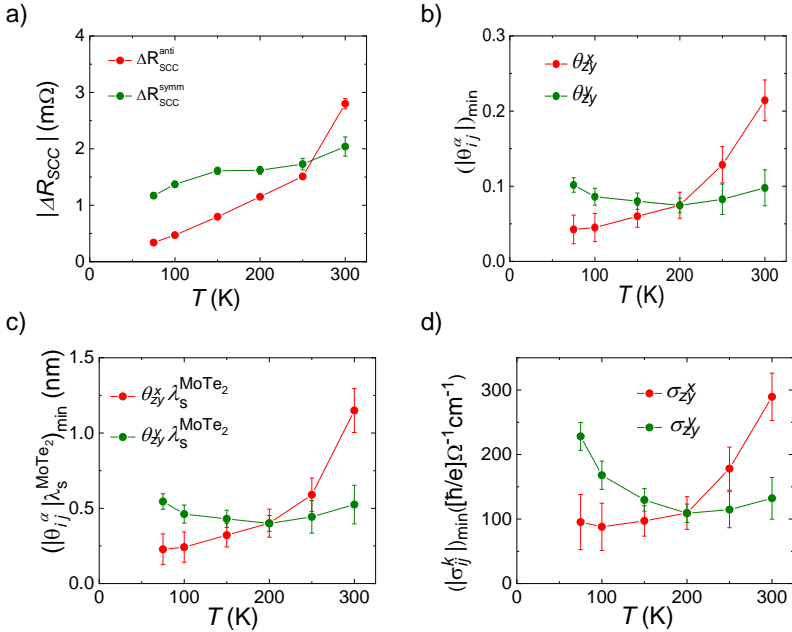


Figure 5.4: **Temperature dependence of the extracted efficiency parameters.** (a) Amplitude $|\Delta R_{SCC}|$ of the two components of the SCC signal, obtained from the antisymmetric and symmetric components of the R_{SCC} vs. B_z . (b) Lower limit of the spin Hall angle of MoTe₂ (θ_{ij}^α). (c) Lower limit of the product of the spin Hall angle and the spin diffusion length of MoTe₂ ($|\theta_{ij}^\alpha \lambda_s^{MoTe_2}|$). (d) Lower limit of the spin Hall conductivity (σ_{ij}^α). All plots show the results for the s_x component (red curve) and s_y component (green curve) or the SCC, which have opposite sign to each other.

Figure 5.4(a) shows the temperature dependence, from 300 K down to 75 K, of the absolute value of the amplitude ΔR_{SCC} of the two observed SCC components [as defined in Fig. 5.3(e,g)]. For both cases, we observe that the SCC signal increases with temperature, reaching the largest value at room

temperature. Such trend arises not only from the temperature dependence of the conversion efficiency but also from the spin transport parameters of Co and graphene, the resistivity of MoTe₂, and the interface resistance at the graphene/MoTe₂ van der Waals gap.

The spin transport parameters were calculated by fitting the non-local Hanle spin precession measurement across the reference LSVs with the solutions of Bloch equations (details are given in Section 5.7.3). We obtained a spin lifetime $\tau_s^{gr} \sim 100$ ps and a spin diffusion coefficient of $D_s^{gr} \sim 1.5 \times 10^{-3}$ m²/s for the graphene and a spin polarization of $|P| \sim 4.15$ % for the Co/graphene interface at room temperature (see Section 5.7.3 for other temperatures). The different resistances were obtained with four-point electrical measurements, and for the interface resistance, we performed a finite element 3D modeling (see Section 5.7.4).

Since we cannot, a priori, distinguish whether the SCCs occur in the MoTe₂ flake at the bulk (via ISHE) or at the proximitized graphene (via IEE), we analyze our data assuming bulk ISHE of MoTe₂ to extract the efficiency given by θ_{ij}^α . In this case, we fit the antisymmetric [Fig. 5.3(e,f)] and symmetric [Fig. 5.3(g,h)] components of the SCC precession curves to the solution of the Bloch equation to extract θ_{zy}^x and θ_{zy}^y , respectively. These values will depend on the value of $\lambda_s^{MoTe_2}$, which is not possible to determine from spin absorption (as discussed in Section 5.7.1). Moreover, the absolute sign of θ_{ij}^α cannot be determined because the sign of P is not known. However, we can extract $|\theta_{ij}^\alpha|$ for a broad range of $\lambda_s^{MoTe_2}$ values (see Section 5.7.5).

On the one hand, we find that, for $\lambda_s^{MoTe_2}$ values similar or longer than the thickness of MoTe₂ flake (11 nm), $|\theta_{ij}^\alpha|$ tends to a low constant value independent of $\lambda_s^{MoTe_2}$, because the SCC process is limited by the MoTe₂ thickness. This behaviour allows us to get a lower limit for $|\theta_{ij}^\alpha|$, which for the case of the conventional component is $|\theta_{zy}^x| \geq 0.21$ at room temperature comparable to the best known spin Hall metals [100,350] and alloys [351,352]. The lower limit for the unconventional component efficiency is also found to be remarkably large ($|\theta_{zy}^y| \geq 0.10$), and with opposite sign, at room temperature. The opposite sign between the conventional and unconventional SCCs observed in our case is not surprising. Indeed, theoretical calculations in MoTe₂ show that even the sign of the conventional spin Hall conductivities with mutually orthogonal symmetries along different crystal axes can be opposite [203].

On the other hand, for $\lambda_s^{MoTe_2}$ values much shorter than the MoTe₂ thickness, it is the $|\theta_{ij}^\alpha \lambda_s^{MoTe_2}|$ product that tends to a low constant value, which is what defines the SCC efficiency [125, 353]. This allows us to give a lower limit for $|\theta_{ij}^\alpha \lambda_s^{MoTe_2}|$, which for the case of the conventional component is $|\theta_{zy}^x \lambda_s^{MoTe_2}| \geq 1.15$ nm at room temperature, much larger than heavy metals (~ 0.1 – 0.3 nm) [100, 350]. The $\theta_{zy}^x \lambda_s^{MoTe_2}$ product can be compared to the to the Edelstein length (λ_{IEE}), the efficiency associated with the IEE. This value would be comparable to the best efficiency reported in topological insulators ($\lambda_{IEE} = 2.1$ nm for α -Sn) [116]. The lower limit for the unconventional component efficiency is $|\theta_{zy}^y \lambda_s^{MoTe_2}| \geq 0.5$ nm at room temperature (with opposite sign to the conventional one). Regardless of the origin of the SCC (bulk or intrface), this quantification demonstrates that MoTe₂ is a very promising material for spintronics applications with the flexibility of obtaining very large SCCs for spins with any in-plane spin polarization at room temperature.

By performing the fittings of the symmetric and the antisymmetric part of the SCC precession curves (R_{SCC} vs. B_z) at different temperatures between 300 K and 75 K, the lower limits for $|\theta_{ij}^\alpha|$ and $|\theta_{ij}^\alpha \lambda_s^{MoTe_2}|$ are calculated and plotted in Fig. 5.4(b,c) respectively. The trend of the efficiency (either $|\theta_{ij}^\alpha|$ or $|\theta_{ij}^\alpha \lambda_s^{MoTe_2}|$) is different for the two different SCC components: whereas the unconventional one does not vary much with temperature, the standard one increases with temperature.

A better parameter to characterize the bulk SHE is the spin Hall conductivity, σ_{ij}^α , which is plotted in Fig. 5.4(d). In metals, σ_{ij}^α is expected to be temperature independent when the intrinsic contribution arising from the Berry curvature of the band structure dominates [100, 350]. This does not seem to be the case for any components in MoTe₂: whereas the unconventional component ($|\sigma_{zy}^y|$) decreases with temperature, the conventional one ($|\sigma_{zy}^x|$) increases. These trend can be explained when an additional mechanism contributes to the SCC. One possibility is the extrinsic (skew scattering and/or side jump) contribution to the SHE with opposite sign [91, 350]. Another possibility is the presence of the IREE in graphene induced by spin-orbit proximity with MoTe₂, which would be detected with the same measurement configuration and has been recently reported in other graphene/TMDCs van der Waals heterostructures [225, 226, 229, 265, 268], and is in detail discussed in Section 2.2.2.2. This contribution decreases with increasing temperature [225, 226], and, therefore, an opposite (same) sign with respect to the intrinsic σ_{zy}^x (σ_{zy}^y) could explain the observed trend. Finally it is also possible that the intrinsic spin Hall conduc-

tivity components of semimetal MoTe₂ have stronger temperature dependence than that of metals. Chapter 6 and 7 provide additional results to help understanding the different mechanisms contributing to the SCC signals.

5.6 Conclusion

In conclusion, we observe and quantify SCC in MoTe₂. Along with a large efficiency in the conventional orthogonal configuration (spin current, charge current, and spin polarization are mutually perpendicular), we also demonstrate SCC in an unusual non-orthogonal geometry, with a charge current arising parallel to the spin orientation. Whereas the low crystal symmetry of MoTe₂ allows for non-orthogonal SCC configurations, the unconventional SCC observed here is only possible if the symmetries of our graphene/MoTe₂ heterostructure are reduced. On the one hand, the MoTe₂ crystal symmetry can be lowered likely due to fabrication-induced shear strain. On the other hand, the symmetries of the graphene/MoTe₂ interface can be reduced if none of the graphene mirrors are aligned with the one of MoTe₂, consequently a non-symmetric interface is created, where there are no restrictions in the SCC configuration via EE in the proximitized graphene. Regardless of the origin, we present here a system where any in-plane polarization of injected spins results into charge conversion, bringing new flexibility to the design of spin logic devices. Inversely, the ability to obtain spin currents with any in-plane spin polarization by applying electrical current along a single direction is a promising feature for spin-orbit torque memories, current-induced domain wall, and skyrmions motion-related applications. All of the above makes MoTe₂ a system of interest for further investigation and a promising material for future spintronic applications.

5.7 Appendices

In this section, complementary data to support our results in previous sections are added.

5.7.1 Spin absorption

To verify whether the spin current is absorbed into MoTe₂, we compare the spin signal measured in the LSV configuration, with and without the MoTe₂ in

between. We clearly see a decrease in the spin signal in LSV with MoTe₂ [Fig. 5.5(a)]. This indicates that the spin current is strongly absorbed by MoTe₂ before reaching the Co detector. The net \mathbf{j}_s reaching the MoTe₂ flake depends on the spin resistance of graphene (R_s^{gr}), the graphene/MoTe₂ interface resistance (R_{int}) and the spin resistance of MoTe₂ ($R_s^{MoTe_2}$). By comparing the spin signal across LSV with and without the SOC material in between, the spin diffusion length of the SOC material can be quantified [298]. However, in our case, the graphene/MoTe₂ interface resistance dominates the spin absorption. Therefore, within the resolution of our measurement and calculation, it is not possible to extract the value of $\lambda_s^{MoTe_2}$.

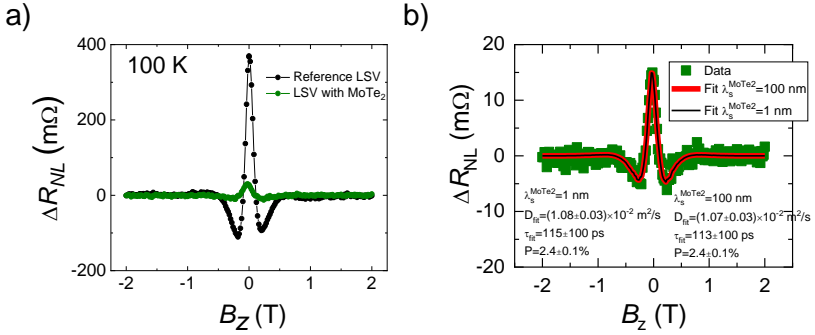


Figure 5.5: **Hanle precession measurement to determine $\lambda_s^{MoTe_2}$.** (a) Comparison of the Hanle spin precession measurement ΔR_{NL} at 100 K for the reference LSV ($V_{21}I_{36}$) and the LSV with the MoTe₂ in between ($V_{56}I_{31}$) shown in black and green, respectively. The spin signal for the latter is much smaller than the former, indicating the absorption of spin current to MoTe₂. (b) Fit to the Hanle precession data measured at 100 K across the MoTe₂ for $\lambda_s^{MoTe_2} = 1$ and 100 nm using Eq. 2.20. Both values give the same fitting since the spin absorption is dominated by R_{int} .

By fitting the Hanle precession measured at 100 K across the LSV with the MoTe₂ in between [Fig. 5.5(b)] for $\lambda_s^{MoTe_2} = 1$ and 100 nm to Eq. 2.20, we observed that both values of $\lambda_s^{MoTe_2}$ provide the same fitting to the data. Because $R_s^{MoTe_2} < R_{int}$, the spin absorption is dominated by R_{int} , hence, there is no relevant effect of changing $\lambda_s^{MoTe_2}$ as shown in Fig. 5.5(b) where the two values fit the experimental data. This prevent us to quantify the value of $\lambda_s^{MoTe_2}$.

5.7.2 Temperature dependence of the spin-to-charge conversion measurements

Only two representative temperatures have been discussed before (300 K and 100 K). However, the spin-to-charge conversion signals have been measured at different temperatures between 300 K and 75 K while sweeping the magnetic field along the in-plane hard axis (B_x , Fig. 5.6 and 5.7), easy axis (B_y , Fig. 5.8), and out-of-plane direction (B_z , Fig. 5.9). For all the temperatures, the spin-to-charge conversion signal (R_{SCC}) was calculated, followed by a deconvolution in which the antisymmetric (R_{SCC}^{anti}) and symmetric components were calculated (R_{SCC}^{symm}). For the particular case of B_x the average is also shown. While the average is defined as $R_{NL}^{average} = (R_{NL}^{\uparrow} + R_{NL}^{\downarrow})/2$, the spin-to-charge conversion signal is $R_{SCC} = (R_{NL}^{\uparrow} - R_{NL}^{\downarrow})/2$.

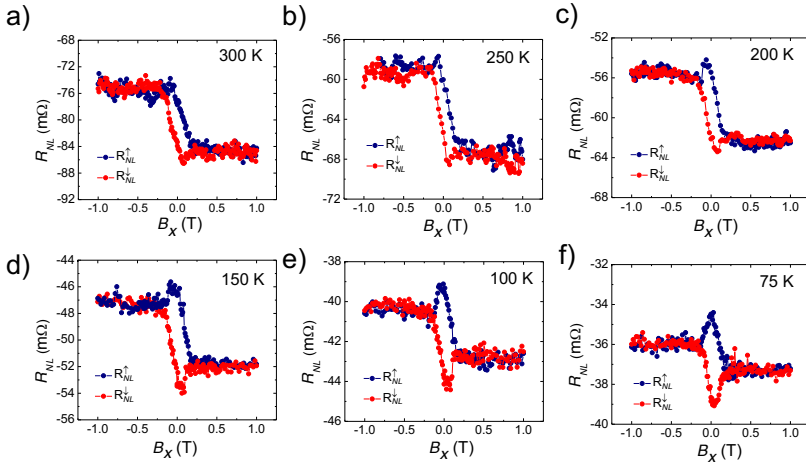


Figure 5.6: Spin-to-charge conversion in MoTe_2 using graphene-based LSV with in-plane magnetic field along the hard axis of the Co electrode (B_x) at various temperatures. Initial magnetization of the Co electrode saturated along positive (blue) and negative (red) y -direction at temperature (a) 300 K, (b) 250 K, (c) 200 K, (d) 150 K, (e) 100 K, and (f) 75 K.

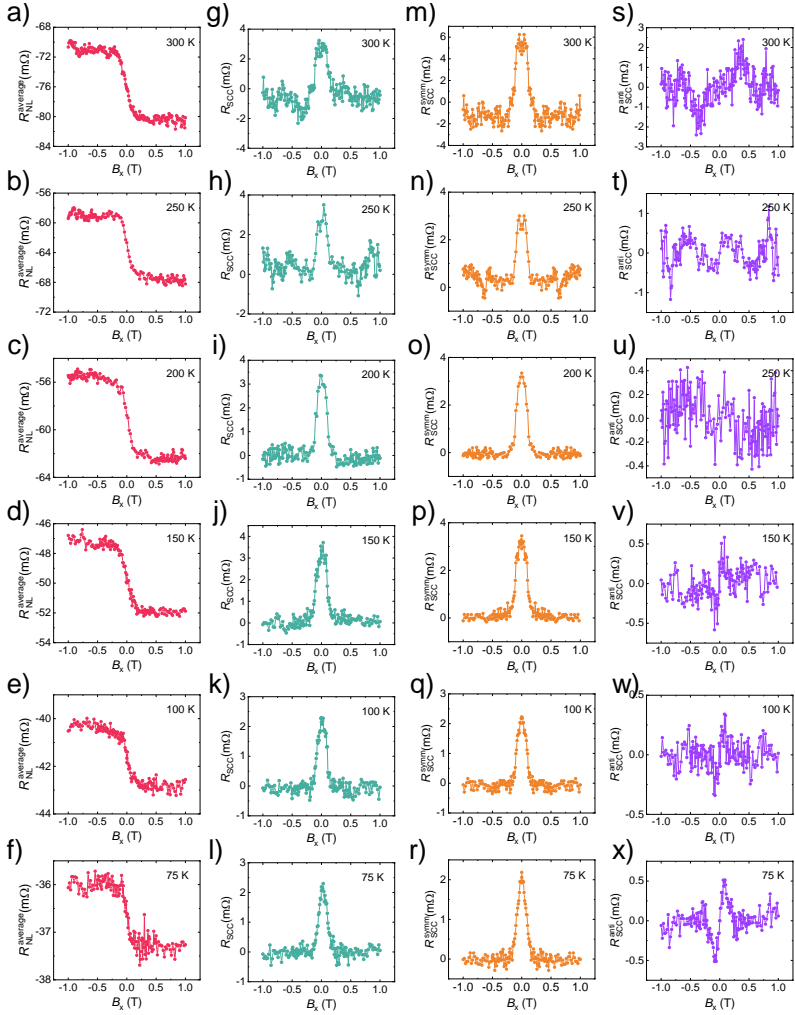


Figure 5.7: **Spin-to-charge conversion contributions from R_{NL} vs. B_x at different temperatures.** (a-f) The average non-local resistance defined as $R_{NL}^{average} = (R_{NL}^{\uparrow} + R_{NL}^{\downarrow})/2$ for 300 K, 250 K, 200 K, 150 K, 100 K, and 75 K. This signal shows an S-shape, as described in Section 2.2.3.1, arising from the SCC from s_x . (g-l) Spin-to-charge conversion resistance, defined as $R_{SCC} = (R_{NL}^{\uparrow} - R_{NL}^{\downarrow})/2$. (m-r) Symmetric component of R_{SCC} . As described in Section 2.2.3.1, this signal corresponds to the SCC from s_y . (s-x) Antisymmetric component of R_{SCC} . As described in Section 2.2.3.1, the absence of the antisymmetric component implies no SCC from s_z . Data extracted from Fig. 5.6.

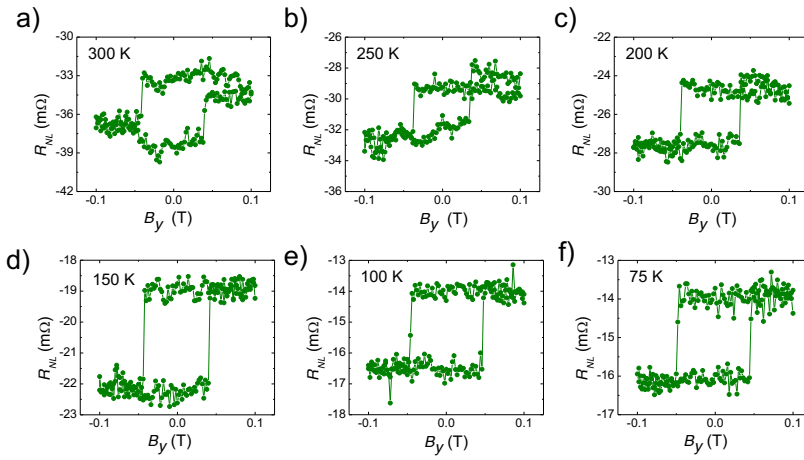


Figure 5.8: Spin-to-charge conversion in MoTe_2 using graphene-based LSV with in-plane magnetic field along the easy axis of the Co electrode (B_y) at various temperatures. (a) 300 K, (b) 250 K, (c) 200 K, (d) 150 K, (e) 100 K, and (f) 75 K.

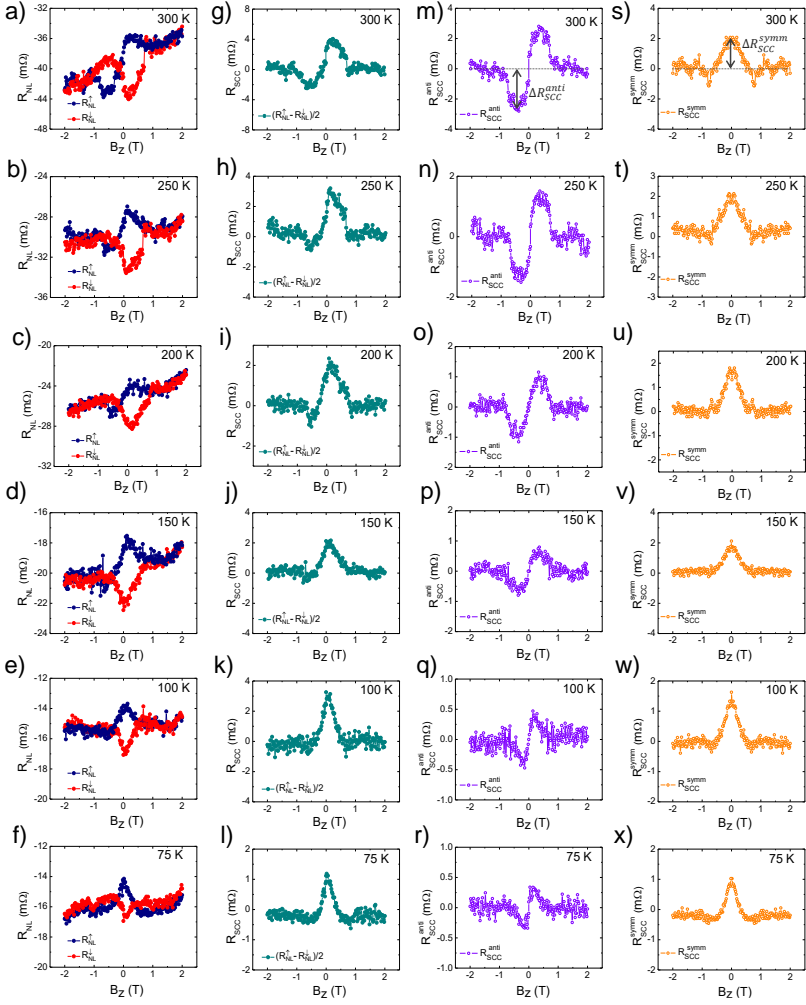


Figure 5.9: Spin-to-charge conversion in MoTe₂ using graphene-based LSV with out-of-plane magnetic field (B_z) at various temperatures. (a-f) R_{NL} vs. B_z for the initial positive (blue) and negative (red) magnetization direction of the Co electrode at different temperatures from 300 K to 75 K. (g-l) R_{SCC} obtained from the raw data in panels (a-f). (m-r) Antisymmetric component of the R_{SCC} curve. It corresponds to the contribution of s_x to SCC as detailed in Section 2.2.3.2. The amplitude of the signal is defined from the background to the minimum of the peak. (s-x) Symmetric component of the R_{SCC} curve. It corresponds to the contribution of s_y to the SCC as detailed in Section 2.2.3.2. The amplitude of the signal is defined from the background to the maximum of the peak.

5.7.3 Spin transport in the reference graphene channel and easy axis determination

The net \mathbf{j}_s reaching the graphene/MoTe₂ interface depends on different spin transport parameters: the spin polarization of the Co/graphene interface injector and detector (P_{inj} and P_{det} , respectively), the spin lifetime (τ_s^{gr}) and the spin diffusion coefficient (D_s^{gr}) of graphene. To quantify them, we performed standard Hanle precession measurements using the reference LSV as follows: first, by applying B_y , the initial state of the magnetization of the two Co electrodes are fixed either parallel or antiparallel to each other. Second, for each case, R_{NL} was measured by applying the external magnetic field along the out-of-plane hard axis (B_z). As explained in Section 2.1.2.1, B_z causes precession and decoherence of the spins, resulting in the oscillation and decay of the signal. In addition, the rotation of the Co magnetization with B_z tends to reach parallel magnetization along the z -direction at saturation magnetic fields. By combining the Hanle measurements for initial parallel (R_{NL}^P) and antiparallel (R_{NL}^{AP}) states of the Co electrodes (Fig. 5.10), the contribution from spin precession and decoherence, ΔR_{NL} , can be obtained [Fig. 5.11(a)]. The Hanle curve for the spin precession and decoherence is then fitted to the solution of the Bloch equation, Eq. 2.2. From this fitting, the τ_s^{gr} , D_s^{gr} and $P = \sqrt{P_{inj}P_{det}}$ values at each temperature are obtained [Fig. 5.11(b-d), respectively]. Note that P_{inj} and P_{det} cannot be obtained separately.

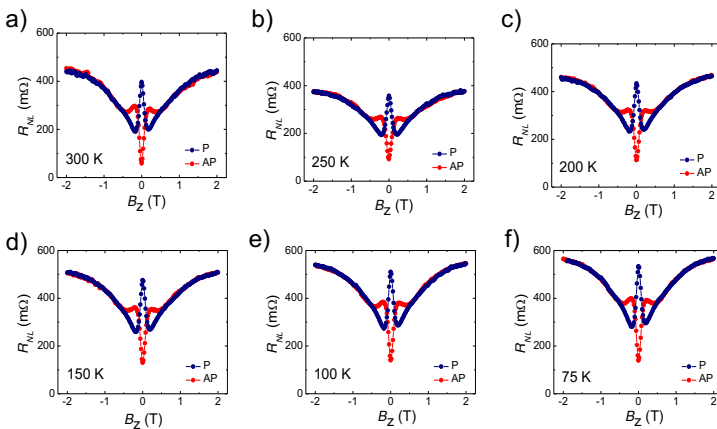


Figure 5.10: Hanle precession at the reference LSV by applying B_z . Blue (R_{NL}^P) and red (R_{NL}^{AP}) curves correspond to the initial parallel and antiparallel state of the Co electrodes, respectively. Measurements are performed at various temperatures (a) 300 K, (b) 250 K, (c) 200 K, (d) 150 K, (e) 100 K, and (f) 75 K.

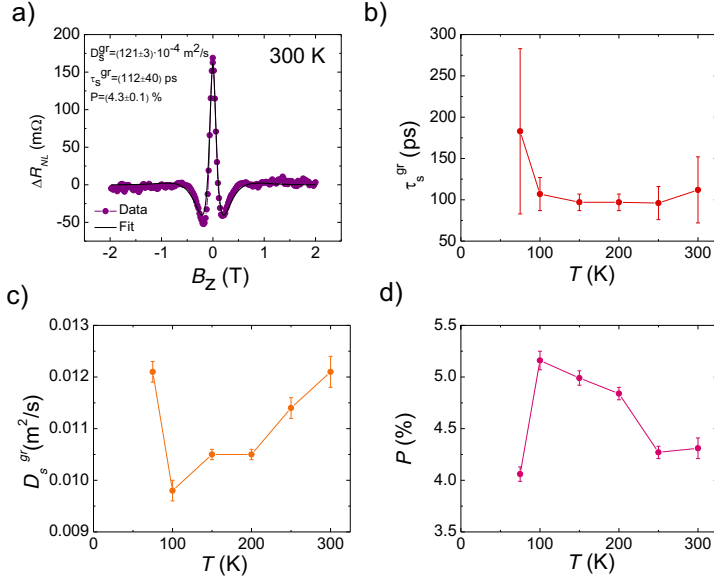


Figure 5.11: **Fittings from the Hanle precession at the reference LSV.** (a) The ΔR_{NL} vs. B_Z at 300 K, obtained from the experimental data in Fig. 5.10 (a) (purple solid circle) and the fitting of the data (black solid line) using the solutions of the Bloch equation, Eq. 2.2. (b) Spin lifetime of pristine graphene (τ_s^{gr}) for 300 K - 75 K temperature range. (c) Spin diffusion coefficient of pristine graphene (D_s^{gr}) for 300 K - 75 K temperature range. (d) Spin polarization of the graphene/Co interface for 300 K - 75 K temperature range.

Even though the magnetization of the ferromagnetic electrodes (with widths from 250 nm to 400 nm) should be dominated by the shape anisotropy, they could eventually present domains along the hard axis due to the magnetocrystalline anisotropy of Co and show hysteresis loops. Since B_x is applied perpendicular to the long direction of the FM electrodes (y -axis), the magnetization of Co is pulled towards the direction of the field an angle Θ . Based on the conventional Hanle precession data in the parallel and antiparallel configuration shown in Fig. 5.12(a), we can determine Θ for each value of the magnetic field. One of the terms of the Hanle precession data includes the signal due to non-precessing spins, parallel to the magnetic field, which has the same sign for R_{NL}^P and R_{NL}^{AP} and it is proportional to $\sin^2 \Theta$ (see Eq. 2.19). To obtain the data plotted in Fig. 5.12(b), we have normalized $0 < R_{NL}^P + R_{NL}^{AP} < 1$ and taken the arc-sine of its square root to obtain Θ as a function of the magnetic field. Based on the values of Θ at zero and low values of the magnetic field, we conclude that the easy axis of the magnetization is along the y -axis.

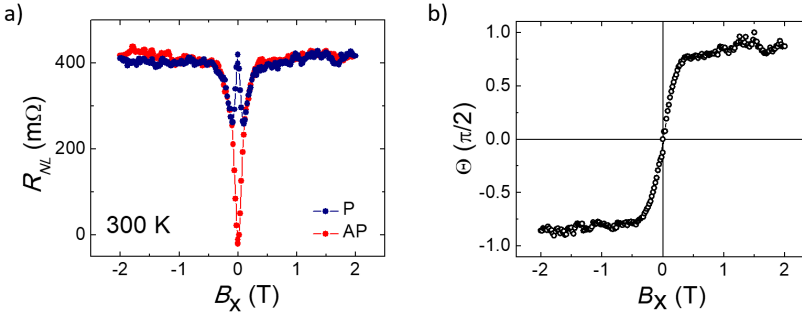


Figure 5.12: Hanle precession at the reference LSV by applying B_x . (a) Conventional Hanle precession measurement at 300 K in the parallel (blue curve) and antiparallel (red curve) states of the Co electrodes, while the magnetic field is swept along the in-plane hard axis (B_x). (b) Angle Θ between the Co magnetization and the easy axis extracted from the data in panel a.

5.7.4 Interface resistance between graphene and MoTe_2

When measuring the graphene/ MoTe_2 interface resistance by applying the charge current from contact 7 to contact 6 and picking up the voltage from 4 to 1 ($V_{41}I_{76}$, see Fig. 5.1) the values of the resistance measured at room temperature are negative. In this measurement configuration, it is important to simulate the interface resistance taking into account the graphene sheet resistance (R_{sq}^{gr}) [Fig. 5.13(a)], the resistivity of MoTe_2 (ρ_{MoTe_2}) [Fig. 5.13(b)], the measured interface resistance (R_{cross}) [Fig. 5.13(c)], and the geometrical parameters as width and thickness of graphene and MoTe_2 .

In order to obtain the interface resistance (R_{int}), the charge current distribution between the graphene channel and MoTe_2 has to be simulated with finite element method (FEM) [354, 355]. By introducing the experimental R_{sq}^{gr} , ρ_{MoTe_2} , and the geometrical dimensions in the FEM simulation, varying the interface resistance area product ($R_{int}A_{int}$), we can recover the measured value across the interface (R_{cross}) for a given value of $R_{int}A_{int}$. This is done for each temperature. When R_{int} is small enough, it can even lead to negative values of the measured R_{cross} , as we observe at room temperature [Fig. 5.13(c)]. From the FEM simulation, we also extract the shunting factor (χ_{shunt}) needed to properly quantify the spin-to-charge conversion signal (Eq. 2.21).

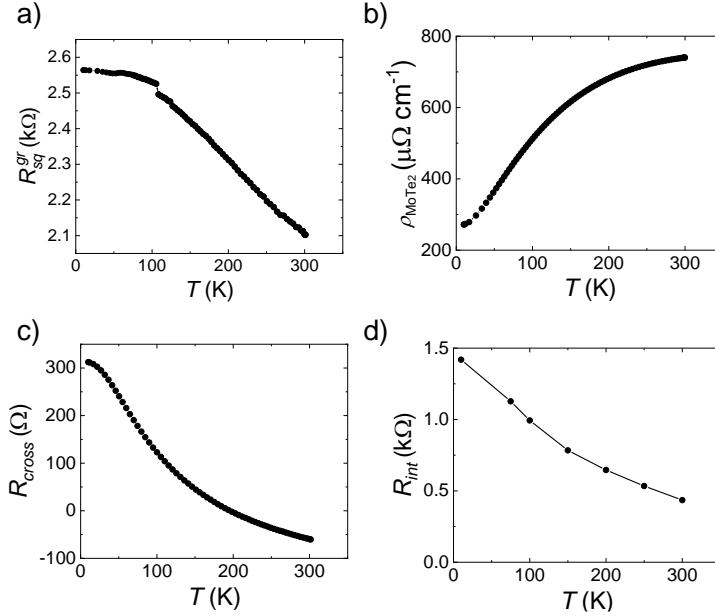


Figure 5.13: **Temperature dependence of sheet resistance of graphene, resistivity of MoTe₂, and graphene/MoTe₂ interface resistance.** (a) Sheet resistance (R_{sq}^{gr}) of the graphene flake in the same graphene/MoTe₂ LSV device, obtained from 4-point electrical measurement ($V_{23}I_{16}$). (b) Resistivity of MoTe₂ (ρ_{MoTe_2}) obtained from 2-point electrical measurement ($V_{74}I_{74}$) as a function of the temperature. If the material undergoes a phase transition from the 1T' to the 1T_d phase, a jump of the resistivity with an hysteretic behaviour around 240 K is expected [356]. In our case, this is not observed, evidencing that our MoTe₂ flake does not change phase in the range of temperatures we measure. The absence of transition has been reported by Stiehl and co-workers [202]. (c) Resistance (R_{cross}) obtained from 4-point electrical measurement across the graphene/MoTe₂ interface. (d) Simulated interface resistance using the data in panels a-c.

5.7.5 Quantification of the efficiency

In order to extract the SCC efficiencies of our device, because we cannot extract $\lambda_s^{MoTe_2}$ for our experiments, we fit the SCC signal obtained from the non-local resistance as a function of the out-of-plane magnetic field, to the model described in Section 2.3 (Eq. 2.24 and 2.25) for $1 \text{ nm} < \lambda_s^{MoTe_2} < 20 \text{ nm}$. To reduce the amount of fitting parameters, we fixed τ_s^{gr} and P_{inj} (assuming $P = P_{inj} = P_{det}$) to the values extracted from the reference Hanle fittings (Fig. 5.11) and released D_s^{gr} and θ_{ij}^α . Since the sign of P_{inj} is not known, the absolute sign of $\theta_{zy}^{x(y)}$ cannot be determined. In Fig. 5.14, we show the result from such a fit at room temperature for the antisymmetric (θ_{zy}^x) [Fig.

5.14(a)] and symmetric (θ_{zy}^y) [Fig. 5.14(b)] cases. In Fig. 5.14(c), we observe how, for $\lambda_s^{MoTe_2} < t_{MoTe_2}$, $\theta_{zy}^{x(y)}$ is inversely proportional to $\lambda_s^{MoTe_2}$ leading to constant $\theta_{zy}^{x(y)} \lambda_s^{MoTe_2}$ [see Fig. 5.14(d)]. In contrast, when $\lambda_s^{MoTe_2} \sim t_{MoTe_2}$, $\theta_{zy}^{x(y)}$ becomes independent of $\lambda_s^{MoTe_2}$ and $\theta_{zy}^{x(y)} \lambda_s^{MoTe_2}$ increases linearly. This occurs because $\bar{I}_{s_{x(y)}}$ in this range becomes almost independent of $\lambda_s^{MoTe_2}$. We have taken $\theta_{zy}^{x(y)}$ ($\lambda_s^{MoTe_2} = 20$ nm) as the lower limit for $\theta_{zy}^{x(y)}$ and $\theta_{zy}^{x(y)} \lambda_s^{MoTe_2}$ ($\lambda_s^{MoTe_2} = 1$ nm) as the lower limit for $\theta_{zy}^{x(y)} \lambda_s^{MoTe_2}$ for the results plotted in Fig. 5.4.

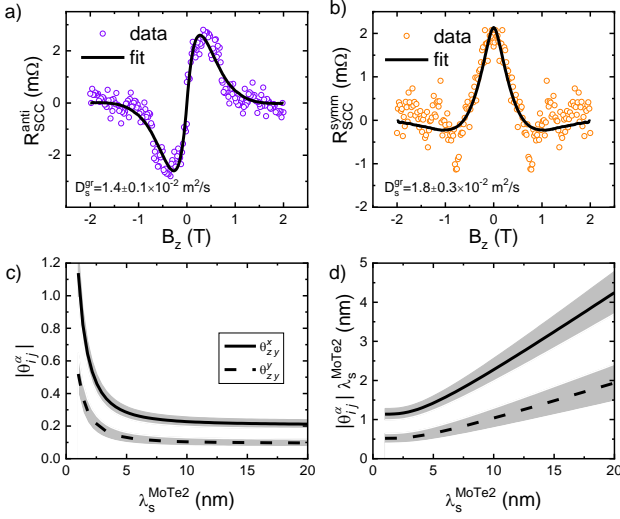


Figure 5.14: Analysis of the SCC data as a function of $\lambda_s^{MoTe_2}$ at 300 K. (a) Antisymmetrized and (b) symmetrized SCC signals corresponding to the s_x and s_y components of SCC, respectively, together with their fits to Eq. 2.24 and Eq. 2.25 respectively. (c) and (d) show $\theta_{zy}^{x(y)}$ and $\theta_{zy}^{x(y)} \lambda_s^{MoTe_2}$, respectively, as a function of $\lambda_s^{MoTe_2}$. The grey areas in (c) and (d) correspond to the uncertainties coming from the fittings errors.

5.7.6 Reproducibility

Although in Section 5.5 we focus on the results obtained in one device, we observed qualitatively similar SCC signals in another device (device 2, characterized in Fig. 5.15), showing the robustness of the unconventional SCC signals in our graphene/MoTe₂ van der Waals heterostructures (Fig. 5.16 and 5.17). A complete set of data could not be measured in this device, preventing us from quantifying the SCC efficiency in this case.

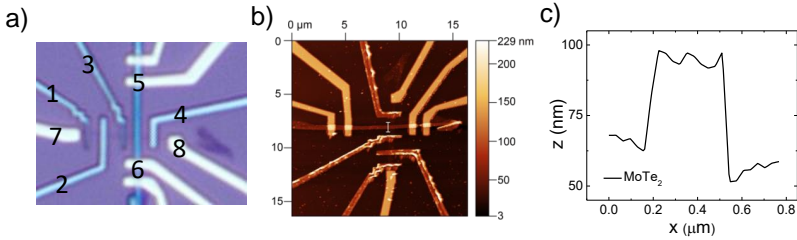


Figure 5.15: **Device 2 characterization.** (a) Optical image of device 2. (b) Area scan showing the topography of device 2 after the electrical measurement. (c) Line profile across the MoTe₂ flake along the marked line in panel b. The thickness of the MoTe₂ flake is 40 ± 5 nm.

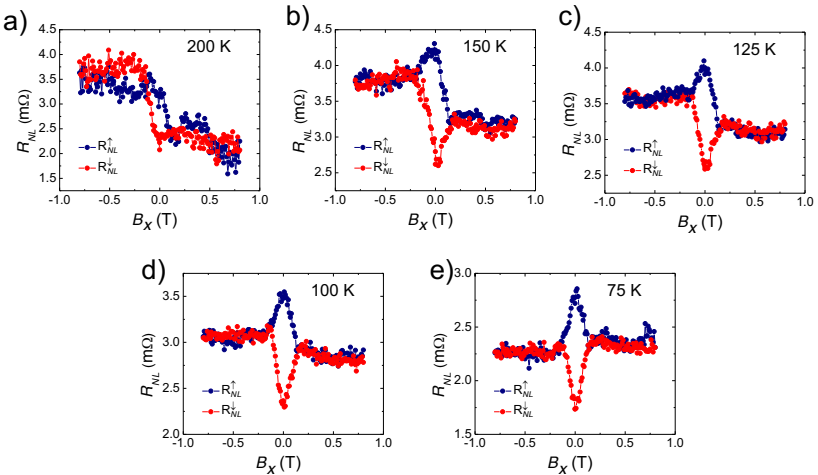


Figure 5.16: **Device 2 spin-to-charge conversion in MoTe₂ using graphene-based LSV with in-plane magnetic field along the hard axis of the Co electrode (B_x) at various temperatures.** Initial magnetization of the Co electrode saturated along positive (blue) and negative (red) y -direction at temperature (a) 200 K, (b) 150 K, (c) 125 K, (d) 100 K, and (e) 75 K. Above 200 K, the signal to noise ratio decrease so that no spin signal could be distinguished. These results are qualitatively similar to the measurement in device 1 (see Fig. 5.6).

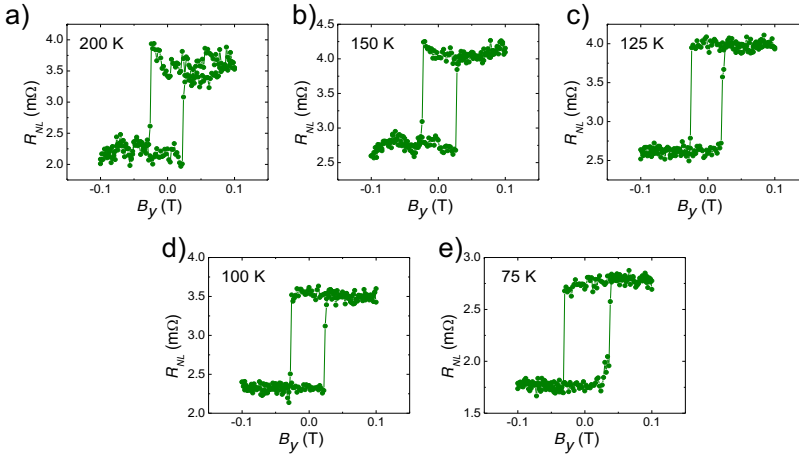


Figure 5.17: **Device 2 spin-to-charge conversion in MoTe₂ using graphene-based LSV with in-plane magnetic field along the easy axis of the Co electrode (B_y) at various temperatures.** At temperature (a) 200 K, (b) 150 K, (c) 125 K, (d) 100 K, and (e) 75 K. These results are qualitatively similar to the measurement in device 1 (see Fig. 5.8).

5.7.7 Spin injection from both sides of the MoTe₂ flake

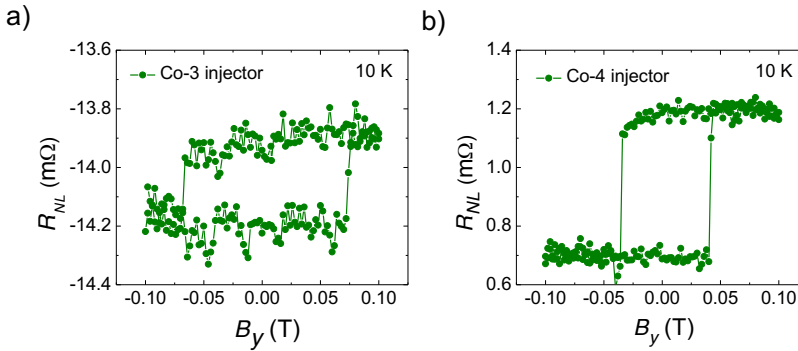


Figure 5.18: **Injection of the spin current from two Co electrodes with different coercive fields.** R_{NL} vs. B_y , in device 2, at 10 K using (a) Co contact 3 as injector of spin current ($V_{56}I_{37}$) and (b) Co contact 4 as the injector ($V_{56}I_{48}$). The switching of R_{NL} occurs at the coercive fields of the corresponding Co injector. The width of the Co contact 3 is narrower compared to that of Co contact 4. Due to shape anisotropy, the coercivity of Co contact 3 is larger than of Co contact 4.

5.7.8 Onsager reciprocity

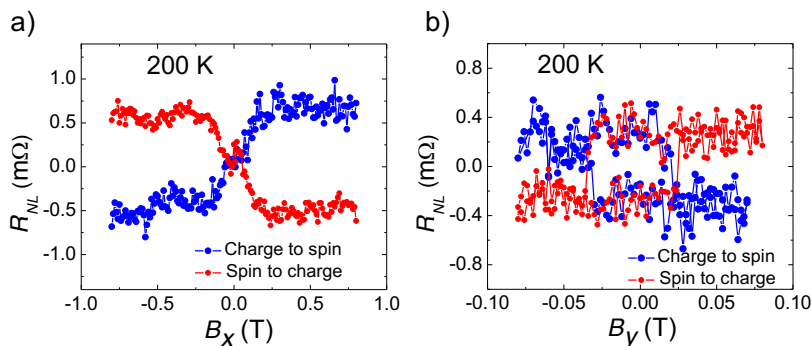


Figure 5.19: **Onsager reciprocity.** By swapping the current and the voltage terminals between Co and MoTe₂, in device 2, we measured the spin-to-charge (red, electrical configuration $V_{56}I_{48}$) and the charge-to-spin (blue, electrical configuration $V_{48}I_{56}$) processes. (a) The average of R_{NL}^{\uparrow} and R_{NL}^{\downarrow} vs. B_x measurement at 200 K. This signal corresponds to the s_x contribution to the SCC. (b) R_{NL} vs. B_y measurement at 200 K associated to the SCC from s_y . All these confirms the expected Onsager reciprocity for both s_x and s_y components of the SCC.

Chapter 6

Low-temperature spin-to-charge conversion in graphene/MoTe₂

6.1 Introduction

In the previous Chapter, SCC was studied in graphene/MoTe₂ from room temperature to a moderately high temperature (75 K). However, at lower temperatures, other SCC mechanisms might become relevant. That is the case for the SCC arising from the the proximity-induced spin-orbit interaction in graphene. As explained in Section 2.2.1.2, when a high-SOC material is placed in contact with graphene, forming a van der Waals heterostructure, the SOC in graphene can be enhanced by proximity. This effect is dominant at low temperatures [225,226] and, hence, expected to display below 75 K in graphene/MoTe₂ heterostructure. By using a graphene-based LSV combined with MoTe₂, the SCC due to each of the three possible orientations of the spin polarization can be studied in the same device, regardless of its origin. In this Chapter, we report an omnidirectional SCC in graphene/MoTe₂ at low temperature. Along with the SCC of in-plane spin polarizations (both s_x and s_y), already reported in Chapter 5, a new SCC arising from the out-of-plane spin polarization (s_z) is also observed. The origin of the latter is likely due to the proximity-induced SHE in graphene.

6.2 Spin-to-charge conversion by applying in-plane magnetic fields

In a single experiment, i.e., measuring the non-local voltage across the MoTe₂ when sweeping the magnetic field along the in-plane hard axis (B_x), the contributions to the SCC from the three spin polarizations (s_x , s_y and s_z) can be disentangled as detailed in Section 2.2.3.1. Initially, at zero magnetic field, the injected spins are polarized along the Co easy axis (y -direction). If they are converted into charge current, the non-local resistance will depend on the initial state of the Co magnetization, which is either along the $+y$ or the $-y$ direction [see Fig. 2.6(a)]. As long as B_x increases, the s_y component decays due to the spin precession in the $y-z$ -plane [see Fig. 2.6(c)]. From all this, the contribution to the SCC signal coming from s_y is symmetric with B_x and maximum at zero field [see Fig. 2.6(b)]. In a second stage, due also to precession in the $y-z$ -plane with increasing B_x field, s_z component increases, until it reaches its maximum at certain value of B_x , when the spins arriving to the SCC region are mostly aligned in the z -direction [see Fig. 2.6(c)]. Hence, the contribution to the SCC from s_z comes from precession and is described by an antisymmetric Hanle curve. This signal also depends on the initial state of the injector magnetization since it is determined by precession [see Fig. 2.6(d)]. In final stage, for large values of B_x , the magnetization of Co is aligned with the direction of the field and, hence, the injected spins are polarized along the x -direction and no precession occurs [see Fig. 2.6(e)]. Thus, the contribution to the SCC from s_x will show a linear variation at low fields with two saturation values at large magnetic field, S-shaped curve, taking opposite values at $+B_x$ and $-B_x$, and it will not depend on the initial state of the injector magnetization [see Fig. 2.6(f)].

The non-local resistance (R_{NL}) associated to SCC is measured when sweeping B_x for two different initial states of the Co magnetization. Initially, the magnetization is set along the $+y$ -direction [R_{NL}^\uparrow , blue curve in Fig. 6.1(a-c)] prior to each sweep of the field from 0 to 1 T and from 0 to -1 T. Lastly, the protocol is repeated but, in this case, the magnetization of the Co is initially set along the $-y$ -direction [R_{NL}^\downarrow , red curve in Fig. 6.1(a-c)]. This process is done for 50 K, 25 K and 10 K. The shape of the signal is different for each temperature, therefore, in order to extract the different contributions to the SCC signal, it is crucial to consider which ones depend on the initial state of the magnetization of Co electrode and which ones do not.

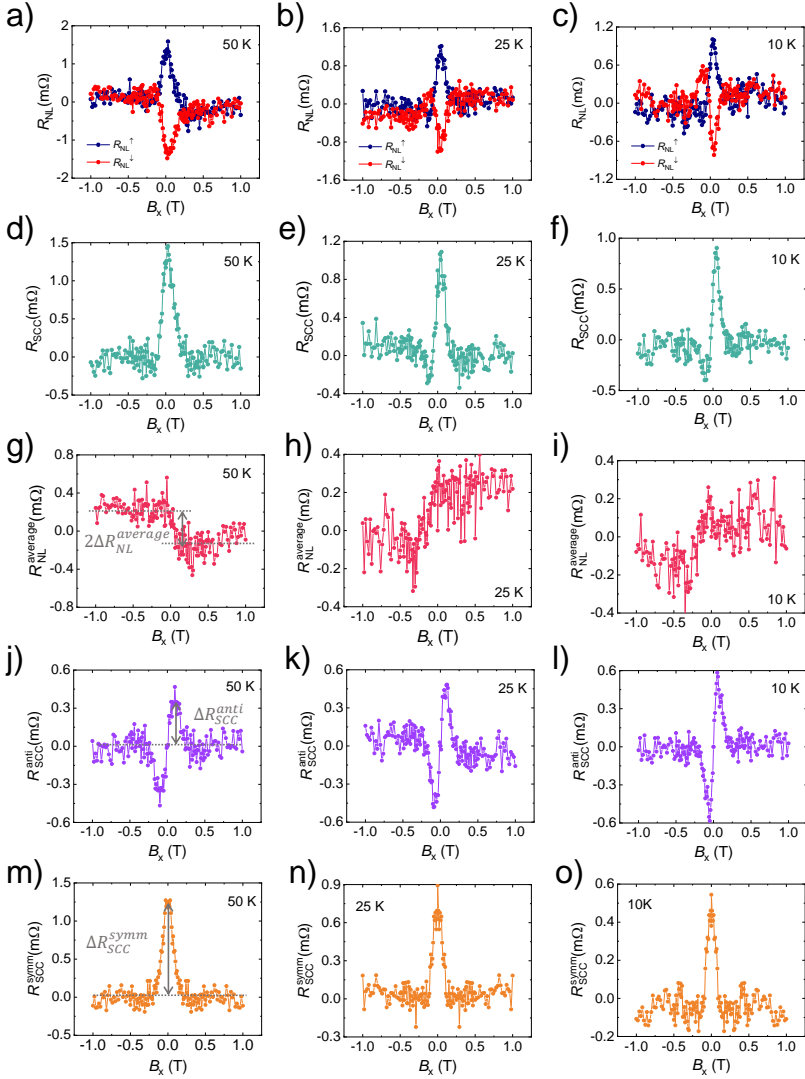


Figure 6.1: Spin-to-charge conversion in MoTe₂ using graphene-based LSV with in-plane magnetic field along the in-plane hard axis of the Co electrode (B_x) at low temperatures. (a-c) R_{NL} vs. B_x for the two different initial states of the Co magnetization, along the $+y$ - (blue) and $-y$ -direction (red). (d-f) The SCC signal defined as $R_{SCC} = (R_{NL}^{\uparrow} - R_{NL}^{\downarrow})/2$ obtained from data in panels a-c. (g-i) The average non-local resistance, defined as $R_{NL}^{average} = (R_{NL}^{\uparrow} + R_{NL}^{\downarrow})/2$ obtained from data in panels a-c. (j-l) Antisymmetric component of the R_{SCC} obtained from data in panels a-c. (m-o) Symmetric component of the R_{SCC} obtained from data in panels a-c. All the data is shown at 50 K, 25 K, and 10 K.

On the one hand, the contribution of s_y clearly depends on the initial state of the magnetization, since it is determined by the conversion of $+s_y$ or $-s_y$ spins [see Fig. 2.6(b)]. Moreover, the contribution of s_z will also depend on the initial state of the magnetization since it comes from the spin precession, which is determined by the polarization of the injected spins [see Fig. 2.6(d)]. Therefore, both contributions are included in the calculated R_{SCC} signal with $R_{SCC} = (R_{NL}^\uparrow - R_{NL}^\downarrow)/2$. While the s_y contribution is symmetric with respect to B_x , the contribution of s_z is an antisymmetric Hanle as a function of B_x . This difference allows us to establish an univocal relation between the SCC from s_y (s_z) and R_{SCC}^{symm} (R_{SCC}^{anti}).

On the other hand, the contribution of s_x does not depend on the initial state of the magnetization, since it occurs at large magnetic fields, when the magnetization of the Co is pulled in the direction of the field [see Fig. 2.6(f)]. In order to remove any signal that depends on the initial state of the magnetization, the average of R_{NL}^\uparrow and R_{NL}^\downarrow is extracted $R_{NL}^{average} = (R_{NL}^\uparrow + R_{NL}^\downarrow)/2$.

Taking a closer look to $R_{NL}^{average}$, the signals measured at all temperatures display two saturating states above the saturation field of Co [Fig. 6.1(g-i)]. This signal is associated to the SCC from s_x spins, as it was proven at higher temperatures via precession with B_z . Interestingly, R_{SCC}^{anti} shows an antisymmetric Hanle curve for the three low temperatures [Fig. 6.1(j-l)]. These signals evidence the SCC from s_z spins, which has not been observed at higher temperatures. Additionally, R_{SCC}^{symm} shows a maximum at zero field and decays at the saturation B_x field [Fig. 6.1(m-o)]. This signal is associated to the SCC from s_y spins, as it was proven at higher temperatures via precession with B_z .

Furthermore, if the magnetic field is swept along the in-plane easy axis direction, the direction of the magnetization is reversed at certain value of B_y . By measuring R_{NL} while sweeping B_y , a square hysteresis loop is observed (Fig. 6.2) with a switching sign at the coercive field of the Co electrode. This signal corresponds to the SCC from s_y spins. The same behaviour was also observed at higher temperatures (see Fig. 5.8).

It is important to note that the signals from Fig. 6.1 are measured as a function of the in-plane hard axis magnetic field (B_x) and, then, only the s_z contribution arises from precession. The dependence of R_{SCC}^{symm} with B_x is not a symmetric Hanle curve, since the SCC from s_y spins is determined by the pulling of the Co magnetization, not by precession, as demonstrated in Section 5.7.3. The SCC signal from s_x arises also from the pulling of the

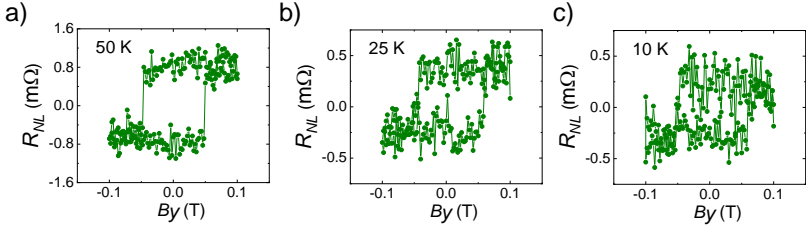


Figure 6.2: Spin-to-charge conversion in MoTe₂ using graphene-based LSV with in-plane magnetic field applied along the easy axis of the Co electrode (B_y) at low temperatures. R_{NL} vs. B_y , for (a) 50 K, (b) 25 K, and (c) 10 K.

Co magnetization, thus no precession occur either. In order to prove the spin origin of the s_x and s_y SCC signals, spin precession measurements should be done by applying out-of-plane fields (B_z). However, at low temperatures, large backgrounds coming from magnetoresistances of MoTe₂ and/or graphene (see Section 4.4) prevented us from measuring clear signals (see Section 6.5.1). Such precession measurements were done at higher temperatures, confirming the SCC from s_x and s_y (see Section 5.9). Since the temperature evolution of s_x and s_y , extracted from their dependence with B_x at higher temperatures (see Fig. 5.7), matches with the one extracted at low temperatures (Fig. 6.3), we can infer the spin origin of $R_{NL}^{average}$ and R_{SCC}^{symm} signals. Most importantly in this Chapter, the SCC signal related to s_z arises from spin precession and, consequently, its spin origin is also confirmed.

6.3 Unveiling the origin of each spin-to-charge conversion contribution

The evolution with temperature for each component of the total SCC signal is represented in Fig. 6.3. The solid circles corresponds to the amplitude at lower temperatures extracted from Fig. 6.1, and the open squares correspond to the amplitudes at higher temperatures, extracted from Fig. 5.7. If we focus only on the results at low temperature (inset in Fig. 6.3), the red circles represent $\Delta R_{NL}^{average}$ and shows a sign change when lowering the temperature. Whereas at 50 K and higher temperatures the amplitude is negative, at 25 K and 10 K it is positive. The sign change can be attributed to a competition of different effects with opposite sign in the efficiencies. While at higher temperatures it was considered to come from the conventional SHE in the bulk of MoTe₂, where

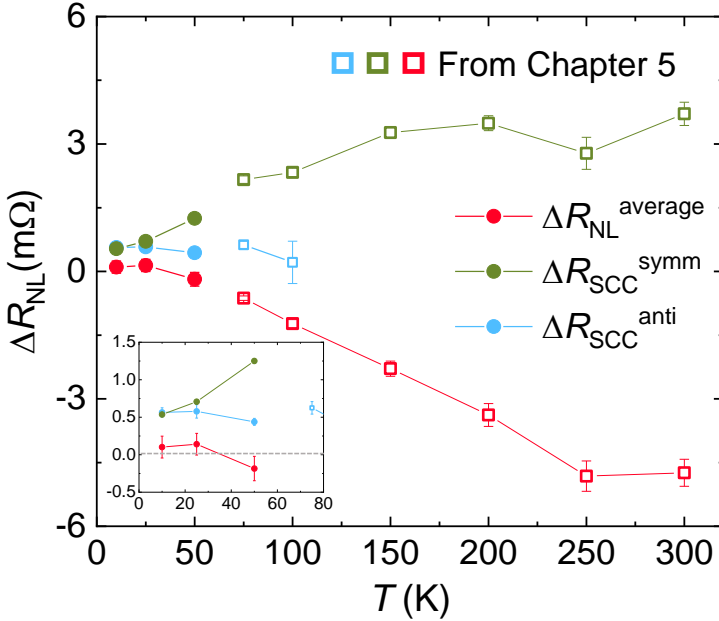


Figure 6.3: **Temperature dependence of the amplitude of the signal** The low temperature amplitude data, represented by dots, are extracted from Fig. 6.1. The high temperature data, represented by squares, are extracted from Fig. 5.7. The signal $R_{NL}^{average}$ is the contribution of s_x to the SCC, R_{SCC}^{symm} is the contribution of s_z , and R_{SCC}^{anti} is the contribution of s_y . The inset is a zoom at low temperature. The dashed lined is a guide for the eyes at zero amplitude.

the charge current, spin current and spin polarizations are mutually orthogonal; the conventional EE at the proximitized graphene will also induce SCC from s_x (see Fig. 6.4). At low temperatures, the proximity-induced EE in graphene tends to be large [225]. Therefore, the efficiency of the EE in proximitized graphene can overcome the bulk SHE in MoTe_2 and change the sign of the overall detected signal (see Section 6.5.4 for reproducibility of this effect).

Likewise, ΔR_{SCC}^{symm} (green solid circles in Fig. 6.3) decreases with decreasing the temperature, although no sign change is observed. This tendency is also seen when the magnetic field is swept along the y -direction, where the amplitude of the respective hysteresis loop decreases with the temperature and becomes barely visible at 10 K [Fig. 6.2(c)]. In order to observe this signal, the symmetries of the system have to be reduced. It can be attributed to an unconventional SHE in MoTe_2 , the crystal symmetries of MoTe_2 must be broken (represented by the zigzag lines in Fig. 6.4), or to an unconventional EE in the

proximitized graphene (see Section 2.2.2.2 for a thorough discussion). The latter origin has been recently taken into consideration since the shear strain needed to break the MoTe₂ crystal symmetries in MoTe₂ is expected to be sample-dependent [357], and this signal has been observed in several graphene/MoTe₂ heterostructures we have measured. Moreover, the misalignment between the mirror planes of graphene and MoTe₂ creates a non-symmetric interface, which enables the unconventional EE mechanism in proximitized graphene, in which the spin polarization and charge current direction are parallel [346, 347]. This scenario is represented in Fig. 6.4, where the zigzag lines in the proximitized area represent a non-symmetric interface.

Interestingly, the new component observed at low temperatures, coming from the SCC from s_z spins, presents its largest value at 10 K and it slightly decreases with increasing temperature. Two possible origins can generate out-of-plane spin polarization: non-orthogonal SHE in MoTe₂, where the spin polarization is parallel to the spin current direction and it is allowed by the crystal symmetries ($\mathbf{j}_s \parallel \mathbf{s} \perp \mathbf{j}_c$) corresponding to σ_{zy}^z , and the conventional SHE in proximitized graphene ($\mathbf{j}_s \perp \mathbf{s} \perp \mathbf{j}_c$) (see Fig. 6.4).

In order to check whether this effect comes from the proximity-induced SHE in graphene or via non-orthogonal SHE in MoTe₂, a control experiment can be performed. By injecting the spins into the graphene channel using the Co electrodes on both sides of MoTe₂ (using electrodes 3 and 4 in Fig. 5.1), the spin current direction in graphene is reversed. If the SCC origin is SHE in proximitized graphene, since the direction of the spin current is reversed while the polarization is kept, the direction of the charge current will reverse as well in order to fulfill Eq. 1.18. The antisymmetric Hanle curve, R_{SCC}^{anti} , will then reverse. If such sign change is not observed, R_{SCC}^{anti} must arise from the σ_{zy}^z element in bulk MoTe₂, because the spin current will not change the direction along z when absorbed into the MoTe₂ when changing the Co injector side. Unfortunately, such experiment could not be performed in this device. The non-orthogonal SHE in MoTe₂ has been reported before, but, the efficiency is ~ 8 times smaller than the conventional SCC where the spin polarization is along x (the one related to $\Delta R_{NL}^{average}$) [202].

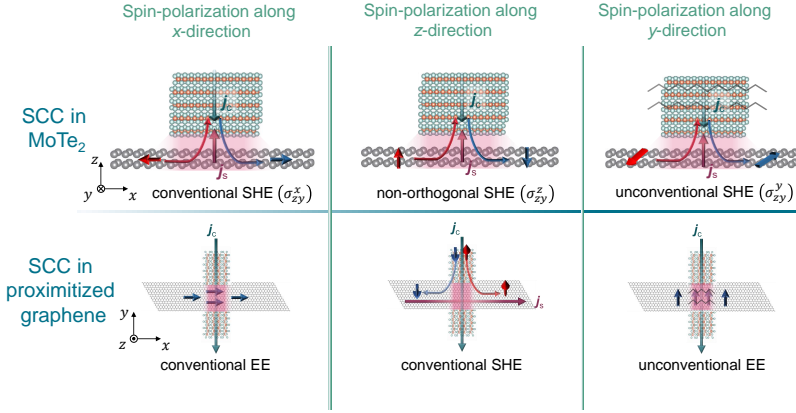


Figure 6.4: **Summary of spin-to-charge conversion contributions that can occur in graphene/MoTe₂ van der Waals heterostructure.** In graphene/MoTe₂ heterostructures, the SCC processes can take place at the bulk of the MoTe₂ flake or at the proximitized graphene region, which is represented by the pink halo. For a fixed direction of the charge current, y -direction, three different spin polarization can be induced. A spin polarization along the x -direction can stem from conventional SHE in MoTe₂, where $\mathbf{j}_c \perp \mathbf{j}_s \perp \mathbf{s}$, or to a conventional REE in the proximitized graphene where $\mathbf{j}_c \perp \mathbf{s}$. Additionally, a spin polarization along the z -direction can be attributed to a non-orthogonal SHE in MoTe₂, allowed by the 1T' crystal symmetry, where $\mathbf{j}_c \perp \mathbf{j}_s \parallel \mathbf{s}$, or to a conventional SHE in proximitized graphene where $\mathbf{j}_c \perp \mathbf{j}_s \perp \mathbf{s}$. Finally, spin polarization along the y -direction can be induced if the mirror symmetry of 1T'-MoTe₂ or the ones of graphene/MoTe₂ interface are broken (represented by the zigzag line). In that case, s_y polarization can be induced via unconventional SHE in MoTe₂, where $\mathbf{j}_c \parallel \mathbf{j}_s \perp \mathbf{s}$, or via unconventional EE in proximitized graphene, where $\mathbf{j}_c \parallel \mathbf{s}$.

6.4 Conclusion

In conclusion, we report omnidirectional SCC in graphene/MoTe₂ van der Waals heterostructure at low temperatures. Along with an in-plane SCC from both spin polarizations (s_x and s_y), an out-of-plane SCC from s_z spin polarization is also observed at low temperatures. As temperature decreases, the strength of the proximity effect increases, thus, the SCC from s_z spins is likely due to proximity-induced SHE in graphene, as it is only observed at very low temperatures. However, another effect can also lead to such SCC, a non-orthogonal SHE in MoTe₂, which is allowed due to the reduced crystal symmetry of 1T'-MoTe₂. The in-plane SCC from s_x is attributed to a combination of orthogonal SHE in MoTe₂ and EE in proximitized graphene. Both

effects, allowed by crystal symmetries, might have opposite sign in the efficiencies. This would explain the change in the sign of the SCC signal associated at s_x at low temperatures. The unconventional SCC from s_y spins requires the symmetries of MoTe₂ to be broken, if the effect occurs at the bulk of MoTe₂, or to have absence of symmetries at the interface between graphene and MoTe₂, if the origin is unconventional EE in the proximitized graphene. All the possibilities are summarized in Figure 6.4. Overall, the results presented in Chapter 5 and 6 make graphene/MoTe₂ a fascinating heterostructure where a plethora of SCC processes from different origins can be present. Although our results unveil a rich variety of possibilities, further studies in order to disentangle the exact origin of each SCC will be required.

6.5 Appendices

6.5.1 Spin-to-charge conversion by applying out-of-plane magnetic field

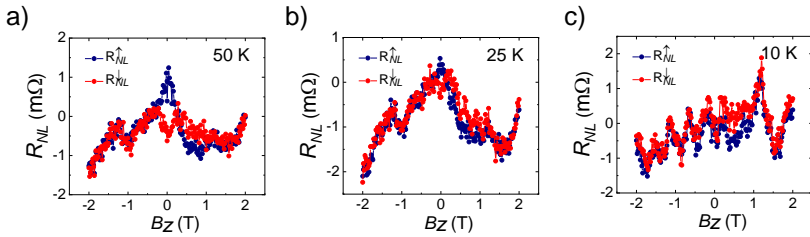


Figure 6.5: **Spin-to-charge conversion in MoTe₂ using graphene-based LSV with out-of-plane magnetic field (B_z) at low temperatures.** The non-local resistance is measured for both initial positive (blue) and negative (red) magnetization directions of the Co electrode for (a) 50 K, (b) 25 K, and (c) 10 K. Strong backgrounds prevent the observation of spin precession.

By applying B_x , a spin precession in the x – y -plane is induced. It discerns the signals arising from s_x and s_y spins from the ones whose origin comes from spurious effects. Nevertheless, the precession with B_z observed at higher temperatures (Fig. 5.9) make us confident that the signals extracted from R_{NL} vs. B_x (Fig. 6.1) and vs. B_y (Fig. 6.2) arise from s_x and s_y spins.

6.5.2 Spin transport in the reference graphene channel

Hanle spin precession transport in a reference LSV with pristine graphene was also measured at lower temperatures. It is noticeable the oscillations in the signals at large values of the out-of-plane magnetic field, being more evident at 10 K. Such oscillations are attributed to a magnetoresistance of graphene, which is dominant at low temperatures, but whose origin has not been elucidated.

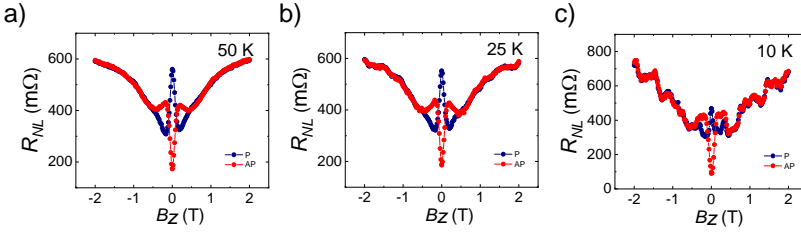


Figure 6.6: Measurement of the Hanle precession at the reference LSV by applying B_z at low temperatures. Initial magnetization of the Co electrode saturated along positive (blue) and negative (red) y -direction at temperature (a) 50 K, (b) 25 K, and (c) 10 K.

6.5.3 Temperature dependence of the interface resistance, MoTe_2 resistivity, and graphene sheet resistance

In order to have a full picture, the resistivity of the MoTe_2 flake, measured in two-points ($V_{74}I_{74}$), the sheet resistance of graphene ($V_{23}I_{16}$) and the calculated interface resistance from the measured cross resistance, are shown in Fig. 5.13. At 10 K, MoTe_2 has one third of the resistivity at room temperatures. In contrast, the graphene sheet resistance and the interface resistance present higher values at 10 K than at room temperature.

6.5.4 Reproducibility

In Chapter 5, another device (device 2) showed qualitatively the same results at temperatures above 75 K (Section 5.7.6). However, the behaviour at low temperatures of device 2 does not display SCC from s_z spins within the resolution of our measurements. Nevertheless, it shows a sign change in $R_{NL}^{average}$ when lowering the temperature between 100 K and 75 K as reported in Fig. 5.16, supporting the possibility of coexistence of conventional EE in proximitized graphene and conventional SHE in MoTe_2 for the SCC from s_x with

opposite sign.

In Fig. 6.7(a-d), the non-local resistance as a function of the in-plane magnetic field along the hard axis of the Co electrode (B_x) is shown for 75 K, 50 K, 25 K, and 10 K, respectively. At 75 K and 50 K, the signal depends on the initial state of the magnetization, i.e., R_{NL}^\uparrow and R_{NL}^\downarrow take different values at low B_x . However, for 25 K and 10 K, there is no dependence on the initial state of the magnetization.

Interestingly, the average signal [Fig. 6.7(e-f)] shows spin-to-charge conversion from s_x at all the low temperatures and it has opposite sign to the one measured at higher temperatures (see Fig. 5.16). This supports the assumption of opposite signs in the efficiencies of EE effect in proximitized graphene and conventional SHE in MoTe₂.

The absence of dependence on the initial state of the magnetization at 25 K and 10 K means that there is no SCC from s_y nor s_z , since both signals come from such dependence and, thus, R_{SCC}^{symm} and R_{SCC}^{anti} at 25 K and 10 K do not show any signal [Fig. 6.7(h,i,k,l)]. In contrast, at 50 K, R_{SCC}^{symm} [Fig. 6.7(g)] displays signal coming from the SCC from s_y spins and R_{SCC}^{anti} seems to show an antisymmetric Hanle coming from SCC from s_z spins [Fig. 6.7(j)]. Since the background of R_{SCC}^{anti} at 50 K, is different from both saturating fields, and it is the only temperature displaying such behavior, this signal cannot be surely attributed to spin-to-charge conversion. Moreover, the respective signal is also represented at 75 K, and any spin-related signal is observed in R_{SCC}^{anti} .

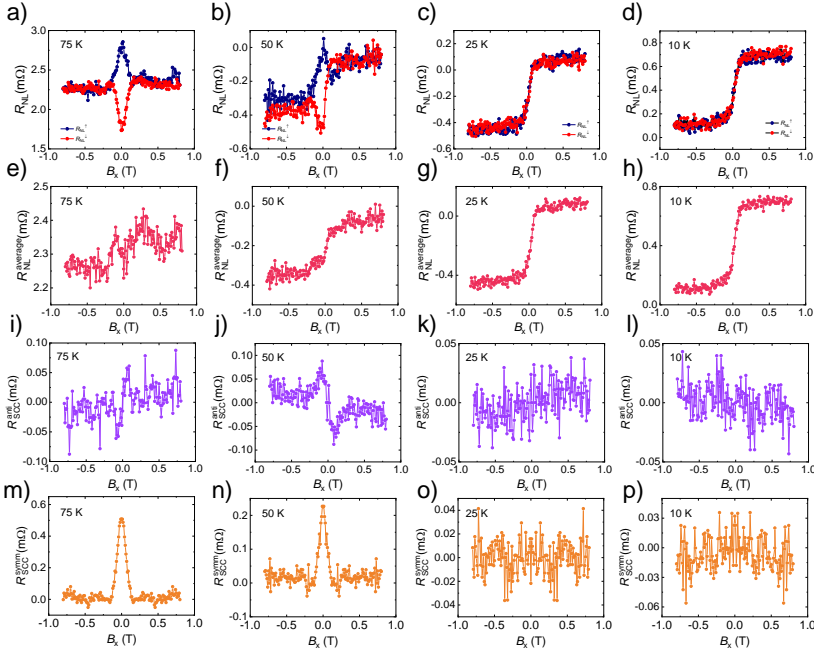


Figure 6.7: Device 2 spin-to-charge conversion in MoTe₂ using graphene-based LSV with in-plane magnetic field along the in-plane hard axis of the Co electrode (B_x) at low temperatures. (a-d) R_{NL} vs. B_x for the two different initial states of the Co magnetization, along the $+y$ - (blue) and $-y$ -direction (red). (e-h) The average non-local resistance, defined as $R_{NL}^{average} = (R_{NL}^{\uparrow} + R_{NL}^{\downarrow})/2$ obtained from data in panels a-d. i-l) Antisymmetric component of the R_{SCC} obtained from data in panels a-d. (m-o) Symmetric component of the R_{SCC} obtained from data in panels a-d. All the data is shown at 75 K, 50 K, 25 K, and 10 K.

In literature, it has been reported the need of the annealing process to enhance the spin-orbit proximity (see Section S10 from the supplementary information of Ref. [224]). However, in our samples, we do not perform any annealing since the crystal phase of MoTe₂ is sensitive to the temperature and phase transitions can be induced [358, 359]. Since the proximity is not enhanced via annealing, it might add variability in our samples, preventing the observation of the spin-orbit proximity in certain graphene/MoTe₂ heterostructures.

Chapter 7

Spin-to-charge conversion in a high-quality interface graphene/MoTe₂ van der Waals heterostructure

7

7.1 Introduction

In Chapters 5 and 6, 1T'-MoTe₂ has been studied as a SCC material using graphene-based LSVs. Besides, results from SOT experiments using MoTe₂ can also be found in literature [202, 282]. While in a non-local configuration using LSVs any artefact induced by the local charge current is avoided, the charge current is limited to one direction in the SOC material. Thus, certain components of the spin Hall conductivity tensor remain unexplored. In the basis of non-local LSVs, a versatile device geometry is required to study unexplored SCC components. Recently, a new measurement geometry, where the charge current propagates in the three different spatial directions, was implemented, leading to the observation of different SCC components in graphene/BiTeBr [296] and graphene/WTe₂ [233] heterostructures. In these studies, the charge current was applied between the high-SOC material and the graphene channel. These experiments, however, only gave a measurable signal when the interface resistance

was high enough and the spin absorption into the high-SOC material was suppressed, implying that the simultaneous detection of SCC in the standard and the new “3D-current” configuration could not be achieved.

In this Chapter, we combine the standard SCC measurement geometry [Fig. 7.1(a)], with the recently introduced 3D-current configuration [Fig. 7.1(b)], in order to characterize SCC in a graphene/MoTe₂ van der Waals heterostructure. The high-quality interface between graphene and MoTe₂, indicated by a low interface resistance, allows us to measure for the first time SCC both in the standard and 3D-current configurations in the same device, at room temperature. By combining these configurations, we discover that spin generation occurs when a charge current flows through the MoTe₂ flake in any of its two in-plane directions, gaining deeper insights into the multiple SCC process in graphene/MoTe₂. Whereas the unconventional SCC component from s_y spins parallel to the charge current direction (y -direction) has been measured before, as shown in Chapter 5 and 6, a new orthogonal component, in which a charge current along the mirror plane (x -direction) generates a spin current with in-plane orthogonal polarization (s_y), is measured here for the first time. The origin of the latter contribution is compatible with SHE in MoTe₂ or EE in the proximitized graphene. The large SCC signals measured at room temperature, together with the versatility in the 3D-current configurations, makes high-quality interface MoTe₂/graphene heterostructure an ideal candidate to be integrated in functional 2D spintronic devices.

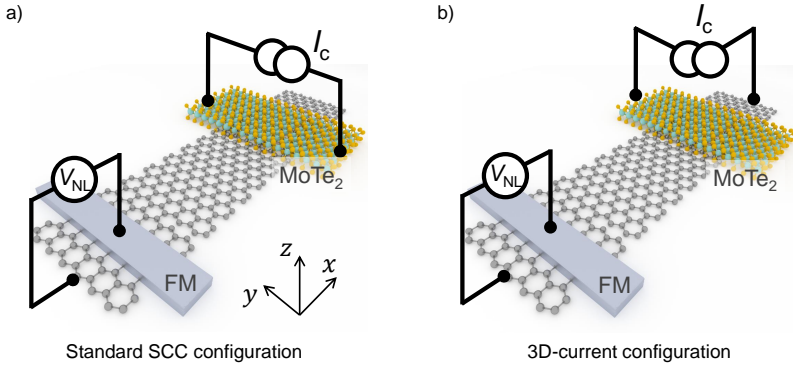


Figure 7.1: **Sketches of the two different SCC configurations in a graphene-based LSV in combination with MoTe₂.** (a) Sketch of the standard SCC configuration. Due to Onsager reciprocity, this configuration is reciprocal to the one sketched in Fig. 2.5, where the voltage and current probes are swapped between the two configurations. The direction of the charge current is limited to the y -direction. The non-local voltage (V_{NL}) is detected using a FM electrode. (b) Sketch of the 3D-current configuration. In this case, the charge current is applied between one side of the MoTe₂ flake and one end of the graphene flake, thus, the charge current flows in the three spatial directions within the MoTe₂ flake. The non-local voltage (V_{NL}) is also detected using a FM electrode.

7.2 Device fabrication and characterization

For the fabrication of the LSV device used here [see Fig. 7.2(a)], MoTe₂, that tends to cleave along the Mo-chain (details in Chapter 4), was mechanically exfoliated in an inert atmosphere and stamped on top of a few-layer exfoliated graphene flake using the dry-viscoelastic technique [302]. In this way, MoTe₂ is not exposed to air preventing oxidation and keeping a clean interface between MoTe₂ and graphene. After the stamping, metallic Ti/Au electrodes contacting MoTe₂ and graphene were fabricated via e-beam lithography, thermal evaporation, and lift-off [labeled with letters in Fig. 7.2(a)]. Subsequently, FM electrodes (TiO_x/Co) were fabricated, using the same techniques, on top of graphene [labeled with numbers in Fig. 7.2(a)]. To characterize the MoTe₂ flake, we have measured its resistance (R) by applying a current between contacts A and B (I_{AB}) and measuring the voltage between the same electrodes (V_{AB}), $V_{AB}I_{AB}$. As shown in Fig. 7.2(b), the resistance of the MoTe₂ flake ($R_{AB} = V_{AB}/I_{AB}$) has a temperature dependence compatible with a semimetallic behavior [190], showing no fingerprint of a phase transition [190] otherwise reported for the bulk material [193] (further details can be

found in Chapter 4). The quality of the interface can be inferred by measuring the interface resistance between graphene and MoTe₂. By applying a charge current between one side of MoTe₂ and graphene, and measuring the voltage between the other two metallic electrodes ($V_{AC}I_{BD}$), the interface resistance ($R_{int} = V_{AC}/I_{BD}$) is probed. As displayed in Fig. 7.2(b), R_{int} shows even negative resistance values at room temperature and increases up to $\sim 100 \Omega$ at 10 K, smaller than graphene square resistance. The low values of R_{int} are required for the spin absorption, as proven in Chapter 5.

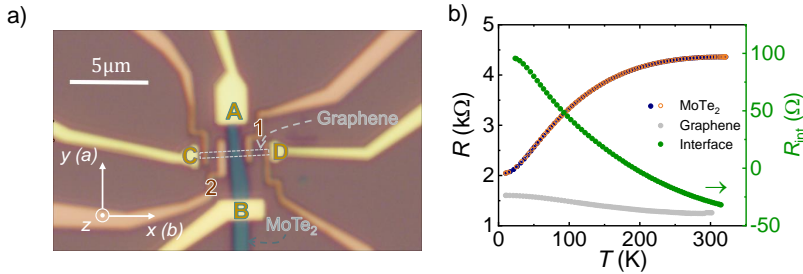


Figure 7.2: Optical image of the MoTe₂/graphene heterostructure and electrical characterization. (a) Optical image of the device. The barely visible narrow graphene flake along x , highlighted by the dashed rectangle, is under the MoTe₂ flake, in blue. The Ti/Au (yellow) electrodes are labeled with letters and the FM TiO₂/Co electrodes (orange) with numbers. The relation between the crystal axes and the space coordinates is as follows: $b = x$ and $a = y$. (b) 2-point resistance as a function of the temperature of the MoTe₂ flake when cooling down (orange open circles) and warming up (blue solid circles). 4-point resistance of the few-layer graphene flake as a function of temperature is also shown (grey circles). The red circles correspond to the interface resistance between graphene and MoTe₂, measured in the $V_{AC}I_{BD}$ configuration.

7.3 Spin-to-charge conversion measurements

Most of the SCC experiments based on spin-orbit proximity place a semiconducting high-SOC van der Waals material on top of graphene which then has to be shaped to be used as an electrode for the proximitized region [225–228, 232]. However, if graphene is combined with a conducting (metallic or semimetallic) van der Waals material, SCC can be measured by directly probing the voltage across both materials. In this case, disentangling the origin of each SCC process remains challenging as SCC can either occur in the proximitized graphene via EE or SHE, and in the high-SOC material itself via the bulk SHE or bulk EE (as discussed in Section 2.2). The standard SCC configuration [Fig. 7.1(a)] in the

reciprocal fashion, meaning that the charge and voltage probes are swapped, is the one used in Chapter 5 and 6. Based on the Onsager reciprocity, both standard configurations lead to the observation of the same SCC results. In the standard configuration the charge current and the spin current are fixed to one direction (y - and z -directions, respectively), while the spin polarization direction is controlled by an external magnetic field. This configuration fails to capture other SCC where the charge current lies along other directions. To further study the SCC in the graphene/MoTe₂ heterostructure, the 3D-current configuration [Fig. 7.1(b)] is employed. In this case, the spin current and the spin polarization will be fixed along the z - and y -directions, respectively, while the charge current direction within the MoTe₂ can be set along the three different directions (x , y , z). The versatility of the 3D-current configuration allows us to directly relate the direction of the charge current with the spin current direction and polarization.

7.3.1 SCC in the standard configuration

We first study SCC by applying the charge current along the MoTe₂ flake [i.e., $\mathbf{I}_c(0, -y, 0)$] while sweeping the magnetic field along the FM easy axis (B_y), using the configurations shown Fig. 7.3(a). The non-local resistance dependence with B_y shows a hysteresis loop with two clear jumps at the switching field of the FM when using contact 2 (left) as a detector [Fig. 7.3(b)]. When B_y is positive (negative), R_{NL} takes its lower (higher) value. Hence, the injected spins are polarized along the $-y$ direction. Note that we have assumed that the graphene/FM contact spin polarization is positive. We keep this convention through all the Chapter. Therefore, we can conclude that s_y spins are generated by applying I_c along the same direction in the MoTe₂ flake. Three possible mechanisms could be behind this spin generation: (i) EE in the proximitized graphene, (ii) SHE in MoTe₂ with spin current along the z -direction, or (iii) SHE in MoTe₂ with spin current along the x -direction. Due to the symmetries of the EE mechanism in the proximitized graphene, a spin accumulation polarized along $-y$ must be generated by a perpendicular charge current (x - or z -direction). However, in this case, the charge current and the spin polarization are parallel, which is forbidden by the crystal symmetry of the proximitized graphene. If we consider SHE in MoTe₂, the only allowed component where the spin polarization and the charge current are parallel is the one where the spin current is also parallel, σ_{yy}^y (see Section 2.2 for the symmetries consideration).

Considering the sample layout, the spin current could only be generated along the x or z -directions, as both SHE components are forbidden by the MoTe₂ crystal symmetries (σ_{xy}^y or σ_{zy}^y , respectively), the considered possible processes are not granted by the crystal symmetries.

To know the direction of the spin current, R_{NL} is measured using contact 1 as a detector (right) while the magnetic field is swept along the FM easy axis as represented in Fig. 7.3(c). The measurement shows the same sign as the one detected on the left side. The absence of a sign reversal further proves that the spin current along the x -direction can be disregarded. Accordingly, two mechanisms remain as possible origins of the signal: (i) unconventional SHE in MoTe₂ with spin current along the z -direction (σ_{zy}^y), or (ii) unconventional EE in the proximitized graphene where the spin polarization and charge current are parallel. Both scenarios are incompatible with the symmetry of MoTe₂ and of graphene, therefore the crystal symmetry of the system must be broken to permit the unconventional SCC. One possibility for creating such symmetry breaking is shear strain developed during the fabrication process, as discussed in Chapter 5. However, this signal has now been reproduced in several samples and the shear strain is expected to be sample-dependent [357], making this hypothesis unlikely. Another possible mechanism, also discussed in Chapter 5, is that the misalignment between the mirror planes of graphene and MoTe₂ creates a non-symmetric interface which enables an unconventional EE in the proximitized graphene, for which the spin polarization is parallel to the charge current direction [346, 347].

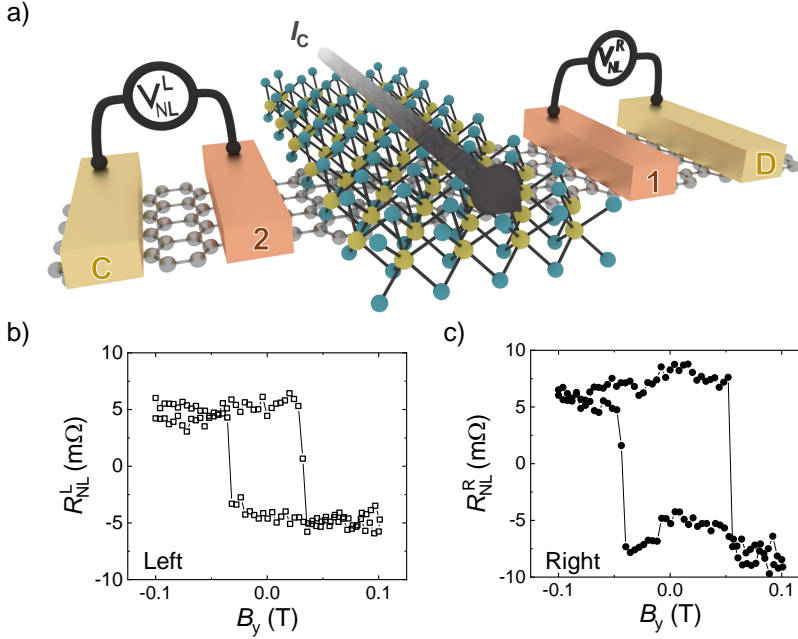


Figure 7.3: **Non-local SCC measurement in the standard configuration.** (a) Sketch of the standard SCC measurement configuration that can be performed in the heterostructure. The charge current (I_c) is applied along MoTe₂ and the voltage is probed using the FM electrode on the left or on the right. (b) Non-local resistance (R_{NL}) measured using the left Co electrode 2 as detector (V_{NL}^L) while sweeping the magnetic field along the in-plane easy axis (y -direction). (c) Same measurement using the right Co electrode 1 as detector (V_{NL}^R). Baselines of 110 m Ω and 26 m Ω are removed, respectively. All measurements are performed at 300 K.

7.3.2 SCC in the 3D-current configuration

Once we have measured the SCC in the standard configuration, we can move to explore the SCC using the 3D-current configuration. To further access different SCC directions, the current path in MoTe₂ must include components along the three different space coordinates. We implement a protocol, known as 3D-current configuration [233, 296], where I_c is injected from MoTe₂ into graphene through their interface using one Ti/Au electrode on graphene (C or D) and one on MoTe₂ (A or B). Because I_c propagates along x , y and z , we use the different possible combinations of $I_{\alpha\beta}V_{\gamma\delta}$ to reverse each component independently. When the relevant component of I_c is reversed, the spin polarization must change sign, regardless of the SCC origin.

The four possible charge current paths within MoTe₂ are sketched in Fig. 7.4(a) when contact 1 is used as the FM detector. The measured R_{NL} as a function of B_y for each configuration is plotted in Fig. 7.4(b), where hysteresis loops are represented with the same color as the respective current path. In order to distinguish the charge current direction creating the spin polarization along y , each charge current path is decomposed in the three space coordinates: dark red path corresponds to $\mathbf{I}_c (-x, -y, -z)$, light red to $\mathbf{I}_c (+x, +y, +z)$, dark blue to $\mathbf{I}_c (-x, +y, -z)$ and light blue to $\mathbf{I}_c (+x, -y, +z)$. As shown in Fig. 7.4(b), dark red and dark blue curves show the same hysteresis loop sign and light red and light blue show also the same sign but opposite to the dark curves. Taking a closer look to the correspondence between the sign of the loop and the charge current coordinates, one can see that the reverse of the signal arises from a reverse of the charge current along the x - or z -direction.

To shed further light on the SCC origin, another measurement using the 3D-current configuration is implemented using contact 2 as the FM detector, which allows us to access four extra current paths [see Fig. 7.4(c)]. Figure 7.4(d) shows R_{NL} as a function of B_y for the four extra configurations. In this case, the decomposition of the charge current is as follows: dark red path corresponds to $\mathbf{I}_c (+x, -y, -z)$, light red to $\mathbf{I}_c (-x, +y, +z)$, dark blue to $\mathbf{I}_c (+x, +y, -z)$ and light blue to $\mathbf{I}_c (-x, -y, +z)$. Table 7.1 contains a summary of the different configurations, the respective components of \mathbf{I}_c , and the amplitude of the signal. It is important to notice that, only the I_c component along the x -direction is reversed when comparing the two sets of data obtained from detector 1 and 2 (configurations with the same color in Fig. 7.4(c) and Fig. 7.4(a) respectively). As a matter of fact, if the same-color signal is compared between the two different configurations [Fig. 7.4(b) vs. Fig. 7.4(d)], a reverse in the signal is observed for each of the four non-local resistance configurations. This implies that it is the charge current along the x -direction that dominates the generation of a spin polarization along the y -direction.

The possible mechanisms behind this SCC are SHE in MoTe₂ or EE in the proximitized graphene. For the former, a charge current along the x -direction will generate a spin current along the z -direction with spin polarization along y (corresponding to σ_{zx}^y). For the latter, a charge current along x generates a spin accumulation with spin polarization along y . This case also corresponds to the expected spin polarization induced by EE in the proximitized graphene. In contrast to the signal measured using the standard SHE configuration [Fig. 7.3(a,b)], and regardless of the origin, this signal is allowed by symmetry and

has not been detected before.

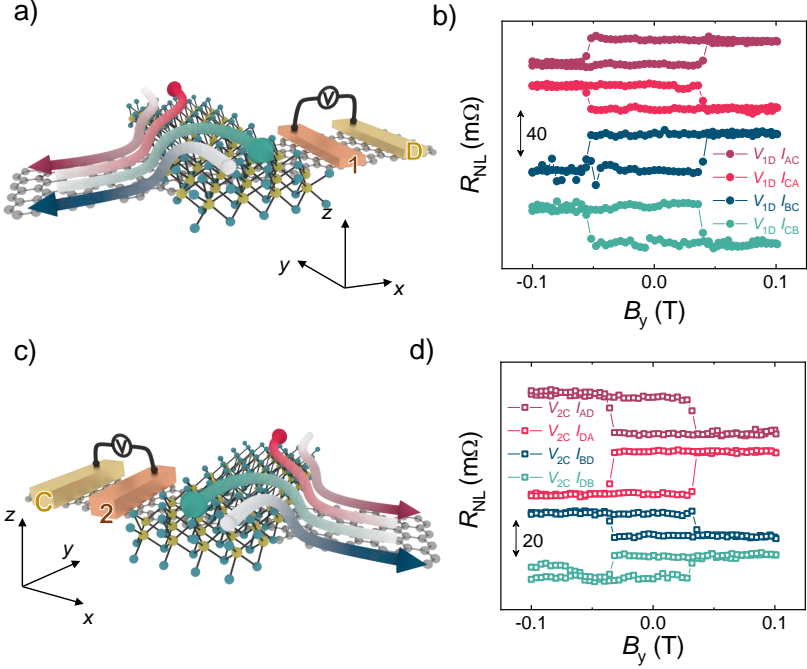


Figure 7.4: Non-local SCC measurements in the 3D-current configuration. (a) Sketch of all 3D-current SCC measurement configurations using contact 1 as a FM detector. The arrows across the MoTe₂/graphene represent the four different current paths. (b) Non-local resistance measured using contact 1 as a FM detector when sweeping the magnetic field along the FM easy axis (B_y) for the different current paths. The curves have been shifted for clarity. The arrow represents an amplitude of 40 m Ω . (c) Sketch of all 3D-current SCC measurement configurations using contact 2 as a FM detector. (d) Non-local resistance measured using contact 2 as a FM detector when sweeping B_y . The curves have been shifted for clarity. The arrow represents an amplitude of 20 m Ω . All measurements are performed at 300 K.

7.4 Discussion of the results

Using both the standard [Fig. 7.1(a)] and the 3D-current [Fig. 7.1(b)] SCC configurations in the graphene/MoTe₂ heterostructure, we have observed how both x - and y -directions of the charge current induce spins polarized along the y -direction. To quantitatively compare them, the amplitude of the SCC signal (ΔR_{NL}) is defined as the difference between the mean value of the non-local resistance at the two saturating states. ΔR_{NL} for each configuration is

plotted in Fig. 7.5 using the two different FM contacts as detectors. For each contact, two configurations show positive amplitude values while the other two are negative. It is remarkable that the amplitude for the two positive (negative) amplitudes is not the same. The difference in ΔR_{NL} between the two positive (negative) amplitudes, that is approximately $10 \text{ m}\Omega$ in both cases, must arise from the SCC of the charge current along the y -direction as discussed next.

In the case of contact 1 working as a detector, the charge current in the dark blue configuration is $\mathbf{I}_c (-x, +y, -z)$ while in the dark red case is $\mathbf{I}_c (-x, -y, -z)$. The only difference between them is the direction of the charge current along the y -direction. From the standard SCC configuration, we know there is SCC signal with spin polarization along y when the charge current is applied along the $-y$ -direction. The amplitude of this SCC signal (solid black circle) is negative, which will add up to the signal coming from the x -direction. The signal along the $-x$ -direction (filled dark blue and filled dark red) is positive, meaning that a charge current along the $-x$ -direction will generate a spin polarization along the $+y$ axis. In contrast, a charge current along the $-y$ -direction will generate a spin polarization along the $-y$ -axis. The combination of the signal coming from charge current flowing along $\pm x$ and $\pm y$ is the responsible of the difference between the two positive (negative) signals, as represented by arrows in Fig. 7.5. Such scenario applies to all the configurations.

Now, if we consider the case of contact 2, the trend of the data is the same as for electrode 1, showing the consistency of the measured signals with the charge current paths. However, the absolute values of ΔR_{NL} are smaller in comparison with contact 1. This can be due to a lower polarization of the FM detector.

Table 7.1: **Summary of the different measurement configurations and their amplitude.** For each configuration, the components of I_c and the respective amplitude of the signals are detailed.

Configuration	Detector	I_c	ΔR_{NL} (m Ω)
Standard Configuration	Contact 1	(0, -y, 0)	-13.6
	Contact 2	(0, -y, 0)	-9.1
3-D current configuration	Contact 1	Dark red circle (-x, -y, -z)	22.2
		Light red circle (+x, +y, +z)	-21.8
		Dark blue circle (-x, +y, -z)	32.4
		Ligh blue circle (+x, -y, +z)	-30.7
	Contact 2	Dark red square (+x, -y, -z)	-21.4
		Light red square (-x, +y, +z)	24.1
		Dark blue square (+x, +y, -z)	-13.1
		Light blue square (-x, -y, +z)	10.6

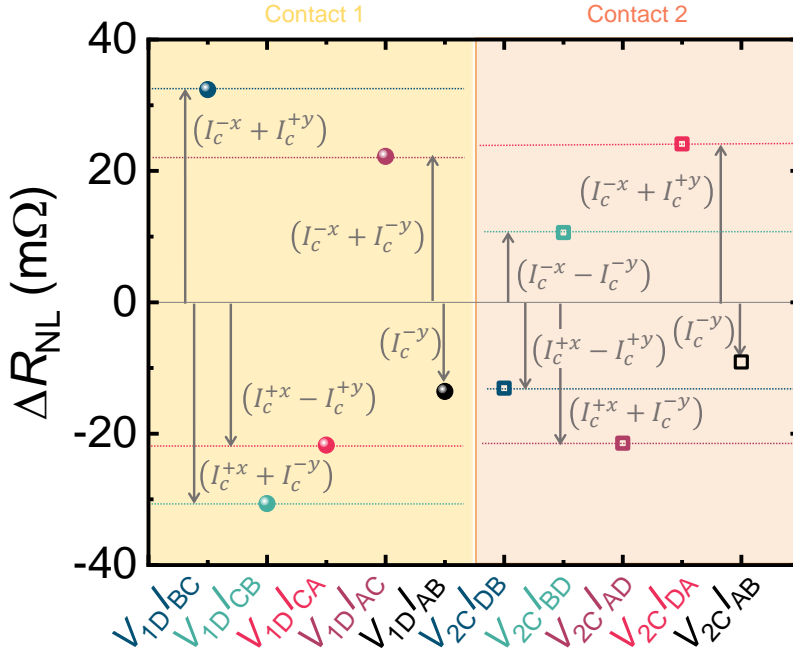


Figure 7.5: **Amplitude of the 8 different SCC signals in the 3D-current and standard configurations.** ΔR_{NL} for each of the eight different current paths in the 3D-current configurations as well as the standard configuration. Each arrow is labeled with the charge current involved in the SCC process for each measurement. Contact 1 was used as a detector for the configuration on the left side (light yellow background), while contact 2 was the detector for the five combinations on the right side (light orange background). The error bars are smaller than the dots.

7.5 Conclusion

In conclusion, we have performed SCC experiments both in the standard and the 3D-current configurations. The combination of the two measurements in the same device, enabled by the high-quality interface of our graphene/MoTe₂ heterostructure, allows us to access an unconventional SCC component where the charge current along y generates a spin polarization parallel to it. Along with it, a new SCC configuration where the x -component of a charge current generates a spin polarization along y in the same device. Since the symmetries of the SHE in MoTe₂ and EE in the proximitized graphene are the same, the precise origin of the latter cannot be confirmed, therefore, the SCC efficiency cannot be calculated. Nevertheless, the amplitude of this signal, which is twice the unconventional signal, is promising for applications in future spin-

tronic devices. Indeed, considering the conversion to occur in bulk MoTe₂, the expected efficiency θ_{zx}^y , must be larger than the reported one in Chapter 5 for θ_{zy}^x , that was already comparable with the best-known spin Hall metals [100,350] and metal alloys [351,352], as theoretically predicted ($\theta_{zx}^y = 2.2\%$ and $\theta_{zy}^x = 2\%$) [78].

Chapter 8

Conclusions and future perspectives

In the course of this Thesis, MoTe₂ has been used as a SOC material in order to study SCC in graphene-based LSVs. 1T'-MoTe₂ is characterized by its low crystal symmetry and high-SOC, crucial ingredients for its implementation in the next generation of spintronic devices. Hereunder, the main findings of the Thesis are summarized, as well as future perspectives using these devices towards the implementation of functional spin-based devices.

Initially, MoTe₂ flakes are characterized in **Chapter 4**. MoTe₂ presents in-plane anisotropy therefore, determining the crystallographic axes of the MoTe₂ flakes is crucial to identify the permitted SCC configurations. By using polarized Raman spectroscopy, and STEM, the orientation of crystal axes of exfoliated MoTe₂ flakes are determined. MoTe₂ tends to cleave along one preferential crystal direction, i.e., along the molybdenum atomic chain (*a*-axis), leading to elongated MoTe₂ flakes. Moreover, it is reported that 1T'-MoTe₂ undergoes a first-order phase transition to the 1T_d phase at ~ 240 K. We observed this transition in bulk crystal via polarized Raman spectroscopy. However, in exfoliated flakes such phase transition is absent. This result is supported by the electrical resistance measured in the flakes as a function of temperature. Besides, the anisotropic crystal structure influences the behaviour of the electrical resistance when an external magnetic field is applied to the system. 1T'-MoTe₂ flake shows large magnetoresistance when the magnetic field is applied along

the out-of-plane direction, that is, along the van der Waals stacking direction, and it increases when decreasing the temperature. At 10 K, the magnetoresistance under the presence of an out-of-plane magnetic field reaches 5% at 9 T.

In terms of SCC, **Chapter 5** presents the results at moderate-high temperatures (300 K - 75 K), where two distinct contributions arising from the conversion of two different spin orientations are detected using the standard SCC configuration in the graphene/MoTe₂ LSV. In addition to the conventional conversion where the spin polarization is orthogonal to the charge current and spin current, we also detect an unconventional conversion where the spin polarization and the charge current are parallel. While the origin of the conventional SCC can be ascribed to bulk ISHE in MoTe₂ or IEE in the proximitized graphene, the origin of the latter can only be explained if the symmetries of the system are reduced. Two possibilities are considered: (i) the MoTe₂ develops shear strain during the fabrication process so the only crystal mirror in 1T'-MoTe₂ is broken; or (ii) the mirrors between graphene and MoTe₂ are not aligned, therefore any spin polarization direction can induce charge current via IEE in the proximitized graphene. Assuming the SCCs to occur in the bulk of MoTe₂, the lower limit at room temperature of the SCC efficiencies, given by the spin Hall angle θ_{ij}^k , for the conventional component is $|\theta_{zy}^x| \geq 0.21$ while for the unconventional is $|\theta_{zy}^y| \geq 0.10$, with opposite sign to each other. Both contributions show large efficiencies comparable to the best spin Hall metals and topological insulators. Our finding enables the simultaneous conversion of spin currents with any in-plane spin polarization in one single experimental configuration.

In **Chapter 6**, SCC in MoTe₂/graphene LSVs is explored at low temperatures, where the proximity-induced SCC becomes relevant. Graphene is very sensitive to the environment, therefore, when it is placed in contact with a SOC material, its properties are altered. This phenomenon is known as spin-orbit proximity, allowing SCC to occur in graphene itself. Along with the charge current generation due to any in-plane spin polarization observed at moderate-high temperatures, an extra component is observed. In this case, the out-of-plane spin polarization induces a charge current which is probed using the same standard SCC configuration used in Chapter 5. This contribution can be ascribed to ISHE in proximitized graphene or to a non-orthogonal ISHE in MoTe₂, allowed by the reduced crystal symmetries of MoTe₂. Since this component is dominant at low temperatures, this effect is more likely to happen in proximi-

tized graphene and, consequently, a proper analysis of the efficiency cannot be performed.

Thanks to the high-quality interface of our graphene/MoTe₂ heterostructure, the SCC is studied using an alternative 3D-current configuration, as discussed in **Chapter 7**. Since the standard SCC configuration used in Chapters 5 and 6 cannot capture all the permitted SCC processes in MoTe₂, a new measurement configuration is employed in the same graphene/MoTe₂ van der Waals heterostructures. Besides the previously observed unconventional SCC, where a spin generation polarized parallel to the direction of the charge current occurs, our experiment also reveals a spin generation polarized in-plane perpendicular to the direction of the current. The origin of this SCC component can be attributed to SHE in MoTe₂ or to EE in the proximitized graphene. The symmetries of both origins are the same, therefore, the precise origin cannot be confirmed. The combination of the 3D-current configuration together with the standard configuration gives new insights into the SCC processes in low symmetry materials. The large SCC signals obtained at room temperature, along with the versatility of the 3D-current configuration, opens the door to new architectures in spin-based devices.

Considering all the above, the graphene/MoTe₂ van der Waals heterostructure is a hopeful one to be integrated into functional 2D devices. Although it is difficult to know the precise origin of the SCC signal, if we assume to happen in the MoTe₂ via bulk SHE, the efficiency is comparable to the best-known spin Hall metals. Other than the reported large efficiency, the 2D nature of these devices paves the way towards to successful downscaling of spintronic devices.

In order to better understand the SCC origin, a detailed study of the alignment of the mirrors between graphene and MoTe₂ should be done. By annealing the heterostructure, the mirrors of both materials tend to align [348,349]. The alignment of the mirrors would increase the symmetries of the interface so that fewer non-orthogonal SCC effects would be allowed. By comparing the SCC signal obtained in the annealed device with the ones in the non-annealed devices shown in this Thesis, the effects coming from the non-symmetric interface can be determined. In the case of graphene/MoTe₂ we did not perform any annealing process because it could result in an undesired phase transition from the 1T' phase to a high-symmetry phase (2H) when the temperature of the system is increased.

Regardless of the SCC origin, low symmetry materials displaying multidirec-

tional SCC open the door to the realization of new architectures in spin-based devices such as the MESO logic device proposed by Intel. For real-world applications large-scale manufacturing of the devices is a must. Therefore, a step forward in graphene-based LSVs in combination with 2D materials is the implementation of CVD-grown graphene instead of exfoliated flakes. The downside of this technique is the requirement of extra fabrication steps which can give rise to a lower signal-to-noise ratio. In addition, MoTe_2 is air-sensitive, and air exposure has to be avoided. The use of other low-symmetry materials with better air-stability would be convenient. Thus, the investigation of air-insensitive low-symmetry 2D materials is required towards the application of the exciting properties of these materials in real devices.

Publications

This thesis is based on the following publications:

- **Large multidirectional spin-to-charge conversion in low-symmetry semimetal MoTe₂ at room temperature.**

C.K. Safeer*, Nerea Ontoso*, Josep Ingla-Aynés, Franz Herling, Van Tuong Pham, Annika Kurzmam, Klaus Ensslin, Andrey Chuvilin, Iñigo Robredo, Maia G. Verghoiry, Fernando de Juan, Luis E. Hueso, M. Reyes Calvo, Fèlix Casanova.

* Equal contributors.

Nano Letters, **19**, 8758 (2019).

(Chapter 5)

- **Low-temperature spin-to-charge conversion in graphene/MoTe₂.**

Nerea Ontoso, C.K. Safeer, Franz Herling, Josep Ingla-Aynés, M. Reyes Calvo, Luis E. Hueso, Fèlix Casanova.

In preparation (2022).

(Chapter 6)

- **Spin-charge interconversion in a high-quality interface graphene/MoTe₂ van der Waals heterostructure.**

Nerea Ontoso, C.K. Safeer, Inge Groen, Franz Herling, Josep Ingla-Aynés, Haozhe Yang, Zhendong Chi, M. Reyes Calvo, Luis E. Hueso, Fèlix Casanova.

In preparation (2022).

(Chapter 7)

Other publications:

- **Reliability of spin-to-charge conversion measurements in graphene-based lateral spin valves.**

C.K. Safeer, Franz Herling, Won Young Choi, Nerea Ontoso, Josep Ingla-Aynés, Luis E. Hueso, Fèlix Casanova.
2D Materials **9**, 015024 (2021).

- **Gate tunability of highly efficient spin-to-charge conversion by spin Hall effect in graphene proximitized with WSe₂.**

Franz Herling, C.K. Safeer, Josep Ingla-Aynés, Nerea Ontoso, Luis E. Hueso, Fèlix Casanova.
APL Materials **8**, 071103 (2020).

- **Spin Hall effect in bilayer graphene combined with an insulator up to room temperature.**

C.K. Safeer, Josep Ingla-Aynés, Nerea Ontoso, Franz Herling, Wenjing Yan, Luis E. Hueso, Fèlix Casanova.
Nano Letters **6**, 4573 (2020).

- **Tailoring the interaction between spin waves and domain walls in nanostripes with perpendicular magnetic anisotropy.**

Rocio Yanes, Nerea Ontoso, Luis Torres, Luis Lopez-Diaz.
Journal of Physics D: Applied Physics **52**, 175002 (2019).

- **Room-temperature spin Hall effect in graphene/MoS₂ van der Waals heterostructure.**

C.K. Safeer, Josep Ingla-Aynés, Franz Herling, José H Garcia, Marc Vila, Nerea Ontoso, M. Reyes Calvo, Stephan Roche, Luis E. Hueso, Fèlix Casanova.
Nano Letters **19**, 1074 (2019).

Acknowledgements

Finally, after all the symmetries and spin-to-charge conversion processes, the time has arrived to thank all those who have been by my side during this thesis and since much earlier.

First of all, I want to thank my supervisors Reyes and Fèlix. Fèlix, thank you for your undeniable availability. Reyes, for the good times during the first years of my PhD. Thank you both for enrolling me in this adventure. Luis, although you are not my official supervisor, I also appreciate your support. Fernando, for being the translator between theory and experiments.

Safeer, Pep it has been a real pleasure to work with you. Franz, my hand-to-hand *graphene lover*. All the previous pages would not have been possible without you, guys. To all the present and former members of nanodevices group. Won Young, Tuong, Isabel, Haozhe, David... Honestly, I was about to enumerate all of you, but I feel afraid to forget someone! Thank you for the great atmosphere in the group.

Roger, no solo por tu apoyo, pero también por los experimentos de viernes tarde. Aunque con ninguno hemos conseguido un Nobel, me he divertido y aprendido mucho contigo en el laboratorio. To Ralph, for your support and patience.

Special thanks to all nanogune people that make the lunchtime and coffee break a moment to enjoy and laugh. Thanks to Eneko, por alumbrarme en la tesis con las luces antiniebla, María, por hacer de psicóloga en los días duros de laboratorio, Ion, Jaione, Iker, Gabriele, Andoni, Beatriz, Charlie... Sin vosotros hubiese sido más duro hacer esta tesis.

To Juanma, for being always there, ready for a beer, and to make you smile. To Inge, you have been a great support during the last months, and my polpettone per avermi insegnato l'italiano e coccolandomi. To Josu, Edurne, Amiginho fofinho, Franz, Eva, Sarai, Jakob, Elias, Paz, Jon. Guys, you make me feel at home in Donosti. You make me enjoy life. You make me happy.

Going back to my roots and my hometown... A mis choches, por ser siempre casa, por ser amigas desde siempre y para siempre. A Noe y mis caza varones, por todos los momentos que hemos pasado juntas y me han llevado hasta aquí. A César, por hacerme trabajar duro en Librerías y en tus visitas a Donosti; a Javi y Germán, porque sin ellos tampoco hubiese sobrevivido a la carrera.

A Mónica, Lea y Greta. Como diría Simone de Beauvoir, "*Que nada os limite. Que nada os defina. Que nada os sujete. Que la libertad sea vuestra propia sustancia.*"

A Sergio, gracias por ser mi alegría y mi apoyo, eres imprescindible. Por los buenos ratos, por las risas y por lo que nos queda por vivir.

A mis padres, por todo. Y porque sin su confianza en mí, esto no hubiese sido posible.

To all of you who have shared this time with me, eskerrik asko!

:)

Bibliography

- [1] Nikonov, D. E. & Young, I. A. Overview of beyond-CMOS devices and a uniform methodology for their benchmarking. *Proceedings of the IEEE* **101**, 2498 (2013).
- [2] Nikonov, D. E. & Young, I. A. Benchmarking of beyond-CMOS exploratory devices for logic integrated circuits. *IEEE Journal on Exploratory Solid-State Computational Devices and Circuits* **1**, 3 (2015).
- [3] Bohr, M. T. & Young, I. A. CMOS scaling trends and beyond. *IEEE Micro* **37**, 20 (2017).
- [4] Manipatruni, S. *et al.* Scalable energy-efficient magnetoelectric spin-orbit logic. *Nature* **565**, 35 (2019).
- [5] Mott, N. F. The resistance and thermoelectric properties of the transition metals. *Proceedings of the Royal Society of London. Series A-Mathematical and Physical Sciences* **156**, 368 (1936).
- [6] Campbell, I., Fert, A. & Pomeroy, R. Evidence for two current conduction iron. *Philosophical Magazine* **15**, 977 (1967).
- [7] Fert, A. & Campbell, I. A. Two-current conduction in nickel. *Physical Review Letters* **21**, 1190 (1968).
- [8] Binasch, G., Grünberg, P., Saurenbach, F. & Zinn, W. Enhanced magnetoresistance in layered magnetic structures with antiferromagnetic interlayer exchange. *Physical Review B* **39**, 4828 (1989).
- [9] Baibich, M. N. *et al.* Giant magnetoresistance of (001)Fe/(001)Cr magnetic superlattices. *Physical Review Letters* **61**, 2472 (1988).
- [10] The Royal Swedish Academy of Sciences. The discovery of giant magnetoresistance (2007).
- [11] Parkin, S. S. P., Bhadra, R. & Roche, K. P. Oscillatory magnetic exchange coupling through thin copper layers. *Physical Review Letters* **66**, 2152 (1991).
- [12] Parkin, S., Li, Z. & Smith, D. J. Giant magnetoresistance in antiferromagnetic Co/Cu multilayers. *Applied Physics Letters* **58**, 2710 (1991).
- [13] Allred, J., Lyman, R., Kornack, T. & Romalis, M. V. High-sensitivity atomic magnetometer unaffected by spin-exchange relaxation. *Physical Review Letters* **89**, 130801 (2002).
- [14] Freitas, P. *et al.* Spintronic platforms for biomedical applications. *Lab on a Chip* **12**, 546 (2012).

- [15] Shen, H.-M., Hu, L. & Fu, X. Integrated giant magnetoresistance technology for approachable weak biomagnetic signal detections. *Sensors* **18**, 148 (2018).
- [16] Jullière, M. Tunneling between ferromagnetic films. *Physics Letters A* **54**, 225 (1975).
- [17] Moodera, J. S., Kinder, L. R., Wong, T. M. & Meservey, R. Large magnetoresistance at room temperature in ferromagnetic thin film tunnel junctions. *Physical Review Letters* **74**, 3273 (1995).
- [18] Parkin, S. S. *et al.* Giant tunnelling magnetoresistance at room temperature with MgO (100) tunnel barriers. *Nature materials* **3**, 862 (2004).
- [19] Yuasa, S., Nagahama, T., Fukushima, A., Suzuki, Y. & Ando, K. Giant room-temperature magnetoresistance in single-crystal Fe/MgO/Fe magnetic tunnel junctions. *Nature materials* **3**, 868 (2004).
- [20] Parkin, S. Giant magnetoresistance in magnetic nanostructures. *Annual Review of Materials Science* **25**, 357 (1995).
- [21] Uwe, H. Magnetic multilayers and giant magnetoresistance (1999).
- [22] Ennen, I., Kappe, D., Rempel, T., Glenske, C. & Hütten, A. Giant magnetoresistance: basic concepts, microstructure, magnetic interactions and applications. *Sensors* **16**, 904 (2016).
- [23] Slonczewski, J. C. Current-driven excitation of magnetic multilayers. *Journal of Magnetism and Magnetic Materials* **159**, 1 (1996).
- [24] Berger, L. Emission of spin waves by a magnetic multilayer traversed by a current. *Physical Review B* **54**, 9353 (1996).
- [25] MRAM - Info. The MRAM experts. <https://www.mram-info.com/>. Accessed: 2022-01-11.
- [26] Guo, Z. *et al.* Spintronics for Energy-Efficient Computing: An Overview and Outlook. *Proceedings of the IEEE* (2021).
- [27] Manchon, A. *et al.* Current-induced spin-orbit torques in ferromagnetic and antiferromagnetic systems. *Reviews of Modern Physics* **91**, 035004 (2019).
- [28] Shao, Q. *et al.* Roadmap of spin-orbit torques. *IEEE Transactions on Magnetism* (2021).
- [29] Datta, S. & Das, B. Electronic analog of the electro-optic modulator. *Applied Physics Letters* **56**, 665 (1990).
- [30] Dery, H., Dalal, P., Cywiński, L. & Sham, L. J. Spin-based logic in semiconductors for reconfigurable large-scale circuits. *Nature* **447**, 573 (2007).
- [31] Behin-Aein, B., Datta, D., Salahuddin, S. & Datta, S. Proposal for an all-spin logic device with built-in memory. *Nature nanotechnology* **5**, 266 (2010).
- [32] Idzuchi, H., Fukuma, Y. & Otani, Y. Spin transport in non-magnetic nano-structures induced by non-local spin injection. *Physica E: Low-dimensional Systems and Nanostructures* **68**, 239–263 (2015).
- [33] Ando, K. Dynamical generation of spin currents. *Semiconductor Science and Technology* **29**, 043002 (2014).
- [34] Slachter, A., Bakker, F. L., Adam, J.-P. & van Wees, B. J. Thermally driven spin injection from a ferromagnet into a non-magnetic metal. *Nature Physics* **6**, 879 (2010).
- [35] Kimura, T., Otani, Y., Sato, T., Takahashi, S. & Maekawa, S. Room-temperature reversible spin Hall effect. *Physical Review Letters* **98**, 156601 (2007).

- [36] Sinova, J., Valenzuela, S. O., Wunderlich, J., Back, C. & Jungwirth, T. Spin Hall effects. *Reviews of modern physics* **87**, 1213 (2015).
- [37] Ando, Y. & Shiraishi, M. Spin to charge interconversion phenomena in the interface and surface states. *Journal of the Physical Society of Japan* **86**, 011001 (2017).
- [38] Isshiki, H., Muduli, P., Kim, J., Kondou, K. & Otani, Y. Phenomenological model for the direct and inverse Edelstein effects. *Physical Review B* **102**, 184411 (2020).
- [39] Blundell, S. Magnetism in condensed matter (2003).
- [40] van Son, P. C., van Kempen, H. & Wyder, P. Boundary resistance of the ferromagnetic-nonferromagnetic metal interface. *Physical Review Letters* **58**, 22713 (1987).
- [41] Schmidt, G., Ferrand, D., Molenkamp, L. W., Filip, A. T. & van Wees, B. J. Fundamental obstacle for electrical spin injection from a ferromagnetic metal into a diffusive semiconductor. *Physical Review B* **62**, 4790 (2000).
- [42] Takahashi, S. & Maekawa, S. Spin injection and detection in magnetic nanostructures. *Physical Review B* **67**, 052409 (2003).
- [43] Casanova, F., Sharoni, A., Erekhinsky, M. & Schuller, I. K. Control of spin injection by direct current in lateral spin valves. *Physical Review B* **79**, 184415 (2009).
- [44] Fabian, J., Matos-Abiague, A., Ertler, C., Stano, P. & Zutic, I. Semiconductor spintronics. *Acta Physica Slovaca* **57**, 565 (2007).
- [45] Johnson, M. & Silsbee, R. H. Interfacial charge-spin coupling: Injection and detection of spin magnetization in metals. *Physical Review Letters* **55**, 1790 (1985).
- [46] Kikkawa, J. M. & Awschalom, D. D. Lateral drag of spin coherence in gallium arsenide. *Nature* **397**, 139–141 (1999).
- [47] Ohno, Y. *et al.* Electrical spin injection in a ferromagnetic semiconductor heterostructure. *Nature* **402**, 790 (1999).
- [48] Malajovich, I., Kikkawa, J., Awschalom, D., Berry, J. & Samarth, N. Coherent transfer of spin through a semiconductor heterointerface. *Physical Review Letters* **84**, 1015 (2000).
- [49] Fiederling, R., Grabs, P., Ossau, W., Schmidt, G. & Molenkamp, L. W. Detection of electrical spin injection by light-emitting diodes in top- and side-emission configurations. *Applied Physics Letters* **82**, 2160–2162 (2003).
- [50] Lee, W. *et al.* Magnetization reversal and magnetoresistance in a lateral spin-injection device. *Journal of Applied Physics* **85**, 6682 (1999).
- [51] Hammar, P., Bennett, B., Yang, M. & Johnson, M. Observation of spin injection at a ferromagnet-semiconductor interface. *Physical Review Letters* **83**, 203 (1999).
- [52] Gardelis, S., Smith, C., Barnes, C., Linfield, E. & Ritchie, D. Spin-valve effects in a semiconductor field-effect transistor: A spintronic device. *Physical Review B* **60**, 7764 (1999).
- [53] Hu, C.-M., Nitta, J., Jensen, A., Hansen, J. B. & Takayanagi, H. Spin-polarized transport in a two-dimensional electron gas with interdigital-ferromagnetic contacts. *Physical Review B* **63**, 125333 (2001).
- [54] Monzon, F., Tang, H. & Roukes, M. Magnetoelectronic phenomena at a ferromagnet-semiconductor interface. *Physical Review Letters* **84**, 5022 (2000).
- [55] Johnson, M. Spin accumulation in gold films. *Physical Review Letters* **70**, 2142 (1993).
- [56] Filip, A. T. *et al.* Experimental search for the electrical spin injection in a semiconductor. *Physical Review B* **62**, 9996 (2000).

- [57] Gregg, J., Petej, I., Jouguelet, E. & Dennis, C. Spin electronics—a review. *Journal of Physics D: Applied Physics* **35**, R121 (2002).
- [58] Rashba, E. I. Theory of electrical spin injection: Tunnel contacts as a solution of the conductivity mismatch problem. *Physical Review B* **62**, 16267 (2000).
- [59] Fert, A. & Jaffrès, H. Conditions for efficient spin injection from a ferromagnetic metal into a semiconductor. *Physical Review B* **64**, 184420 (2001).
- [60] Jedema, F., Nijboer, M., Filip, A. & Van Wees, B. Spin injection and spin accumulation in all-metal mesoscopic spin valves. *Physical Review B* **67**, 085319 (2003).
- [61] Žutić, I., Fabian, J. & Sarma, S. D. Spintronics: Fundamentals and applications. *Reviews of modern physics* **76**, 323 (2004).
- [62] Jedema, F. J., Filip, A. & Van Wees, B. Electrical spin injection and accumulation at room temperature in an all-metal mesoscopic spin valve. *Nature* **410**, 345 (2001).
- [63] Jedema, F., Heersche, H., Filip, A., Baselmans, J. & Van Wees, B. Electrical detection of spin precession in a metallic mesoscopic spin valve. *Nature* **416**, 713 (2002).
- [64] Wu, M., Jiang, J. & Weng, M. Spin dynamics in semiconductors. *Physics Reports* **493**, 61 (2010).
- [65] Elliott, R. J. Theory of the effect of spin-orbit coupling on magnetic resonance in some semiconductors. *Physical Review* **96**, 266 (1954).
- [66] Yafet, Y. g factors and spin-lattice relaxation of conduction electrons. *Solid State Physics* **14**, 1 – 98 (1963).
- [67] D'Yakonov, M. I. & Perel', V. I. Spin relaxation of conduction electrons in noncentrosymmetric semiconductors. *Soviet Physics Solid State* **13**, 3581 (1971).
- [68] Dyakonov, M. I. & Khaetskii, A. *Spin physics in semiconductors* (Springer, 2008).
- [69] Bir, G., Aronov, A. & Pikus, G. Spin relaxation of electrons scattered by holes. *Soviet Journal of Experimental and Theoretical Physics* **42**, 705 (1976).
- [70] Aronov, A., Pikus, E. & Titkov, A. Spin relaxation of conduction electrons in p-type iii-v compounds. *Soviet Journal of Experimental and Theoretical Physics* **84**, 1170 (1983).
- [71] Dzhioev, R. *et al.* Low-temperature spin relaxation in n-type gaas. *Physical Review B* **66**, 245204 (2002).
- [72] Kavokin, K. Spin relaxation of localized electrons in n-type semiconductors. *Semiconductor Science and Technology* **23**, 114009 (2008).
- [73] Messiah, A. *Quantum mechanics*, vol. ii (1965).
- [74] Griffiths, D. J. & Schroeter, D. F. *Introduction to quantum mechanics* (Cambridge University Press, 2018).
- [75] D'Yakonov, M. I. & Perel', V. I. Spin Orientation of Electrons Associated with the Interband Absorption of Light in Semiconductors. *Soviet Journal of Experimental and Theoretical Physics* **33**, 1053 (1971).
- [76] Hirsch, J. E. Spin Hall effect. *Physical Review Letters* **83**, 1834 (1999).
- [77] Zhang, Y. *et al.* Spin-orbitronic materials with record spin-charge conversion from high-throughput ab initio calculations. *arXiv preprint arXiv:1909.09605* (2019).
- [78] Roy, A., Guimarães, M. H. D. & Sławińska, J. Unconventional spin Hall effects in nonmagnetic solids. *arXiv preprint arXiv:2110.09242* (2021). 2110.09242.
- [79] Stamm, C. *et al.* Magneto-optical detection of the spin Hall effect in Pt and W thin films. *Physical Review Letters* **119**, 087203 (2017).

- [80] Hall, E. XVIII. on the “rotational coefficient” in nickel and cobalt. *The London, Edinburgh, and Dublin Philosophical Magazine and Journal of Science* **12**, 157 (1881).
- [81] Karplus, R. & Luttinger, J. M. Hall effect in ferromagnetics. *Physical Review* **95**, 1154 (1954).
- [82] Smit, J. The spontaneous Hall effect in ferromagnetics ii. *Physica* **24**, 39 (1958).
- [83] Berger, L. Side-jump mechanism for the Hall effect of ferromagnets. *Physical Review B* **2**, 4559 (1970).
- [84] Guo, G.-Y., Murakami, S., Chen, T.-W. & Nagaosa, N. Intrinsic spin Hall effect in platinum: First-principles calculations. *Physical Review Letters* **100**, 096401 (2008).
- [85] Tanaka, T. *et al.* Intrinsic spin hall effect and orbital hall effect in 4 d and 5 d transition metals. *Physical Review B* **77**, 165117 (2008).
- [86] Gradhand, M., Fedorov, D. V., Zahn, P. & Mertig, I. Extrinsic spin Hall effect from first principles. *Physical Review Letters* **104**, 186403 (2010).
- [87] Nagaosa, N., Sinova, J., Onoda, S., MacDonald, A. H. & Ong, N. P. Anomalous Hall effect. *Review Modern Physics* **82**, 1539 (2010).
- [88] Lowtizer, S. *et al.* Extrinsic and intrinsic contributions to the spin Hall effect of alloys. *Physical Review Letters* **106**, 056601 (2011).
- [89] Fert, A. & Levy, P. M. Spin Hall effect induced by resonant scattering on impurities in metals. *Physical Review Letters* **106**, 157208 (2011).
- [90] Zimmermann, B. *et al.* Skew scattering in dilute ferromagnetic alloys. *Physical Review B* **90**, 220403 (2014).
- [91] Omori, Y. *et al.* Relation between spin Hall effect and anomalous Hall effect in 3 d ferromagnetic metals. *Physical Review B* **99**, 014403 (2019).
- [92] Ashcroft, N. W., Mermin, N. D. *et al.* Solid state physics (1976).
- [93] Xiao, D., Chang, M.-C. & Niu, Q. Berry phase effects on electronic properties. *Review Modern Physics* **82**, 1959 (2010).
- [94] Gradhand, M. *et al.* First-principle calculations of the Berry curvature of Bloch states for charge and spin transport of electrons. *Journal of Physics: Condensed Matter* **24**, 213202 (2012).
- [95] Zhang, S. Spin Hall effect in the presence of spin diffusion. *Physical Review Letters* **85**, 393 (2000).
- [96] Shchelushkin, R. & Brataas, A. Spin Hall effects in diffusive normal metals. *Physical Review B* **71**, 045123 (2005).
- [97] Shchelushkin, R. & Brataas, A. Spin Hall effect, Hall effect, and spin precession in diffusive normal metals. *Physical Review B* **72**, 073110 (2005).
- [98] Valenzuela, S. O. & Tinkham, M. Direct electronic measurement of the spin Hall effect. *Nature* **442**, 176 (2006).
- [99] Vila, L., Kimura, T. & Otani, Y. Evolution of the spin Hall effect in Pt nanowires: size and temperature effects. *Physical Review Letters* **99**, 226604 (2007).
- [100] Sagasta, E. *et al.* Tuning the spin Hall effect of Pt from the moderately dirty to the superclean regime. *Physical Review B* **94**, 060412 (2016).
- [101] Kimura, T., Otani, Y. & Hamrle, J. Enhancement of spin accumulation in a nonmagnetic layer by reducing junction size. *Physical Review B* **73**, 132405 (2006).
- [102] Maekawa, S. *et al.* *Concepts in spin electronics* (Oxford University Press on Demand, 2006).

- [103] Ganichev, S. D. *et al.* Spin-galvanic effect. *Nature* **417**, 153 (2002).
- [104] Aronov, A. & Lyanda-Geller, Y. B. Nuclear electric resonance and orientation of carrier spins by an electric field. *Soviet Journal of Experimental and Theoretical Physics* **50**, 431 (1989).
- [105] Edelstein, V. M. Spin polarization of conduction electrons induced by electric current in two-dimensional asymmetric electron systems. *Solid State Communications* **73**, 233 (1990).
- [106] Gambardella, P. & Miron, I. M. Current-induced spin-orbit torques. *Philosophical Transactions of the Royal Society A: Mathematical, Physical and Engineering Sciences* **369**, 3175 (2011).
- [107] Sánchez, J. R. *et al.* Spin-to-charge conversion using Rashba coupling at the interface between non-magnetic materials. *Nature communications* **4**, 2944 (2013).
- [108] Isasa, M. *et al.* Origin of inverse Rashba-Edelstein effect detected at the Cu/Bi interface using lateral spin valves. *Physical Review B* **93**, 014420 (2016).
- [109] Karube, S., Kondou, K. & Otani, Y. Experimental observation of spin-to-charge current conversion at non-magnetic metal/Bi₂O₃ interfaces. *Applied Physics Express* **9**, 033001 (2016).
- [110] Puebla, J. *et al.* Photoinduced Rashba spin-to-charge conversion via an interfacial unoccupied state. *Physical Review Letters* **122**, 256401 (2019).
- [111] Kato, Y., Myers, R., Gossard, A. & Awschalom, D. Current-induced spin polarization in strained semiconductors. *Physical Review Letters* **93**, 176601 (2004).
- [112] Silov, A. Y. *et al.* Current-induced spin polarization at a single heterojunction. *Applied physics Letters* **85**, 5929 (2004).
- [113] Culcer, D., Hwang, E., Stanescu, T. D. & Sarma, S. D. Two-dimensional surface charge transport in topological insulators. *Physical Review B* **82**, 155457 (2010).
- [114] Pesin, D. & MacDonald, A. H. Spintronics and pseudospintronics in graphene and topological insulators. *Nature materials* **11**, 409 (2012).
- [115] Mellnik, A. *et al.* Spin-transfer torque generated by a topological insulator. *Nature* **511**, 449 (2014).
- [116] Rojas-Sánchez, J.-C. *et al.* Spin to charge conversion at room temperature by spin pumping into a new type of topological insulator: α -sn films. *Physical Review Letters* **116**, 096602 (2016).
- [117] Zhang, S. & Fert, A. Conversion between spin and charge currents with topological insulators. *Physical Review B* **94**, 184423 (2016).
- [118] Lesne, E. *et al.* Highly efficient and tunable spin-to-charge conversion through Rashba coupling at oxide interfaces. *Nature materials* **15**, 1261 (2016).
- [119] Vaz, D. C. *et al.* Mapping spin-charge conversion to the band structure in a topological oxide two-dimensional electron gas. *Nature materials* **18**, 1187 (2019).
- [120] Manchon, A., Koo, H. C., Nitta, J., Frolov, S. & Duine, R. New perspectives for Rashba spin-orbit coupling. *Nature materials* **14**, 871 (2015).
- [121] LaShell, S., McDougall, B. & Jensen, E. Spin splitting of an Au (111) surface state band observed with angle resolved photoelectron spectroscopy. *Physical Review Letters* **77**, 3419 (1996).
- [122] Ast, C. R. *et al.* Giant spin splitting through surface alloying. *Physical Review Letters* **98**, 186807 (2007).

- [123] Bihlmayer, G., Blügel, S. & Chulkov, E. V. Enhanced Rashba spin-orbit splitting in Bi/ Ag (111) and Pb/ Ag (111) surface alloys from first principles. *Physical Review B* **75**, 195414 (2007).
- [124] Moras, P. *et al.* Magnetization-dependent rashba splitting of quantum well states at the Co/W interface. *Physical Review B* **91**, 195410 (2015).
- [125] Rojas-Sánchez, J.-C. & Fert, A. Compared efficiencies of conversions between charge and spin current by spin-orbit interactions in two-and three-dimensional systems. *Physical Review Applied* **11**, 054049 (2019).
- [126] Vaz, D. C., Barthélémy, A. & Bibes, M. Oxide spin-orbitronics: New routes towards low-power electrical control of magnetization in oxide heterostructures. *Japanese Journal of Applied Physics* **57**, 0902A4 (2018).
- [127] Shiomi, Y. *et al.* Spin-electricity conversion induced by spin injection into topological insulators. *Physical Review Letters* **113**, 196601 (2014).
- [128] Novoselov, K. S. *et al.* Two-dimensional atomic crystals. *Proceedings of the National Academy of Sciences* **102**, 10451 (2005).
- [129] Yi, M. & Shen, Z. A review on mechanical exfoliation for the scalable production of graphene. *Journal of Materials Chemistry A* **3**, 11700 (2015).
- [130] Wallace, P. R. The band theory of graphite. *Physical Review* **71**, 622 (1947).
- [131] Xiao, D., Yao, W. & Niu, Q. Valley-contrasting physics in graphene: magnetic moment and topological transport. *Physical Review Letters* **99**, 236809 (2007).
- [132] Gusynin, V. & Sharapov, S. Unconventional integer quantum Hall effect in graphene. *Physical Review Letters* **95**, 146801 (2005).
- [133] Tan, Y.-W. *et al.* Measurement of scattering rate and minimum conductivity in graphene. *Physical Review Letters* **99**, 246803 (2007).
- [134] Heersche, H. B., Jarillo-Herrero, P., Oostinga, J. B., Vandersypen, L. M. & Morpurgo, A. F. Bipolar supercurrent in graphene. *Nature* **446**, 56 (2007).
- [135] Min, H. *et al.* Intrinsic and Rashba spin-orbit interactions in graphene sheets. *Physical Review B* **74**, 165310 (2006).
- [136] Huertas-Hernando, D., Guinea, F. & Brataas, A. Spin-orbit coupling in curved graphene, fullerenes, nanotubes, and nanotube caps. *Physical Review B* **74**, 155426 (2006).
- [137] Trauzettel, B., Bulaev, D. V., Loss, D. & Burkard, G. Spin qubits in graphene quantum dots. *Nature Physics* **3**, 192 (2007).
- [138] Yao, Y., Ye, F., Qi, X.-L., Zhang, S.-C. & Fang, Z. Spin-orbit gap of graphene: First-principles calculations. *Physical Review B* **75**, 041401 (2007).
- [139] Gmitra, M., Konshuh, S., Ertler, C., Ambrosch-Draxl, C. & Fabian, J. Band-structure topologies of graphene: Spin-orbit coupling effects from first principles. *Physical Review B* **80**, 235431 (2009).
- [140] Konshuh, S., Gmitra, M. & Fabian, J. Tight-binding theory of the spin-orbit coupling in graphene. *Physical Review B* **82**, 245412 (2010).
- [141] Han, W., Kawakami, R. K., Gmitra, M. & Fabian, J. Graphene spintronics. *Nature nanotechnology* **9**, 794 (2014).
- [142] Wojtaszek, M., Vera-Marun, I. & van Wees, B. Transition between one-dimensional and zero-dimensional spin transport studied by Hanle precession. *Physical Review B* **89**, 245427 (2014).

- [143] Tombros, N., Jozsa, C., Popinciuc, M., Jonkman, H. T. & van Wees, B. J. Electronic spin transport and spin precession in single graphene layers at room temperature. *Nature* **448**, 571 (2007).
- [144] Cho, S., Chen, Y.-F. & Fuhrer, M. S. Gate-tunable graphene spin valve. *Applied Physics Letters* **91**, 123105 (2007).
- [145] Popinciuc, M. *et al.* Electronic spin transport in graphene field-effect transistors. *Physical Review B* **80**, 214427 (2009).
- [146] Józsa, C., Popinciuc, M., Tombros, N., Jonkman, H. & Van Wees, B. Electronic spin drift in graphene field-effect transistors. *Physical Review Letters* **100**, 236603 (2008).
- [147] Józsa, C., Popinciuc, M., Tombros, N., Jonkman, H. & Van Wees, B. Controlling the efficiency of spin injection into graphene by carrier drift. *Physical Review B* **79**, 081402 (2009).
- [148] Ingla-Aynés, J., Meijerink, R. J. & Wees, B. J. v. Eighty-eight percent directional guiding of spin currents with 90 μm relaxation length in bilayer graphene using carrier drift. *Nano Letters* **16**, 4825 (2016).
- [149] Zomer, P., Guimarães, M., Tombros, N. & Van Wees, B. Long-distance spin transport in high-mobility graphene on hexagonal boron nitride. *Physical Review B* **86**, 161416 (2012).
- [150] Guimarães, M. H. D. *et al.* Controlling spin relaxation in hexagonal bn-encapsulated graphene with a transverse electric field. *Physical Review Letters* **113**, 086602 (2014).
- [151] Ingla-Aynés, J., Guimarães, M. H. D., Meijerink, R. J., Zomer, P. J. & van Wees, B. J. 24- μm spin relaxation length in boron nitride encapsulated bilayer graphene. *Physical Review B* **92**, 201410 (2015).
- [152] Gurram, M. *et al.* Spin transport in fully hexagonal boron nitride encapsulated graphene. *Physical Review B* **93**, 115441 (2016).
- [153] Avsar, A. *et al.* Electronic spin transport in dual-gated bilayer graphene. *NPG Asia Materials* **8**, 274 (2016).
- [154] Yamaguchi, T. *et al.* Electrical spin injection into graphene through monolayer hexagonal boron nitride. *Applied Physics Express* **6**, 073001 (2013).
- [155] Kamalakar, M. V., Groenveld, C., Dankert, A. & Dash, S. P. Long distance spin communication in chemical vapour deposited graphene. *Nature Communications* **6**, 6766 (2015).
- [156] Singh, S. *et al.* Nanosecond spin relaxation times in single layer graphene spin valves with hexagonal boron nitride tunnel barriers. *Applied Physics Letters* **109**, 122411 (2016).
- [157] Neto, A. C. & Novoselov, K. New directions in science and technology: two-dimensional crystals. *Reports on Progress in Physics* **74**, 082501 (2011).
- [158] Novoselov, K. S., Andreeva, D. V., Ren, W. & Shan, G. Graphene and other two-dimensional materials. *Frontiers of Physics* **14**, 13301 (2019).
- [159] Mak, K. F., Lee, C., Hone, J., Shan, J. & Heinz, T. F. Atomically thin MoS₂: a new direct-gap semiconductor. *Physical Review Letters* **105**, 136805 (2010).
- [160] Radisavljevic, B. & Kis, A. Mobility engineering and a metal-insulator transition in monolayer MoS₂. *Nature materials* **12**, 815 (2013).

- [161] LaMountain, T., Lenferink, E. J., Chen, Y.-J., Stanev, T. K. & Stern, N. P. Environmental engineering of transition metal dichalcogenide optoelectronics. *Frontiers of Physics* **13**, 138114 (2018).
- [162] Xiao, D., Liu, G.-B., Feng, W., Xu, X. & Yao, W. Coupled spin and valley physics in monolayers of MoS₂ and other group-VI dichalcogenides. *Physical Review Letters* **108**, 196802 (2012).
- [163] Mak, K. F., He, K., Shan, J. & Heinz, T. F. Control of valley polarization in monolayer MoS₂ by optical helicity. *Nature nanotechnology* **7**, 494 (2012).
- [164] Zeng, H., Dai, J., Yao, W., Xiao, D. & Cui, X. Valley polarization in MoS₂ monolayers by optical pumping. *Nature nanotechnology* **7**, 490 (2012).
- [165] Cao, T. *et al.* Valley-selective circular dichroism of monolayer molybdenum disulphide. *Nature communications* **3**, 887 (2012).
- [166] Schaibley, J. R. *et al.* Valleytronics in 2d materials. *Nature Reviews Materials* **1**, 16055 (2016).
- [167] Dean, C. R. *et al.* Boron nitride substrates for high-quality graphene electronics. *Nature nanotechnology* **5**, 722 (2010).
- [168] Zunger, A., Katzir, A. & Halperin, A. Optical properties of hexagonal boron nitride. *Physical Review B* **13**, 5560 (1976).
- [169] Caldwell, J. D. *et al.* Photonics with hexagonal boron nitride. *Nature Reviews Materials* **4**, 552 (2019).
- [170] Keyes, R. W. The electrical properties of black phosphorus. *Physical Review* **92**, 580 (1953).
- [171] Li, L. *et al.* Black phosphorus field-effect transistors. *Nature nanotechnology* **9**, 372 (2014).
- [172] Ling, X., Wang, H., Huang, S., Xia, F. & Dresselhaus, M. S. The renaissance of black phosphorus. *Proceedings of the National Academy of Sciences* **112**, 4523 (2015).
- [173] Avsar, A. *et al.* Gate-tunable black phosphorus spin valve with nanosecond spin lifetimes. *Nature Physics* **13**, 888 (2017).
- [174] Avsar, A. *et al.* Air-stable transport in graphene-contacted, fully encapsulated ultrathin black phosphorus-based field-effect transistors. *ACS nano* **9**, 4138 (2015).
- [175] Nye, J. F. *et al.* *Physical properties of crystals: their representation by tensors and matrices* (Oxford university press, 1985).
- [176] Ma, Q. *et al.* Observation of the nonlinear Hall effect under time-reversal-symmetric conditions. *Nature* **565**, 337 (2019).
- [177] Lee, J., Wang, Z., Xie, H., Mak, K. F. & Shan, J. Valley magnetoelectricity in single-layer MoS₂. *Nature materials* **16**, 887 (2017).
- [178] Pop, F., Auban-Senzier, P., Canadell, E., Rikken, G. L. & Avarvari, N. Electrical magnetochiral anisotropy in a bulk chiral molecular conductor. *Nature communications* **5**, 3757 (2014).
- [179] Calavalle, F. *et al.* Gate-tuneable and chirality-dependent charge-to-spin conversion in tellurium nanowires. *arXiv preprint arXiv:2201.00359* (2022).
- [180] Chi, Z. *et al.* Superconductivity in pristine 2H_a- MoS₂ at ultrahigh pressure. *Physical Review Letters* **120**, 037002 (2018).
- [181] Calandra, M. & Mauri, F. Charge-density wave and superconducting dome in tise 2 from electron-phonon interaction. *Physical Review Letters* **106**, 196406 (2011).

- [182] Qian, X., Liu, J., Fu, L. & Li, J. Quantum spin Hall effect in two-dimensional transition metal dichalcogenides. *Science* **346**, 1344 (2014).
- [183] Fei, Z. *et al.* Edge conduction in monolayer WTe₂. *Nature Physics* **13**, 67 (2017).
- [184] Tang, S. *et al.* Quantum spin Hall state in monolayer 1T'-WTe₂. *Nature Physics* **13**, 683 (2017).
- [185] Wu, S. *et al.* Observation of the quantum spin Hall effect up to 100 Kelvin in a monolayer crystal. *Science* **359**, 76 (2018).
- [186] Fei, Z. *et al.* Ferroelectric switching of a two-dimensional metal. *Nature* **560**, 336 (2018).
- [187] El-Mahalawy, S. & Evans, B. Temperature dependence of the electrical conductivity and Hall coefficient in 2H-MoS₂, MoSe₂, WSe₂, and MoTe₂. *physica status solidi (B)* **79**, 713 (1977).
- [188] Ruppert, C., Aslan, O. B. & Heinz, T. F. Optical properties and band gap of single- and few-layer MoTe₂ crystals. *Nano Letters* **14**, 6231 (2014).
- [189] Chen, B. *et al.* Environmental changes in MoTe₂ excitonic dynamics by defects-activated molecular interaction. *ACS Nano* **9**, 5326 (2015).
- [190] Deng, Y. *et al.* MoTe₂: Semiconductor or semimetal? *ACS nano* **15**, 12465 (2021).
- [191] Clarke, R., Marseglia, E. & Hughes, H. A low-temperature structural phase transition in β -MoTe₂. *Philosophical Magazine B* **38**, 121 (1978).
- [192] Chen, S.-Y., Goldstein, T., Venkataraman, D., Ramasubramaniam, A. & Yan, J. Activation of new raman modes by inversion symmetry breaking in type II Weyl semimetal candidate T'-MoTe₂. *Nano Letters* **16**, 5852 (2016).
- [193] Zhang, K. *et al.* Raman signatures of inversion symmetry breaking and structural phase transition in type-II Weyl semimetal MoTe₂. *Nature communications* **7**, 13552 (2016).
- [194] Qi, Y. *et al.* Superconductivity in Weyl semimetal candidate MoTe₂. *Nature communications* **7**, 11038 (2016).
- [195] Deng, K. *et al.* Experimental observation of topological fermi arcs in type-II Weyl semimetal MoTe₂. *Nature Physics* **12**, 1105 (2016).
- [196] Tamai, A. *et al.* Fermi arcs and their topological character in the candidate type-II Weyl semimetal MoTe₂. *Physical Review X* **6**, 031021 (2016).
- [197] Huang, L. *et al.* Spectroscopic evidence for a type II Weyl semimetallic state in MoTe₂. *Nature materials* **15**, 1155 (2016).
- [198] Jiang, J. *et al.* Signature of type-II Weyl semimetal phase in MoTe₂. *Nature communications* **8**, 13973 (2017).
- [199] Zhou, L. *et al.* Sensitive phonon-based probe for structure identification of 1T' MoTe₂. *Journal of the American Chemical Society* **139**, 8396 (2017).
- [200] He, R. *et al.* Dimensionality-driven orthorhombic MoTe₂ at room temperature. *Physical Review B* **97**, 041410 (2018).
- [201] Zhong, S. *et al.* Origin of magnetoresistance suppression in thin γ - MoTe₂. *Physical Review B* **97**, 241409 (2018).
- [202] Stiehl, G. M. *et al.* Layer-dependent spin-orbit torques generated by the centrosymmetric transition metal dichalcogenide β - MoTe₂. *Physical Review B* **100**, 184402 (2019).

- [203] Zhou, J., Qiao, J., Bournel, A. & Zhao, W. Intrinsic spin Hall conductivity of the semimetals MoTe₂ and WTe₂. *Physical Review B* **99**, 060408 (2019).
- [204] Manzeli, S., Ovchinnikov, D., Pasquier, D., Yazyev, O. V. & Kis, A. 2d transition metal dichalcogenides. *Nature Reviews Materials* **2**, 17033 (2017).
- [205] Geim, A. K. & Grigorieva, I. V. Van der waals heterostructures. *Nature* **499**, 419 (2013).
- [206] Britnell, L. *et al.* Field-effect tunneling transistor based on vertical graphene heterostructures. *Science* **335**, 947 (2012).
- [207] Georgiou, T. *et al.* Vertical field-effect transistor based on graphene–WS₂ heterostructures for flexible and transparent electronics. *Nature nanotechnology* **8**, 100 (2013).
- [208] Ajayan, P., Kim, P. & Banerjee, K. van der waals materials. *Physics Today* **69**, 38 (2016).
- [209] Cao, Y. *et al.* Correlated insulator behaviour at half-filling in magic-angle graphene superlattices. *Nature* **556**, 80 (2018).
- [210] Cao, Y. *et al.* Unconventional superconductivity in magic-angle graphene superlattices. *Nature* **556**, 43 (2018).
- [211] Drögeler, M. *et al.* Spin lifetimes exceeding 12 ns in graphene nonlocal spin valve devices. *Nano Letters* **16**, 3533 (2016).
- [212] Gebeyehu, Z. M. *et al.* Spin communication over 30 μm long channels of chemical vapor deposited graphene on SiO₂. *2D Materials* **6**, 034003 (2019).
- [213] Khokhriakov, D. *et al.* Robust spin interconnect with isotropic spin dynamics in chemical vapor deposited graphene layers and boundaries. *ACS nano* **14**, 15864 (2020).
- [214] Panda, J., Ramu, M., Karis, O., Sarkar, T. & Kamalakar, M. V. Ultimate spin currents in commercial chemical vapor deposited graphene. *ACS nano* **14**, 12771 (2020).
- [215] Kim, H. H. *et al.* One million percent tunnel magnetoresistance in a magnetic van der waals heterostructure. *Nano Letters* **18**, 4885 (2018).
- [216] Song, T. *et al.* Giant tunneling magnetoresistance in spin-filter van der Waals heterostructures. *Science* **360**, 1214 (2018).
- [217] Klein, D. R. *et al.* Probing magnetism in 2D van der Waals crystalline insulators via electron tunneling. *Science* **360**, 1218 (2018).
- [218] Wen, H. *et al.* Experimental demonstration of xor operation in graphene magnetologic gates at room temperature. *Physical Review Applied* **5**, 044003 (2016).
- [219] Khokhriakov, D. *et al.* Multifunctional spin logic gates in graphene spin circuits. *arXiv preprint arXiv:2108.12259* (2021).
- [220] Lin, C.-C. *et al.* Spin transfer torque in a graphene lateral spin valve assisted by an external magnetic field. *Nano Letters* **13**, 5177 (2013).
- [221] Lin, C.-C. *et al.* Improvement of spin transfer torque in asymmetric graphene devices. *ACS nano* **8**, 3807 (2014).
- [222] Yan, W. *et al.* A two-dimensional spin field-effect switch. *Nature communications* **7**, 13372 (2016).
- [223] Dankert, A. & Dash, S. P. Electrical gate control of spin current in van der waals heterostructures at room temperature. *Nature communications* **8**, 16093 (2017).
- [224] Inгла-Aynés, J., Herling, F., Fabian, J., Hueso, L. E. & Casanova, F. Electrical control of valley-zeeman spin-orbit-coupling-induced spin precession at room temperature. *Physical Review Letters* **127**, 047202 (2021).

- [225] Ghiasi, T. S., Kaverzin, A. A., Blah, P. J. & van Wees, B. J. Charge-to-spin conversion by the Rashba–Edelstein effect in two-dimensional van der waals heterostructures up to room temperature. *Nano Letters* **19**, 5959 (2019).
- [226] Safeer, C. *et al.* Room-temperature spin Hall effect in graphene/mos2 van der waals heterostructures. *Nano Letters* **19**, 107 (2019).
- [227] Herling, F. *et al.* Gate tunability of highly efficient spin-to-charge conversion by spin Hall effect in graphene proximitized with WSe₂. *APL Materials* **8**, 071103 (2020).
- [228] Benitez, L. A. *et al.* Tunable room-temperature spin galvanic and spin Hall effects in van der waals heterostructures. *Nature materials* **19**, 1705 (2020).
- [229] Li, L. *et al.* Gate-tunable reversible Rashba–Edelstein effect in a few-layer graphene/2H-TaS₂ heterostructure at room temperature. *ACS nano* **14**, 5251 (2020).
- [230] Hoque, A. M., Khokhriakov, D., Karpiak, B. & Dash, S. P. Charge-spin conversion in layered semimetal TaTe₂ and spin injection in van der waals heterostructures. *Physical Review Research* **2**, 033204 (2020).
- [231] Zhao, B., Hoque, A. M., Khokhriakov, D., Karpiak, B. & Dash, S. P. Charge-spin conversion signal in WTe₂ van der waals hybrid devices with a geometrical design. *Applied Physics Letters* **117**, 242401 (2020).
- [232] Khokhriakov, D., Hoque, A. M., Karpiak, B. & Dash, S. P. Gate-tunable spin-galvanic effect in graphene-topological insulator van der waals heterostructures at room temperature. *Nature communications* **11**, 3657 (2020).
- [233] Zhao, B. *et al.* Unconventional charge–spin conversion in Weyl-semimetal WTe₂. *Advanced Materials* **32**, 2000818 (2020).
- [234] Zhao, B. *et al.* Observation of charge to spin conversion in Weyl semimetal wte₂ at room temperature. *Physical Review Research* **2**, 013286 (2020).
- [235] Hoque, A. M. *et al.* All-electrical creation and control of spin-galvanic signal in graphene and molybdenum ditelluride heterostructures at room temperature. *Communications Physics* **4**, 124 (2021).
- [236] Yang, T.-Y. *et al.* Observation of long spin-relaxation times in bilayer graphene at room temperature. *Physical Review Letters* **107**, 047206 (2011).
- [237] Wang, W. *et al.* Magnetotransport properties of mesoscopic graphite spin valves. *Physical Review B* **77**, 020402 (2008).
- [238] Dlubak, B. *et al.* Homogeneous pinhole free 1 nm al₂o₃ tunnel barriers on graphene. *Applied Physics Letters* **101**, 203104 (2012).
- [239] Yamaguchi, T., Masubuchi, S., Iguchi, K., Moriya, R. & Machida, T. Tunnel spin injection into graphene using al₂o₃ barrier grown by atomic layer deposition on functionalized graphene surface. *Journal of magnetism and magnetic materials* **324**, 849 (2012).
- [240] Komatsu, K. *et al.* Spin injection and detection in a graphene lateral spin valve using an yttrium-oxide tunneling barrier. *Applied Physics Express* **7**, 085101 (2014).
- [241] Singh, S. *et al.* Strontium oxide tunnel barriers for high quality spin transport and large spin accumulation in graphene. *Nano Letters* **17**, 7578 (2017).
- [242] Han, W. *et al.* Tunneling spin injection into single layer graphene. *Physical Review Letters* **105**, 167202 (2010).

- [243] Fu, W., Makk, P., Maurand, R., Bräuninger, M. & Schönenberger, C. Large-scale fabrication of bn tunnel barriers for graphene spintronics. *Journal of applied physics* **116**, 074306 (2014).
- [244] Friedman, A. L., van't Erve, O. M., Li, C. H., Robinson, J. T. & Jonker, B. T. Homoepitaxial tunnel barriers with functionalized graphene-on-graphene for charge and spin transport. *Nature communications* **5**, 3161 (2014).
- [245] Friedman, A. L., van't Erve, O. M., Robinson, J. T., Whitener Jr, K. E. & Jonker, B. T. Hydrogenated graphene as a homoepitaxial tunnel barrier for spin and charge transport in graphene. *ACS nano* **9**, 6747 (2015).
- [246] Friedman, A. L., van 't Erve, O. M., Robinson, J. T., Whitener Jr, K. E. & Jonker, B. T. Homoepitaxial graphene tunnel barriers for spin transport. *AIP Advances* **6**, 056301 (2016).
- [247] Gurram, M., Omar, S. & van Wees, B. J. Bias induced up to 100% spin-injection and detection polarizations in ferromagnet/bilayer-hBN/graphene/hBN heterostructures. *Nature communications* **8**, 248 (2017).
- [248] Leutenantsmeyer, J. C., Ingla-Aynés, J., Gurram, M. & van Wees, B. J. Efficient spin injection into graphene through trilayer hBN tunnel barriers. *Journal of Applied Physics* **124**, 194301 (2018).
- [249] Kamalakar, M. V., Dankert, A., Kelly, P. J. & Dash, S. P. Inversion of spin signal and spin filtering in ferromagnet— hexagonal boron nitride-graphene van der waals heterostructures. *Scientific reports* **6**, 21168 (2016).
- [250] Vila Tusell, M. *Fundamentals of Spin Dynamics in Two-Dimensional Materials*, 13 (Springer International Publishing, Cham, 2022).
- [251] Wojtaszek, M., Vera-Marun, I., Whiteway, E., Hilke, M. & van Wees, B. Absence of hyperfine effects in 13 c-graphene spin-valve devices. *Physical Review B* **89**, 035417 (2014).
- [252] Huertas-Hernando, D., Guinea, F. & Brataas, A. Spin-orbit-mediated spin relaxation in graphene. *Physical Review Letters* **103**, 146801 (2009).
- [253] Ochoa, H., Castro Neto, A. H. & Guinea, F. Elliot-yafet mechanism in graphene. *Physical Review Letters* **108**, 206808 (2012).
- [254] Ochoa, H., Neto, A. C., Fal'Ko, V. & Guinea, F. Spin-orbit coupling assisted by flexural phonons in graphene. *Physical Review B* **86**, 245411 (2012).
- [255] Avsar, A. *et al.* Colloquium: Spintronics in graphene and other two-dimensional materials. *Reviews of Modern Physics* **92**, 021003 (2020).
- [256] Van Tuan, D., Ortmann, F., Soriano, D., Valenzuela, S. O. & Roche, S. Pseudospin-driven spin relaxation mechanism in graphene. *Nature Physics* **10**, 857 (2014).
- [257] Kochan, D., Gmitra, M. & Fabian, J. Spin relaxation mechanism in graphene: resonant scattering by magnetic impurities. *Physical Review Letters* **112**, 116602 (2014).
- [258] Lundeborg, M. B., Yang, R., Renard, J. & Folk, J. A. Defect-mediated spin relaxation and dephasing in graphene. *Physical Review Letters* **110**, 156601 (2013).
- [259] Soriano, D. *et al.* Spin transport in hydrogenated graphene. *2D Materials* **2**, 022002 (2015).
- [260] Droggeller, M. *et al.* Nanosecond spin lifetimes in single-and few-layer graphene-hBN heterostructures at room temperature. *Nano Letters* **14**, 6050 (2014).

- [261] Drögeler, M., Volmer, F., Stampfer, C. & Beschoten, B. Simulations on the influence of spatially varying spin transport parameters on the measured spin lifetime in graphene non-local spin valves. *physica status solidi (b)* **254**, 1700293 (2017).
- [262] Dyrdał, A., Barnaś, J. & Dugaev, V. Current-induced spin polarization in graphene due to Rashba spin-orbit interaction. *Physical Review B* **89**, 075422 (2014).
- [263] Gmitra, M. & Fabian, J. Graphene on transition-metal dichalcogenides: A platform for proximity spin-orbit physics and optospintronics. *Physical Review B* **92**, 155403 (2015).
- [264] Gmitra, M., Kochan, D., Högl, P. & Fabian, J. Trivial and inverted Dirac bands and the emergence of quantum spin Hall states in graphene on transition-metal dichalcogenides. *Physical Review B* **93**, 155104 (2016).
- [265] Offidani, M., Millettari, M., Raimondi, R. & Ferreira, A. Optimal charge-to-spin conversion in graphene on transition-metal dichalcogenides. *Physical Review Letters* **119**, 196801 (2017).
- [266] Garcia, J. H., Cummings, A. W. & Roche, S. Spin Hall effect and weak antilocalization in graphene/transition metal dichalcogenide heterostructures. *Nano Letters* **17**, 5078 (2017).
- [267] Millettari, M., Offidani, M., Ferreira, A. & Raimondi, R. Covariant conservation laws and the spin Hall effect in Dirac-Rashba systems. *Physical Review Letters* **119**, 246801 (2017).
- [268] Garcia, J. H., Vila, M., Cummings, A. W. & Roche, S. Spin transport in graphene/transition metal dichalcogenide heterostructures. *Chemical Society Reviews* **47**, 3359 (2018).
- [269] Žutić, I., Matos-Abiague, A., Scharf, B., Dery, H. & Belashchenko, K. Proximitized materials. *Materials Today* **22**, 85 (2019).
- [270] Wang, Z. *et al.* Strong interface-induced spin-orbit interaction in graphene on WS₂. *Nature communications* **6**, 8339 (2015).
- [271] Yang, B. *et al.* Tunable spin-orbit coupling and symmetry-protected edge states in graphene/WS₂. *2D Materials* **3**, 031012 (2016).
- [272] Zihlmann, S. *et al.* Large spin relaxation anisotropy and valley-zeeman spin-orbit coupling in WSe₂/graphene/h-BN heterostructures. *Physical Review B* **97**, 075434 (2018).
- [273] Wakamura, T. *et al.* Strong anisotropic spin-orbit interaction induced in graphene by monolayer ws 2. *Physical Review Letters* **120**, 106802 (2018).
- [274] Yang, B. *et al.* Effect of distance on photoluminescence quenching and proximity-induced spin-orbit coupling in graphene/WSe₂ heterostructures. *Nano Letters* **18**, 3580 (2018).
- [275] Ghiasi, T. S., Ingla-Aynés, J., Kaverzin, A. A. & van Wees, B. J. Large proximity-induced spin lifetime anisotropy in transition-metal dichalcogenide/graphene heterostructures. *Nano Letters* **17**, 7528 (2017).
- [276] Cummings, A. W., Garcia, J. H., Fabian, J. & Roche, S. Giant spin lifetime anisotropy in graphene induced by proximity effects. *Physical Review Letters* **119**, 206601 (2017).
- [277] Benítez, L. A. *et al.* Strongly anisotropic spin relaxation in graphene-transition metal dichalcogenide heterostructures at room temperature. *Nature Physics* **14**, 303 (2018).
- [278] Gallego, S. V., Etxebarria, J., Elcoro, L., Tasci, E. S. & Perez-Mato, J. M. Automatic calculation of symmetry-adapted tensors in magnetic and non-magnetic materi-

- als: a new tool of the bilbao crystallographic server. *Acta Crystallographica Section A: Foundations and Advances* **75**, 438 (2019).
- [279] MacNeill, D. *et al.* Control of spin-orbit torques through crystal symmetry in WTe₂/ferromagnet bilayers. *Nature Physics* **13**, 300 (2017).
- [280] MacNeill, D. *et al.* Thickness dependence of spin-orbit torques generated by WTe₂. *Physical Review B* **96**, 054450 (2017).
- [281] Guimaraes, M. H., Stiehl, G. M., MacNeill, D., Reynolds, N. D. & Ralph, D. C. Spin-orbit torques in nbse₂/permalloy bilayers. *Nano Letters* **18**, 1311 (2018).
- [282] Song, P. *et al.* Coexistence of large conventional and planar spin Hall effect with long spin diffusion length in a low-symmetry semimetal at room temperature. *Nature materials* **19**, 292 (2020).
- [283] Castro Neto, A. H. & Guinea, F. Impurity-induced spin-orbit coupling in graphene. *Physical Review Letters* **103**, 026804 (2009).
- [284] Weeks, C., Hu, J., Alicia, J., Franz, M. & Wu, R. Engineering a robust quantum spin Hall state in graphene via adatom deposition. *Physical Review X* **1**, 021001 (2011).
- [285] Ma, D., Li, Z. & Yang, Z. Strong spin-orbit splitting in graphene with adsorbed Au atoms. *Carbon* **50**, 297 (2012).
- [286] Gmitra, M., Kochan, D. & Fabian, J. Spin-orbit coupling in hydrogenated graphene. *Physical Review Letters* **110**, 246602 (2013).
- [287] Ferreira, A., Rappoport, T. G., Cazalilla, M. A. & Neto, A. C. Extrinsic spin Hall effect induced by resonant skew scattering in graphene. *Physical Review Letters* **112**, 066601 (2014).
- [288] Pachoud, A., Ferreira, A., Özyilmaz, B. & Neto, A. C. Scattering theory of spin-orbit active adatoms on graphene. *Physical Review B* **90**, 035444 (2014).
- [289] Irmer, S. *et al.* Spin-orbit coupling in fluorinated graphene. *Physical Review B* **91**, 115141 (2015).
- [290] Tan, J. *et al.* Electronic transport in graphene-based heterostructures. *Applied Physics Letters* **104**, 183504 (2014).
- [291] Avsar, A. *et al.* Spin-orbit proximity effect in graphene. *Nature communications* **5**, 4875 (2014).
- [292] Cresti, A., Nikolić, B. K., García, J. H. & Roche, S. Charge, spin and valley hall effects in disordered graphene. *La Rivista del Nuovo Cimento* **39**, 587 (2016).
- [293] Johansson, A., Henk, J. & Mertig, I. Edelstein effect in Weyl semimetals. *Physical Review B* **97**, 085417 (2018).
- [294] Wan, X., Turner, A. M., Vishwanath, A. & Savrasov, S. Y. Topological semimetal and Fermi-arc surface states in the electronic structure of pyrochlore iridates. *Physical Review B* **83**, 205101 (2011).
- [295] Ishizaka, K. *et al.* Giant rashba-type spin splitting in bulk BiTeI. *Nature materials* **10**, 521 (2011).
- [296] Kovács-Krausz, Z. *et al.* Electrically controlled spin injection from giant rashba spin-orbit conductor BiTeBr. *Nano Letters* **20**, 4782 (2020).
- [297] Li, Y. *et al.* Nonreciprocal charge transport up to room temperature in bulk rashba semiconductor α -geTe. *Nature communications* **12**, 540 (2021).
- [298] Yan, W. *et al.* Large room temperature spin-to-charge conversion signals in a few-layer graphene/Pt lateral heterostructure. *Nature communications* **8**, 661 (2017).

- [299] Zhao, B. *et al.* Electrically controlled spin-switch and evolution of hane spin precession in graphene. *2D Materials* **6**, 035042 (2019).
- [300] Zhao, B. *et al.* Van der waals magnet based spin-valve devices at room temperature. *arXiv preprint arXiv:2107.00310* (2021).
- [301] Ghiasi, T. S. *et al.* Electrical and thermal generation of spin currents by magnetic bilayer graphene. *Nature nanotechnology* **788** (2021).
- [302] Castellanos-Gomez, A. *et al.* Deterministic transfer of two-dimensional materials by all-dry viscoelastic stamping. *2D Materials* **1**, 011002 (2014).
- [303] Blake, P. *et al.* Making graphene visible. *Applied physics Letters* **91**, 063124 (2007).
- [304] Zhang, X., Wan, S., Pu, J., Wang, L. & Liu, X. Highly hydrophobic and adhesive performance of graphene films. *Journal of Materials Chemistry* **21**, 12251–12258 (2011).
- [305] Graphene - Info. The Graphene experts. <https://www.graphene-info.com/>. Accessed: 2022-01-15.
- [306] Nitto. Innovation for costumers. https://www.nitto.com/eu/en/products/surface/spv_metal017/. Accessed: 2022-01-17.
- [307] Mirabelli, G. *et al.* Air sensitivity of MoS₂, MoSe₂, MoTe₂, HfS₂, and HfSe₂. *Journal of Applied Physics* **120**, 125102 (2016).
- [308] Zheng, X. *et al.* Controlled layer-by-layer oxidation of MoTe₂ via O₃ exposure. *ACS applied materials & interfaces* **10**, 30045 (2018).
- [309] Pham, T. T., Castelino, R., Felten, A. & Sporcken, R. Study of surface oxidation and recovery of clean MoTe₂ films. *Surfaces and Interfaces* 101681 (2021).
- [310] Liu, H., Han, N. & Zhao, J. Atomistic insight into the oxidation of monolayer transition metal dichalcogenides: from structures to electronic properties. *Rsc Advances* **5**, 17572 (2015).
- [311] Raith nanofabrication. <https://www.raith.com/>. Accessed: 2022-01-16.
- [312] Instruments, K. *Model 2182 and 2182A Nanovoltmeter. Users Manual*. Keithley Instruments. Available at https://download.tek.com/manual/2182A-900-01_May_2017.pdf.
- [313] Agilent — trusted answers. <https://www.agilent.com/>. Accessed: 2022-01-16.
- [314] Witec. an Oxford instruments company. <https://www.witec.de>. Accessed: 2022-01-16.
- [315] Renishaw apply innovation. <https://www.renishaw.com/en/>. Accessed: 2022-01-16.
- [316] Linkam. <https://www.linkam.co.uk/>. Accessed: 2022-01-16.
- [317] Ferrari, A. C. *et al.* Raman spectrum of graphene and graphene layers. *Physical Review Letters* **97**, 187401 (2006).
- [318] Malard, L., Pimenta, M., Dresselhaus, G. & Dresselhaus, M. Raman spectroscopy in graphene. *Physics Reports* **473**, 51 (2009).
- [319] Ferrari, A. C. & Basko, D. M. Raman spectroscopy as a versatile tool for studying the properties of graphene. *Nature nanotechnology* **8**, 235–246 (2013).
- [320] Dawson, W. & Bullett, D. Electronic structure and crystallography of MoTe₂ and WTe₂. *Journal of Physics C: Solid State Physics* **20**, 6159 (1987).
- [321] Beams, R. *et al.* Characterization of few-layer 1T' MoTe₂ by polarization-resolved second harmonic generation and raman scattering. *ACS nano* **10**, 9626 (2016).

- [322] Heikes, C. *et al.* Mechanical control of crystal symmetry and superconductivity in Weyl semimetal MoTe₂. *Physical Review Materials* **2**, 074202 (2018).
- [323] Rhodes, D. *et al.* Engineering the structural and electronic phases of MoTe₂ through W substitution. *Nano Letters* **17**, 1616 (2017).
- [324] Oliver, S. M. *et al.* The structural phases and vibrational properties of Mo_{1-x}W_xTe₂ alloys. *2D Materials* **4**, 045008 (2017).
- [325] Kim, H.-J., Kang, S.-H., Hamada, I. & Son, Y.-W. Origins of the structural phase transitions in MoTe₂ and WTe₂. *Physical Review B* **95**, 180101 (2017).
- [326] Cardonlichtbuer, P. M. & Taylor, P. L. Theory of the saturation magnetoresistance in cubic metals. *Physical Review B* **14**, 1341 (1976).
- [327] Pippard, A. *Magnetoresistance in metals* Cambridge University Press (1989).
- [328] Liang, T. *et al.* Ultrahigh mobility and giant magnetoresistance in the dirac semimetal Cd₃As₂. *Nature materials* **14**, 280 (2015).
- [329] Wang, K., Graf, D., Li, L., Wang, L. & Petrovic, C. Anisotropic giant magnetoresistance in NbSb₂. *Scientific reports* **4**, 7328 (2014).
- [330] Ali, M. N. *et al.* Large, non-saturating magnetoresistance in WTe₂. *Nature* **514**, 205 (2014).
- [331] Shekhar, C. *et al.* Extremely large magnetoresistance and ultrahigh mobility in the topological Weyl semimetal candidate NbP. *Nature Physics* **11**, 645 (2015).
- [332] Pai, C.-F. *et al.* Spin transfer torque devices utilizing the giant spin Hall effect of tungsten. *Applied Physics Letters* **101**, 122404 (2012).
- [333] Liu, L. *et al.* Spin-torque switching with the giant spin Hall effect of tantalum. *Science* **336**, 555 (2012).
- [334] Wang, X., Pauyac, C. O. & Manchon, A. Spin-orbit-coupled transport and spin torque in a ferromagnetic heterostructure. *Physical Review B* **89**, 054405 (2014).
- [335] Gómez, J. *et al.* Spin transport parameters in Ni₈₀Fe₂₀/Ru and Ni₈₀Fe₂₀/Ta bilayers. *Physical Review B* **90**, 184401 (2014).
- [336] Vila, M. *et al.* Low-symmetry topological materials for large charge-to-spin interconversion: The case of transition metal dichalcogenide monolayers. *Physical Review Research* **3**, 043230 (2021).
- [337] Liu, L., Chen, C.-T. & Sun, J. Spin Hall effect tunnelling spectroscopy. *Nature Physics* **10**, 561 (2014).
- [338] Rijks, T. G., Coehoorn, R., De Jong, M. & De Jonge, W. Semiclassical calculations of the anisotropic magnetoresistance of nife-based thin films, wires, and multilayers. *Physical Review B* **51**, 283 (1995).
- [339] Jedema, F., Nijboer, M., Filip, A. & Van Wees, B. Spin injection and spin accumulation in Permalloy–Copper mesoscopic spin valves. *Journal of superconductivity* **15**, 27 (2002).
- [340] van Staa, A. & Meier, G. Anisotropic magnetoresistance and spin-valve effect in all-metal mesoscopic spin-valve devices. *Physica E: Low-dimensional Systems and Nanostructures* **31**, 142 (2006).
- [341] Stiehl, G. M. *et al.* Current-induced torques with Dresselhaus symmetry due to resistance anisotropy in 2D materials. *ACS nano* **13**, 2599 (2019).

- [342] de Vries, E. K. *et al.* Towards the understanding of the origin of charge-current-induced spin voltage signals in the topological insulator Bi_2Se_3 . *Physical Review B* **92**, 201102 (2015).
- [343] Li, P., Appelbaum, I. *et al.* Interpreting current-induced spin polarization in topological insulator surface states. *Physical Review B* **93**, 220404 (2016).
- [344] Torres, W. S. *et al.* Spin precession and spin Hall effect in monolayer graphene/Pt nanostructures. *2D Materials* **4**, 041008 (2017).
- [345] Li, P. *et al.* Spin-momentum locking and spin-orbit torques in magnetic nano-heterojunctions composed of Weyl semimetal WTe_2 . *Nature communications* **9**, 3990 (2018).
- [346] David, A., Rakyta, P., Kormányos, A. & Burkard, G. Induced spin-orbit coupling in twisted graphene-transition metal dichalcogenide heterobilayers: Twistronics meets spintronics. *Physical Review B* **100**, 085412 (2019).
- [347] Li, Y. & Koshino, M. Twist-angle dependence of the proximity spin-orbit coupling in graphene on transition-metal dichalcogenides. *Physical Review B* **99**, 075438 (2019).
- [348] Woods, C. *et al.* Commensurate-incommensurate transition in graphene on hexagonal boron nitride. *Nature physics* **10**, 451 (2014).
- [349] Wang, L. *et al.* Evidence for a fractional fractal quantum Hall effect in graphene superlattices. *Science* **350**, 1231 (2015).
- [350] Sagasta, E. *et al.* Unveiling the mechanisms of the spin Hall effect in Ta. *Physical Review B* **98**, 060410 (2018).
- [351] Niimi, Y. *et al.* Giant spin Hall effect induced by skew scattering from bismuth impurities inside thin film cubi alloys. *Physical Review Letters* **109**, 156602 (2012).
- [352] Laczkowski, P. *et al.* Large enhancement of the spin Hall effect in Au by side-jump scattering on Ta impurities. *Physical Review B* **96**, 140405 (2017).
- [353] Pham, V. T. *et al.* Spin-orbit magnetic state readout in scaled ferromagnetic/heavy metal nanostructures. *Nature Electronics* **3**, 309 (2020).
- [354] Geuzaine, C. GetDP: a general finite-element solver for the de Rham complex. In *PAMM: Proceedings in Applied Mathematics and Mechanics*, vol. 7, 1010603 (2007).
- [355] Saverio Torres, W. *et al.* Using domain walls to perform non-local measurements with high spin signal amplitudes. *Applied Physics Letters* **109**, 042405 (2016).
- [356] Zhou, Q. *et al.* Hall effect within the colossal magnetoresistive semimetallic state of MoTe_2 . *Physical Review B* **94**, 121101 (2016).
- [357] Couto, N. J. *et al.* Random strain fluctuations as dominant disorder source for high-quality on-substrate graphene devices. *Physical Review X* **4**, 041019 (2014).
- [358] Zhu, H. *et al.* Defects and surface structural stability of MoTe_2 under vacuum annealing. *ACS nano* **11**, 11005 (2017).
- [359] Tan, Y. *et al.* Controllable 2H-to-1T' phase transition in few-layer MoTe_2 . *Nanoscale* **10**, 19964 (2018).

